

***PROPERTIES OF BIOLOGICALLY RELEVANT NANOCOMPOSITES:***  
**EFFECTS OF CALCIUM PHOSPHATE**  
**NANOPARTICLE ATTRIBUTES AND BIODEGRADABLE**  
**POLYMER MORPHOLOGY**

A Dissertation  
Presented to  
The Academic Faculty

by

Jasmeet Kaur

In Partial Fulfillment  
of the Requirements for the Degree  
Doctor of Philosophy in the Polymer, Textile and Fiber Engineering

Georgia Institute of Technology  
May 2010

**COPYRIGHT 2010 BY JASMEET KAUR**

***PROPERTIES OF BIOLOGICALLY RELEVANT NANOCOMPOSITES:***  
**EFFECTS OF CALCIUM PHOSPHATE**  
**NANOPARTICLE ATTRIBUTES AND BIODEGRADABLE**  
**POLYMER MORPHOLOGY**

Approved by:

Dr. Meisha L. Shofner, Advisor  
School of Polymer, Textile and Fiber  
Engineering  
*Georgia Institute of Technology*

Dr. David G. Bucknall  
School of Polymer, Textile and Fiber  
Engineering  
*Georgia Institute of Technology*

Dr. Johnna S. Temenoff  
The Wallace H. Coulter Department of  
Biomedical Engineering  
*Georgia Institute of Technology*

Dr. Yonathan S. Thio  
School of Polymer, Textile and Fiber  
Engineering  
*Georgia Institute of Technology*

Dr. Donggang Yao  
School of Polymer, Textile and Fiber  
Engineering  
*Georgia Institute of Technology*

Date Approved: March 31, 2010

*This thesis is dedicated to my parents and the Almighty without whose blessings  
and grace this work would not have been possible.*

## ACKNOWLEDGEMENTS

I would like to take this opportunity to express my sincerest thanks and gratitude to my advisor Dr. Meisha L. Shofner for her invaluable advice, guidance, patience and constant support during my research. I would like to thank Dr. David G. Bucknall, Dr. Johnna S. Temenoff, Dr. Yonathan S. Thio and Dr. Donggang Yao for taking out time to serve as my thesis committee members and for their suggestions.

In addition I am also grateful to Yolande Berta for providing me training on the electron microscope, EDX and for her personal guidance on the use of these instruments. I am sincerely thankful to Dr. Jung-il Hong for providing me training on the X-ray machine and for helping in the analysis of nanoparticle X-ray diffraction.

My sincerest thanks to my current group members Michelle Schlea, Bradley Johnson, Ji Hoon Lee and Jae Ik Choi for their valuable support and discussions. I would also like to thank my former group members Eric Crawford and Dr. Xiaolan Hu. I would like to thank Dr. Marilyn L. Minus for her valuable suggestions for my thesis and help with the microscopy study. I am grateful to Dr. Sudhakar Jagannathan for helping out with the surface area measurements.

I am thankful to my friends, Ramasubramani Kuduva Raman Thanumoorthy, Erica Ford, Yubin Shen, Mihir Oka and Sungwon Ma who were a constant support both emotionally and technically during my research.

Last but not the least I would like to express my sincere love and respect for my parents, Bhupinder Singh and Gursharan Kaur, who have been a pillar of support and encouragement. I am truly indebted to them for the sacrifices they have made for my

education. I am grateful to my parents-in law, Kuldip Singh and Amarjeet Kaur, for their support and love. Words fall short in expressing my heartfelt thanks to my husband Shivinder Singh, who has been there day and night to support and encourage me to finish my thesis.

# TABLE OF CONTENTS

	Page
ACKNOWLEDGEMENTS	v
LIST OF TABLES	xi
LIST OF FIGURES	xiii
LIST OF SYMBOLS AND ABBREVIATIONS	xvii
SUMMARY	xx
<u>CHAPTER</u>	
1. INTRODUCTION	1
2. BACKGROUND	5
2.1. Nanocomposites: Introduction	5
2.2. Classification of Nanocomposites	6
2.2.1. Nanoplatelet/Layered Composites (2-dimensional)	6
2.2.2. Nanofiber/tube Composites (1-dimensional)	8
2.2.3. Nanoparticulate Composites (0-dimensional)	9
2.3. Nanoparticle Attributes	10
2.3.1. Particle Size	11
2.3.2. Dispersion and Surface Chemistry	11
2.3.3. Shape	13
2.4. Networks of Polymer Nanocomposites	13
2.5. Calcium Phosphates and their Properties	15
2.5.1. Hydroxyapatite (HAp)	16
2.5.2. Calcium-deficient Hydroxyapatite (CDHAp)	17

2.5.3. Dicalcium Phosphate Anhydrous (DCPA)/Monetite	18
2.5.4. Octacalcium Phosphate (OCP)	18
2.5.6. Chlorapatite	19
2.6. Microemulsion Technique	19
2.7. Hydrothermal Technique	21
2.8. Factors Affecting Synthesis of Calcium Phosphate Nanoparticles	22
2.8.1. Effect of $W_0 = ([\text{H}_2\text{O}] / [\text{Surfactant}])$	23
2.8.2. Effect of Co-surfactant to Surfactant ratio $P_0$	24
2.8.3. Effect of Mixed Surfactant	24
2.8.4. Effect of Reactant Concentration, Ageing Time	25
2.8.5. Effect of Temperature	25
2.8.6. Effect of pH	26
2.9. Biodegradable Polymers	27
2.9.1. Poly ( $\epsilon$ -caprolactone) (PCL)	28
2.9.2. Poly (3-hydroxybutyrate) (PHB)	29
3. EFFECT OF NANOPARTICLE SURFACE AREA ON THE PROPERTIES OF NANOCOMPOSITES	32
3.1. Introduction	32
3.2. Experimental	34
3.2.1. Materials	34
3.2.2. HAp Nanoparticle Synthesis	35
3.2.3. Particle Characterization	36
3.2.4. Nanocomposite Processing	38
3.2.5. Nanocomposite Characterization	38
3.2. Results and Discussion	40

3.3.1. Morphology and Size of HAp nanoparticles	40
3.3.2. Chemical Structure of HAp nanoparticles	42
3.3.3. Crystal Structure of HAp nanoparticles	43
3.3.4. Specific Surface area and Density of HAp Nanoparticles	43
3.3.5. Dispersion and Distribution of HAp Particles in Nanocomposites	44
3.3.6. Thermal properties and Crystallization Kinetics of Nanocomposites	46
3.3.7. Viscoelastic Properties of Nanocomposites	50
3.3.8. Mechanical Composite models	57
3.4. Conclusions	62
4. EFFECT OF MATRIX CRYSTALLINITY ON THE PROPERTIES OF NANOCOMPOSITES	63
4.1. Introduction	63
4.2. Experimental	65
4.2.1. Materials	65
4.2.1. Nanocomposite Processing	66
4.2.3. Nanocomposite Characterization	66
4.3. Results and Discussion	69
4.3.1. Dispersion and Distribution of HAp in Nanocomposites	70
4.3.2. Thermal Properties and Crystallization Kinetics of Nanocomposites	72
4.3.3. Viscoelastic Properties of Nanocomposites	81
4.4. Conclusions	89
5. EFFECT OF NANOPARTICLE SHAPE ON THE PROPERTIES OF NANOCOMPOSITES	91
5.1. Introduction	91



5.2. Experimental	93
5.2.1. Materials for Synthesis of Near-Spherical Calcium Phosphate Nanoparticles	93
5.2.2. Synthesis of Near-Spherical Calcium Phosphate Nanoparticles	94
5.2.3. Materials for Synthesis of Calcium Phosphate Nanofibers	95
5.2.4. Synthesis of Calcium Phosphate Nanofibers	95
5.2.5. Nanoparticle Characterization	96
5.2.6. Nanocomposite Preparation	98
5.2.7. Nanocomposite Characterization	99
5.3. Results and Discussion	102
5.3.1. Morphology of Nanoparticles	102
5.3.2. Chemical Structure of Nanoparticles	103
5.3.3. Crystal Structure of Nanoparticles	105
5.3.4. Elemental Analysis, Ca/P Ratio and Density of Nanoparticles	108
5.3.5. Nanoparticle Size and Specific Surface Area	109
5.3.6. Dispersion and Distribution of Nanoparticles in Nanocomposites	110
5.3.7. Thermal Properties and Crystallization Kinetics of Nanocomposites	114
5.3.8. Viscoelastic Properties of Nanocomposites	124
5.3.9. X-ray diffraction of Nanocomposites	130
5.3.10. Micromechanical Modelling	133
5.4. Conclusions	136
6. CONCLUSIONS	138
APPENDIX A	144

APPENDIX B	145
APPENDIX C	150
APPENDIX D	153
REFERENCES	164

## LIST OF TABLES

Table	Page
Table 2. 1. Typical thermal and mechanical properties of PCL and PHB polymers. ....	28
Table 3. 1. Plane spacings observed in X-ray powder diffraction pattern of HAp and comparison with respective data for stoichiometric HAp. ....	43
Table 3. 2. Percent crystallinity of neat PCL and HAp/PCL composite samples from first and second heat cycles of DSC. <sup>[70]</sup> .....	46
Table 3. 3. Isothermal crystallization parameters for PCL, HAp60 and HAp111/PCL composite samples at $T_c = 40^\circ\text{C}$ . <sup>[70]</sup> .....	50
Table 4. 1. Differences in thermal properties and crystallinity of Neat PCL and PHB polymers. ....	70
Table 4. 2. Melting ( $T_m$ ) and crystallization ( $T_c$ ) temperatures of neat PHB and PCL and their composites with HAp111 nanoparticles from first heat. ....	76
Table 4. 3. Isothermal crystallization parameters for PHB and HAp111/PHB composite samples at $T_c = 120, 125$ and $130^\circ\text{C}$ . ....	80
Table 5. 1. $2\theta$ and d-spacing of NF-CaP nanoparticles from XRD scan in descending order of intensity compared to d-spacing from PDF card files of DCPA/Monetite and Chlorapatite phases. ....	107
Table 5. 2. Particle size measurement from DLS and TEM and comparison of surface area of nanoparticles measured from TEM dimensions and from BET. ....	109
Table 5. 3. Peak melting ( $T_m$ ) and crystallization ( $T_c$ ) temperatures of neat PHB, NS-CaP/PHB nanocomposites and NF-CaP/PHB nanocomposites from first heating and cooling cycle. ....	115
Table 5. 4. Isothermal crystallization parameters for NS-CaP/PHB and NF-CaP/PHB nanocomposite samples at $T_c = 120, 125$ and $130^\circ\text{C}$ . ....	121
Table 5. 5. Rigid amorphous fraction (RAF) of NS-CaP/PHB and NF-CaP/PHB nanocomposites as a function of nanoparticle concentration. ....	122
Table 5. 6. Effect of NS-CaP and NF-CaP nanoparticles on the FWHM and crystallite size for (020) and (110) reflections. ....	133
Table A. 1. Different phases of calcium phosphates, their chemical formulas, Ca/P ratios, density and crystal structure. ....	144

Table B. 1. Isothermal crystallization parameters of neat PCL, HAp60 and HAp111/PCL composites at 40, 42, 44 and 46°C. ....	149
Table C. 1. First and second heat crystallinity values of neat PHB and HAp111/PHB composites.....	150
Table C. 2. Melting ( $T_m$ ) and crystallization ( $T_c$ ) temperatures of neat PHB and PCL and their composites with HAp111 nanoparticles from second heat.....	151
Table D. 1. $2\theta$ and d-spacing of NF-CaP nanoparticles from XRD scan in descending order of intensity compared to d-spacing from PDF card files of other phases of calcium phosphates.....	154
Table D. 2. $2\theta$ and d-spacing of NS-CaP nanoparticles from XRD scan in descending order of intensity compared to d-spacing from PDF card file of CDHAp ....	155
Table D. 3. Percent crystallinity of neat PHB and NS-CaP/PHB composite samples from first and second heating cycles of DSC.....	155
Table D. 4. Percent crystallinity of neat PHB, and NF-CaP/PHB composite samples from first and second heating cycles of DSC.....	156
Table D. 5. Peak Melting ( $T_m$ ) and crystallization ( $T_c$ ) temperatures of neat PHB, NS-CaP/PHB and NF-CaP/PHB nanocomposites from second heating and cooling cycle. ....	156
Table D. 6. Thermogravimetric analysis of neat PHB, NS-CaP/PHB and NF-CaP/PHB nanocomposites. The temperature of 50% weight loss and peak temperature of degradation from derivative of weight% with respect to temperature. ....	163

## LIST OF FIGURES

Figure	Page
Figure 2. 1.Nano/microstructures formed in nanocomposites at increasing nanoparticle concentration. ....	15
Figure 2. 2.Simplified representation of organized structures formed by surfactants. ....	20
Figure 2. 3.Synthesis of poly ( $\epsilon$ -caprolactone) (PCL) by ring opening polymerization....	28
Figure 2. 4.Structure of repeat unit of poly (3-hydroxybutyrate) (PHB).....	29
Figure 3.1.Morphology of HAp nanoparticles as observed in TEM. (A) HAp60 showing platelet shape and (B) HAp111 showing needle-like morphology of individual particles. ....	41
Figure 3. 2.Infrared spectra of as synthesized HAp60 and HAp111 powders normalized to The highest intensity peak corresponding to phosphate functional group...	42
Figure 3. 3.SEM images showing dispersion of HAp nanoparticles in (A) HAp60/PCL (10 wt. %) and, (B) HAp111/PCL (10 wt. %) composite samples. ....	45
Figure 3. 4.% Crystallinity from second heat as a function of filler content for neat, HAp60 and HAp111 composite samples.....	47
Figure 3.5.Half-time crystallization of neat PCL and HAp nanocomposites as a function of crystallization temperature. ....	48
Figure 3.6.Storage modulus values of neat PCL and (a) HAp60 and (b) HAp111 nanocomposite samples.. ....	51
Figure 3.7.Loss modulus values of neat PCL and (a) HAp60 and (b) HAp111 nanocomposite samples. ....	53
Figure 3.8.Normalized storage modulus curves for 10 wt. % HAp/PCL nanocomposite samples.....	54
Figure 3.9.Normalized loss modulus curves for 10 wt. % HAp/PCL nanocomposite samples. similar amounts of reinforcement are seen in loss modulus in both composites above $T_g$ . ....	56
Figure 3.10.The dependence of relative storage modulus ( $G_r'$ ) as a function of filler volume fraction compared to the simplified Kerner model at (a) $-80^\circ\text{C}$ and (b) $-10^\circ\text{C}$ .. ....	59

Figure 3.11. Relative storage modulus as a function of filler surface area (per gram of nanocomposite sample) dependence for the composite samples with HAp60 and HAp111 (Temperature = -10°C).	61
Figure 4. 1. SEM images showing dispersion of HAp nanoparticles in (a) 0.5 wt. % HAp111/PHB, (b) 1 wt. % HAp111/PHB, (c) 5 wt. % HAp111/PHB and, (d) 10 wt. % HAp111/PHB composite samples.	72
Figure 4. 2. Crystallinity from first heat as a function of filler content for neat PHB and PCL as well as HAp111/PHB and HAp111/PCL composite samples.	73
Figure 4. 3. Isothermal crystallization of neat PHB and HAp111/PHB composites at 120°C.	77
Figure 4. 4. Half-time crystallization of (a) neat PCL and HAp111/PHB and (b) neat PHB and HAp111/PHB nanocomposites samples as a function of crystallization temperature.	78
Figure 4. 5. Storage modulus values of (a) neat PCL and HAp111/PCL and (b) neat PHB and HAp111/PHB nanocomposite samples.	82
Figure 4. 6. Loss modulus values of (a) neat PCL and HAp111/PCL and (b) neat PHB and HAp111/PHB nanocomposite samples.	85
Figure 4. 7. Normalized storage modulus curves for (a) 1 and 10 wt. % HAp111/PCL and (b) 1 and 10 wt. % HAp111/PHB nanocomposite samples.	88
Figure 5. 1. Morphology of the near-spherical calcium phosphate nanoparticles as seen in TEM.	103
Figure 5. 2. Morphology of the nanofiber calcium phosphate nanoparticles as seen in TEM.	103
Figure 5.3. Infrared spectra of as synthesized near-spherical (NS) and nanofiber calcium phosphate (NF-CaP) nanoparticles normalized to the highest intensity peak corresponding to phosphate functional group	104
Figure 5. 4. XRD patterns of synthesized near-spherical (NS) and nanofiber calcium phosphate (NF-CaP) nanoparticles.	106
Figure 5. 5. Energy dispersive x-ray analysis (EDX) of the synthesized NS and NF-CaP nanoparticles.	108
Figure 5. 6. SEM images of a) 0.5wt. % HAp-NS, b) 1wt. % HAp-NS, c) 5wt. % HAp-NS, d) 10wt. % HAp-NS, e) 15wt. % HAp-NS, and f) 20wt. % HAp-NS and PHB composites.	112

Figure 5. 7.SEM images of a) 0.5wt% HAp-NF, b) 1wt% HAp-NF, c) 5wt% HAp-NF, and d) 10wt% HAp-NF and PHB composites. ....	113
Figure 5. 8.Crystallinity from first heat as a function of filler content for neat PHB and NS-CaP/PHB as well as NF-CaP/PHB composite samples.....	116
Figure 5. 9.Half-time crystallization of (a) NS-CaP/PHB and (b) NF-CaP/PHB nanocomposites samples as a function of crystallization temperature. ....	118
Figure 5. 10.Isothermal crystallization of (a) NS-CaP/PHB composites and(b) NF-CaP/PHB composites at 125°C.....	120
Figure 5. 11.Shear storage modulus ( $G'$ ) values of neat PHB and (a) NS-CaP/PHB and (b) NF-CaP/PHB nanocomposite samples as a function of temperature.....	126
Figure 5. 12.X-ray diffraction of (a) neat PHB, NS-CaP/PHB nanocomposites and NS-CaP nanoparticles, and (b) NF-CaP/PHB nanocomposites and NF-CaP nanoparticles.. ....	132
Figure 5. 13.Theoretical Grandom of 0.17 and 0.22 vol. % of NS-CaP and NF-CaP nanoparticles as a function of aspect ratio in comparison to experimental modulus $G'$ at 25°C for 0.5 wt. % NS-CaP/PHB and NF-CaP/PHB nanocomposites.....	135
Figure B. 1.TEM images of HAp60 nanoparticles with platelet morphology.....	145
Figure B. 2.TEM images of HAp111 nanoparticles with spherical assemblies of needle-like nanoparticles. ....	145
Figure B. 3.SEM images of (a) 0.5 wt. %, (b) 1 wt. % and, (c) 5 wt. % HAp60/PCL composites. The scale bar in all the images represents 2 $\mu$ m. ....	146
Figure B. 4.SEM images of (a) 0.5 wt. % and, (b) 5 wt. % HAp111/PCL composites. The scale bar in all the images represents 2 $\mu$ m. ....	146
Figure B. 5.DSC first heating and cooling cycle of neat PCL and HAp60/PCL composites.....	147
Figure B. 6.DSC first heating and cooling cycle of neat PCL and HAp111/PCL composites.....	148
Figure C. 1. DSC first heating and cooling cycle of neat PHB and HAp111/PHB composites.....	150
Figure C. 2.Isothermal crystallization of HAp111/PHB composites at 125 °C. ....	151
Figure C. 3.Isothermal crystallization of HAp111/PHB composites at 130 °C. ....	152

Figure D. 1.SEM image of near-spherical calcium phosphate (NS-CaP) nanoparticles.	153
Figure D. 2.SEM image of nanofiber calcium phosphate (NF-CaP) nanoparticles.....	153
Figure D. 3.Isothermal crystallization of (a)NS-CaP/PHB composites and(b) NF-CaP/PHB composites at 120 °C.....	157
Figure D. 4.Isothermal crystallization of (a) NS-CaP/PHB composites and(b) NF-CaP/PHB composites at 130°C.....	158
Figure D. 5.Shear storage modulus ( $G'$ ) values of neat PHB and (a) NS-CaP/PHB and (b) NF-CaP/PHB nanocomposite samples as a function of temperature at a frequency of 50 Hz.....	160
Figure D. 6.Shear storage modulus ( $G'$ ) values of neat PHB and (a) NS-CaP/PHB and (b) NF-CaP/PHB nanocomposite samples as a function of temperature at a frequency of 10 Hz.....	161
Figure D. 7.Shear storage modulus ( $G'$ ) values of neat PHB and (a) NS-CaP/PHB and (b) NF-CaP/PHB nanocomposite samples as a function of temperature at a frequency of 0.1 Hz.....	162



## LIST OF SYMBOLS AND ABBREVIATIONS

PCL	Poly( $\epsilon$ -caprolactone)
PHB	Poly(3-hydroxybutyrate)
Hap	Hydroxyapatite
CDHAp	Calcium - deficient hydroxyapatite
MMT	Montmorillonite
EMI	Electromagnetic Interference
CNF	Carbon Nanofiber
CNT	Carbon Nanotube
SWNT	Single-walled Nanotube
MWNT	Multi-walled Nanotube
CVD	Chemical Vapor Deposition
POSS	Polyhedral Oligomeric Silsesquioxane
PA <sub>66</sub>	Polyhexamethylene Adipamide
M (PMA-ala)	Monomer Methacrylated Pyromellitylimidoalanine
PM (PMA-ala)	Poly (methacrylated pyromellitylimidoalanine)
PLA	Poly (D, L-lactide)
PLLA	Poly (L-lactic acid)
DMF	N, N, dimethylformamide
PVAc	Poly (vinyl acetate)
DCPA	Dicalcium Phosphate Anhydrous

OCP	Octacalcium Phosphate
CdS	Cadmium Sulphide
AOT	Bis (2-ethylhexyl) Sulphosuccinate
CTAB	Cetyltrimethylammonium Bromide
Tween 60	Polyoxyethylene (20) Sorbitan Monostearate
PGA	Poly (glycolic acid)
HB	3-hydroxybutyrate
HV	3-hydroxypentanoate
PVA	Polyvinyl Alcohol
PDMS	Poly (dimethylsiloxane)
QENS	Quasielastic Neutron Scattering
NP-5	Poly (oxyethylene) <sub>5</sub> Nonylphenol Ether
NP-12	Poly (oxyethylene) <sub>12</sub> Nonylphenol Ether
TEM	Transmission Electron Microscopy
FTIR	Fourier Transform Infrared Spectroscopy
KBr	Potassium Bromide
DLS	Dynamic Light Scattering
BET	Brunauer, Emmet, and Teller
SEM	Scanning Electron Microscopy
DSC	Differential Scanning Calorimetry
DMA	Dynamic Mechanical Analysis

MDSC	Modulated Differential Scanning Calorimetry
MAF	Mobile Amorphous Fraction
CF	Crystalline Fraction
RAF	Rigid Amorphous Fraction
Triton X-100	Octyl Phenol Ethoxylate
EDX	Energy Dispersive X-ray Spectroscopy
WAXS	Wide-angle X-ray Scattering
XRD	X-ray Diffraction
FWHM	Full Width Half Maximum

## SUMMARY

This research is directed toward understanding the effect of nanoparticle attributes and polymer morphology on the properties of the nanocomposites with analogous nanoparticle chemistry. In order to develop this understanding, polymer nanocomposites containing calcium phosphate nanoparticles of different specific surface areas and shapes were fabricated and characterized through thermal and thermomechanical techniques. Nanoparticles were synthesized using reverse microemulsion technique. For nanocomposites with different surface area particles, the mobility of amorphous polymer chains was restricted significantly by the presence of particles with an interphase network morphology at higher loadings. Composites fabricated with different crystallinity matrices showed that the dispersion characteristics and reinforcement behavior of nanoparticles were governed by the amount of amorphous polymer fraction available. The study conducted on the effect of nanoparticle shape with near-spherical and nanofiber nanoparticles illustrated that the crystallization kinetics and the final microstructure of the composites was a function of shape of the nanoparticles. The results of this research indicate that nanoparticle geometry and matrix morphology are important parameters to be considered in designing and characterizing the structure-property relationship in polymer nanocomposites.

# **CHAPTER 1**

## **INTRODUCTION**

The transition from micro to nanocomposites has led to a dramatic improvement in the properties attributed to the higher surface area and interfacial energies associated with the nanoparticles. Use of nanoscale reinforcement increases the area of interfacial interaction and hence results in larger volume fractions of the polymer matrix in contact with the filler surface. This region is known as the interphase. The interphase region is important as it can have different structure and properties than the bulk polymer and affect the properties of the resulting nanocomposites. Apart from the size of the nanofiller, understanding the effect of the shape, aspect ratio, volume fraction, surface chemistry and dispersion level of the nanoparticles on the nanocomposite's properties impacts its design. This research was directed towards understanding the coupled effects of the nanoparticle geometry and matrix morphology on the properties of biologically relevant nanocomposites. Thus, the objectives of this research were:

1. Synthesis of calcium phosphate nanoparticles of controlled shapes and sizes using reverse microemulsion technique.
2. Design of nanocomposites using these nanoparticles of controlled shape and sizes and varying concentrations.
3. Investigate the effect of matrix morphology on the properties of the nanocomposites.
4. Characterization of the nanocomposites to isolate the contribution of the nanocomposite constituents on the properties.

Chapter 2 reviews the literature on polymer nanocomposites with 0, 1 and 2-dimensional fillers, attributes in the context of the available literature concerning calcium phosphate particularly hydroxyapatite (HAp) nanocomposites, different phases of calcium phosphates in context to phases synthesized in this work, reverse microemulsion technique and parameters affecting shape and size of calcium phosphate nanoparticles and background about the poly ( $\epsilon$ -caprolactone) (PCL) and polyhydroxybutyrate (PHB) matrices used in this work. Based on the objectives, this work has been structured in to three studies presented in Chapters 3-5. The synthesis of HAp of different surface areas, their processing into nanocomposites and the properties is presented in Chapter 3. The effect of matrix crystallinity on the properties of nanocomposites is discussed in Chapter 4. Chapter 5 is devoted to the synthesis of calcium phosphate nanoparticles of near-spherical and fiber-like shapes, their processing into nanocomposites and the coupled effect of shape and matrix morphology on the nanocomposite properties. The overall conclusions of this work and future recommendations are reported in Chapter 6.

In the first study (Chapter 3), the contribution of nanoparticle surface area to the properties of nanocomposite materials was investigated. HAp nanoparticles with different specific surface areas ( $60 \text{ m}^2/\text{g}$  and  $111 \text{ m}^2/\text{g}$ ) were synthesized using reverse microemulsion and processed into nanocomposites using poly ( $\epsilon$ -caprolactone) (PCL) as the matrix. Experimental results indicated that the thermomechanical reinforcement did show a dependence on nanoparticle surface area although the transition temperatures did not. The reinforcement trends were dependent on temperature, suggesting that the nanoparticles had a greater impact on the amorphous polymer chains. It was shown that the reinforcement above  $T_g$  could be plotted against nanoparticle surface area to obtain a

single reinforcement trend, suggesting that surface area is a general parameter for nanocomposite property control.

In the second study (Chapter 4), the effect of matrix crystallinity on the nanocomposite properties was studied using similar filler but different semi-crystalline matrices with approximately 30% difference in crystallinity. Polymer nanocomposites containing HAp particles with specific surface area of 111 m<sup>2</sup>/g and poly ( $\epsilon$ -caprolactone) (PCL) or polyhydroxybutyrate (PHB) matrix were prepared. The dispersion of nanoparticles in the two polymer systems and the nanocomposite properties were found to be governed by the differences in the matrix morphology. The thermal transitions and crystallization kinetics of PHB were significantly affected by even small concentrations of particles but were not changed significantly for PCL composites until sufficient particle concentrations. The reinforcement behavior in the two polymer systems also showed variations based on the morphology. In case of the lower crystallinity matrix PCL, the composite microstructure changed from bulk to interphase network at higher concentrations but changed from bulk to particle network for higher crystallinity matrix PHB.

In the third study (Chapter 5), the effect of nanoparticle shape on the properties of nanocomposites was examined. Calcium phosphate (CaP) nanoparticles of two different shapes, near-spherical (NS-CaP) and nanofiber (NF-CaP) were synthesized using a combination of reverse microemulsion and solvothermal techniques. Nanocomposites using NS-CaP and NF-CaP nanoparticles were prepared through solution processing route with different concentrations to elucidate the role of both nanoparticle shape and arrangements on the properties of the resulting nanocomposites. In both the systems,

nanoparticles were dispersed to single particle level at 0.5 wt. % concentration only and were homogeneously distributed at higher particle concentrations. The crystallization kinetics were found to be more sensitive to differences in the shape than the thermomechanical properties.



## **CHAPTER 2**

### **BACKGROUND**

The background related to the research concentrates on the nanocomposites and their classification, different nanoparticle attributes and how they affect the nanocomposite properties, networks in polymer nanocomposites, calcium phosphate ceramics and their types in context of the calcium phosphate phases synthesized in this research, description of microemulsion and hydrothermal nanoparticle synthesis technique used in this work, the parameters in microemulsion that control the shape and size of nanoparticles, and biodegradable polymers, poly ( $\epsilon$ -caprolactone) (PCL) and poly(3-hydroxybutyrate) (PHB) as the polymer matrices used in this research.

#### **2.1. Nanocomposites: an Introduction**

Organic and inorganic fillers have been used in polymeric materials for many years to modify properties, reduce material costs and improving the processing. A number of such composites with micrometer scale fillers such as ceramics, metals, and minerals are available in the market and are being used for various applications. But for the past 20 years, research in the area of polymer nanocomposites is evolving rapidly due to advantages associated with nanoscale reinforcement. Polymer nanocomposites may be broadly defined as polymers containing fillers where at least one of the filler dimensions is less than 100 nm. Where conventional polymer composites require higher loadings (15-40 vol %) of filler materials for property enhancement, lower concentrations (1-10 vol %) of the nanofiller gives comparable properties.<sup>[1]</sup> The use of nanometer sized

reinforcement provides an advantage in the form of higher specific surface area. The increase in interfacial interaction due to reduced size of the filler leads to large volume fractions of polymer in contact with the filler surface. The polymer in this region called the interphase can have different structure and properties than the bulk polymer matrix. The strength and dimensions of the interphase can affect the properties of the resulting nanocomposites significantly.<sup>[2-6]</sup> A number of value-added properties such as reduced gas permeability,<sup>[7, 8]</sup> optical clarity,<sup>[8]</sup> and increased ablation resistance<sup>[9]</sup> are also obtained using nanoscale reinforcement. Apart from the property improvement, the lower filler loadings enable ease of processing and weight reduction.<sup>[10]</sup> Additionally, nanocomposites have been present in nature for millions of years in the form of shells, wood, and bones.<sup>[11]</sup> Research in this area can elucidate the science behind unique properties of these natural materials and apply it to generate synthetic materials for future applications.

## **2.2. Classification of Nanocomposites**

Nanocomposites may be classified based on the morphology of the reinforcement: nanoplatelet/layered composites (2-dimensional), nanofiber/tube composites (1-dimensional), nanoparticulate composites (0-dimensional).<sup>[12]</sup>

### **2.2.1. Nanoplatelet/Layered Composites (2-dimensional)**

The unique feature of platelet or layered reinforcement is the high aspect ratio and surface area. The platelets have nanometer thickness with lateral dimensions in the range of 30nm to several microns.<sup>[13]</sup> This morphology of platelets makes them more effective

in controlling the gas barrier and flame retardant properties of the resulting nanocomposites, as they provide a more tortuous path for the passage of gas molecules.<sup>[8, 9]</sup> One of the first studies in the field of nanoplatelet/layered polymer composites involved used of clay or silicates with nanoscale plate thickness. The work done in the late 1980s and early 1990s at Toyota Central Research Laboratories in Japan involved development of Nylon6-clay composites that had remarkable thermal and mechanical properties by using small loadings of clay.<sup>[14]</sup> This dramatic property improvement was attributed to the higher surface area of the clay platelets which led to enhanced interfacial interaction with the polymer matrix. Two types of materials which exist as platelets or layered structures are clay and graphite. The full potential of this type of reinforcement takes place when the layers are separated and dispersed uniformly throughout the polymer matrix. When the polymer is not able to penetrate between the layers of the filler, a phase separated composite is obtained which has properties that are equivalent to conventional composites. When the polymer penetrates into the gallery region between the adjacent layers, the layers expand and an intercalated state is achieved. When the structure is fully exfoliated, the layers are individually dispersed in the polymer matrix, leading to large scale change in the bulk polymer structure. The most common silicate clay materials which have been used for making nanocomposites are montmorillonite (MMT), saponite and synthetic mica. The advantages of clay based polymer nanocomposites include the enhancement of modulus, strength, toughness, thermal stability as well as improved gas barrier properties, reduction of coefficient of thermal expansion and less cost.<sup>[13-22]</sup> Apart from the property improvement given by clay, exfoliated graphite sheets also give enhancement of electrical conductivity of polymeric materials when a threshold

percolation based on the weight content is reached.<sup>[23-25]</sup> These nanocomposites based on layered reinforcement are finding applications in the automobile industry as well as in the case of graphite as electromagnetic interference (EMI) shielding, electrostatic paint and polymer sheath of electric cables.<sup>[12]</sup>

### **2.2.2. Nanofiber/tube Composites (1-dimensional)**

The unique feature of fiber shaped reinforcement is the nanometer range of diameter giving them very high aspect ratios. The morphology of fibers also makes them very effective as stress bearing components of the composite. Most studies of 1-d nanofillers concern carbon nanofibers (CNFs), carbon nanotubes (CNTs) and cellulose whiskers. Carbon nanofibers are a unique form of vapour-grown carbon fibers which have been used to reinforce polymers such as polycarbonate,<sup>[26]</sup> polypropylene,<sup>[27]</sup> nylon,<sup>[28]</sup> PET,<sup>[29]</sup> and epoxy.<sup>[30]</sup> CNFs have different morphologies such as bamboo-like structures, truncated cones, stacked coins etc.<sup>[31, 32]</sup> They have a larger surface area than conventional carbon fibers because of a reduced diameter (in the range 50-200 nm) and an aspect ratio greater than 100. They are synthesized by methods such as electrospinning, template synthesis or drawing.<sup>[33, 34]</sup> CNFs are being used for several aerospace applications such as fire retardant coatings, lightning strike protection, conductive aerospace adhesives etc. CNTs are essentially graphene sheets rolled into tubes with diameters between 1-50 nm and lengths up to centimeters. They can have aspect ratios greater than 1000. They are classified into single-walled nanotubes (SWNTs) and multi-walled nanotubes (MWNTs) based on shell versus multiple tubes packed concentrically, respectively. CNTs have unique mechanical and electrical properties. They possess an

elastic modulus up to 1 TPa and a bending strength of about 14 GPa.<sup>[35]</sup> The electrical properties of CNTs can range from metallic to semiconducting depending on the chirality and diameter of the nanotubes.<sup>[36]</sup> The three main methods to synthesize CNTs are direct-current arc discharge,<sup>[37]</sup> laser ablation<sup>[38, 39]</sup> and chemical vapour deposition (CVD).<sup>[40, 41]</sup> All of these methods require three sources: carbon, heat and a metal catalyst. Cellulose whiskers are another example of 1D reinforcement. These whiskers are based on cellulose biopolymer which is a linear condensation polymer of poly- $\beta$  (1,4)-D-glucose residues. The degree of polymerization ranges from 2500 to 15000 units depending on the source e.g. wood, cotton etc.<sup>[42]</sup> The whiskers can be obtained by acid hydrolysis of cellulose microfibrils.<sup>[43]</sup> The aspect ratio and properties of the whiskers depended on the crystallinity of the raw material, e.g. more than 10 wt. % of starch microcrystals (aspect ratio close to unity) gave equivalent reinforcement effect as 1 wt. % tunicin whiskers (aspect ratio 67).<sup>[44]</sup>

### **2.2.3. Nanoparticulate Composites (0-dimensional)**

The unique feature of particulate nanocomposites are the nanoparticles, which have size less than 100nm and can be varied to design nanocomposite for desired application. Particles like carbon black, calcium carbonate and silica in micron size range have been added to polymers to improve the mechanical properties of the polymer matrix. Reducing the particle size to the nanometer scale has opened up novel applications in biology, electronics and advanced materials e.g. use of metallic nanoparticles and semiconductor quantum dots in bio-sensors for detecting certain metabolites such as glucose, lactase etc.<sup>[45]</sup> as well as for bio-imaging and cell-

targeting.<sup>[46]</sup> Nanoparticles for particulate nanocomposites have been made from materials like metals (Ag, Au, Cu), metal oxides ( $\text{Al}_2\text{O}_3$ ,  $\text{CaCO}_3$ ,  $\text{TiO}_2$ ) and ceramics (SiC, calcium phosphate) as well as organic nanoparticles like polyhedral oligomeric silsesquioxane (POSS). These nanoparticles have been synthesized using wet chemical technique such as microemulsion (reverse and normal) where surfactants and other colloidal assemblies act as templates,<sup>[47-49]</sup> as well as other techniques such as hydrothermal,<sup>[50, 51]</sup> sonochemical,<sup>[52]</sup> photochemical,<sup>[53, 54]</sup> microwave,<sup>[55]</sup> sputter deposition,<sup>[56]</sup> and electrochemical synthesis.<sup>[57]</sup> The choice of the nanoparticles depends on the type of property improvement required, such as metallic nanoparticles for electrical properties, silica, alumina and  $\text{CaCO}_3$  particles for mechanical properties as well as thermal properties, or ceramic particles like hydroxyapatite (HAp) for their biological properties.<sup>[13, 58]</sup>

### **2.3. Nanoparticle Attributes**

Understanding the effect of different nanoparticle attributes on the properties of nanocomposites is important to design nanocomposites with desirable properties for specific applications. Some nanoparticle attributes which influence nanocomposite properties are: particle size, surface area, volume fraction of particles, dispersion, surface chemistry, shape and aspect ratio. Because the overall goal of this work is to work with calcium phosphate mainly HAp nanoparticles, the following section discusses these attributes in the context of available literature pertaining to these composites.

### 2.3.1. Particle Size

The particle size and surface area of nanosized reinforcement has a significant effect on the properties of the resulting nanocomposites due to the increased contact with the polymer matrix. In order to compare the effect of size of the HAp particles on the mechanical properties Wang *et al.*<sup>[59]</sup> prepared composites of polyhexamethylene adipamide (PA<sub>66</sub>) with nano-hydroxyapatite (n-HAp) as well as micro-hydroxyapatite ( $\mu$ -HAp) with similar surface chemistry. Infrared spectroscopy showed H-bond interaction between n-HAp and PA<sub>66</sub>. For the same HAp content the n-HAp/ PA<sub>66</sub> composites had higher bending strength and modulus as well as tensile strength than  $\mu$ -HAp/ PA<sub>66</sub> composites. The improved properties were attributed to the larger surface area of n-HAp leading to stronger interaction between the n-HAp and polyamide. The tensile strength increased with the increase in concentration of n-HAp from 50 to 55 wt. % in the PA<sub>66</sub> whereas there was deterioration in case of increased content of  $\mu$ -HAp.

### 2.3.2. Dispersion and Surface Chemistry

The homogeneous dispersion of nanoparticles in the polymer matrix is necessary to utilize the higher surface area of nanoparticles. The effective surface area of the nanofiller available for interaction with the polymer is severely reduced if the dispersion is not uniform. Li *et al.*<sup>[60]</sup> reported homogeneous dispersion of HAp through combined in-situ HAp synthesis and in-situ polymerization. HAp nanoparticles were synthesized by hydrothermal method and dispersed in anhydride monomer methacrylated pyromellitylimidoalanine M(PMA-ala) and then photo-polymerization was done using UV rays in the presence of photo-initiator to give cross-linked network

poly(methacrylated pyromellitylimidoalanine) PM(PMA-ala). The composites showed an increase in the compressive and flexural strength as well as modulus with respect to the neat polymer. The presence of dispersed HAp in the cross-linked polymer network also increased the stability of the composites against degradation. In another study, poly (D,L-lactide)(PLA) was reinforced with calcium-deficient hydroxyapatite (CDHAp) nanocrystals and formed into nanocomposites using solvent casting. The tensile modulus of the composites increased with the loading % of CDHAp nanocrystals and the improvement was attributed to better dispersion of the nanocrystals in the matrix giving rise to better interaction between the filler and the polymer.<sup>[58]</sup>

To obtain a strong interface, the filler should have an attractive interaction with the matrix. The interaction may be achieved through surface chemistry in the form of functionalization with chemical moieties or grafted polymer. Hong *et al.* grafted poly (L-lactic acid) (PLLA) chains onto the surface of HAp nanoparticles. It was observed that the surface grafted n-HAp particles showed good dispersion in chloroform compared to the n-HAp particles that tended to agglomerate. The PLLA-g-HAp particles acted both as a toughening and reinforcing agent. Also, the crystallinity of PLLA matrix was found to increase with increasing PLLA-g-HAp content.<sup>[61, 62]</sup> In another study, composites were prepared by directly blending HAp with poly ( $\epsilon$ -caprolactone) (PCL) as well as by grafting PCL on the HAp particles. The composites which contained HAp grafted with PCL chains showed better mechanical properties, better dispersion and degradation stability. This was ascribed to the stronger interaction between the grafted HAp and the PCL matrix compared to the HAp blended directly with PCL.<sup>[63]</sup>



### **2.3.3. Shape**

The shape of the nanoparticle can also have an impact on the structure of the interphase and hence the properties of the composites. However, to date, few studies concerning this parameter in chemically similar systems have been done. Kalfus and Jancar <sup>[64]</sup> involved the incorporation of spherical and platelet shaped HAp to reinforce a poly(vinyl acetate) (PVAc) matrix. The specific surface area of the spherical and the platelet shape HAp was 133 and 201 m<sup>2</sup>/g, respectively. The authors state that at all temperatures nanoparticle surface area led to reinforcement and above the glass transition reinforcement also arose from altered polymer chain dynamics surrounding the HAp particles. The effect of the shape of the HAp particles on the properties was suggested to be secondary. However, the HAp particles had relatively low aspect ratios, limiting this conclusion.

## **2.4. Networks of Polymer Nanocomposites**

In addition to the nanoparticle geometry, the arrangement of nanoparticles in the composites also plays a role in the nanocomposite properties. The nanoscale size leads to higher surface area and magnifies the effect of other nanoparticle attributes such as surface chemistry or shape on properties by perturbing a greater quantity of polymer chains as the nanoparticle/polymer interfacial area increases. These relationships lead to a network view of nanocomposite morphology.<sup>[65]</sup> Large amounts of interphase are present in the composite due to the large surface area of nanoparticles, leading to three separate microstructures. At low nanoparticle concentrations, the polymer matrix is continuous and the nanoparticles and interphase material are isolated from each other. At

increasing concentrations the interphase forms continuous network, known as rheologically percolated structure and rheological measurements show a discontinuity reflecting the physical network formed by the interphase regions. For a strong interface in this structure, the nanocomposite properties will exceed those predicted by micromechanics and these results have been observed experimentally.<sup>[66]</sup> Thresholds for rheological percolation as low as 0.11 wt. % for SWNTs and 1.2 wt. % for MWNTs/polymer nanocomposites have been observed.<sup>[65, 67]</sup> In case of spherical carbon black nanoparticles of mean diameter of 20 nm, the rheological percolation threshold was approximately 16 wt. %.<sup>[68]</sup> Therefore, the thresholds for such physical network formation vary with the shape and aspect ratio of the nanoparticles.<sup>[65, 68, 69]</sup> At still higher concentrations, the particle-particle network is formed, representing a condition of geometrical percolation. The threshold for electrical percolation is higher than rheological percolation as the smaller distance between nanoparticles is required for electrical conductivity. These transformations, shown schematically in Figure 2.1, can be envisioned with many nanoparticle attributes. In these three structures, the nanocomposite's constituents contribute differently to the properties of the bulk material.

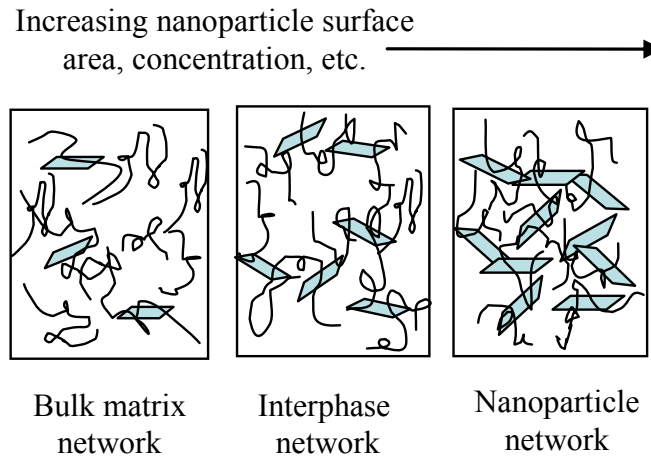


Figure 2. 1. Nano/microstructures formed in nanocomposites at increasing nanoparticle concentration. When the bulk polymer matrix is continuous, the contributions of the nanoparticles and interphase are additive. When the interphase becomes continuous, a physical network is formed that affects the polymer dynamics. When the nanoparticles form a continuous network, a percolated structure is formed that reflects the nanoparticle properties in the nanocomposite. Schematic was inspired by Du *et al.*<sup>[65]</sup> Figure from Kaur and Shofner, 2009.<sup>[70]</sup>

## 2.5. Calcium Phosphates and their Properties

Calcium phosphates serve a common interest among various fields such as geology, biology, chemistry, dentistry and medicine. Calcium phosphates occur naturally in the form of mineral ore.<sup>[71]</sup> Calcium phosphates are known for their structural and compositional resemblance to natural tissues such as bone and teeth. This makes them an ideal biomaterial for applications such as bone grafts, coatings for bone prostheses, cements, composites and scaffolds for hard tissue regeneration, and in dentistry.<sup>[71-74]</sup> They are biocompatible, bioactive (can induce direct bone bonding), help bone cell adhesion, growth and proliferation as well as offer variable resorbability based on their composition.<sup>[72, 73]</sup> Apart from biological applications, the calcium phosphate mineral

provides the world's main supply for phosphorous to make agricultural fertilizers and various phosphorous containing chemicals. Calcium phosphates have various forms and phases with the calcium to phosphorous (Ca/P) molar ratios between 0.5 and 2.0. They are mostly soluble in acids, sparingly soluble in water and totally insoluble in alkaline solutions.<sup>[71]</sup> The different phases of calcium phosphates are monocalcium phosphate monohydrate and monocalcium phosphate anhydrous, dicalcium phosphate dihydrate/brushite, dicalcium phosphate anhydrous/monetite, hydroxyapatite (HAp), calcium-deficient hydroxyapatite (CDHAp), octacalcium phosphate, fluorapatite, chlorapatite, tricalcium phosphate, amorphous calcium phosphate and tetracalcium phosphate. The following section briefly describes those phases of calcium phosphates which were synthesized in this research. Table A.1 in Appendix A shows the different phases of calcium phosphates, their chemical formulas, Ca/P ratios, density and crystal structure.

### **2.5.1. Hydroxyapatite (HAp)**

Hydroxyapatite (HAp), fluorapatite, and chlorapatite belong to the apatite family of minerals that share the general formula  $A_{10}(PO_4)_6(OH, F, Cl)_2$ . The A cation could be barium, strontium or magnesium besides calcium. The chemical formula for HAp is  $Ca_{10}(PO_4)_6(OH)_2$ . It has many synonym abbreviations such as OHAp, HAp, HAP, and HA. HAp constitutes the most predominant phase of both animal bone (60wt. %) and teeth (90wt. %). HAp belongs to hexagonal crystal system. The crystal form of chemically pure HAp is monoclinic with four units in each cell. A transformation from monoclinic to hexagonal form has been observed at higher temperatures. The hexagonal

form is more stable form of HAp which has some impurities substituting hydroxide or phosphate groups.<sup>[71, 75]</sup> HAp can be made in various forms like porous scaffolds, granules, powder and as dense bodies by sintering.<sup>[76]</sup> HAp has medical applications such as bone grafting, artificial bone, coatings on implants, bone fillers, middle ear prostheses, joint material, and scaffolds in the form of composites. HAp/polymer composites are inspired by biological design, such as bone tissue and nacre. Other medical applications include tooth roots, toothpaste, canal filler and cement. HAp finds its use in other applications as a catalyst, fertilizer and as an adsorbent for protein separation.<sup>[74, 76]</sup>

### **2.5.2. Calcium-deficient Hydroxyapatite (CDHAp)**

Deviation from stoichiometric Ca/P ratio of 1.67 during synthesis of hydroxyapatite results in non-stoichiometric or calcium-deficient Hydroxyapatite (CDHAp). The Ca/P ratio for such apatites is in the range of 1.33 to 1.67 and these apatites form due to the loss of  $\text{Ca}^{2+}$  ions from the unit cell with the formula  $\text{Ca}_{10-x}(\text{HPO}_4)_x(\text{PO}_4)_{6-x}(\text{OH})_{2-x}$ .<sup>[77]</sup> Vacancies of  $\text{Ca}^{2+}$  and  $\text{OH}^-$  in the crystal structure of CDHAp may be substituted by other ions depending on the counter-ions of the precursors used in the synthesis or by water molecules. The precipitated CDHAp has similar c-axis dimensions as HAp but higher a-axis parameter due to lattice-substitutions.<sup>[78]</sup> The bone mineral is mainly CDHAp with Ca/P ratio of 1.5 and hence is structurally similar to stoichiometric HAp but has chemical and compositional similarity to tricalcium phosphate.<sup>[79]</sup> CDHAp because of its structural similarity to natural bone finds applications such as bone substitutes and implant coatings.<sup>[71]</sup>

### 2.5.3. Dicalcium Phosphate Anhydrous (DCPA)/Monetite

Dicalcium phosphate anhydrous (DCPA), or monetite ( $\text{CaHPO}_4$ ), is formed when dicalcium phosphate dihydrate (DCPD), or brushite ( $\text{CaHPO}_4 \cdot 2\text{H}_2\text{O}$ ) loses its two water molecules. Monetite can also be precipitated from aqueous solutions similar to brushite but at  $100^\circ\text{C}$ . It is a less soluble phase compared to brushite because of the absence of water molecules. It is not found in pathological calcifications but has been shown to be present in fracture callus. The crystal form of monetite is triclinic with four units per unit cell. It crystallizes mainly as tablets and plates but prismatic, rod, and whisker forms also occur. Monetite has been found to be bioactive and is finding applications as dental cements and restorative materials.<sup>[80]</sup> Other applications of monetite are supplements in enriched flour and cereals, tableting agents in pharmaceutical industry and in toothpastes.<sup>[71, 75, 78]</sup>

### 2.5.4. Octacalcium Phosphate (OCP)

Octacalcium phosphate (OCP) has the chemical formula  $\text{Ca}_8(\text{HPO}_4)_2(\text{PO}_4)_4 \cdot 5\text{H}_2\text{O}$ . The formation of this phase as a precursor phase is thermodynamically favorable before undergoing change into more stable calcium phosphate phases such as HAp and other biological apatites. OCP is an important phase for studying the biomineralization process in dental and bone tissues. OCP has been found to be a constituent of dental calculus and other pathological calcifications. The lattice of OCP is triclinic with two units per unit cell. It crystallizes as thin blades elongated along c-axis. OCP is implanted into bone defects in surgery.<sup>[71, 78]</sup>

### 2.5.5 Chlorapatite

Chlorapatite ( $\text{Ca}_{10}(\text{PO}_4)_6(\text{Cl})_2$ ) like HAp belongs to the apatite family of minerals. Pure or stoichiometric chlorapatite has monoclinic structure at room temperature with four formula units per unit cell. The hexagonal form of chlorapatite is associated with non-stoichiometry similar to HAp and has two formula units. The conversion from monoclinic to hexagonal form has been observed at temperatures above  $310^\circ\text{C}$ . A significant expansion of the unit cell dimensions and volume is observed in chlorapatite compared to HAp. Chlorapatite can convert to HAp when heated above  $800^\circ\text{C}$  in steam. Chlorine can be also incorporated in the HAp lattice by replacing the hydroxyl group.<sup>[78, 81, 82]</sup> Chlorapatite in combination with fluorapatite has been used as the major phosphor component in fluorescent lamps.<sup>[83]</sup> Chloride ions help in activating bone cells for bone resorption process by providing an acidic environment on the surface of the bone.<sup>[84]</sup>

## 2.6. Microemulsion Technique

Multiple techniques have been used to make different phases of calcium phosphates. Some of the common techniques are microemulsion, hydrothermal, hydrolysis, solid state reaction, sol-gel, flux method (using fused salt reaction), pH-shock wave,<sup>[85]</sup> electrocrystallization<sup>[86]</sup> and microwave irradiation.<sup>[87]</sup> Microemulsion technique is a wet chemical precipitation synthesis method. This technique uses colloidal assemblies such as reverse and normal micelles to synthesize nanoparticles of controlled size and polydispersity. Microemulsions consist of an oil and water phase stabilized by means of surfactants. Surfactants are molecules with a polar hydrophilic head and a hydrophobic chain. Surfactants can arrange into various assemblies and micelles as

shown in Figure 2.2., when the hydrophobic chain end of surfactant in order to avoid contact with water forms the center of micelle whereas the hydrophilic end remains in contact with the water or solvent.<sup>[88]</sup> The shape of the surfactant assemblies depends on various parameters such as packing factor, surfactant concentration, presence of salt, presence of alcohols, and change of pH or temperature which determines the structure formed by a surfactant in a medium.

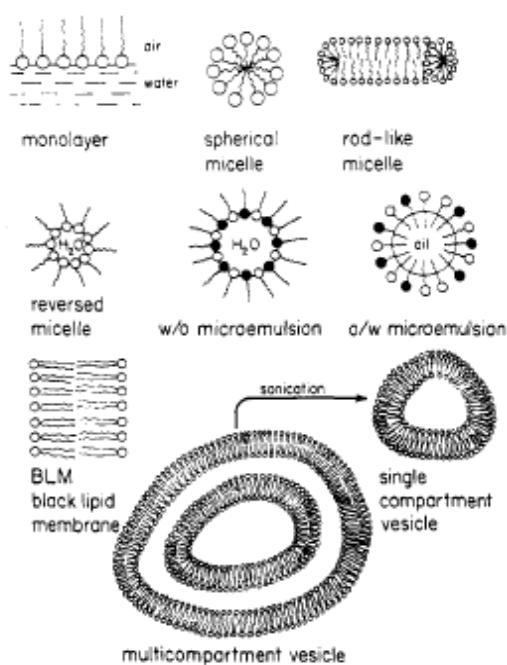


Figure 2. 2.Simplified representation of organized structures formed by surfactants.<sup>[89]</sup>

In case of non-polar solvents, it is thermodynamically favorable for the hydrophilic part of the surfactant to form the inner core to avoid contact with the solvent and the hydrophobic part favors to remain outside in contact with the solvent. Therefore the inside of the micelle acts as a water pool and would solubilise any water soluble precursor. Such system is called water- in -oil microemulsion and the micelles are called reverse or inverted micelles.<sup>[89]</sup> Reverse micelles can be used as micro or nanoreactors



because of their small size and ability to solubilize reactant molecules in the water pool. The micelles collide with each other due to Brownian motion and exchange the intermicellar content which then gets redistributed within all the micelles. This process has been used to make nanosized inorganic particles such as cadmium sulphide(CdS),<sup>[90]</sup> silver(Ag),<sup>[48]</sup> gold(Au),<sup>[91]</sup> as well as calcium phosphate<sup>[92]</sup> by either chemical reduction of metal ions or coprecipitation reactions. Thus the nucleation and growth of crystals takes place within the micelles.

The reverse micellar process is successful for synthesizing monodisperse particles as it keeps the nucleation and the growth stage of the particles separated. The particle nucleation takes place simultaneously within a large number of micelles, and they are kept separated by the surfactant layer acting as a stabilizer for the formed particles.

## **2.7. Hydrothermal Technique**

Reverse micelles have been used as templates to synthesize calcium phosphate nanoparticles of controlled shapes and sizes, but well crystallized nanoparticles are not obtained due to room temperature synthesis. An additional step of calcination is used to increase the crystallinity of the particles and obtain well defined crystals. However, calcination reduces the surface area of nanoparticles due to sintering. The hydrothermal technique gives well crystallized nanoparticles without the need of carrying out a post-calcination step.<sup>[93]</sup> The hydrothermal/solvothermal technique is defined as a process of using water or solvent as a medium to carry out chemical reactions above the boiling point of water or solvent in a closed system. Under these high temperature and pressure conditions the precipitated solids can dissolve and recrystallize into more stable forms

which otherwise are insoluble under ordinary conditions.<sup>[50]</sup> A combination of the hydrothermal technique with reverse microemulsion can be used to synthesize nanoparticles for various applications. The synergistic effect of both the techniques gives the flexibility to control shape, size, physical and chemical characteristics as well as yield nanoparticles of high purity and crystallinity.

## **2.8. Factors Affecting Synthesis of Calcium Phosphate Nanoparticles**

There are a number of factors which can affect the morphology and the size of the resultant nanomaterial starting with the type of the surfactant (ionic, cationic), oil phase (chain length), co-surfactant, metal salts, molar ratio of water to surfactant ( $W_0$ ) and /or between co-surfactant and surfactant ( $P_0$ ), concentration of reactants within the reverse micelles, pH, temperature, the sequence of introduction of the components in the micellar mixture, or single or multiple microemulsion synthesis approach.<sup>[94]</sup>  $W_0$  controls the size of the water pool inside the micelle and hence controls the size of the resulting nanoparticles.<sup>[92, 95]</sup> The type of surfactant, ionic or non-ionic influences the geometry of the surfactant assembly such as normal micelles, reverse micelles, bicontinuous or other structures based on the area of polar head groups and length of the hydrocarbon chain. Also, the amounts of water solubilised vary with the type of surfactant.<sup>[88, 96]</sup> Similarly, the type of co-surfactant and  $P_0$  control the stability and size of the micelles as well as inter-micellar reactant exchange rate. Co-surfactants take the place between the surfactant molecules at the interface of oil and water and reduce the repulsion between the surfactant head groups.<sup>[97, 98]</sup> The temperature of synthesis influences the properties of the resulting nanoparticles such as crystallinity as well as size and shape of micelles in

case of the non-ionic surfactants.<sup>[99]</sup> The pH of the microemulsion affects the morphology of the nanoparticles when the surfactant used is ionic. The pH not only influences the stability of the precipitated phase but also controls the shape and size of the particles depending on the strength of interaction between the ionic surfactant head group and reactant molecules.<sup>[93]</sup> In the following paragraphs, the examples of effects of  $W_o$ , co-surfactant to surfactant ratio  $P_o$ , mixed surfactants, concentration of the reactants, temperature and pH on the shape and size of calcium phosphate nanoparticles is presented.

### **2.8.1. Effect of $W_o = ([H_2O] / [Surfactant])$**

The most critical parameter which influences the size and shape of the micelle core is the molar ratio  $W_o$  of water to surfactant ( $[H_2O] / [Surfactant]$ ). Calcium phosphate nanoparticles with different sizes and morphologies have been synthesized by varying  $W_o$  in the range of 1.4-15 in sodium bis(2-ethylhexyl) sulphosuccinate(AOT)/isooctane as well as in a  $C_{12}E_8$ / cyclohexane/water reverse micelle system. The change in size and morphology of the nanoparticles is attributed to the water structure inside the reverse micelles. When  $W_o$  is small, most of the water inside the reverse micelle is in the form of bound water and some intermediate water; as  $W_o$  increases the bound water converts to free or bulk water. This multilayered water structure inside the micelles influences the size and morphology of the resulting nanoparticles.<sup>[92, 95]</sup> In another study, the shape of the nanoparticles changed from nanobelts to nanospheres and then to larger sheets when  $W_o$  was changed from 10 to 15 to 20. This is because initially the micelles were wormlike and growth was directed by the

micelle template. Then as  $W_0$  increased, the micelles swelled and grew larger, and the morphology was influenced more by the intermicellar reactant exchange rather than by the micelle template.<sup>[97]</sup>

### **2.8.2. Effect of Co-surfactant to Surfactant Ratio, $P_0$**

Particle growth and size are also affected by the adsorption of co-surfactants (short chain alcohols) to the water-in-oil interfacial film, causing reductions in its rigidity, changing the surfactant packing parameters, and affecting the radius of curvature of the micelle in reverse microemulsion. The morphology of calcium phosphate nanoparticles changed from nanobelts to spherical when  $P_0$  was changed from 5 to 10 while keeping  $W_0$  constant. This was attributed to the fact that at lower  $P_0$  the reverse micelles formed using cetyltrimethylammonium bromide (CTAB) had a stiffer interface (stronger interaction between the tetrahedral  $\text{CTA}^+$  ion of CTAB and  $\text{PO}_4^{3-}$  ion from phosphorus precursor) and particle growth was directed in one direction with the micelle acting as a template. As  $P_0$  was increased, the interaction between the tetrahedral  $\text{CTA}^+$  ion of CTAB and  $\text{PO}_4^{3-}$  ion from phosphorus precursor decreased giving unstable conditions for crystal growth and hence different morphology of nanoparticles.<sup>[97]</sup> In another study the shape of calcium phosphate particles changed from nanowires to brushlike to fiber bundles in changing  $P_0$  from 3 to 5 and 10, respectively, with a similar discussion as above.<sup>[92]</sup>

### **2.8.3. Effect of Mixed Surfactant**

The use of mixed surfactant system in synthesizing nanoparticles can affect the morphology of the resulting nanoparticles. In one study, HAp was synthesized in

presence of nonaethyleneglycol monododecyl ether ( $C_{12}EO_9$ ) as well as in presence of mixed surfactant system of  $C_{12}EO_9$  and polyoxyethylene(20) sorbitan monostearate (Tween 60). The single surfactant system led to the formation of aggregates of platelike HAp particles of 20-40 nm size whereas the mixed surfactant system produced non-aggregated nanoparticles with higher surface area. The Tween 60 acted both as a templating and encapsulating agent whereas the  $C_{12}EO_9$  acted as a particle separating agent preventing the aggregation of HAp nanoparticles.<sup>[100]</sup>

#### **2.8.4. Effect of Reactant Concentration, Ageing Time**

The reactant concentration (ionic strength) and ageing time can also influence the particle size and morphology. In a study by Bose and Saha,<sup>[101]</sup> increasing the ageing time transformed platy to spherical and increased the size of the HAp crystals. The increase in the concentration of the  $Ca^{2+}$  ion from 1.0M to 5.0M increased the surface area of the resulting particles and changed the morphology from spherical (1.0M) to needle-shaped (5.0M).

#### **2.8.5. Effect of Temperature**

The temperature of the both the reverse micellar solution as well as hydrothermal temperature has also been found to be an important factor affecting the crystallinity and morphology of the resulting nanoparticles. Temperature affects the hydrophobicity of the nonionic surfactants. Micelle shape and size increases above the surfactant cloud point which influences the shape and size of the particles. Spherical and rod-shaped crystals of HAp with different size were obtained below and above the cloud point of the surfactant,

respectively.<sup>[102]</sup> In another study, at the same  $W_0$  and  $P_0$  but changing the reaction temperature from 50 to 90 to 130 and, finally, to 170°C changed the calcium phosphate nanoparticle morphology from sheet-like to small nanowires to nanobelts to small platelets (broken nanobelts due to higher temperature). Also at higher temperatures pure HAp was obtained whereas at lower temperatures HAp and other calcium phosphate phases coexisted.<sup>[97]</sup>

#### **2.8.6. Effect of pH**

The pH of the reverse microemulsion can affect the morphology of the nanoparticles when the surfactant used is an ionic surfactant such as CTAB or AOT. Also, different phases of calcium phosphates are stable at different pH values. Calcium phosphate nanoparticles of different morphology as well as crystallinity were synthesized by changing the pH of the reverse micellar solution. The crystallinity of the particles increases with the increase in pH. The shape of the particles changed from long nanowires at  $\text{pH} \leq 6$  to shorter nanowires at 7.5, to short rods at 8.5 and, finally, elliptical particles with round edges at 9.5. This behavior was attributed to the change in the strength of interaction between the  $\text{CTA}^+$  ion of CTAB and  $\text{PO}_4^{3-}$  ion from a phosphorus precursor with the change in pH. At a lower pH  $\text{CTA}^+$  ions associated strongly with  $\text{PO}_4^{3-}$  ions due to structure complementarity and the particle growth and shape was guided by the surfactant template. However, when the pH is increased,  $\text{CTA}^+$  ions interact more with the  $\text{OH}^-$  ions from the ammonium hydroxide leading and surfactant molecules no longer guide the growth, resulting in particles with small aspect ratios. Also, as the pH

increased HAp became the dominant phase while, at lower pH, both monetite and HAp were present.<sup>[93]</sup>

## **2.9. Biodegradable Polymers**

The need of biodegradable polymers is increasing day by day due to the dwindling petroleum reserves and more awareness to reduce the carbon footprint in order to protect the environment. Biodegradable polymers are defined as polymers which can undergo decomposition either by hydrolysis, oxidation, dissolution or enzymatic action of microorganisms into CO<sub>2</sub>, methane, or biomass in a specified period of time.<sup>[103, 104]</sup> Broadly, the biodegradable polymers can be classified as bulk degradable or surface erodative polymers based on the physical changes taking place in the polymer during degradation. Poly (glycolic acid) (PGA), poly(lactic acid) (PLA), PCL and poly(3-hydroxybutyrate) (PHB) are examples of bulk degradable polymers whereas poly(anhydrides) and poly(ortho-esters) are surface erodative polymers. Biodegradable polymers can be naturally occurring or synthesized chemically. These polymers find applications as environmentally friendly packaging materials, as matrix for bio-based composites or green composites, as tissue regeneration scaffolds, medical composites, drug delivery, or as coatings for implants.<sup>[74, 104, 105]</sup> The following section discusses two kinds of biodegradable polyesters: synthetically derived PCL and naturally derived poly(3-hydroxybutyrate) (PHB). Both of these are used in this research and some of the typical properties of PCL and PHB are given in Table 2.1.

Table 2. 1. Typical thermal and mechanical properties of PCL and PHB polymers.<sup>[104-108]</sup>

Polymer	Glass Transition Temperature (°C)	Melting Temperature (°C)	Tensile Strength (MPa)	Tensile Modulus (MPa)	Elongation at Break (%)
PCL	-65 to -60	55-63	20-34	2300	300-700
PHB	-5 to 20	160-180	36	2500	2.5

### 2.9.1. Poly ( $\epsilon$ -caprolactone) (PCL)

PCL is a semi-crystalline polymer synthesized by the ring opening polymerization of a cyclic ester monomer,  $\epsilon$ -caprolactone in the presence of a catalyst, stannous octanoate (Figure 2.3).<sup>[109]</sup>

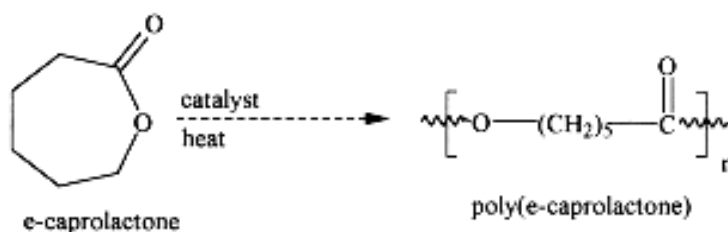


Figure 2. 3.Synthesis of poly ( $\epsilon$ -caprolactone) (PCL) by ring opening polymerization.<sup>[109]</sup>

PCL is highly soluble in a wide range of solvents such as chloroform, dichloromethane, or DMF. It can form miscible blends with a number of polymers, and hence is used as a compatibilizer in many polymer formulations. It undergoes hydrolytic degradation due to the presence of the aliphatic ester linkage and implants of PCL show a slow degradation rate (2-3 years) *in vivo*.<sup>[110]</sup> The low glass transition temperature of PCL leads to its use as soft blocks for segmented polyurethanes. The crystal structure of PCL is orthorhombic with dimensions  $a = 7.496$ ,  $b = 4.974$  and  $c = 17.297\text{\AA}$  (fiber axis).



The space group is  $P2_12_12_1$  and has two chains with opposite orientation in the unit cell.<sup>[111]</sup> Due to its biocompatibility and slower degradation, PCL is used for a number of biomedical applications such as a drug delivery vehicle or as scaffold for bone tissue engineering. PCL has also been copolymerized with glycolide and lactic acid to increase its degradation rate for certain applications like sutures.<sup>[104, 105, 112]</sup>

### 2.9.2. Poly (3-hydroxybutyrate) (PHB)

PHB is aliphatic polyester produced by bacteria as a carbon and energy storage medium when the cells are deprived of certain essential nutrients such as nitrogen or phosphorous. The chemical structure of the PHB repeat unit is given in Figure 2.4.

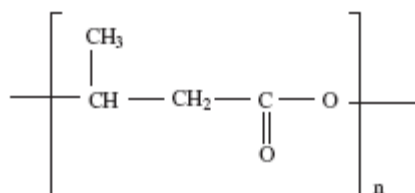


Figure 2. 4. Structure of repeat unit of poly (3-hydroxybutyrate) (PHB).<sup>[105]</sup>

The biosynthetic way to synthesis PHB polymer involves conversion of low alcohols and acids, sugars, or a carbon substrate to acetate. An enzyme cofactor bonded by a thioester is put as a handle on the acetate molecules by the bacteria to give acetyl coenzyme-A. Acetoacetyl coenzyme-A is formed by the condensation of two molecules of this acetyl coenzyme-A. 3-hydroxybutyryl coenzyme-A is formed by the reduction of acetoacetyl coenzyme-A gives. These units are joined together to form PHB by the final polymerase enzyme. The copolymers of (R)-3-hydroxybutyrate (HB) and (R)-3-hydroxypentanoate (HV) are formed under the depletion of nitrogen and phosphorous by feeding the bacteria

a mixture of acetic and propionic acids. Instead of condensation of two molecules of this acetyl coenzyme-A in the case of synthesis of PHB, condensation of one molecule of propionate with one molecule of acetate takes place to give 3-hydroxypentanoate. PHB is commercially produced by two-way batch fermentation. In addition to synthesis by microbial fermentation, PHB can be chemically synthesized from substituted propiolactones, but it is not commercially favorable as it involves the use of costly and toxic lactone monomers.<sup>[113]</sup>

PHB is a semi-crystalline isotactic polymer that undergoes degradation through surface erosion by hydrolytic cleavage of the ester bonds. PHB is a stereoregular polyester capable of achieving high levels of crystallinity resulting in brittleness and has a narrow processing window. Therefore, to improve the properties of PHB, various copolymers of PHB containing hydroxyalkanoate units such as 3-hydroxyvaleric acid (3HV) have been biosynthesized (PHB-co-PHV). The comonomer reduces the crystallinity and also the melting point of the homopolymer.<sup>[104, 105, 112]</sup> The degradation temperature of PHB is between 250 and 300 °C, which is associated with the complete weight loss due to conversion of polymer to crotonic acid. The crystal structure consists of the arrangement of the polymer chains in 2<sub>1</sub>/1 helices in orthorhombic crystals with P2<sub>1</sub>2<sub>1</sub>2<sub>1</sub> space group. The unit cell dimensions are a= 5.76 Å, b=13.20 Å and c=5.96Å.<sup>[114]</sup> PHB has high crystallinity which makes it difficult to solubilize in most of the solvents. The most common solvent for PHB is chloroform. Most of the solution processing of this polymer has been done by dissolving in boiling chloroform. Other solvents which have been used to solubilise PHB are 1, 2-dichloroethane, trifluoroethanol and DMF. This polymer is regarded as highly melt-unstable because of its degradation to

crotonic acid at temperatures just slightly above its melting point. PHB and its copolymers have medical applications such as controlled drug release, surgical sutures, bone plates, heart valves, and wound care as well as tissue engineered scaffolds. Other applications include moisture barrier films coverstock in disposable items as diapers or sanitary napkins. PHB also finds some uses in agricultural and horticultural areas like sustained release of plant growth regulators or pesticides.<sup>[104, 105, 108, 112, 115]</sup>

## **CHAPTER 3**

### **EFFECT OF NANOPARTICLE SURFACE AREA ON THE PROPERTIES OF NANOCOMPOSITES**

#### **3.1. Introduction**

The influence of nanoparticle surface area as an important nanoparticle attribute, on the properties of the nanocomposites was identified in this study. The interphase development and the resulting nanocomposite properties have been shown to be greatly impacted by nanoparticle attributes such as size, shape, aspect ratio, concentration and surface chemistry. Many experimental studies have been performed to understand the impact of particle morphology (size, shape, and aspect ratio) on nanocomposite properties. Mechanical properties, such as strength and modulus, have generally increased with decreasing particle size in polymer nanocomposites,<sup>[116, 117]</sup> and direct comparisons between micron-scale and nanoscale particles showed improved mechanical properties in nanocomposites when compared at the same filler loading.<sup>[59]</sup> With regard to particle shape, experimental and computational research concerning chemically similar nanoparticles with different shapes has indicated that shape does not play a primary role in nanocomposite reinforcement when the aspect ratio of the nanoparticles was low.<sup>[64,</sup>  
<sup>118]</sup> Nanocomposites showed the same reinforcement trend with increasing surface area for spherical and platelet (aspect ratio = 10) shaped particles.<sup>[64]</sup> Carbon nanotubes and nanoplatelets possessed similar reinforcing capabilities at an aspect ratio of 10 in both aligned and random configurations, but, at an aspect ratio of 1000, the particle shape did

impact the mechanical properties because nanoplatelets provided higher reinforcement than nanotubes.<sup>[118]</sup>

The effect of surface area may be linked to the nanoparticle attributes listed above. For example, at a fixed material density, the nanoparticle surface area contained in the composite will increase with decreasing nanoparticle size and increasing nanoparticle concentration. Also, surface area can magnify the effect of nanoparticle surface chemistry on properties by perturbing a greater quantity of polymer chains as the nanoparticle/polymer interfacial area increases.

Studies concerning surface area explicitly have shown that reinforcement and the amount of interphase may be related to nanoparticle surface area.<sup>[119-121]</sup> In polyvinyl alcohol (PVA) composites made with single-, double-, multi-walled as well as catalytic and functionalized carbon nanotubes, the highest reinforcement was seen with the smallest diameter nanotubes.<sup>[119]</sup> Another tan delta peak appeared corresponding to overlapping regions of polymer chains adjacent to the immobilized polymer adsorbed on the filler surface. Its appearance was due to the large volume of immobilized polymer which was a direct result of the high surface area of the filler. Similar peaks were also found in composites of silica nanoparticles with polystyrene, poly(4-vinylpyridine), styrene-butadiene-rubber and poly(dimethylsiloxane) (PDMS) at 10 wt.% or higher and were attributed to slower dynamics of the interface material which made up a significant portion of the total polymer volume.<sup>[120]</sup> Analogous results have been obtained for silica nanocomposites using quasielastic neutron scattering (QENS).<sup>[121]</sup> Slow relaxation of polymer chains adsorbed on the higher surface area silica nanoparticles gave rise to an elastic component in QENS data in addition to the quasielastic broadening caused by the

free polymer chains. In this chapter we discuss the effect of nanoparticle surface area on the nanocomposite properties below and above the glass transition temperature ( $T_g$ ). The results of this study show that surface area may be used as a design parameter with predictive capabilities above  $T_g$ .

## **3.2. Experimental**

### **3.2.1. Materials**

HAp/PCL nanocomposites were made from synthesized HAp nanoparticles and commercially available PCL by a solvent casting technique. HAp nanoparticles were synthesized via a reverse microemulsion method using calcium nitrate tetrahydrate ( $\text{Ca}(\text{NO}_3)_2 \cdot 4\text{H}_2\text{O}$ ) (Alfa Aesar) and phosphoric acid ( $\text{H}_3\text{PO}_4$ ) (Fisher Scientific) as the calcium and phosphorous precursors, respectively. The organic phase of the reverse micelle system was formed using cyclohexane (Fisher Scientific) and a combination of poly(oxyethylene)<sub>5</sub> nonylphenol ether (NP-5) and poly(oxyethylene)<sub>12</sub> nonylphenol ether (NP-12) surfactants (Aldrich). The aqueous solutions of the precursors were prepared using deionized water. Ammonium hydroxide ( $\text{NH}_4\text{OH}$ ) (Mallinckrodt Chemicals) was used for maintaining pH during synthesis and aging. The solvent cast composites were prepared using solvent grade dichloromethane (Alfa Aesar) and PCL with number average molecular weight of 80,000 g/mol (Sigma-Aldrich). All materials were used as received from the suppliers.

### 3.2.2. HAp Nanoparticle Synthesis

The HAp synthesis was performed using a microemulsion technique based on a protocol from Bose and Saha.<sup>[102]</sup> The conditions that produced the highest surface area values in their work were used in this study. This method is summarized briefly here. 5M calcium nitrate tetrahydrate and 2.99M phosphoric acid solutions were prepared in deionized water. The molar ratios of the precursors were selected to maintain calcium to phosphorous atomic ratio (Ca/P) of 1.67:1. NP-5 and NP-12 surfactants were mixed in a 1:1 ratio by volume and added at a concentration of 10 vol.-% to cyclohexane, the organic phase. The aqueous and organic phases were combined in ratios of 1:5 and 1:10 (by volume), respectively, to obtain the reverse micelle systems. These two aqueous to organic ratios produced nanoparticles with different amounts of surface area for study. The emulsion formed by mixing the aqueous and the organic phase converted to a highly viscous transparent gel after stirring. The pH of the emulsion was adjusted to 7.0 by adding concentrated ammonium hydroxide solution drop wise with continuous stirring. The pH of the emulsion was checked regularly with each addition since HAp is formed in neutral and alkaline environments.<sup>[76]</sup> The emulsion was aged for 12 hours at room temperature to complete the reaction. After aging, the gel was filtered and washed. Several washings with distilled water were added to the original protocol to ensure the removal of nitrate and ammonium ions.<sup>[122]</sup> On filtration, a white cake was formed and subsequently dried in a vacuum oven at 150°C to remove traces of solvent and water. Finally, the dried white cake was calcined at 450 °C in a muffle furnace for one hour to obtain a white powder.

### 3.2.3. Particle Characterization

The morphology, chemical structure, crystal structure, specific surface area, and density of the synthesized HAp powders were characterized as described below. The morphology of the HAp particles was examined by transmission electron microscopy (TEM) using a JEOL 100CX-2 microscope operating at 100 kV. Samples were prepared by dispersing a small quantity of the HAp particles in ethanol and allowing a small amount to air dry on a lacey carbon coated copper TEM grid. Dynamic light scattering was also used to determine the particle size. The HAp particles were dispersed in ethanol using sonication to form a suspension with a HAp concentration of 0.01% by weight. The measurements were performed using a Brookhaven BI-200SM goniometer (He-Ne laser with wavelength of 633nm) and a BI-9000AT correlator. The results were analyzed using the CONTIN analysis method for multimodal particle size distributions.<sup>[123]</sup>

Fourier transform infrared spectroscopy (FTIR) was performed to determine chemical structure using a Bruker Vector 22 FTIR spectrometer. The HAp powder was mixed with KBr (EMD Chemicals) and pressed into a pellet. The pellet contained 2 mg of HAp powder and 100 mg of KBr powder. The spectra were recorded at room temperature in the range 4000-400cm<sup>-1</sup> using 32 scans and a resolution of 4 cm<sup>-1</sup>. X-ray powder diffraction studies were performed to determine crystal structure using a Rigaku Micro Max 002 X-ray generator with CuK<sub>α</sub> radiation ( $\lambda = 1.5405\text{\AA}$ ), an R-axis IV++ detector system, 45kV accelerating voltage, and 0.66mA current. The powder was ground and placed in a glass capillary (Special glass 10, Inner diameter-1mm, glass wall thickness 0.1mm). The background was subtracted using an empty glass capillary.



The surface area of the HAp powders was determined using a Surface Area and Porosity Analyzer (ASAP 2020) from Micromeritics, Inc. Prior to the measurement, the samples were degassed for 16 hours at 90°C to remove moisture. Isothermal N<sub>2</sub> gas adsorption and desorption was carried out at 77 K using a liquid nitrogen enclosure. The specific surface area was determined with the Brunauer, Emmet, and Teller (BET) method.<sup>[124]</sup> The density of the HAp powders were measured using a glass pycnometer. The dry weight of pycnometer was determined using an analytical balance. Approximately 0.5 g of HAp powder was put in the dry pycnometer. The pycnometer was weighed again using the analytical balance to determine the exact weight of the powder. The pycnometer was then filled with water up to the appropriate mark, and the mixture was sonicated in a bath sonicator for 20 minutes. Then, the mixture was degassed using vacuum for 20 minutes. After these steps, the pycnometer with water and HAp powder was weighed again, and the weight was recorded. Then, the water and HAp powder mixture was removed from the pycnometer, and the same procedure was performed for the pycnometer filled with water only. Using these weights, the density of the powder is obtained using the equation given below:

$$\rho_{pow} = \frac{W_{pow}}{(W_{pyc-wat} - (W_{pyc-wat-pow} - W_{pow}))} \quad (1)$$

Where:

$W_{pow}$  = Weight of HAp powder

$W_{pyc-wat}$  = Weight of pycnometer + water

$W_{pyc-wat-pow}$  = Weight of pycnometer + water + HAp powder

#### **3.2.4. Nanocomposite Processing**

Nanocomposites were prepared using a solution processing technique. The HAp nanoparticles were dispersed in dichloromethane by sonication in a cup-horn sonicator at a power of 84W for 30 minutes to reduce the size of nanoparticle aggregates. A circulator was used to maintain the water temperature in the sonicator at approximately room temperature. At the end of this sonication step, the suspension appeared homogeneous to the naked eye, and no aggregates were observed. The PCL polymer was dissolved in the HAp sol to form a 20 wt. % polymer solution by stirring. To disperse the nanoparticles in the PCL, the nanocomposite solution was further sonicated for 30 minutes at room temperature. Nanocomposite films were prepared by solvent casting onto a preheated casting dish. Further drying was performed in a vacuum oven at 40 °C for 24 hours to remove the solvent traces. Solvent cast composite films were prepared with 0.5, 1, 5 and 10 wt. % of HAp particles. A neat PCL sample was also prepared using the same processing conditions as the composite samples for comparison.

#### **3.2.5. Nanocomposite Characterization**

The HAp/PCL composites were characterized for dispersion and distribution, thermal properties, and thermomechanical properties. Nanoparticle dispersion and distribution were observed by scanning electron microscopy (SEM). Cryo-fractured surfaces of the composite specimens were gold coated using an ISI Sputter Coater and then imaged using a LEO 1530 SEM at a voltage of 10 kV. In the context of this research, dispersion was indicated by an increase in nanoparticle surface area available to the polymer (aggregates broken down), and distribution was indicated by a homogeneous

distribution of nanoparticles in the matrix (individual or aggregated). Thermal transitions were measured by differential scanning calorimetry (DSC) with a Seiko DSC 220. The specimens were heated from -20 to 100°C at a rate of 10°C/min under nitrogen gas flow. After a 10 min dwell, the specimens were cooled back to -20°C at the same rate. Two such cycles were performed on each specimen. From the melting peak of the first and the second run, the crystallinity ( $X_c$  %) of the polymer was calculated according to the equation:

$$X_c (\%) = \left( \frac{\Delta H_m}{\Delta H_m^\circ} \right) \frac{1}{(1 - \phi)} \cdot 100 \quad (2)$$

where  $\Delta H_m$  is the enthalpy of melting measured during the heating cycle,  $\Delta H_m^\circ$  is the enthalpy of melting of a completely crystalline PCL ( $\Delta H_m^\circ = 139$  J/g) and  $\phi$  is the weight fraction of filler in the composites.<sup>[125]</sup> The percent crystallinity was reported as the average value obtained from two DSC runs on two samples.

To further understand the polymer morphology, isothermal crystallization studies were carried out using a TA Instruments DSC Q-200. The samples were heated from room temperature to 100°C at a rate 10 °C/min under nitrogen atmosphere and held at 100°C for 10 min and then cooled rapidly (60°C/min) to the crystallization temperatures ( $T_c = 40, 42, 44, 46^\circ\text{C}$ ) for the isothermal experiments. The samples were then heated again to 100°C at 10°C/min. Two isothermal studies were performed on each nanoparticle concentration and averaged. The crystallization kinetics was studied using the Avrami equation to determine  $n$  and  $k$  parameters:

$$\ln [-\ln[1-X(t,T)]] = \ln k(T) + n \ln t \quad (3)$$

where  $X(t,T)$  is the crystalline fraction of the material at time,  $t$ , with respect to the total crystallinity at infinite time at isothermal temperature( $T$ );  $n$  and  $k$  are the Avrami crystallization parameters and  $n$  is related to the mechanism of crystallization whereas  $k$  is the crystallization rate constant.<sup>[126]</sup>

Dynamic mechanical analysis (DMA) was conducted on a Mettler Toledo DMA861<sup>°</sup> using shear deformation. Compression molded samples with a nominal thickness of 1 mm were used. The measurements were performed in the linear viscoelastic range, established using room temperature strain sweep measurements for all of the specimens. The testing was performed using force amplitude of 4.0N below  $T_g$  and a strain amplitude of 0.5  $\mu\text{m}$  above  $T_g$ . The temperature was varied from -100 to 40°C with a heating rate of 2°C/min, and the measurements were performed at a frequency of 1 Hz. Two temperature scan tests were conducted on each material.

### **3.3. Results and Discussion**

#### **3.3.1. Morphology and Size of HAp Nanoparticles**

Using the synthesis method outlined above, two systems of HAp nanoparticles were produced, with specific surface areas of 60 m<sup>2</sup>/g and 111 m<sup>2</sup>/g. In the following discussion, the particles will be designated HAp60 and HAp111, respectively. The morphology of the HAp particles was determined using TEM. The HAp60 particles showed predominantly platelet shaped morphology whereas in case of the HAp111 particles, the predominant shape produced was an aggregate of needle-like primary particles as shown in Figure 3.1. These aggregates had an approximately spherical shape. The HAp111 nanoparticles also contained some plates of similar dimensions to the

HAp60 nanoparticles. In addition to specific surface area and morphology, the mean effective hydrodynamic diameter of the HAp nanoparticles measured using dynamic light scattering and deduced from CONTIN analysis was  $680 \pm 87$  nm for HAp111 nanoparticles and  $1100 \pm 180$  nm for HAp60 nanoparticles. The standard deviations given here describe the variation in the mean value calculated from four separate dynamic light scattering experiments. The range of values calculated from a single experiment was on the order of hundreds of nanometers, indicating that each particle system was polydisperse. For the HAp111 nanoparticles, the hydrodynamic diameter represented aggregates, whereas the value measured for HAp60 represented an individual particle. Since vigorous ultrasonic processing did not disrupt the HAp111 aggregates prior to TEM and dynamic light scattering experiments, the aggregates structure was robust and held together by tight physical clustering of primary particles or fused contact points between primary particles during the calcination step. More TEM images of particles can be found in Appendix B.

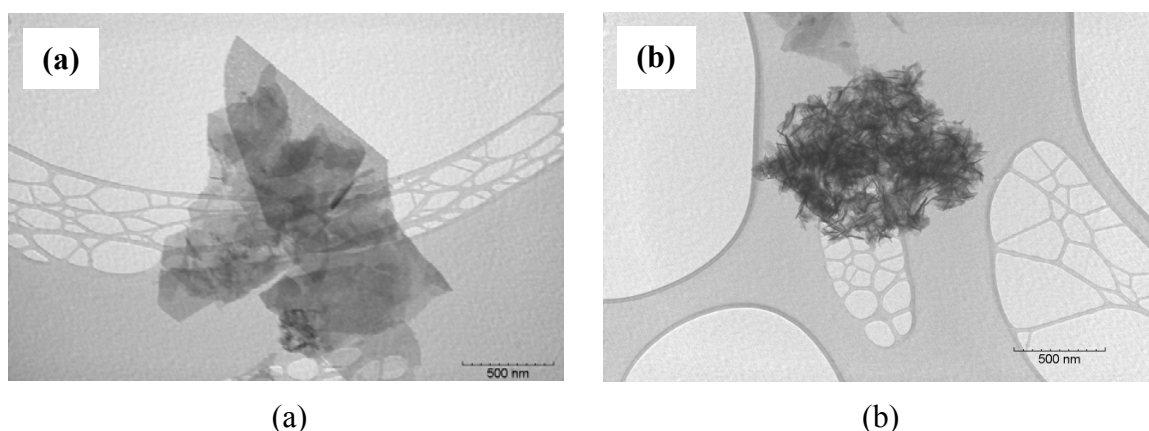


Figure 3. 1. Morphology of HAp nanoparticles as observed in TEM. (a) HAp60 showing platelet shape and (b) HAp111 showing needle-like morphology of individual particles. The scale bar represents 500nm.<sup>[70]</sup>

### 3.3.2. Chemical Structure of HAp Nanoparticles

Figure 3.2 shows the FTIR spectra for both nanoparticle systems where the intensity was normalized to the highest intensity phosphate peak ( $\text{PO}_4^{3-}$   $1030\text{cm}^{-1}$ ). The FTIR spectra were similar to the spectra for HAp found in the literature.<sup>[127]</sup> The absorption bands at 600 and  $1000\text{--}1200\text{ cm}^{-1}$  were due to vibrations of the phosphate group and the absorption bands at 630 and  $3572\text{cm}^{-1}$  to the hydroxyl ( $\text{OH}^{-1}$ ) group.<sup>[127, 128]</sup> The peak at  $1630\text{ cm}^{-1}$  and the broad absorption band at  $3400\text{ cm}^{-1}$  correspond to the water associated with the HAp.<sup>[127]</sup> The presence of the stretching mode of the hydroxyl group indicates a possible compatibility of the synthesized HAp with the carbonyl group ( $\text{C=O}$ ) of the PCL matrix for H-bond formation. Also, the FTIR studies confirmed that the HAp powders were free from  $\text{CO}_3$  inclusion.<sup>[127]</sup>

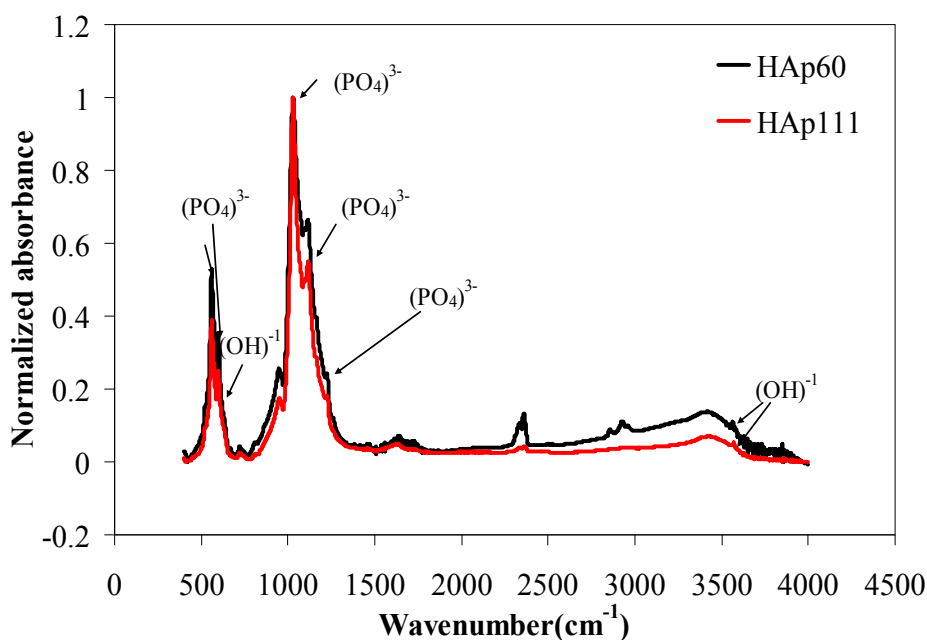


Figure 3. 2. Infrared spectra of as synthesized HAp60 and HAp111 powders normalized to the highest intensity peak corresponding to phosphate functional group ( $\text{PO}_4^{3-}$   $1030\text{cm}^{-1}$ ).<sup>[70]</sup>

### 3.3.3. Crystal Structure of HAp Nanoparticles

The crystal structure of the calcined HAp was analyzed using X-ray diffraction. The results were compared to the major reflections of stoichiometric HAp obtained from the ASTM card file 9-432. As shown in Table 3.1, the d spacing for the major reflections were similar between the HAp60 and HAp111 nanoparticles, and the spacings matched those listed in the standard card file. The unit cell dimensions of the synthesized powders were determined to be  $a = b = 9.444 \text{ \AA}$  and  $c = 6.863 \text{ \AA}$ , similar to values found in the literature ( $a = b = 9.423 \text{ \AA}$  and  $c = 6.875 \text{ \AA}$ ).<sup>[76, 127]</sup>

Table 3. 1. Plane spacings observed in X-ray powder diffraction pattern of HAp and comparison with respective data for stoichiometric HAp.<sup>[70]</sup>

<b>HAp60 d(Å)</b>	<b>HAp111 d(Å)</b>	<b>ASTM Card No. 9-432 for stoichiometric HAp</b>	
		<b>d(Å)</b>	<b>Miller Indices</b>
5.212	5.273	5.250	(101)
3.890	3.890	3.880	(111)
3.432	3.432	3.440	(002)
4.149	4.092	4.070	(200)
2.912	2.801	2.814	(211)
1.838	1.836	1.841	(213)
2.219	2.267	2.262	(310)
1.722	1.718	1.722	(004),(411)

### 3.3.4. Specific Surface Area and Density of HAp Nanoparticles

The specific surface area of the HAp particles was determined using the BET surface area analysis. As indicated by the naming system, the HAp60 particles have

smaller specific surface area than the HAp111 particles. The differences observed between the two nanoparticle systems resulted from the size of the water core of the reverse micelle during HAp synthesis. As the aqueous to organic ratio increased, the size of the water core containing the calcium and phosphorous precursors increased, leading to larger particle size (smaller specific surface area at equal density). The density of HAp powders was determined using a glass pycnometer. The measured densities of HAp60 and HAp111 were 2.87 and 2.97 g/cm<sup>3</sup> respectively.

### **3.3.5. Dispersion and Distribution of HAp Particles in Nanocomposites**

These two particles systems were used to produce nanocomposite samples at HAp loadings of 0.5, 1, 5 and 10 wt. %. The dispersion of the HAp nanoparticles achieved in the PCL matrix was observed using SEM. As shown in Figure 3.3 for 10 wt. % HAp, the HAp60 nanoparticles appeared uniformly dispersed and distributed to the individual nanoparticle level in the PCL matrix. The edges of individual plates are visible at the fracture surface, and no particle aggregates were observed. The HAp60 particles also demonstrated uniform dispersion in the PCL matrix at 0.5, 1, and 5 wt. % concentrations. The HAp111 nanoparticles showed a different dispersion behavior. They also appeared to be well distributed, but the aggregates of smaller needle shaped particles that were observed in the TEM and dynamic light scattering experiments were still present in the nanocomposites. Overall, the HAp111 nanoparticles appeared to possess smaller dimensions than the HAp60 nanoparticles. Similar observations were made for the other HAp111 nanoparticle loadings. For SEM images of dispersion at other concentrations please refer to Appendix B.



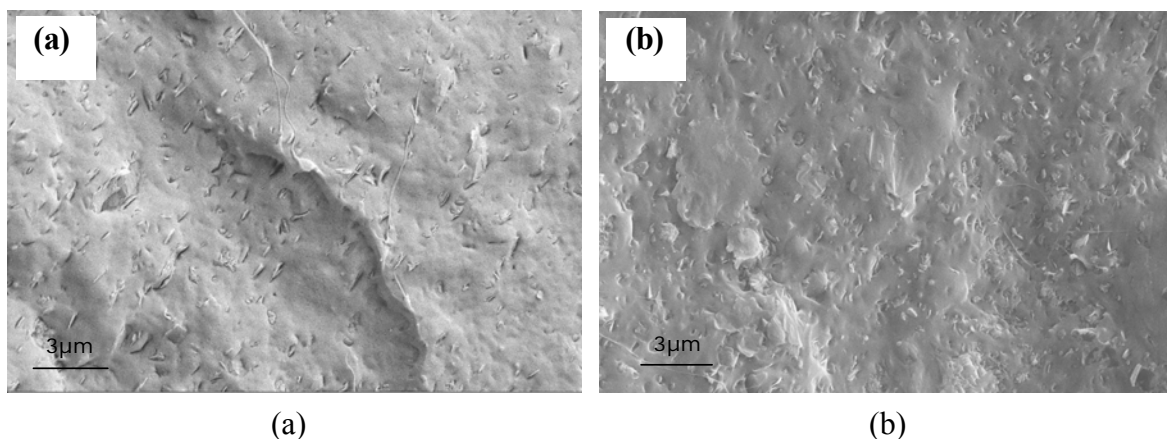


Figure 3. SEM images showing dispersion of HAp nanoparticles in (a) HAp60/PCL (10 wt.%) and, (b) HAp111/PCL (10 wt.%) composite samples. Homogenous distribution was attained in both nanoparticle systems at all concentrations.<sup>[70]</sup>

In order to compare the particle sizes obtained prior to composite processing from dynamic light scattering to the particle sizes observed in the composites, the dimensions of HAp60 and HAp111 nanoparticles were measured using SEM images of the nanocomposite fracture surfaces. The number of particles measured in each system was approximately 100. The HAp60 nanoparticles possessed an average plate length of  $990 \pm 430$  nm and an average plate thickness of  $20 \pm 7$  nm. Since the HAp60 nanoparticle length is much greater than its thickness, the length of a diagonal constructed across the face and through the particle are the same values as the particle length when considering significant figures, so the nanoparticle length is used for comparison with the dynamic light scattering data. The HAp111 nanoparticle aggregates possessed an average diameter of  $660 \pm 310$  nm. Since the measurements from SEM images were largely consistent with the hydrodynamic diameters obtained from dynamic light scattering, the specific surface area measurements for the HAp nanoparticles were assumed to be apply to the composites as well.

Table 3. 2.Percent crystallinity of neat PCL and HAp/PCL composite samples from first and second heat cycles of DSC.<sup>[70]</sup>

Sample	% Crystallinity First Heat	% Crystallinity Second Heat
Neat PCL	40.2 ± 1.6	36.1 ± 1.8
0.5 wt.% HAp60/PCL	40.5 ± 2.3	34.8 ± 1.3
1 wt.% HAp60/PCL	39.0 ± 0.5	36.3 ± 3.0
5 wt.% HAp60/PCL	36.2 ± 1.8	36.3 ± 1.7
10 wt.% HAp60/PCL	45.2 ± 2.2	38.7 ± 0.3
0.5 wt.% HAp111/PCL	34.5 ± 1.4	30.9 ± 0.7
1 wt.% HAp111/PCL	40.2 ± 3.3	32.8 ± 0.9
5 wt.% HAp111/PCL	45.3 ± 3.2	37.3 ± 0.5
10 wt.% HAp111/PCL	44.7 ± 0.1	38.2 ± 0.1

### 3.3.6. Thermal Properties and Crystallization Kinetics of Nanocomposites

Thermal transitions and crystallization behavior for the neat PCL and the nanocomposite samples were measured using DSC. Table 3.2 lists the percent crystallinity values of the neat PCL and the HAp/PCL composites, taken from both the first and second heating cycles of the DSC measurement. The melting temperature was largely unchanged for all of the materials and was 59°C. Approximately 2°C separated all of the values. The amount of crystallinity achieved showed some variation with nanoparticle loading as shown in Table 3.2 and Figure 3.4. Since all crystallinity values for the nanocomposites were within approximately 5% of the neat polymer, no changes were regarded as significant. Similar behavior has been seen in other nanocomposite materials and may be linked to the strength and nature of the interfacial interaction. Covalent bonds across the interface have been shown to increase crystallinity whereas attractive non-covalent

interactions have shown decreased or similar crystallinity to the neat polymer.<sup>[129-131]</sup> In nanocomposites with non-covalent interactions, strong attractions can inhibit crystallinity through constraining polymer molecules at the surface, and weak attractions show little or no change to the polymer crystallinity. Our results are consistent with the latter case, indicating that the interfacial interactions are likely weakly attractive.

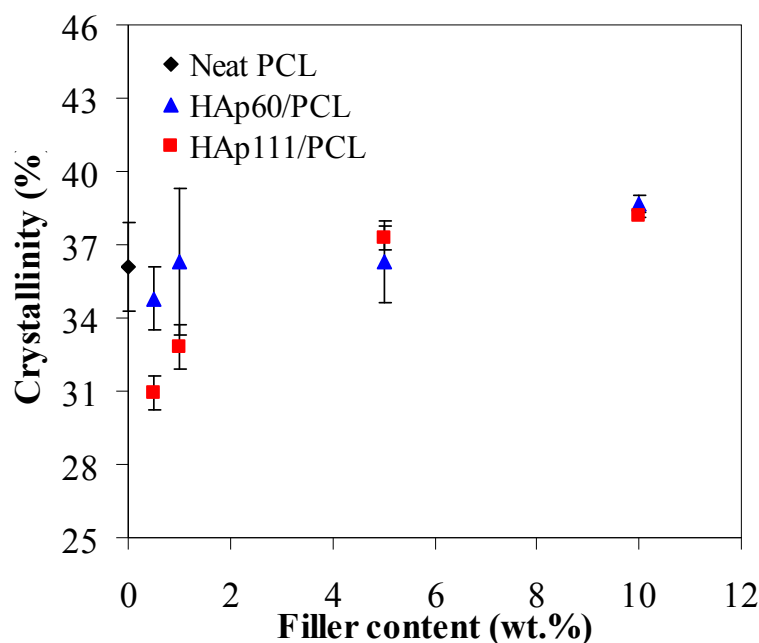


Figure 3. 4.% Crystallinity from second heat as a function of filler content for neat, HAp60 and HAp111 composite samples.<sup>[70]</sup>

The crystallization temperatures (defined as the peak temperature value for the event) of the 10 wt. % HAp60/PCL and the 10 wt. % HAp111/PCL were increased 2.4°C and 1.4°C, respectively. The increased crystallization temperature suggested that the presence of HAp nanoparticles has some nucleating capability at sufficient nanoparticle loadings consistent with previous observations.<sup>[132]</sup> However, the crystalline morphology

of the polymer was not affected as the melting point and crystallinity did not show significant changes. Therefore the nucleating effect was attributed to the increase in polymer viscosity in presence of nanoparticles which helped in formation of stable nuclei.

To understand the nanoparticles' impact on the kinetics, isothermal crystallization studies were conducted on the neat PCL, 1 wt.%, 5 wt.% and 10 wt.% nanocomposites. The half-time crystallization ( $t_{1/2}$ ) is a measure of overall crystallization rate and is related to the rate constant. The half-time values can be calculated from the equation as:

$$t_{1/2} = \left( \frac{\ln 2}{k} \right)^{1/n} \quad (3)$$

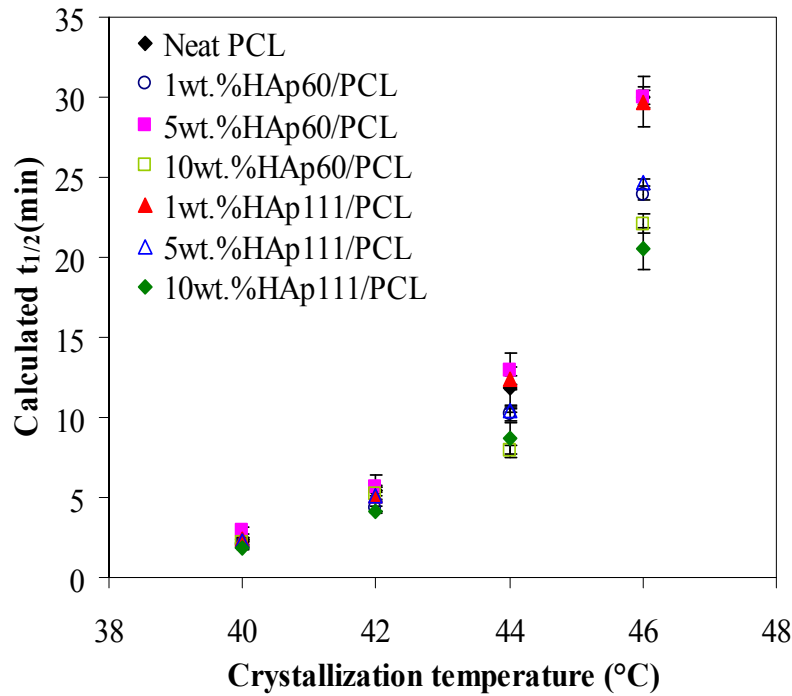


Figure 3. 5. Half-time crystallization of neat PCL and HAp nanocomposites as a function of crystallization temperature. With the exception of the 5 wt.% HAp60/PCL samples at 40°C, the addition of the nanoparticles had a nucleating effect on PCL as evidenced by the decreased  $t_{1/2}$ .<sup>[70]</sup>

Figure 3.5 shows  $t_{1/2}$  as a function of isothermal crystallization temperature. With the exception of one composite at one crystallization temperature, all the composite samples showed a lower  $t_{1/2}$  than the neat PCL. The reduced time translated to a higher crystallization rate and suggested that the HAp nanoparticles were acting as nucleating agents for the crystallization of the PCL matrix. These results were supported by the increase in the kinetic constant  $k$  of the Avrami equation (Table 3.3). The Table shows the  $t_{1/2}$  as well as  $n$  and  $k$  values at 40°C. All the samples showed a decrease in  $t_{1/2}$  values and an increase in the crystallization rate except at 40°C for the 5 wt. % HAp60/PCL sample which also showed a decrease in overall crystallinity as seen from the first heat DSC values. At all other temperatures, in all of the samples regardless of HAp concentration, the  $k$  decreased and  $t_{1/2}$  increased with increasing isothermal crystallization temperature ( $T$ ) from 40-46 °C because of a gradual decrease in supercooling. The constant  $n$ , which is related to the mechanism of crystallization, had a value between 2 and 3 for PCL indicative of athermal nucleation and subsequent three-dimensional crystal growth. Mixed nucleation and growth produced nonintegral  $n$  values in all of the materials.<sup>[133]</sup> The value of  $n$  was not modified largely by the presence of HAp particles suggesting that the crystallization mechanism was heterogeneous and athermal. The HAp111/PCL composites show slightly higher increase in crystallization rate compared to the HAp60/PCL composites due to its smaller particle size and higher surface area. The isothermal crystallization parameters at 42, 44 and 46°C are given in Appendix B.

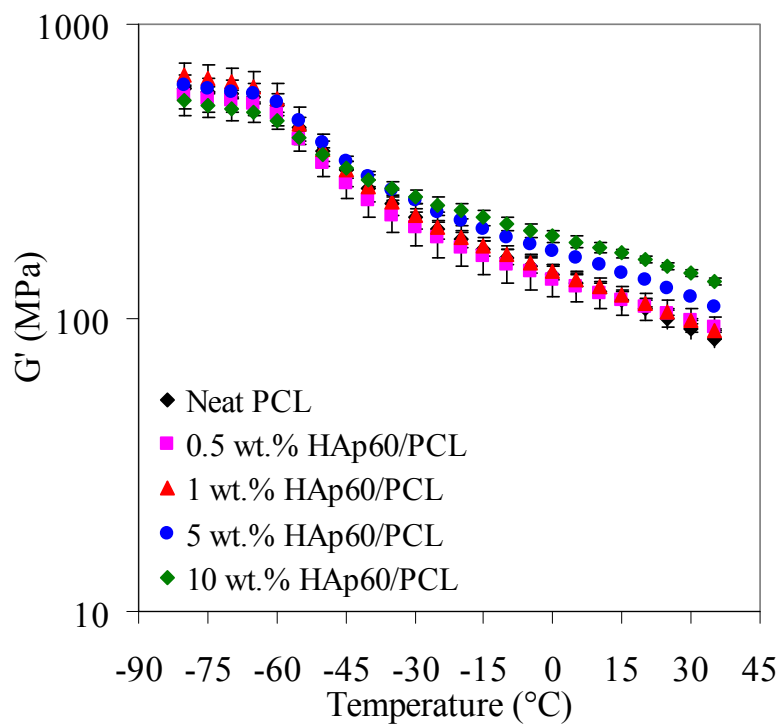
Table 3. 3.Isothermal crystallization parameters for PCL, HAp60 and HAp111/PCL composite samples at  $T_c = 40^\circ\text{C}$ .<sup>[70]</sup>

Samples	$t_{1/2}$ (min)	$n$	$k$
Neat PCL	$2.4 \pm 0.1$	$2.5 \pm 0.0$	$7.7 \cdot 10^{-02} \pm 6.5 \cdot 10^{-03}$
1 wt.% HAp60/PCL	$2.1 \pm 0.1$	$2.5 \pm 0.1$	$1.2 \cdot 10^{-01} \pm 0.0 \cdot 10^{+00}$
5 wt.% HAp60/PCL	$2.9 \pm 0.2$	$2.2 \pm 0.2$	$6.9 \cdot 10^{-02} \pm 1.1 \cdot 10^{-02}$
10 wt.% HAp60/PCL	$2.2 \pm 0.3$	$2.1 \pm 0.2$	$1.3 \cdot 10^{-01} \pm 2.3 \cdot 10^{-02}$
1 wt.% HAp111/PCL	$2.4 \pm 0.0$	$2.6 \pm 0.1$	$7.6 \cdot 10^{-02} \pm 0.0 \cdot 10^{+00}$
5 wt.% HAp111/PCL	$2.3 \pm 0.0$	$2.6 \pm 0.1$	$8.4 \cdot 10^{-02} \pm 1.7 \cdot 10^{-03}$
10 wt.% HAp111/PCL	$1.9 \pm 0.2$	$2.3 \pm 0.1$	$1.7 \cdot 10^{-01} \pm 3.4 \cdot 10^{-02}$

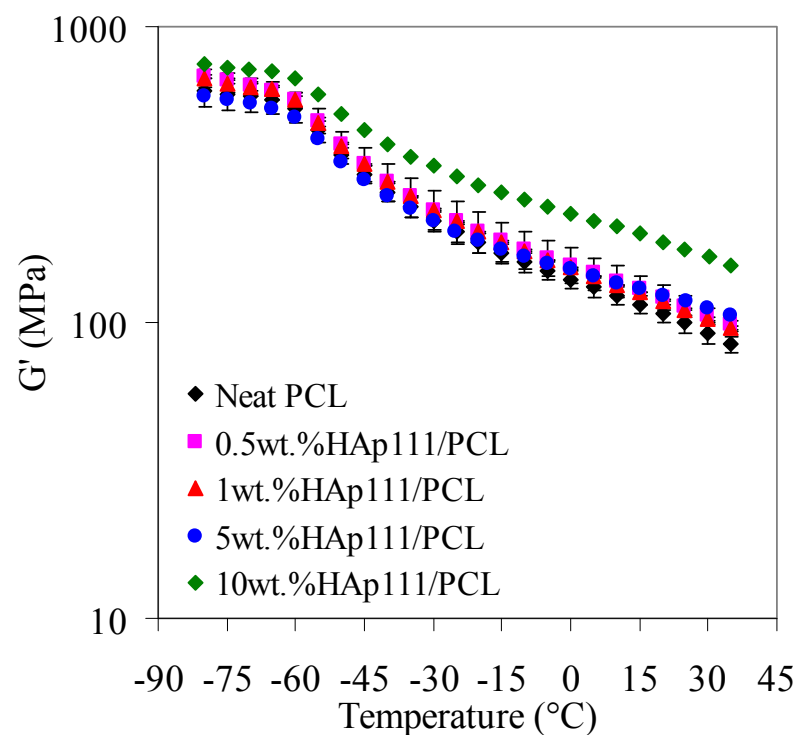
### 3.3.7. Viscoelastic Properties of Nanocomposites

Whereas the DSC experiments were largely concerned with the crystalline portion of the PCL matrix, DMA measurements were performed to understand the dynamics of the amorphous PCL chains in the presence of HAp nanoparticles. The quantities calculated by the DMA measurements were storage modulus ( $G'$ ) and loss modulus ( $G''$ ), representing the elastic and viscous nature, respectively, of the polymer. These quantities

were obtained as temperature was increased through  $T_g$ , and changes in the magnitude of  $G'$  as a function of temperature and changes in the shape of  $G''$  were used to interpret the impact of HAp addition on the amorphous polymer chains. The crystalline portion of the polymer is expected to remain unchanged through this temperature range since the onset melting point of PCL is approximately  $30^\circ\text{C}$ . Additionally, data obtained from the first heating cycle of DSC measurements indicated that the overall crystalline content of the polymer was not changed significantly by the addition of HAp nanoparticles at all loadings and processing conditions used here, so no



(a)



(b)

Figure 3. 6.Storage modulus values of neat PCL and (a) HAp60 and (b) HAp111 nanocomposite samples. Both nanocomposite systems showed reinforcement above  $T_g$ . The 10 wt. % HAp111/PCL sample showed reinforcement at all temperatures studied. The points represent the average value of two separate experiments.<sup>[70]</sup>

appreciable differences in the magnitude of  $G'$  and  $G''$  were expected due to differences in matrix crystallinity. Previous research has shown that the modulus of PCL was unchanged after the crystallinity reaches a value of approximately 40%.<sup>[134]</sup>

The  $G'$  values as a function of temperature are shown in Figures 3.6a and 3.6b, respectively, for the HAp60 and HAp111 nanocomposites. Each point represents the average value obtained from two tests performed using the same parameters, and the error bars represent the spread in the data from those two tests. The two nanoparticle systems showed different storage modulus trends with temperature. The HAp60 composites showed reinforcement only above  $T_g$ , and the HAp111 nanoparticles showed reinforcement below and above  $T_g$ . The reinforcement below  $T_g$  in the HAp111 composites was associated with the inherent nanoparticle properties whereas the reinforcement above  $T_g$  of the matrix was due to the nanoparticle properties and the interaction between the polymer and the particles defined by the surface area and surface chemistry of the particles.<sup>[135-138]</sup> Above  $T_g$ , the storage modulus of both composite samples increased with increasing HAp particle loading. Compared to neat PCL, the HAp60 and HAp111 composites showed increases of 51% and 79%, respectively, at 10 wt. % HAp loading and 25°C. The  $G''$  data were used to observe changes in the vicinity of  $T_g$ .

In order to compare the data clearly, the  $G''$  data was normalized to peak temperature as shown in Figures 3.7a and 3.7b for the HAp60 and HAp111 composites, respectively. Each point represents the average value obtained from two tests performed using the same parameters, and the error bars represent the spread in the data from those two tests. For all of the samples, small shifts in the peak temperature were observed.



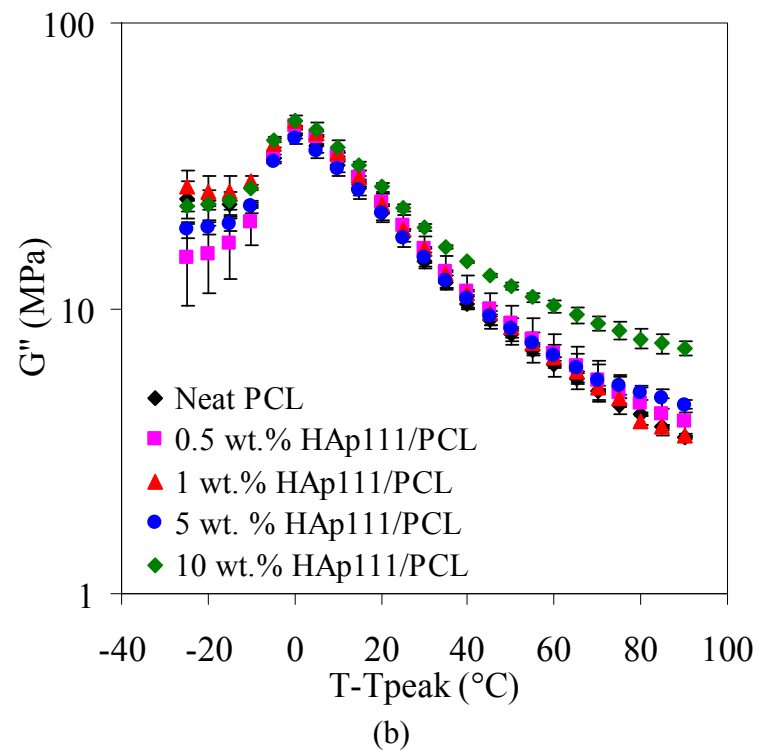
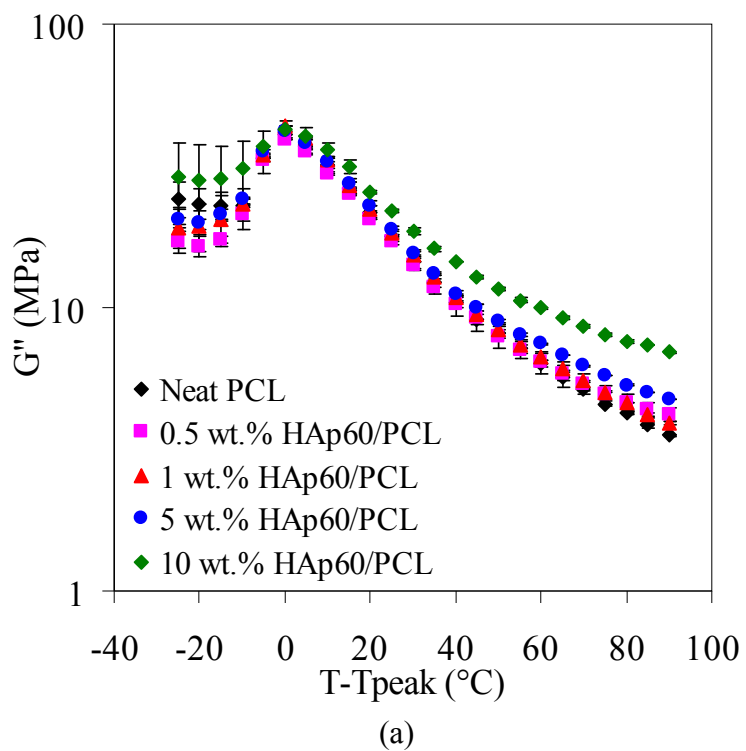


Figure 3. 7. Loss modulus values of neat PCL and (a) HAp60 and (b) HAp111 nanocomposite samples. The loss modulus increased above  $T_g$  with the increasing HAp content in both nanoparticle systems. No appreciable shift in  $T_g$  ( $-55 \pm 2^\circ\text{C}$ ) was observed with loading. The peak temperature ( $T_{peak}$ ) of neat PCL was  $-55^\circ\text{C}$  and for the composites  $T_{peak}$  was within  $\pm 2^\circ\text{C}$  of neat PCL. The points represent the average value of two separate experiments.<sup>[70]</sup>

The peak temperatures for all of the composites samples fell within 2°C of the neat PCL. Unlike the  $G'$  data, the  $G''$  curves were similar for the two nanoparticle systems below and above  $T_g$ . Both of the composite systems showed comparable increases in the loss modulus above  $T_g$  with increasing particle loadings. Also, both systems showed increased peak broadening with increasing particle loadings on the high temperature side of the transition which implies a change in the mobility of the interfacial polymer chains.<sup>[135, 137-139]</sup> This change was most noticeable at 10 wt. % HAp loading. A discontinuous change in  $G''$  was observed between 5 and 10 wt. % loading in both nanoparticle systems.

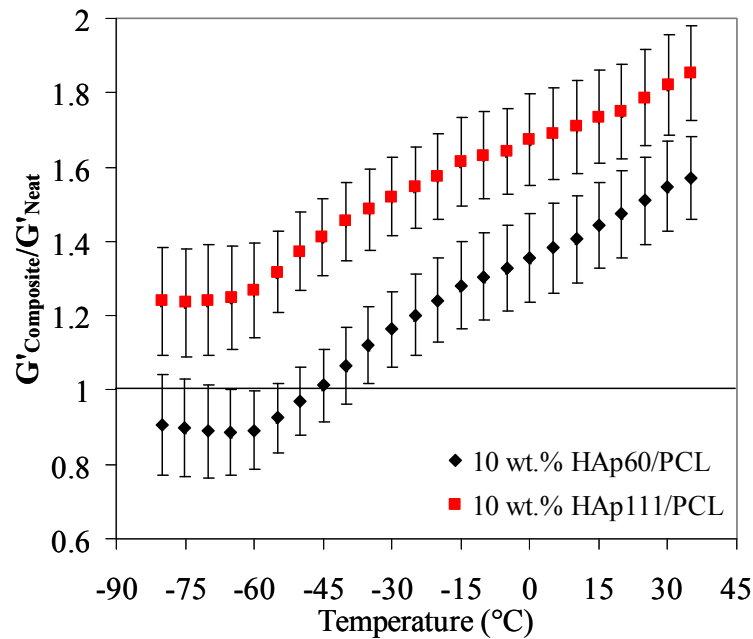


Figure 3. 8. Normalized storage modulus curves for 10 wt. % HAp/PCL nanocomposite samples. The reinforcement in both samples increased with temperature above  $T_g$  (-55°C). Higher reinforcement was seen in the HAp111 sample at all temperatures studied.<sup>[70]</sup>

To understand more fully the reinforcement trends in both nanoparticle systems,  $G'$  and  $G''$  were normalized with respect to neat PCL and the reinforcement values were plotted against temperature. These data are shown in Figures 3.8 and 3.9, respectively, for HAp loading of 10 wt. %. The error bars in these plots represent the propagated error from the composite sample and the neat PCL calculated using standard rules for the result of division. As seen in the Figure 3.8, the 10 wt. % HAp111 nanocomposite showed a relatively constant level of reinforcement (approximately 1.2x) below  $T_g$  which was attributed to the nanoparticle properties. The relative storage modulus of the 10 wt. % HAp60 composite was also relatively constant but with no appreciable reinforcement since the average value is below one. Above  $-60^\circ\text{C}$ , the slope of the reinforcement curve changes to a positive value indicating that the reinforcement of both of the composites increased with temperature above  $T_g$ . The HAp111 composite possessed a higher reinforcement at all temperatures compared to the HAp60 composite sample since it began at a higher level, but the slopes of both curves are similar. The increased reinforcement afforded by the HAp111 nanoparticle was attributed to the smaller size of the nanoparticle aggregate with respect to an individual HAp60 nanoparticle and the strong forces holding the aggregate together. The reinforcement indicated that the aggregate acted as a single particle and its structure was not perturbed during testing which is consistent with aggregate formation occurring before composite processing.

In contrast, the reinforcement in loss modulus is nearly identical for the two samples above  $T_g$ , as shown in Figure 3.9. The reinforcement of loss modulus is greater than 2x at the maximum temperature studied here. The different degrees of storage modulus and loss modulus reinforcement indicated that the increased surface area was

able to promote a greater degree of elastic coupling between the nanoparticle and the polymer. However, the similar degree of viscous coupling, represented by loss modulus reinforcement, indicated that the interfacial interactions were of the same magnitude in both systems.<sup>[138]</sup>

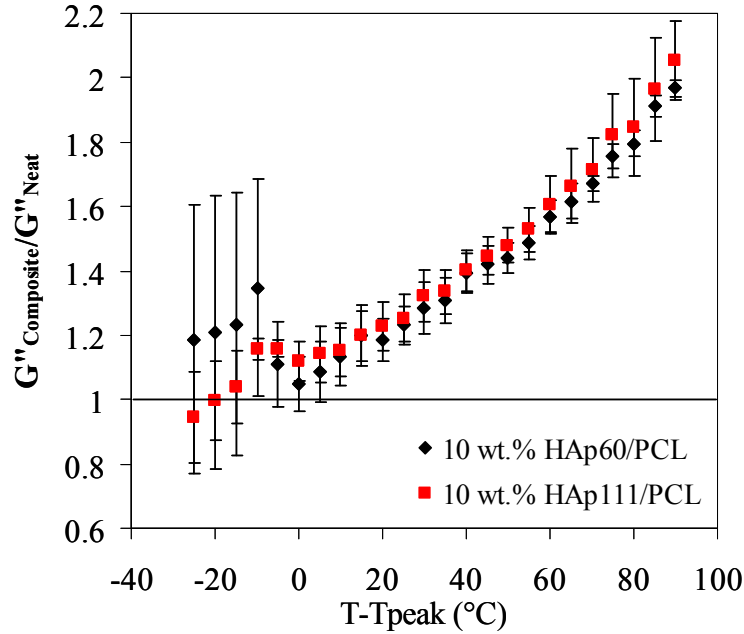


Figure 3. 9. Normalized loss modulus curves for 10 wt. % HAp/PCL nanocomposite samples. Similar amounts of reinforcement are seen in loss modulus in both composites above  $T_g$ .<sup>[70]</sup>

Based on the DMA results, the two nanoparticle systems have shown different reinforcing capabilities. The particle characterization indicated that the surface chemistry and crystallinity of the HAp60 and HAp111 nanoparticles were similar. The main differences have arisen in overall particle morphology and surface area. The HAp60 nanoparticles were plate-like particles and could be dispersed and distributed in the polymer matrix to the level of individual nanoparticles. These composites have shown no appreciable, distinct change in mechanical properties at temperatures below PCL's  $T_g$ .

The HAp111 nanoparticles contained a majority population of needle-like particles aggregated into spherical structures with a minor population of plate-like particles. The needle-like particles could not be dispersed to the single particle level in the composites due to strong physical or chemical bonds between the primary particles but were evenly distributed. These composites showed an ability to elastically reinforce the polymer matrix at temperatures below  $T_g$ . Since the particles possessed similar chemical and crystalline structure, these data indicated that the nanoparticle dispersion was able to play a role in the reinforcement behavior when the polymer chains are essentially frozen below  $T_g$ . Above  $T_g$ , the particle systems displayed similar trends in reinforcement to  $G'$  and  $G''$ . These data suggest that an interaction between the nanoparticles and the polymer chains was present. Since there is a continuous dependence on the reinforcement with temperature and the reinforcement was observed for both  $G'$  and  $G''$ , the interaction was with the amorphous chains as opposed to the crystalline chains. For amorphous chains, this interaction may manifest itself as adsorption of the polymer chains on the nanoparticles<sup>[140]</sup> or increased entanglement density at the interface.<sup>[138]</sup> Either mechanism will lead to a restricted mobility of the chains, causing slower chain relaxation and an increased reinforcement above  $T_g$ . From this analysis, the nanoparticle shape and dispersion characteristics did not have a pronounced effect above  $T_g$  but did influence the properties before the onset of long range polymer mobility.

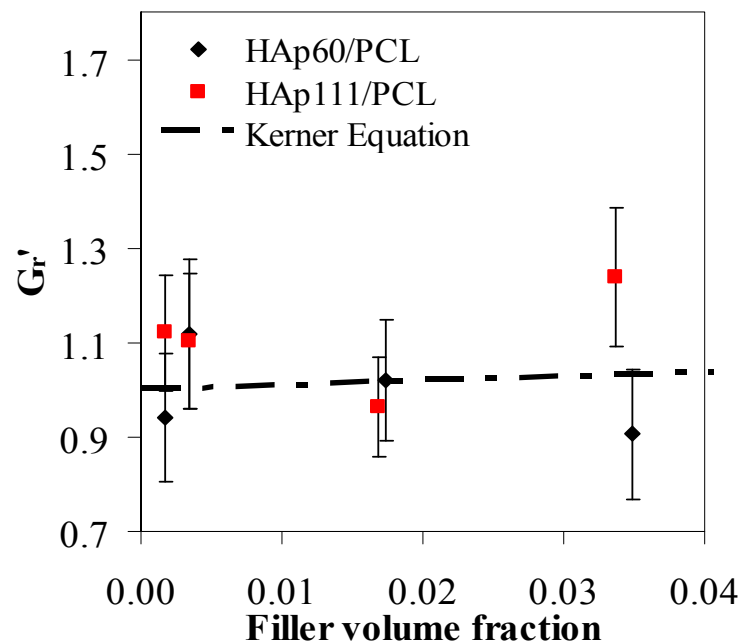
### **3.3.8. Mechanical Composite Models**

Previous research has shown that for particle shapes with similar aspect ratios the particle shape did not play a significant role in the mechanical properties,<sup>[64, 118]</sup> and this

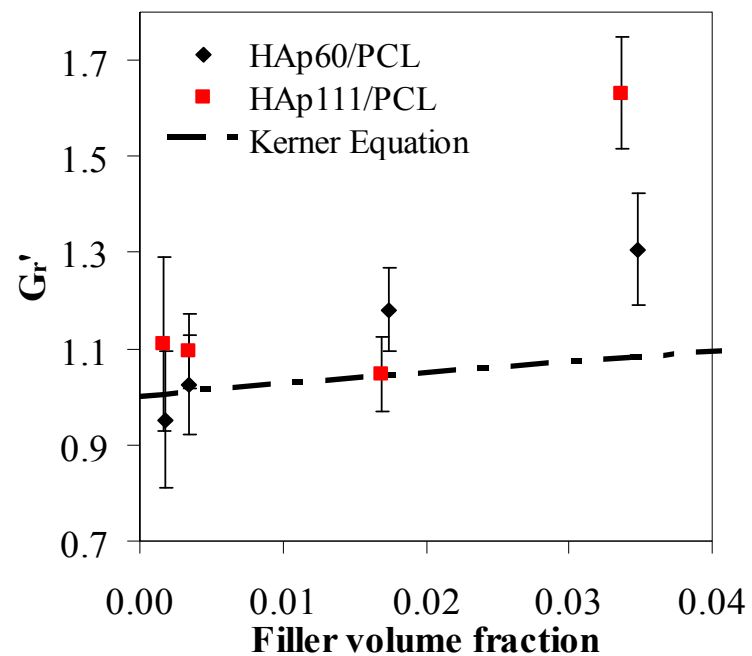
research supports this view above  $T_g$ . The effect of surface area is more complicated. To examine the differences in the HAp60 and HAp111 composites, two approaches have been used: comparison to a micromechanical model and scaling with specific composite surface area. The simplified Kerner equation, which assumes some adhesion between the filler and the matrix, was employed to the storage modulus data of the composites below (-80°C) and above (-10°C) the glass transition temperature of PCL (-60°C). The simplified Kerner equation for moderate concentrations of fillers which are more rigid than the polymer matrix is given by:

$$G_r' = \frac{G'}{G_1'} = 1 + \frac{15(1 - \nu_1)}{8 - 10\nu_1} \frac{\phi_2}{\phi_1} \quad (4)$$

where,  $G_r'$  is the relative storage modulus,  $G'$  and  $G_1'$  are the storage modulus of the composite and the neat polymer respectively,  $\nu_1$  is the Poisson's ratio of the matrix,  $\phi_2$  and  $\phi_1$  are the volume fractions of the filler and matrix, respectively.<sup>[141]</sup> The relative storage modulus  $G_r'$  for both HAp60 and HAp111/PCL composites was calculated at -80 and -10°C using the storage modulus data and compared to the simplified Kerner prediction. Poisson's ratio of the matrix  $\nu_1$  was taken as 0.3 below and 0.5 above  $T_g$ .<sup>[142]</sup> Figure 3.10 gives the dependence of relative storage modulus ( $G_r'$ ) as a function of filler volume fraction compared to the simplified Kerner model at -80°C and -10°C. Below  $T_g$ ,  $G_r'$  for both composite systems agreed with the prediction at -80°C for the three lowest nanoparticle loadings. However, the measured values deviated from the prediction for both HAp60/PCL and HAp111/PCL composite samples at the highest filler volume fraction (0.035, 10 wt. %). At this particle loading,  $G_r'$  was above the prediction for the 10 wt. % HAp111/PCL composite and below the prediction for the 10 wt. % HAp60/PCL. For both materials, the error bars were bordering the prediction, indicating



(a)



(b)

Figure 3. 10. The dependence of relative storage modulus ( $G_r'$ ) as a function of filler volume fraction compared to the simplified Kerner model at (a)  $-80^\circ\text{C}$  and (b)  $-10^\circ\text{C}$ . Deviations from the Kerner prediction were ascribed to the formation of an interphase network in the composites. Adapted from Kaur and Shofner.<sup>[70]</sup>

that the deviation was not large. The measured values and the prediction from the simplified Kerner equation showed agreement between the two lowest particle loadings in both systems. The HAp111 system also agreed with the prediction at 2 vol. % (5 wt. %) and showed a deviation at only the highest nanoparticle loading. The HAp60 composite showed an earlier deviation at 2 vol. % (5 wt. %) and the degree of deviation for prediction increased at the highest particle loading. The measured values that follow the prediction were considered to have morphology with a continuous bulk polymer matrix network. When the measured values deviated from the prediction, the morphology of the nanocomposite was dominated by an interphase network. The HAp111 would be expected to form an interphase network at lower nanoparticle loadings since more surface area was available. However, this discrepancy was attributable to the different dispersion levels achieved.

As shown in Figure 3.10b, the HAp 60 and HAp111 composites showed different amounts of reinforcement at particle loadings of 5 wt. % and 10 wt. %, but the simplified Kerner model predicts the same relative storage modulus for the nanocomposites at a given particle loading. Therefore, the relative modulus was plotted as a function of nanoparticle surface area to determine the correlation between the two HAp systems, as shown in Figure 3.11. Data from Kalfus and Jancar<sup>[64]</sup> were plotted on the same chart. These data were for HAp nanocomposites containing either spherical or platelet nanoparticles in a poly (vinyl acetate) (PVAc) matrix. The relative modulus values shown were collected at approximately 50°C above  $T_g$  of each matrix: 90°C for PVAc and -10°C for PCL. The relative modulus of the both HAp60 and HAp111 composites was found to follow the same trend as the data corresponding to the different shaped HAp



particles. These results suggest that the polymer morphology (semi-crystalline PCL and amorphous PVAc) did not play a significant role in the degree of reinforcement above  $T_g$  in the nanocomposites since the data fall on a continuous curve. The common reinforcement trend also indicates that in the system studied here the amorphous chains were primarily responsible for reinforcement in the nanocomposites that showed a deviation from the simplified Kerner model. In addition, these data showed that the reinforcement can be scaled with the amount of nanoparticle surface area available in a polymer nanocomposite in a general way, suggesting that it may be used as a parameter to modify physical models concerning nanocomposite properties.

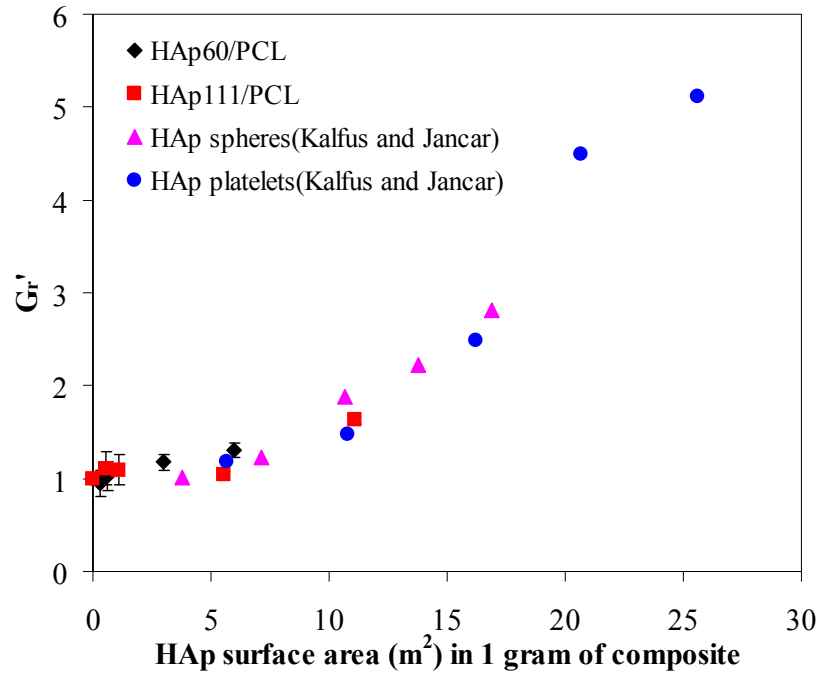


Figure 3. 11. Relative storage modulus as a function of filler surface area (per gram of nanocomposite sample) dependence for the composite samples with HAp60 and HAp111 (temperature =  $-10^{\circ}\text{C}$ ). The graph has additional data corresponding to HAp spheres and platelets in a PVAc matrix presented by Kalfus and Jancar ( $90^{\circ}\text{C}$ ).<sup>[64]</sup> Adapted from Kaur and Shofner.<sup>[70]</sup>

### 3.4. Conclusions

Polymer nanocomposites containing HAp nanoparticles with different amounts of specific surface area were processed and characterized to elucidate the effects of nanoparticle surface area and polymer morphology on nanocomposite properties. Through these studies, a relationship between the amount of nanoparticle surface area available in a composite and the reinforcing efficacy was indicated. While DSC measurements did not show significant alterations to the crystalline content of PCL, DMA measurements did suggest that the mobility of the amorphous polymer chains were restricted by the addition of nanoparticles in both HAp60 and HAp111 composites. In the nanocomposites, the interphase network was formed at 5 wt.% HAp60 and 10 wt.% HAp111 as evidenced by a discontinuous increase in storage modulus above  $T_g$  and reinforcement values higher than those predicted by micromechanics. Differences in the formation of an interphase network can be attributed to different dispersion characteristics of the two nanoparticle systems. A comparison to data collected for amorphous polymer nanocomposites also indicate that the reinforcement achieved is a general behavior for nanocomposites containing low aspect ratio particles and that available surface area is a valid parameter for nanocomposite design and modeling prior to the formation of a nanoparticle network.

## CHAPTER 4

### EFFECT OF MATRIX CRYSTALLINITY ON THE PROPERTIES OF NANOCOMPOSITES

#### 4.1. Introduction

The bulk polymer matrix morphology in a nanocomposite is one possible material parameter that can influence the reinforcing efficacy of nanoparticles and hence properties of the resulting nanocomposites. The degree and mechanism of reinforcement can change based on the bulk morphology of a thermoplastic polymer such as amorphous or semi-crystalline morphology. In the case of an amorphous polymer matrix composite, the immobilization of the amorphous polymer chains by the high surface area nanoparticles has been described as one of the mechanisms of reinforcement above the  $T_g$  of the bulk polymer matrix.<sup>[14, 137, 139, 143-145]</sup> The nanoparticles in semicrystalline polymer composites can cause changes in both the amorphous and crystalline phases by restricting the mobility of amorphous polymer chains or by inducing changes in crystal phases, crystallinity or crystal size.<sup>[143, 146-151]</sup> Similarly, the change in crystal morphology and crystal size of polymer matrix in presence of nanoparticles can lead to increased toughness in nanocomposites.<sup>[143, 148, 149]</sup> The crystallite morphology of polymer matrix also can transform from large spherulitic structure to fiber-like crystallites in presence of nanoparticles, changing the toughening mechanism of polymer nanocomposites.<sup>[147]</sup> The interfacial interactions and the reinforcement in semi-crystalline polymers is also influenced by the certain crystallization morphologies such as shish-kabab<sup>[151]</sup> developed in solution, or shish-calabash,<sup>[150]</sup> developed in melt blending as a result of the nucleation

of polymer on the filler surface. In semicrystalline polymer composites when the nanoparticles are well dispersed at loadings greater than 20 wt. %, the growing crystalline lamellae can form thermodynamically more favorable thicker lamellas by pushing the nanoparticles out, and hence controlling their distribution in the matrix.<sup>[152]</sup> The degree of exfoliation of organoclay and the mechanical properties of the composites were found to be governed by the morphological and chemical structure differences between nylon 6 and nylon 66.<sup>[153]</sup> Carbon nanofiber (CNF) reinforcement below  $T_g$  was dependent on the bulk polymer morphology in chemically similar but morphologically different amorphous and semicrystalline polyamide matrix nanocomposites.<sup>[28]</sup> Tensile modulus increased more in CNF/Amorphous polymer matrix composite fibers in comparison to CNF/semicrystalline polymer matrix composite fibers.<sup>[29, 154]</sup> This indicated that even though the filler is same, the bulk polymer morphology is playing a role in guiding the reinforcement in these composites. Similarly, reinforcement above polymer  $T_g$  was found to be related to the amount of available amorphous content in polymer matrices differing in the amount of crystallinity.<sup>[155]</sup> Also, the percolation threshold of nanoparticles in a polymer nanocomposite has been shown to be inversely related to the matrix crystallinity.<sup>[156]</sup> Thus the matrix morphology has the potential to influence the properties of nanocomposites and be used as a materials design tool.

In the studies described above, the effect of bulk polymer morphology in semicrystalline matrices on the thermal and thermomechanical properties has not been evaluated collectively. In this chapter, dependence of all these properties as well as dispersion of nanoparticles on the polymer crystallinity has been investigated. Two nanocomposite systems were studied where the nature of the interfacial interaction was

similar, but the biodegradable polymer matrices had different amounts of crystallinity. The specific materials studied were hydroxyapatite (HAp)/ polycaprolactone (PCL) nanocomposites<sup>[70]</sup> and HAp/ polyhydroxybutyrate (PHB) nanocomposites.<sup>[157]</sup> The experimental results indicated that the dispersion characteristics, thermal properties and the reinforcement behavior of the nanocomposites was governed by the differences in the matrix crystallinity.

## **4.2. Experimental**

### **4.2.1. Materials**

Nanocomposites containing HAp particles and a PHB matrix were prepared using a solution processing route. HAp nanoparticles were synthesized via a reverse microemulsion method following a protocol from Bose and Saha.<sup>[102]</sup> The HAp nanoparticles produced by this method contained by number, about 40% plate shaped particles and 60% near-spherical particle assemblies formed from the coalescence of individual needle shaped particles during calcination. The specific surface area of the particles was measured to be 111 m<sup>2</sup>/g. More information regarding the surface chemistry, crystal structure, and other particle characterization is available in Chapter 3. The two polymers PCL and PHB had different amounts of crystallinity, PCL was approximately 40% crystalline, and PHB was approximately 70% crystalline. The details about PCL polymer and the solvent used are given in Chapter 3. The PHB composites were prepared using solvent grade chloroform (BDH) and PHB with weight average molecular weight of 426,000 g/mol (Sigma-Aldrich). All materials were used as received from the suppliers.

#### **4.2.2. Nanocomposite Processing of PHB Composites**

The HAp111 nanoparticles were dispersed in chloroform by sonication in a cup-horn sonicator at a power of 84W for 30 minutes to reduce the size of nanoparticle aggregates. A circulator was used to maintain the water temperature in the sonicator at approximately room temperature. At the end of this sonication step, the suspension appeared homogeneous to visual observation, and no aggregates were observed. PHB was dissolved in the particle sol at 55°C to form a 1 wt. % polymer solution by stirring. To disperse the nanoparticles in PHB, the nanocomposite solution was further sonicated for 30 minutes at room temperature. The resulting nanocomposites were collected by precipitation in cold methanol and dried in a vacuum oven at 50 °C. Nanocomposite films were prepared by melt pressing these precipitated composite particles at 175°C for 8 minutes. All samples were cooled from the melt to room temperature in the press using an integrated water cooling system in approximately 13 minutes. The films were homogenous and transparent in appearance. Solvent cast composite films were prepared with 0, 0.5, 1, 5 and 10 wt. % of HAp particles. A neat PHB sample was also prepared using the same processing conditions as composite samples for comparison. The details of the HAp/PCL composite processing is given in Chapter 3.

#### **4.2.3. Nanocomposite Characterization**

The HAp111/PCL and HAp111/PHB composites were characterized for dispersion and distribution, thermal transitions, polymer crystallinity, and thermomechanical properties.

Nanoparticle dispersion and distribution were observed by scanning electron microscopy (SEM) using cryogenically fractured surfaces. Cryo-fractured surfaces of the composite specimens were gold coated using an ISI Sputter Coater and then imaged using a LEO 1530 SEM at a voltage of 5 kV. PCL composite specimens were also cryo-fractured but the voltage used for imaging was 10 kV.

Thermal transitions for neat PCL and composites were measured by differential scanning calorimetry (DSC) with a Seiko DSC 220. The specimens were heated from -20 to 100°C at a rate of 10°C/min under nitrogen gas flow. After a 10 min dwell, the specimens were cooled back to -20°C at the same rate. Two such cycles were performed on each specimen. Thermal transitions and polymer crystallinity of neat PHB and composites were measured by differential scanning calorimetry (DSC) with a TA Q-200 DSC. The specimens were heated from 25 to 190 °C at a rate of 10 °C/min under nitrogen gas flow. After a 1 min dwell, the specimens were cooled back to -40 °C at the same rate. Then they were heated from -40 to 190 °C at a rate of 10 °C/min and after a dwell of 1 min at 190 °C cooled back to -40 °C at the same rate. Two such cycles were performed on each specimen.

The thermal transitions from the experiments were measured as the peak maximum of the melting and crystallization peaks for both PCL and PHB. The crystallinity of the polymer was calculated by dividing the heat of fusion obtained from integrating the melting peak of the first and the second run by the heat of fusion for completely crystalline PHB ( $\Delta H_m^\circ=146 \text{ J/g}$ )<sup>[158]</sup> and PCL ( $\Delta H_m^\circ=139 \text{ J/g}$ ).<sup>[127]</sup> The crystallinity was normalized by the weight fraction of polymer in the case of composite

samples. The percent crystallinity and the thermal transitions were reported as the average value obtained from two DSC runs on two different samples.

Isothermal crystallization studies were also performed to determine the effect of the nanoparticles on crystallization and to further understand the polymer morphology. In case of PCL, the samples were heated from room temperature to 100°C at a rate 10 °C/min under nitrogen atmosphere and held at 100°C for 10 min and then cooled rapidly (60°C/min) to the crystallization temperatures ( $T_c$  = 40, 42, 44, 46°C) for the isothermal experiments. The samples were then heated again to 100°C at 10°C/min. In case of PHB, the samples were heated from room temperature to 190 °C at a rate 100 °C/min under nitrogen atmosphere and held at 190 °C for 3 min and then cooled rapidly (100 °C/min) to crystallization temperatures 120, 125 and 130 °C and held at these temperatures until crystallization was complete. Two isothermal studies were performed on each nanoparticle concentration, and the results were averaged.

Thermomechanical properties were measured with dynamic mechanical analysis (DMA) using a Mettler Toledo DMA861<sup>e</sup> in uniaxial shear deformation. In case of PCL, compression molded samples with a nominal thickness of 1 mm were used. The testing was performed using force amplitude of 4.0N below  $T_g$  and a strain amplitude of 0.5  $\mu$ m above  $T_g$ . The temperature was varied from -100 to 40°C with a heating rate of 2°C/min, and the measurements were performed at a frequency of 1 Hz. In case of PHB, shear sandwich sample was prepared for testing using three individual sample layer separated by aluminum. This method was referred from technical notes of Mettler Toledo DMA861<sup>e</sup> for shear mode testing of thin films. The sample films were thin so in order to reduce the uncertainties in modulus associated with thin samples, the alternate stacking of



sample and aluminum disks was used to build up the thickness. The diameter of the sample films and aluminum disks was 3.18 mm. The aluminum disks and sample films were punched using a metal punch with a punch and die of 3.18 mm diameter. The thicknesses of the aluminum disks were subtracted from the sample thickness to accurately calculate the moduli. Comparison between thin films stacked in this manner and bulk films of the neat PHB showed similar results when tested by DMA. The testing was performed using force amplitude of 3.0 N below  $T_g$  and a strain amplitude of 0.25  $\mu\text{m}$  above  $T_g$  for the neat PHB sample and 3.0N below  $T_g$  and 0.15  $\mu\text{m}$  above  $T_g$  for the composite samples. The heating rate for all tests was 2°C/min, and the measurements were performed at a frequency of 1 Hz in the temperature range from -30 to 100 °C. The measurements were performed in the linear viscoelastic range, which was identified through strain sweep measurements for all of the specimens. Two temperature scan tests were conducted on each material, and the average value was reported.

### **4.3. Results and Discussion**

The results obtained from the materials characterization indicated that the amount of polymer crystallinity played a role in the dispersion and distribution of nanoparticles as well as the thermal and thermomechanical properties of the composites. Table 4.1 highlights the differences in the thermal properties of the two polymers as well as crystallinity. The results of characterization experiments will be discussed in the context of the amount of neat polymer crystallinity.

Table 4. 1.Differences in thermal properties and crystallinity of Neat PCL and PHB polymers.

Polymer	Glass Transition (T <sub>g</sub> from DMA) (°C)	Melting Temperature (T <sub>m</sub> ) (°C)	Crystallinity (%)
PCL	-60	59	40
PHB	10	181	70

#### 4.3.1. Dispersion and Distribution of HAp in Nanocomposites

The dispersion of nanoparticles in the polymer matrix was found to be governed by the polymer morphology. The dispersion of HAp nanoparticles achieved in the PHB matrix was observed using SEM on the cryo-fractured surfaces of the composite samples. In the context of this research as well as HAp/PCL composites in Chapter 3, dispersion was indicated by an increase in nanoparticle surface area available to the polymer (aggregates broken down), and distribution was indicated by a homogeneous distribution of nanoparticles in the matrix (individual or aggregated). Figure 4.1 shows the dispersion of HAp particles in 0.5, 1, 5 and 10 wt. % HAp111/PHB composite samples. The distribution of the HAp filler in the PCL nanocomposites was observed to be homogeneous at all filler loadings studied as shown in Chapter 3<sup>[70]</sup> whereas in the PHB nanocomposites HAp filler particles were well dispersed at filler loadings of 0.5 and 1 wt. % and homogeneously distributed at higher concentrations. At 5 wt. %, small HAp aggregates were observed. The aggregation increased at 10 wt. % loading in PHB composites. This suggested that there was a threshold HAp loading in the PHB system compared to PCL system and that was related to the amount of crystalline polymer in both cases. In the PCL polymer system, the amount of crystalline phase is 40% from the

first heat and hence the amorphous phase is about 60%. In PHB polymer system, the amount crystalline phase is about 70% from first heat and thus the amorphous phase is 30%. The nanoparticles in a polymer are more likely to be dispersed in the amorphous regions of a polymer as the crystalline regions are tightly packed compared to amorphous regions which are more open. In case of PHB which has less amorphous regions, the particles would have to be distributed in less space compared to PCL which explains the increased aggregation in PHB system at higher concentrations. Thus the availability of the amorphous regions guides the dispersion of the particles in the two polymer systems. The percolation threshold for electrical conductivity has been shown to be lower in higher crystallinity matrix as the percolation clusters can be formed at lower concentration of nanoparticles due to the compact arrangement of nanoparticles in smaller amorphous regions.<sup>[156]</sup> The lower crystallinity and hence larger amount of amorphous polymer in PCL aided in the dispersion. In case of PHB, the amount of amorphous polymer was half that of PCL and hence better dispersion was seen only at lower concentrations and aggregation started above 1wt. % filler loading. Therefore, the differences in the dispersion characteristics of particles in the two polymers was related to the matrix crystallinity and hence the amounts of available amorphous polymer.

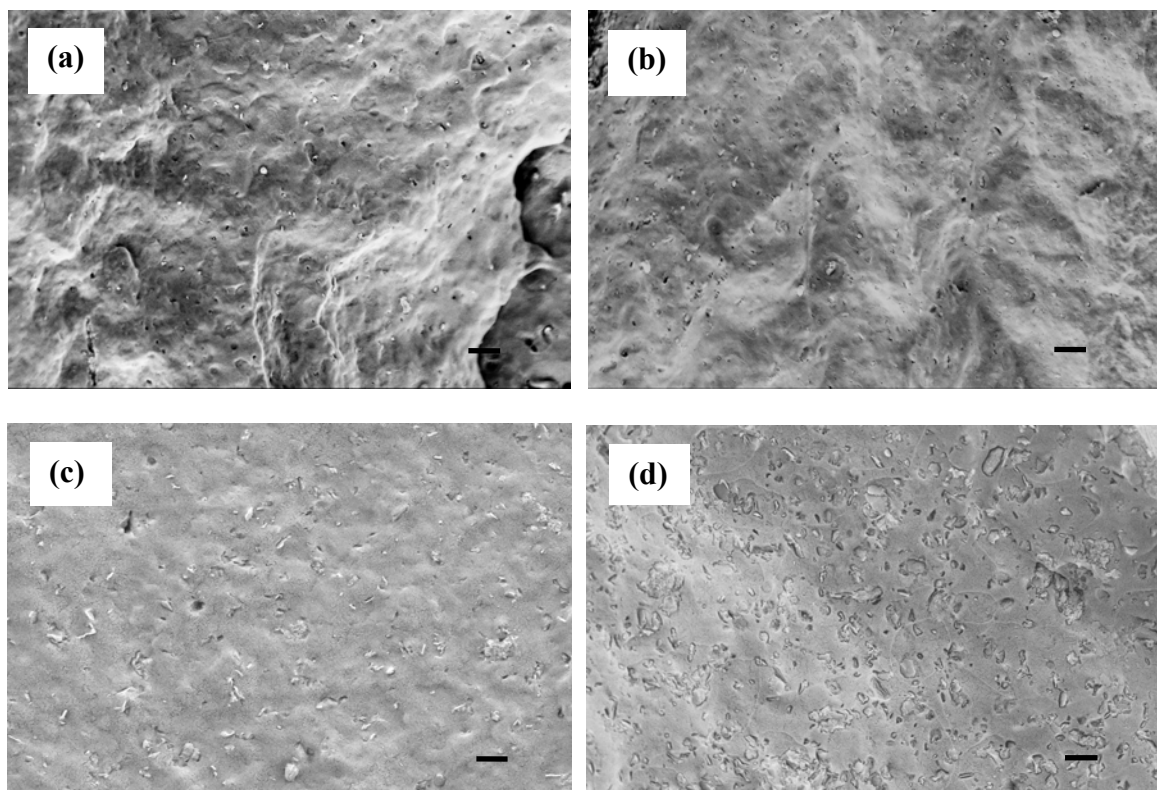


Figure 4. 1.SEM images showing dispersion of HAp nanoparticles in (a) 0.5 wt. % HAp111/PHB, (b) 1 wt. % HAp111/PHB, (c) 5 wt. % HAp111/PHB and, (d) 10 wt. % HAp111/PHB composite samples. Homogenous distribution was attained at all filler loadings. The scale bar in all the images represents 2  $\mu$ m.

#### 4.3.2. Thermal Properties and Crystallization Kinetics of Nanocomposites

DSC experiments showed that the nanoparticle inclusions influenced the thermal transitions and crystallization kinetics differently in polymers with different morphology. The thermal properties of nanocomposites were studied with DSC through nonisothermal, and isothermal experiments. Figure 4.2 shows the change in the first heat crystallinity of PHB matrix with an increase in concentration of HAp111 in comparison to the PCL system. It can be seen that in both polymer systems the crystallinity of the matrix was not significantly affected by the change in filler concentration. The

crystallinity of the composites remained within 5% of both neat PCL and PHB. When the interactions between the particle and the polymer matrix are weakly attractive, little or no changes in polymer crystallinity are observed.<sup>[129-131]</sup> The results given here support this view. Also, significant changes in the polymer crystallinity and crystallite sizes have been seen at filler concentrations higher than 20 wt. %.<sup>[152]</sup> As such changes were not observed here it shows that the nanoparticles in this study are more likely to reside in amorphous regions as compared to crystalline regions as they do not affect the polymer crystallinity. The first heat values are presented here to provide an understanding of the relative crystallinity of the samples used for DMA testing. The amount of crystallinity achieved in the composites from the second heating data was approximately the same as the neat PHB. The table with the crystallinity values from first and second heat of neat PHB and HAp111/PHB is given in Appendix C.

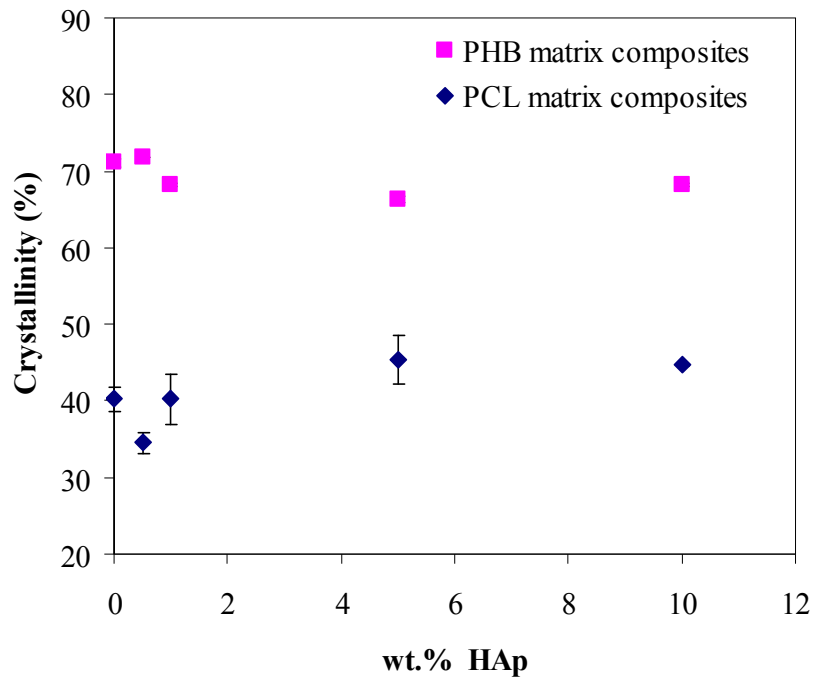


Figure 4. 2. Crystallinity from first heat as a function of filler content for neat PHB and PCL as well as HAp111/PHB and HAp111/PCL composite samples.

Table 4.2 gives the peak melting and crystallization temperatures from the first heat data of neat PHB and HAp111/PHB composites in comparison to the neat PCL and HAp111/PCL composites. First heating cycle data indicated that inclusion of HAp particles did not have a significant effect on the thermal transitions of the PCL system whereas the same particles significantly affected the crystallization temperature of PHB matrix. The melting temperature ( $T_m$ ) of PCL and its composites was  $58 \pm 1^\circ\text{C}$  and was not affected by the increase in particle concentration. Neat PHB and HAp111/PHB composites show double melting peaks in the first heating cycle. DSC first heating and cooling cycle of neat PHB and HAp111/PHB composites is given in Appendix C. The peak maximum temperatures of first and the second melting peaks are given in Table 4.2 as  $T_{m1}$  and  $T_{m2}$ . The multiple melting peaks have been observed in semicrystalline polymers and blends and have been attributed to the reorganization of crystals during heating. The first melting peak is associated with the melting of the small crystals developed during cooling process and the second melting peak or higher melting peak is due to the melting of the thicker or larger crystals formed during the recrystallization. Lower melting crystals convert to higher melting crystals during the course of heating because of recrystallization.<sup>[159-162]</sup> The  $T_{m1}$  and  $T_{m2}$  of the HAp111/PHB composites were observed to be similar to the neat PHB but some differences in the intensities of the peaks were observed. The melting points also did not change with change in nanoparticle concentration. The crystallization temperature ( $T_c$ ) of 10wt. % HAp111/PCL composite was  $1.4^\circ\text{C}$  higher than the neat PCL, but was not affected for lower particle loadings. Therefore, in case of PCL system the HAp nanoparticles acted as nucleating agent but only at sufficient concentrations. For the PHB system, the crystallization temperatures

were significantly affected by even smaller concentrations of HAp111. The peak  $T_c$  of 0.5 wt. % HAp111/PHB composite increased by 6°C with respect to the neat PHB while it decreased with the increase in nanoparticle loading and nearly approached the peak  $T_c$  of neat PHB at 10 wt. %. This trend in the crystallization temperature suggests that the nanoparticles were able to nucleate crystals at lower loadings and inhibited the crystallization at higher loadings. The crystallization temperature increases for 0.5 wt. % HAp111/PHB composite and then decreases with the increase in particle concentration. This behavior can be explained from the particle dispersion and distribution in the PHB matrix. The SEM showed that the particles were dispersed well at lower loadings (0.5 and 1 wt. %) and were distributed homogeneously with aggregation at higher loadings. When the particles are dispersed well, the higher surface area helps the particles to act as nucleating agent but as the aggregation increases the surface area does not increase at the same rate. The change in particle size due to aggregation and the surface characteristics of the particle lead to decrease in crystallization temperature and hence nucleation efficiency. As significant changes were not observed in the crystallinity and melting points of the composites, the nucleation effect of the nanoparticles was related to the increase in polymer viscosity in presence of nanoparticles which helped in formation of stable nuclei. The second heat melting ( $T_m$ ) and crystallization ( $T_c$ ) temperatures of neat PHB and PCL and their composites with HAp111 nanoparticles is given in Appendix C.

Table 4. 2. Melting ( $T_m$ ) and crystallization ( $T_c$ ) temperatures of neat PHB and PCL and their composites with HAp111 nanoparticles from first heat.

Conc.	$T_m$ of PCL matrix composites	$T_m$ of PHB matrix composites		$T_c$ of PCL matrix composites	$T_c$ of PHB matrix composites
		$T_{m1}$	$T_{m2}$		
0 wt. %	$58.7 \pm 0.1$	$172 \pm 0.2$	$184 \pm 0.1$	$27.8 \pm 0.4$	$105 \pm 0.1$
0.5 wt. %	$58.0 \pm 0.3$	$173 \pm 0.5$	$185 \pm 0.1$	$26.3 \pm 0.4$	$111 \pm 0.0$
1 wt. %	$57.9 \pm 0.1$	$173 \pm 0.0$	$183 \pm 0.3$	$26.1 \pm 0.5$	$108 \pm 0.1$
5 wt. %	$58.2 \pm 0.4$	$173 \pm 0.0$	$184 \pm 0.3$	$28.2 \pm 0.7$	$107 \pm 0.1$
10 wt. %	$57.9 \pm 0.1$	$173 \pm 0.4$	$184 \pm 0.3$	$29.2 \pm 0.0$	$106 \pm 0.3$

A large change in the crystallization temperature of the composite samples at lower concentrations indicated that the particles had a nucleating effect on the crystallization of the polymer matrix. Isothermal crystallization studies were conducted on the neat PHB and the composite samples at 120, 125 and 130°C in order to understand the crystallization kinetics.<sup>[163]</sup> The temperature at which maximum rate of nucleation and spherulitic growth takes place in PHB is approximately 80°C,<sup>[163, 164]</sup> so these tests are nucleation limited. The isothermal crystallization data were analyzed using the modified Avrami equation<sup>[165]</sup>

$$\ln(1-X_t) = - (Zt)^n \quad (1)$$

where  $Z$  is the crystallization rate constant,  $n$  is the Avrami exponent which relates to the mechanism of crystallization, and  $X_t$  is the relative crystallinity at time  $t$ . The values of  $Z$  and  $n$  were obtained by plotting a graph of  $\ln(-\ln(1-X_t))$  against  $\ln(t)$ . The half time for crystallization,  $t_{1/2}$  was taken as the time required for 50% transformation to crystal.



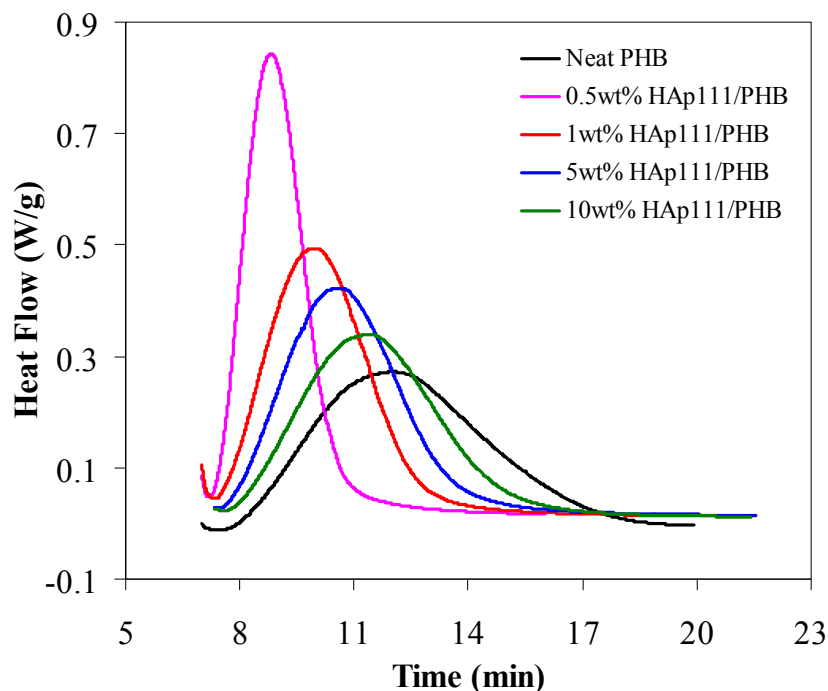
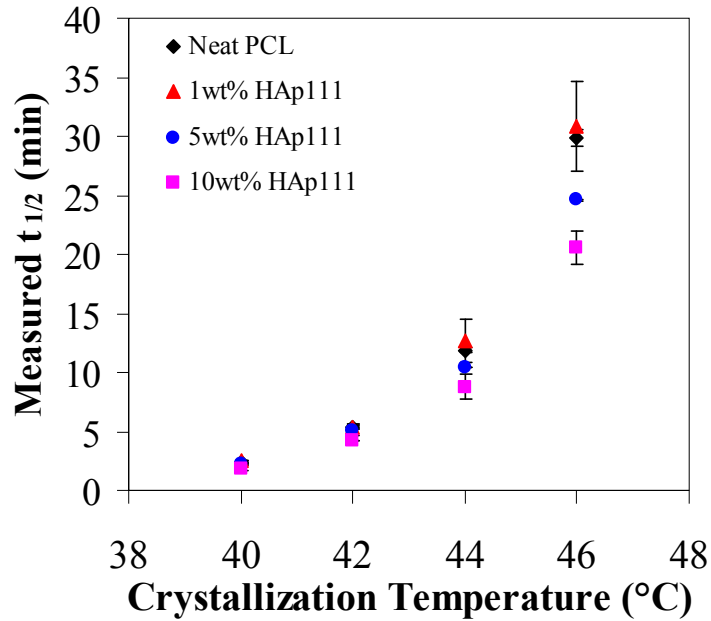
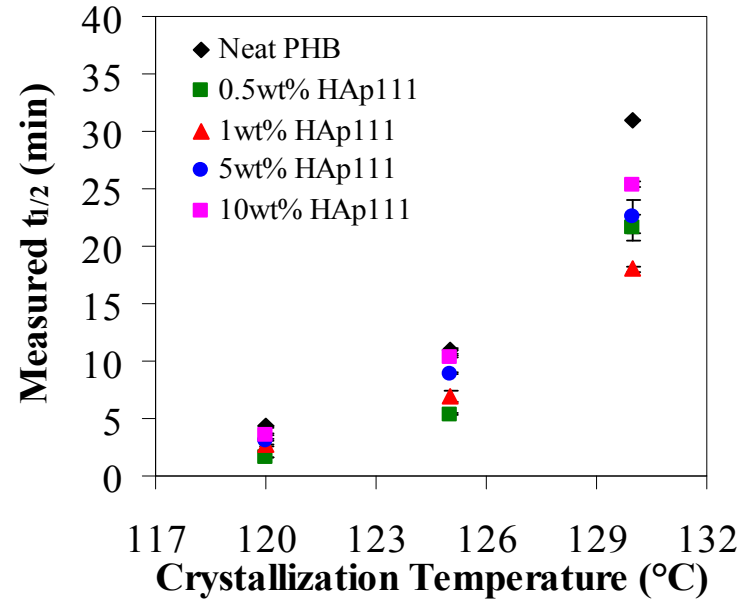


Figure 4. 3. Isothermal crystallization of neat PHB and HAp111/PHB composites at 120°C.

Figure 4.3 shows the isothermal crystallization of neat PHB and HAp111/PHB composites at 120 °C. The isothermal crystallization plots of neat PHB and HAp111/PHB at 125 and 130 °C are given in Appendix C. It can be seen that the 0.5 wt. % composite crystallizes faster than neat PHB and other composites which is consistent with non-isothermal DSC results and dispersion characteristics seen with SEM. Figure 4.4 shows the measured half time ( $t_{1/2}$ ) of crystallization as a function of crystallization temperature for the neat PHB and HAp111/PHB composites in comparison with the neat PCL and HAp111/PCL composites. In the case of PCL system, 5 and 10 wt. % composite samples showed a lower  $t_{1/2}$  than the neat PCL at all crystallization temperatures studied. However, the 1 wt. % HAp111/PCL composite sample showed the same  $t_{1/2}$  as neat PCL. In the case of PHB system, composite samples at all concentrations showed a lower  $t_{1/2}$



(a)



(b)

Figure 4. 4. Half-time crystallization of (a) neat PCL and HAp111/PHB and (b) neat PHB and HAp111/PHB nanocomposites samples as a function of crystallization temperature. The isothermal crystallization temperatures selected for PCL was within 15°C of the crystallization temperature where maximum nucleation rate was determined (25°C).<sup>[166]</sup> The isothermal crystallization temperatures selected for PHB are within 40°C of the crystallization temperature where maximum nucleation rate was determined (80°C).<sup>[158, 163, 164]</sup> Figure 4.4a is adapted from Kaur and Shofner.<sup>[70]</sup>

than the neat PHB at all crystallization temperatures studied. Therefore, PCL polymer needed sufficient concentration of nanoparticles in order to induce any change to the crystallization kinetics whereas in PHB even small concentration of filler can significantly affect the kinetics of crystallization. The 0.5 wt. % HAp111/PHB composite sample showed the lowest  $t_{1/2}$  for the crystallization temperatures of 120 and 125°C with approximately one-third  $t_{1/2}$  than neat PHB at the crystallization temperature of 120°C. However, the  $t_{1/2}$  was found to increase with the increase in filler concentration at both 120 and 125°C, indicating an optimal HAp loading to increase crystallization kinetics at these temperatures. At the crystallization temperature of 130°C, the 1 wt. % HAp111/PHB sample had the lowest  $t_{1/2}$  followed by 0.5 wt. % and then the  $t_{1/2}$  increased again for 5 and 10 wt. % composite samples. The lower  $t_{1/2}$  indicates that the composite samples have higher crystallization rate than the neat PHB.

Table 4.3 shows the  $t_{1/2}$ ,  $n$  and  $Z$  values for neat PHB and all the composites samples at 120, 125 and 130°C. As seen from the table 0.5 wt. % HAp111/PHB composite sample had the rate of crystallization ( $Z$ ) approximately three times higher than the neat PHB at 120°C and the rate decreases with the increase in particle concentration. These observations suggested that the particles acted as nucleating agent but the nucleation capability decreased with increase in particle loading. From the SEM images, it was observed that the distribution was homogenous at all concentrations but with some aggregation at 5 wt. %. The increase in aggregation of particles reduced the amount of surface area available for nucleation and so crystallization kinetics were governed by the particle size distribution. The lowest  $t_{1/2}$  for the 1 wt. % HAp111/PHB sample at 130°C is associated with the decrease in supercooling, and thus more particle

concentration is required to increase the rate of crystallization because of increased stable nuclei size.

Table 4. 3.Isothermal crystallization parameters for PHB and HAp111/PHB composite samples at  $T_c = 120, 125$  and  $130^\circ\text{C}$ .

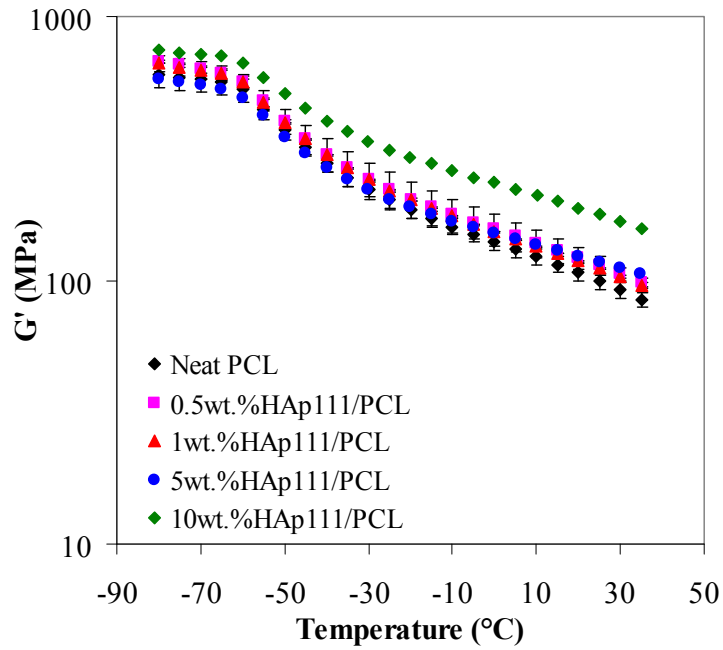
HAp wt. %		Crystallization Temperature ( $^\circ\text{C}$ )		
		120	125	130
<b>0</b>	n	$2.4 \pm 0.0$	$2.3 \pm 0.0$	$2.5 \pm 0.0$
	Z( $\text{min}^{-1}$ )	$2.0 \cdot 10^{-1} \pm 3.6 \cdot 10^{-3}$	$7.8 \cdot 10^{-2} \pm 1.8 \cdot 10^{-3}$	$2.8 \cdot 10^{-2} \pm 1.1 \cdot 10^{-4}$
	$t_{1/2}(\text{min})$	$4.3 \pm 0.1$	$10.9 \pm 0.2$	$30.9 \pm 0.0$
<b>0.5</b>	n	$2.6 \pm 0.0$	$2.7 \pm 0.0$	$2.8 \pm 0.0$
	Z( $\text{min}^{-1}$ )	$5.5 \cdot 10^{-1} \pm 7.5 \cdot 10^{-3}$	$1.6 \cdot 10^{-1} \pm 3.1 \cdot 10^{-3}$	$4.3 \cdot 10^{-2} \pm 2.5 \cdot 10^{-4}$
	$t_{1/2}(\text{min})$	$1.6 \pm 0.0$	$5.4 \pm 0.1$	$20.6 \pm 0.2$
<b>1</b>	n	$2.6 \pm 0.1$	$2.4 \pm 0.0$	$2.4 \pm 0.1$
	Z( $\text{min}^{-1}$ )	$3.3 \cdot 10^{-1} \pm 6.9 \cdot 10^{-3}$	$1.3 \cdot 10^{-1} \pm 8.9 \cdot 10^{-3}$	$4.8 \cdot 10^{-2} \pm 1.2 \cdot 10^{-3}$
	$t_{1/2}(\text{min})$	$2.7 \pm 0.1$	$6.9 \pm 0.5$	$18.0 \pm 0.3$
<b>5</b>	n	$2.6 \pm 0.0$	$2.7 \pm 0.0$	$2.4 \pm 0.1$
	Z( $\text{min}^{-1}$ )	$2.8 \cdot 10^{-1} \pm 4.0 \cdot 10^{-3}$	$9.8 \cdot 10^{-2} \pm 1.5 \cdot 10^{-3}$	$3.8 \cdot 10^{-2} \pm 2.1 \cdot 10^{-3}$
	$t_{1/2}(\text{min})$	$3.1 \pm 0.1$	$8.9 \pm 0.1$	$22.6 \pm 1.4$
<b>10</b>	n	$2.6 \pm 0.0$	$2.6 \pm 0.1$	$2.6 \pm 0.0$
	Z( $\text{min}^{-1}$ )	$2.4 \cdot 10^{-1} \pm 6.2 \cdot 10^{-3}$	$8.4 \cdot 10^{-2} \pm 6.7 \cdot 10^{-4}$	$3.4 \cdot 10^{-2} \pm 2.5 \cdot 10^{-4}$
	$t_{1/2}(\text{min})$	$3.6 \pm 0.1$	$10.4 \pm 0.1$	$25.4 \pm 0.2$

The presence of particles did not affect the crystallization mechanism of PHB as the value of  $n$  remained between 2.4 and 2.8 for both neat PHB and the composites. The  $n$  value of the neat PHB and the composites was similar to  $n$  values found in literature.<sup>[167-169]</sup> The  $n$  does not change significantly with the particle concentration which indicates the nucleation is athermal.<sup>[170]</sup> The  $n$  values of neat PCL and the composites were also

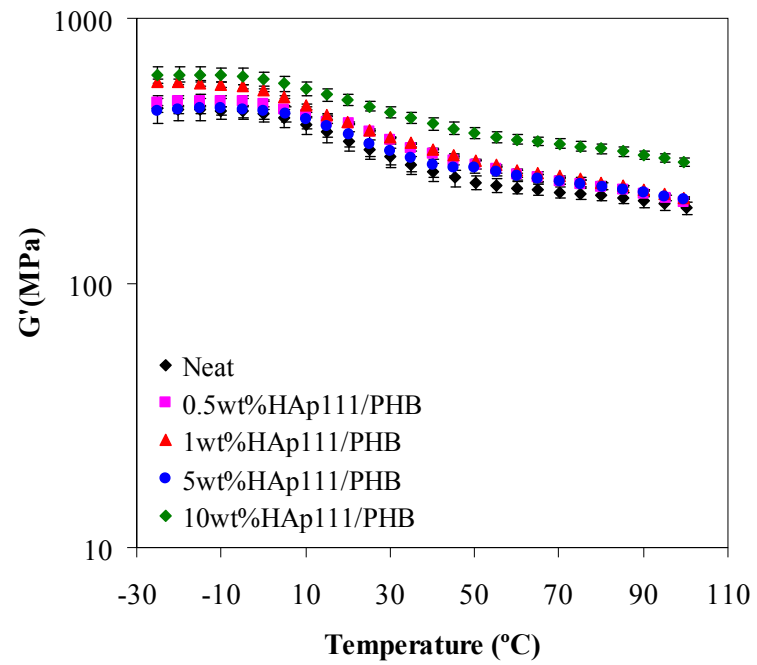
between 2.4 and 2.9 and remained almost unchanged by the particle concentration. Thus the crystal growth was two-dimensional in both systems.

#### **4.3.3. Viscoelastic properties of Nanocomposites**

The results of the thermomechanical experiments showed that the reinforcement in composites was associated with the differences in the polymer morphology between PCL and PHB. The shear storage modulus ( $G'$ ) is plotted against temperature for both neat PCL and PHB and their composites in Figure 4.5. The error bar represents the spread in the data obtained from the two tests on each sample. The shape of the  $G'$  curve between PCL and PHB polymers is different as they differ in the amount of crystallinity. In a polymer with higher crystallinity (in this case PHB) the drop in the modulus at the  $\alpha/T_g$  transition is less steep compared to a polymer with lower crystallinity. Also the rubbery plateau is flatter in PHB compared to PCL, where the modulus is constantly falling with the increase in temperature. The PCL composites showed reinforcement at all concentrations above the  $T_g$  of polymer matrix but the 10 wt. % HAp111/PCL sample showed higher reinforcement both below and above the  $T_g$  of the polymer matrix compared to other concentrations. The 10 wt.% HAp111/PCL composite sample showed storage modulus increase of 24% at -80 °C (20 °C below  $T_g$  of neat PCL) and 63% increase at 10 °C (50 °C above the  $T_g$  of neat PCL). In comparison to the 10 wt. % HAp111/PHB composite, the 10 wt. % HAp111/PCL composite had lower reinforcement in the glassy modulus but higher reinforcement in the rubbery modulus. The 1 wt. % HAp111/PHB had higher reinforcement in the glassy modulus and similar reinforcement



(a)



(b)

Figure 4. 5.Storage modulus values of (a) neat PCL and HAp111/PCL and (b) neat PHB and HAp111/PHB nanocomposite samples. The points represent the average value of two separate experiments. Figure 4.5a is adapted from Kaur and Shofner.<sup>[70]</sup>

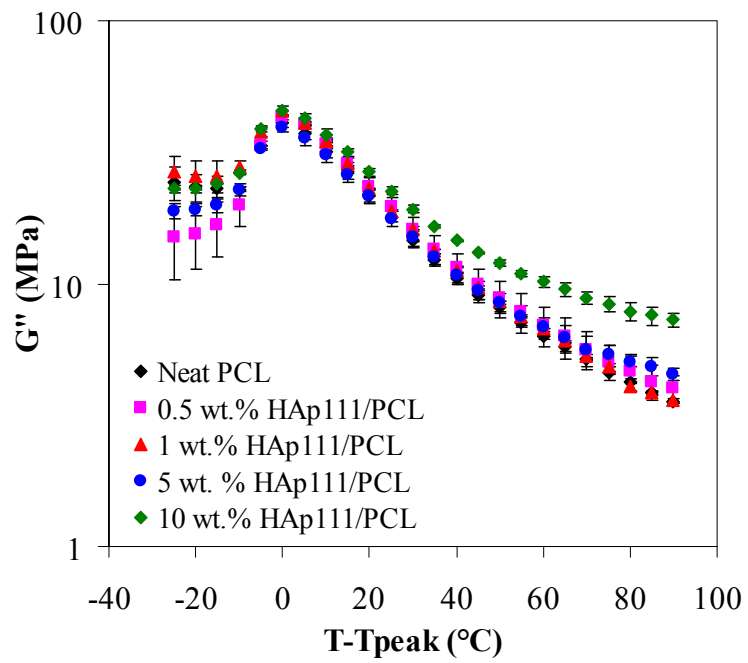
in the rubbery modulus compared to 1 wt. % HAp111/PCL composite. When comparing reinforcement between the PHB composites, 1 and 10 wt. % composites showed higher reinforcement than the neat PHB and other composites, both below and above the  $T_g$  of the polymer matrix. Compared to neat PHB, the 1 and 10 wt. % HAp111/PHB composites showed an increase in storage modulus of 25% and 37% at -10 °C (20 °C below  $T_g$  (10 °C) of neat PHB). The storage modulus increased by 17% and 52% for 1 and 10 wt. % HAp111/PHB composite samples with respect to the neat polymer at 60 °C (50 °C above the  $T_g$ ). The reinforcement for 0.5 and 5 wt. % composite samples was slightly higher than neat but within the experimental error. The 5 wt. % HAp111/PHB composite sample showed a lower reinforcement compared to other concentrations. This behavior was related to dispersion characteristics at this concentration which was in turn related to the polymer morphology. The amorphous regions in PHB are less compared to PCL due to higher matrix crystallinity. Therefore, as the nanoparticle concentration increases, more particles have to be distributed in the lesser amorphous regions in PHB which leads to aggregation. Thus particle aggregation at this concentration was related to the amount of available amorphous polymer regions. The decrease in reinforcement was therefore attributed to the aggregation and reduction in effective surface area. This was confirmed through SEM and the retarded crystallization rates in DSC. The reinforcement below  $T_g$  is attributed to the nanoparticle properties and replacement of portions of softer matrix by stiffer particles. The crystallinity data obtained from the DSC experiments in both PCL and PHB matrix composites has also indicated that the particle concentration did not have significant effect on polymer crystallinity. Therefore the differences in magnitude of  $G'$  of the composites cannot be related to changes in matrix crystallinity.

The 1 wt. % HAp111/PHB composite in case of the PHB matrix composites could reinforce below the  $T_g$  of the matrix compared to 1 wt. % HAp111/PCL composite as the amount of amorphous phase was less in PHB than in case of PCL matrix. The higher reinforcement of 10 wt. % HAp111/PHB below  $T_g$  compared to 10 wt. % HAp111/PCL is attributed to the differences in amounts of amorphous phase as well as dispersion characteristics between the two polymer matrices. The SEM results showed that the 10 wt. % HAp111/PHB sample had homogeneous distribution of particles but in the form of large aggregates compared to 10 wt. % HAp111/PCL which had homogeneous distribution of smaller spherical clusters.

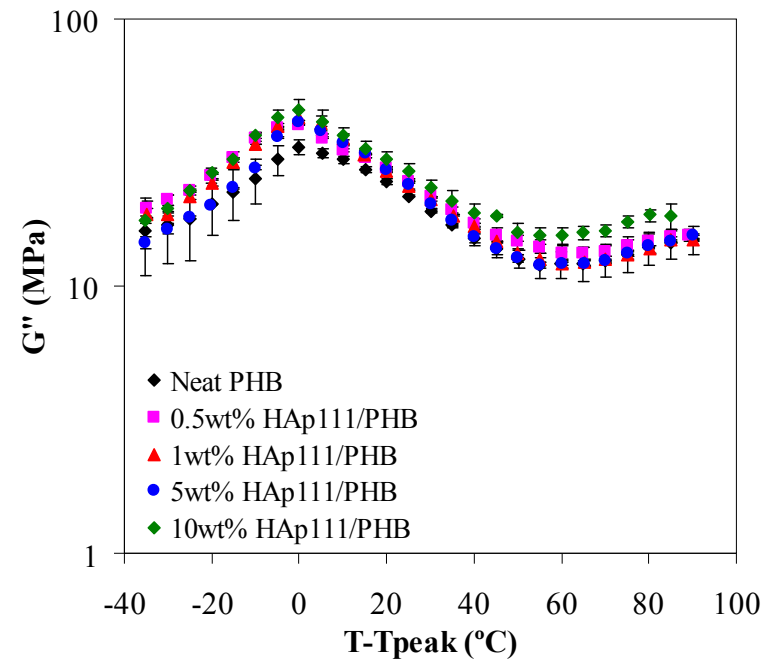
The rubbery modulus, above matrix  $T_g$ , is influenced by the polymer morphology at the polymer/particle interface, strength of polymer-particle interactions and particle size and specific surface area.<sup>[137, 139, 144, 145, 155, 171]</sup> The 10 wt. % HAp111/PHB shows lower reinforcement than 10 wt. % HAp111/PCL 50 °C above the  $T_g$  of both the matrices, attributed to increased particle aggregation and particle-particle interaction in PHB due to higher matrix crystallinity and lesser availability of amorphous phase. Increased matrix stiffness has also been shown to generate higher stresses around the particles and increase dewetting.<sup>[172]</sup> Therefore, the lower reinforcement in PHB composite above  $T_g$  compared to PCL system is due to reduction in effective surface area of particles caused by aggregation and higher matrix stiffness, both governed by the matrix crystallinity. The work of adhesion between PCL and HAp as well as PHB and HAp is given in Appendix C.

The loss modulus ( $G''$ ) data was used to understand the changes near and above  $T_g$  of the matrix. The  $G''$  data was normalized to peak temperature as shown in Figures





(a)



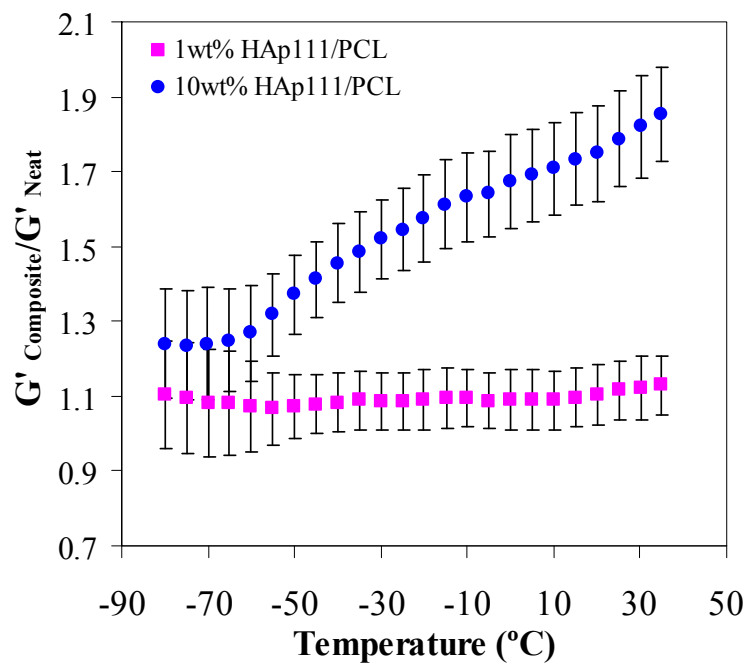
(b)

Figure 4. 6. Loss modulus values of (a) neat PCL and HAp111/PCL and (b) neat PHB and HAp111/PHB nanocomposite samples. The points represent the average value of two separate experiments. The  $T_{peak}$  for neat PCL was -55°C and that for neat PHB was 10°C.

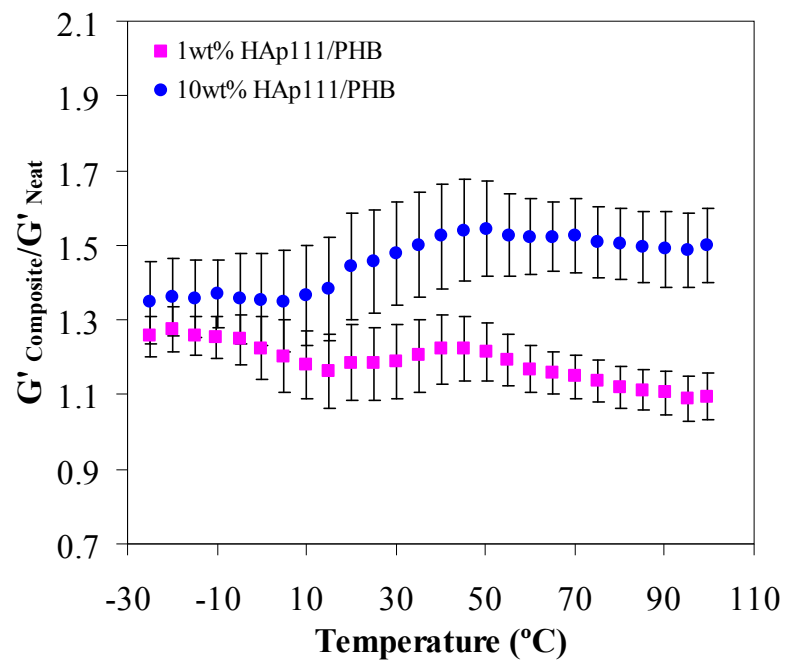
4.6a and 4.6b for the PCL and PHB composites, respectively. Each point represents the average value obtained from two tests performed using the same parameters, and the error bars represent the spread in the data from those two tests. For all of the samples, small shifts in the peak temperature were observed. In case of the PCL system, the  $T_g$  of the neat PCL from the loss modulus peak was  $-55\text{ }^{\circ}\text{C}$  and the  $T_g$  of all composites fell within  $-2\text{ }^{\circ}\text{C}$  of the neat PCL. In case of PHB system, the  $T_g$  of the neat PHB from the loss modulus peak was approximately  $10\text{ }^{\circ}\text{C}$  and the peak temperatures of the composites were same as neat PHB for 0.5, 5 and 10 wt. % composite samples but for 1 wt. % it was within  $-5\text{ }^{\circ}\text{C}$  of the neat PHB. In case of the PCL system, the value of  $G''$  increased with the increase in particle concentration above the  $T_g$  of the matrix. Also the 10 wt. % HAp111/PCL composite showed peak broadening towards the high temperature side of the transition. In case of the PHB system, the  $G''$  of the composites at lower particle loadings was slightly higher than the neat PHB but within experimental error. The 10 wt. % HAp111/PHB composite gave about 28% increase in  $G''$  whereas 10wt.% HAp111/PCL gave an increase in  $G''$  of 48%,  $50\text{ }^{\circ}\text{C}$  above the  $T_g$  of the matrices. Also, all the HAp111/PHB composites showed higher  $G''$  compared to the neat PHB and no peak broadening at any concentration was observed. The interactions between the particles and both polymer systems are chemically similar as both polymers matrices are polyesters differing in the amount of crystallinity. The nanoparticles in PHB composites were dispersed well at lower concentrations as confirmed from SEM imaging and DSC experiments. However, the reduced amount of amorphous polymer led to aggregation at particle loadings of 5 wt. % and above. As a result, the effective surface area of nanoparticles reduced due to aggregation at these concentrations. The amount of

immobilized polymer in a composite is governed both by the surface area of the filler as well as the strength of interaction between the polymer matrix and the filler. In this case, the strength of interaction is similar between the two systems however the effective surface area of particles is reduced in the PHB system. Therefore, the amount of constrained polymer is different in the two systems attributed to differences in particle dispersion which is related to the polymer crystallinity.

To understand more fully the reinforcement trends in both polymer systems,  $G'$  was normalized with respect to neat PCL and neat PHB and the reinforcement values were plotted against temperature. These data are shown in Figures 4.7a and 4.7b, respectively, for HAp111 loading of 1 and 10 wt. %. The error bars in these plots represent the propagated error from the composite sample and the neat PCL and neat PHB calculated using standard rules for the result of division. The reinforcement in the case of 1 wt. % HAp111/PCL is almost constant with temperature for all temperatures while for 10 wt. % HAp111/PCL composite sample, it is constant below  $T_g$  and increases with the increase in temperature above  $T_g$  of the PCL. In case of PHB system, for 1 wt. % HAp111/PHB the reinforcement is relatively constant at all temperatures below  $T_g$  of the matrix, increases at  $T_g$  until 40°C above  $T_g$ , and then remains relatively constant at all other temperatures. The reinforcement trend with temperature for 10 wt. % HAp111/PHB composite is similar to the 1 wt. % composite but showed higher reinforcement. These differences in temperature dependence in the two polymer systems can again be related. In the PCL materials, the mechanical reinforcement was a product of the properties of individual particles and the interactions between the composite components as the reinforcement shows temperature dependence above matrix  $T_g$ . Moreover, PCL has lower



(a)



(b)

Figure 4. 7. Normalized storage modulus curves for (a) 1 and 10 wt. % HAp111/PCL and (b) 1 and 10 wt.% HAp111/PHB nanocomposite samples.

amount of crystallinity and hence higher fraction of amorphous polymer in comparison to PHB. In the PHB materials, the amount of reinforcement attained in a composite morphology with separated particles was lower because only 1 wt. % HAp could be dispersed. The amount of immobilized polymer which arises either due to chain entanglements or adsorption on particle surface will also depend on the amount of amorphous phase available. A constant rubbery modulus above  $T_g$  of a polymer is a general characteristic of higher crystallinity matrices. Therefore, the constant reinforcement above  $T_g$  in case of PHB composites is related to the higher crystallinity of PHB matrix as there is not enough amorphous portion of polymer to show a temperature dependent reinforcement. The reinforcement for 10 wt. % was higher than 1 wt. % HAp111/PHB but constant with temperature, indicating a dependence on particle aggregates and particle-particle interactions and not polymer conformation at the interface.

#### **4.4. Conclusions**

Two composite systems with the same filler but different polymer matrices were processed. The two polymer matrices differed in the amounts of crystallinity. The specific materials studied were HAp/PCL nanocomposites and HAp/PHB nanocomposites. The properties as well the dispersion of nanoparticles in the composites was found to be related to the differences in the polymer crystallinity between the two matrices. The dispersion of nanoparticles was governed by the availability of amorphous regions in each matrix. Larger amounts of matrix crystallinity in PHB decreased dispersion of particles at higher concentrations as the particles had to be distributed in

smaller amorphous regions. These differences in dispersion between the two polymer systems were attributed to the different amounts of crystallinity which in turn influenced both the thermal and thermomechanical properties. The DSC experiments revealed that the thermal transitions and crystallization kinetics in PHB system were affected even with lower concentrations of particles compared to PCL system. However, the amount of crystallinity attained and the crystal structure were not changed with the increase of particle concentration in both the polymer systems. The thermomechanical reinforcement was different in the two polymer systems even though the strength of interaction between the filler and the polymers was similar. This behavior was attributed to the poor dispersion characteristics in the higher crystallinity matrix which translated in to reduced interfacial strength and immobilized polymer compared to the low crystallinity matrix. These results suggested that the structure of the bulk polymer influenced the dispersion characteristics, thermal properties as well as reinforcement behavior of these nanocomposite systems, and may be used as a means to understand nanocomposite properties.

## **CHAPTER 5**

### **EFFECT OF NANOPARTICLE SHAPE ON THE PROPERTIES OF NANOCOMPOSITES**

#### **5.1. Introduction**

Polymer nanocomposites are materials of great interest due to numerous application areas such as automotives,<sup>[173]</sup> optoelectronics,<sup>[174]</sup> tissue engineering<sup>[175]</sup> as well as structural materials.<sup>[176]</sup> It is very important to understand the properties of the constituents of the composites and their synergistic behavior in order to use them in desired application. A large variety of matrix materials ranging from amorphous and semicrystalline polymer matrices to polymer networks have been used for nanocomposites. Similarly, in case of the reinforcement research using clays and graphites (2D), nanotubes and nanofibers (1D) to silica, calcium carbonate etc. has been conducted. The stiffness as well as chemical structure of the matrix can influence the nanocomposite properties. In case of reinforcement, the nanoparticle attributes such as size,<sup>[59]</sup> surface chemistry,<sup>[62]</sup> aspect ratio<sup>[177]</sup> and shape<sup>[64]</sup> have been shown to influence the nanocomposite properties.

Nanocomposites made with fullerenes or silica (0D), carbon nanotubes (1D) and clay or graphene (2D) define three main categories based on dimensionality and shape of the reinforcement. With these three shapes in mind this chapter will look at the influence of nanoparticle shape on the nanocomposite properties when the reinforcement is chemically similar. Nanoparticle shape has been shown to be a contributing factor to the nanocomposite properties.<sup>[64, 70, 118, 178-181]</sup> Both computational and experimental studies

concerning nanoparticle shape have shown relationship between nanocomposite properties and particle shape. Nanoparticle shape was found to influence not only the mechanical properties of the resulting nanocomposites but also their processing and flow behavior. Rod shaped nanoparticles increased the melt viscosity more compared to platelet and icosahedral particles whereas the platelet nanoparticles showed higher tensile strength than rod and icosahedral particles.<sup>[180]</sup> Needle-shaped clay gave higher reinforcement and stronger interaction than platelet-shaped clay. In addition, fiber-like particles provided higher reinforcement in unidirectional composites than platelet-like particles whereas platelets were better when the composites had random distribution of particles.<sup>[179]</sup> Fiber shaped silica nanoparticles showed stronger toughening effect compared to spherical silica nanoparticles.<sup>[181]</sup> When the aspect ratio of the nanoparticles was 10, both experimental and computational studies showed that nanoparticle shape did not influence the nanocomposite reinforcement.<sup>[64, 118]</sup> The role of nanoparticle shape was considered secondary and that of surface area as primary for spherical and platelet (aspect ratio = 10) shaped particles.<sup>[64]</sup> Nanoplatelets showed higher reinforcement than carbon nanotubes when the aspect ratio was 1000, but similar reinforcement behavior in aligned and random configuration when the aspect ratio was 10.<sup>[118]</sup> In our previous work, it was shown that although the nanoparticles were different in shape, platelet and spherical assemblies of needle like particles but surface area differences played major role in reinforcement instead of shape as the aspect ratio of particles was in the range of 0-60. Comparison with another study indicated that reinforcement could be scaled with the amount of nanoparticle surface area available in the polymer nanocomposite irrespective of the polymer matrix, amorphous or semi-crystalline.<sup>[70]</sup>



Although research has been directed to understand the effect of nanoparticle attributes and matrix morphology individually but there is still a lack of understanding in terms of their coupled effect. Therefore, in this study we address the coupled effects of nanoparticle shape and matrix morphology. Nanoparticles synthesized had same surface area but differed in shape. The matrix crystallinity was seen to have significant effect on the dispersion characteristics of nanoparticles as well as other properties in Chapter 4. However, the particles used were large in size (>600 nm). PHB was again used as a matrix in this study to understand if the matrix crystallinity effects change when the particles have smaller size (50-100 nm) and different morphology. Calcium phosphate nanoparticles of two different shapes, near-spherical and fiber-like, were synthesized using a combined reverse microemulsion and solvothermal technique. PHB nanocomposites were designed using these two different shapes at different concentrations by solvent processing. The effect of nanoparticle shape on the dispersion, thermal as well as thermomechanical properties was studied. The crystallization kinetics showed a strong dependence on the morphology of the nanoparticles. The reinforcement behavior was a function of dispersion characteristics of the nanoparticles in both particle systems and the shape of the nanoparticles controlled the ultimate microstructure of the composites.

## **5.2. Experimental**

### **5.2.1. Materials for Synthesis of Near-spherical Calcium Phosphate Nanoparticles**

The near-spherical calcium phosphate nanoparticles were obtained using calcium nitrate tetrahydrate ( $\text{Ca}(\text{NO}_3)_2 \cdot 4\text{H}_2\text{O}$ ) (Alfa Aesar) and diammonium hydrogen phosphate

(NH<sub>4</sub>)<sub>2</sub>HPO<sub>4</sub> (Sigma Aldrich) as the calcium and phosphorous precursors, respectively. The aqueous solutions of the precursors were prepared using deionized water. Ammonium hydroxide (NH<sub>4</sub>OH) (Mallinckrodt Chemicals) was used for maintaining pH during the near-spherical calcium phosphate particles synthesis. The organic phase of the reverse micelle system for the near-spherical calcium phosphate particles was formed using cyclohexane (Fisher Scientific), *n*-pentanol (Aldrich) and octyl phenol ethoxylate (Triton X-100).

### 5.2.2. Synthesis of Near-spherical Calcium Phosphate Nanoparticles

The near-spherical calcium phosphate nanoparticles were synthesized by modifying the protocol by Sun *et al.*<sup>[182]</sup> *N*-pentanol was used as the co-surfactant instead of *n*-butanol used by Sun *et al.* The size of reverse micelles and the curvature of the interface of the micelles has been found to be influenced by the type of co-surfactant. *N*-pentanol was selected as the co-surfactant for the near-spherical nanoparticle synthesis as it has been found to have stronger interaction with the surfactant which in turn helps to control size and stability of the nanoparticles.<sup>[98, 183, 184]</sup> The complete method is described here. 10 ml of 0.5M calcium nitrate tetrahydrate and 0.3M diammonium hydrogen phosphate solutions were prepared in deionized water. The molar ratios of the precursors were selected to maintain calcium to phosphorous atomic ratio (Ca/P) of 1.67:1. The oil phase was formed by combining 18 ml of cyclohexane, 5.3 ml of Triton X-100 and 2 ml of *n*-pentanol. The calcium precursor was added slowly to the oil phase with continuous stirring to form the reverse microemulsion. Next, the phosphorous precursor was added to this reverse microemulsion with continuous stirring. The pH of the solution was adjusted

to 10.5 using ammonium hydroxide. This solution was then transferred to a teflon-lined autoclave and statically heated in an oven at 160 °C for 12 hours. The solution was allowed to cool down to room temperature. The solution was centrifuged and then washed with deionised water to get rid of the solvent and surfactant and a white powder was obtained. The powder was dried in the oven at 60 °C for 24 hours.

### **5.2.3. Materials for Synthesis of Calcium Phosphate Nanofibers**

For the nanofiber calcium phosphate nanoparticles, calcium chloride ( $\text{CaCl}_2$ ) (Sigma Aldrich) was used as the calcium precursor and diammonium hydrogen phosphate  $(\text{NH}_4)_2\text{HPO}_4$  (Sigma Aldrich) was used as the phosphorous precursor. The aqueous solutions of the precursors were prepared using deionized water. The organic phase of the reverse micelle system for the calcium phosphate nanofibers was formed using cyclohexane (Fisher Scientific), *n*-pentanol (Aldrich) and Cetyl trimethylammonium bromide (CTAB) (Sigma Aldrich). CTAB was used as the surfactant.

### **5.2.4. Synthesis of Calcium Phosphate Nanofibers**

The nanofiber calcium phosphate nanoparticles were synthesized by modifying the protocol by Lai Chen *et al.* <sup>[97]</sup> The molar concentration of Ca precursor was modified from 0.5 M to 0.6M in order to keep Ca/P ratio as 1.67. 1M and 0.6M solutions of Ca and P precursors were made in deionised water. 0.1 M of CTAB solution was prepared in cyclohexane. The ratio of co-surfactant to surfactant  $[\text{n-pentanol}]/[\text{CTAB}]$  was maintained as 3. The water to surfactant ratio,  $[\text{H}_2\text{O}] / [\text{CTAB}]$ ,  $w$  was kept as 10. The

CTAB solution was divided into two halves. The reverse micelles were formed by adding the calcium precursor to one part of the surfactant solution with continuous stirring and similarly by adding the phosphorous precursor to the other half. The two reverse microemulsions were stirred for 30 minutes. After 30 minutes the phosphorous reverse micellar solution was mixed with the calcium reverse micellar solution and stirred for another 30 minutes. The resulting solution was transferred to a Teflon lined stainless steel autoclave and statically heated in an oven at 100 °C for 10 hours. The solution was allowed to cool down to room temperature and the product was centrifuged and washed with ether and ethanol to get rid of the organic solvent and surfactant. The white powder obtained was dried at 60 °C in an oven for 24 hours.

#### **5.2.5. Nanoparticle Characterization**

Both near-spherical and nanofiber calcium phosphate nanoparticles were characterized for their morphology, size, chemical and crystal structure, elemental analysis, Ca/P ratio, surface area and density. The near-spherical and nanofiber calcium phosphate nanoparticles were characterized for the morphology and size using JEOL 100CX-2 transmission electron microscope (TEM) operating at 100 kV. The near-spherical and nanofiber nanoparticles were dispersed in ethanol using sonication for 2 and 1.5 hours respectively, and then dropped on a lacey carbon coated copper TEM grid. The TEM grids were air-dried for one day. The chemical structure of the nanoparticles was determined using Bruker Vector 22 Fourier transform infrared spectroscopy (FTIR) spectrometer. The samples for FTIR were prepared by mixing 2 mg of each type of calcium phosphate powder with 100 mg of KBr (EMD Chemicals) separately and then

pressing into pellets. The spectra were recorded at room temperature in the range 4000-400  $\text{cm}^{-1}$  using 32 scans and a resolution of 4  $\text{cm}^{-1}$ . The crystal structure of the calcium phosphate nanoparticles was determined using a PANalytical's X'Pert PRO Alpha-1 at an accelerating voltage of 45 kV and a current of 40 mA using monochromatized Cu K radiation. The powder was ground and compactly filled in a hole in the sample holder. The diffraction pattern was collected over the  $2\theta$  range from 17-55° with a step size of 0.03° and scan rate of 1°/min. The elemental and quantitative analysis of Ca/P ratio was conducted by energy dispersive x-ray spectroscopy (EDX). EDX was performed on a LEO 1530 thermally-assisted FEG SEM equipped with an EDX unit. The data was acquired at an accelerating voltage of 10 kV. Four measurements at 1000X were conducted on each type of nanoparticle system. The size of the nanoparticles was also measured using dynamic light scattering (DLS) apart from TEM. In order to get better estimate of the size of nanoparticles and comparison with nanoparticles in the nanocomposites, the calcium phosphate nanoparticles suspension in ethanol was prepared by sonicating near-spherical and nanofiber nanoparticles for 2 and 1.5 hours, respectively. The concentration of calcium phosphate nanoparticles in ethanol was 0.004 % by weight. The measurements were performed using a Brookhaven BI-200SM goniometer (He-Ne laser with wavelength of 633 nm) and a BI-9000AT correlator. CONTIN analysis method was used for the analysis of the results as it is good method for polydisperse or multimodal particle size distributions. Surface Area and Porosity Analyzer (ASAP 2020) from Micromeritics, Inc. with the Brunauer, Emmet, and Teller (BET) method was used to determine the surface area of the near-spherical and nanofiber calcium phosphate nanoparticles.<sup>[124]</sup> The density of the calcium phosphate powder was

measured using a glass pycnometer. Approximately 0.5 grams of both near-spherical and nanofiber calcium phosphate powder was used for density measurement.

#### **5.2.6. Nanocomposite Preparation**

The nanocomposites were prepared using solvent grade chloroform (BDH), reagent alcohol (Mallinckdrot) and PHB with weight average molecular weight of 426,000 g/mol (Sigma-Aldrich). The PHB was dissolved in chloroform by refluxing and the undissolved matter was filtered. The resulting solution was precipitated in methanol to get purified PHB. The sonication time for both near-spherical and nanofiber calcium phosphate nanoparticles was optimized by carrying out studies using different sonication times and checking the dispersion of nanoparticles using SEM. A dual solvent technique was observed to work well for both type of nanoparticles. Therefore, the nanoparticles were dispersed in ethanol, and the polymer PHB was dissolved in chloroform. The near-spherical and nanofiber calcium phosphate nanoparticles were dispersed in ethanol by sonicating in a cup-horn sonicator at a power of 130 W at room temperature for 2 and 1.5 hours, respectively. The particle sols looked homogeneous and translucent after the sonication indicating that the aggregate size was reduced. The PHB polymer was dissolved separately in chloroform at room temperature for 1 hour and then at 45 °C for 15 minutes to form a 5 wt. % polymer solution by stirring. The calcium phosphate sol in ethanol was then added slowly with continuous stirring to the polymer solution in chloroform. The mixture was stirred for 10 minutes. To disperse the nanoparticles in the PHB, the nanocomposite solution was further sonicated at a power of 87 W for 45 minutes at room temperature. The resulting nanocomposites were collected by

precipitation in cold methanol and dried in vacuum oven at 50 °C for 24 hours. Nanocomposite films were prepared by melt pressing these precipitated composite particles at 180 °C for 8 minutes. All samples were cooled from the melt to room temperature in the press using an integrated water cooling system in approximately 14 minutes. The films were homogenous and transparent in appearance. The composite films were prepared with 0, 0.5, 1, 5, 10, 15 and 20 wt. % of near- spherical calcium phosphate particles and 0.5, 1, 5 and 10 wt. % of nanofiber calcium phosphate nanoparticles. A neat PHB sample was also prepared using the same processing conditions as the composite samples for comparison. For clarity, the near- spherical calcium phosphate (CaP) composites will be referred as NS-CaP/PHB and the nanofiber calcium phosphate composites as NF-CaP/PHB composites.

#### **5.2.7. Nanocomposite Characterization**

The NS-CaP/PHB and NF-CaP/PHB composites were characterized for dispersion and distribution, thermal properties, and thermomechanical properties. Nanoparticle dispersion and distribution were observed by scanning electron microscopy (SEM). Cryo-fractured surfaces of the composite specimens were imaged using a LEO 1530 SEM at a voltage of 5 kV. The composite specimens were gold coated using an ISI Sputter Coater prior to imaging.

Differential Scanning Calorimetry (DSC) experiments were performed on a TA instruments DSC Q-200 in nitrogen. The specimens were heated from -40 to 190 °C at a rate of 10 °C/min under nitrogen gas flow. After keeping the specimens isothermal for 3 minutes, the specimens were cooled back to -40 °C at the same rate. Two such cycles

were performed on each specimen. The crystallinity of the polymer was calculated by dividing area under the melting peak in the first and second heating cycles by the heat of fusion for completely crystalline PHB ( $\Delta H_m^\circ=146$  J/g).<sup>[158]</sup> For composite samples, the value of heat of fusion was normalized by the mass fraction of PHB in the composites for calculating crystallinity of PHB in the composite. The percent crystallinity was reported as the average value obtained from two DSC runs on two different samples. The thermal transitions from the experiments were measured as the peak maximum of the melting and crystallization peaks.

Isothermal crystallization studies were also performed to determine the effect of the nanoparticles shape on crystallization. The samples were heated from room temperature to 190 °C at a rate 100 °C/min under nitrogen atmosphere and held isothermal at 190 °C for 3 minutes and then cooled rapidly (100 °C/min) to crystallization temperatures 120, 125 and 130 °C and held at these temperatures until crystallization was complete. Two isothermal studies were performed on each nanoparticle concentration, and the results were averaged.

The mobile amorphous fraction (MAF) in the composites samples was determined using modulated differential scanning calorimetry (MDSC). The specimens were heated from -50 °C to 60 °C with modulation amplitude of 1°C, a period of 100 s and an underlying heating rate of 3 °C/min. The change in heat capacity ( $\Delta C_p$ ) of each sample was determined at the glass transition temperature ( $T_g$ ). The  $T_g$  was taken at the half height point of the specific heat step from the reversing heat capacity versus temperature plot of MDSC. The MAF was then determined using the following equation,

$$\Delta C_p = \frac{\Delta C_p(\text{sample})}{\Delta C_p(\text{completely amorphous polymer})} \quad (1)$$



Where,  $\Delta C_p$  (sample) was determined from MDSC and the  $\Delta C_p$  for completely amorphous PHB polymer is  $0.5 \text{ J g}^{-1} \text{ }^\circ\text{C}^{-1}$ .<sup>[185, 186]</sup> The crystalline fraction (CF) was obtained from the non-isothermal DSC experiments. Both CF and MAF were normalized to the weight fraction of the PHB. The rigid amorphous fraction (RAF) is defined as the fraction of polymer that lies as an interphase between the crystalline and the amorphous regions due to constrained polymer chains in contact with the crystal. RAF is the fraction of polymer which does not contribute to heat of fusion or the heat capacity change at the glass transition, attributed to crystalline and amorphous fractions of the polymer, respectively.<sup>[187, 188]</sup> RAF is that amorphous phase whose mobility is restricted due to its close association with the interlamellar regions or crystal surfaces whereas the MAF is the region which is postulated to be associated with larger gaps between the lamellar stacks.<sup>[189]</sup> The RAF calculated using the following equation,

$$RAF = 1 - CF - MAF \quad (2)$$

Dynamic mechanical tests performed on a Mettler Toledo DMA861<sup>e</sup> in the shear mode. The specimens for the tests had a nominal thickness of 0.5 mm and a diameter of 3.18 mm. The measurements were performed in the linear viscoelastic range, established using strain sweep measurements for all of the specimens at -25 and 80 °C. The testing was performed using force amplitude of 1.0 N below  $T_g$  and a strain amplitude of 0.1  $\mu\text{m}$  above  $T_g$  for neat PHB sample and 1.5 N and 0.1  $\mu\text{m}$  for the composite samples. The temperature was varied from -30 to 100 °C with a heating rate of 2 °C/min, and the measurements were performed at a frequency of 1 Hz. Also a frequency sweep from 50 to 0.1 Hz was performed at 5 °C intervals from -30 to 100 °C with a heating rate of 2 °C/min. Settling was enabled at all measurement temperatures.

The change in crystal size of PHB due to presence of nanoparticles was determined using a PANalytical's X'Pert PRO Alpha-1 at an accelerating voltage of 45 kV and a current of 40 mA using monochromatized Cu K radiation. The film sample was placed on a glass slide. The glass slide was fixed to the sample holder. The diffraction pattern was collected over the  $2\theta$  range from  $10-50^\circ$  with a step size of  $0.02^\circ$  and scan rate of  $1^\circ/\text{min}$ . The peak profile fitting of the obtained XRD scans was done using MDI Jade 8.1 software. The crystallite size from the XRD peaks was calculated using Scherrer's equation,

$$\tau = \frac{K\lambda}{\beta \cos \theta} \quad (3)$$

Where,  $K$  is the shape factor with a value of 0.9,  $\lambda$  is the x-ray wavelength  $1.54 \text{ \AA}$ ,  $\beta$  is the line broadening at half the maximum intensity (FWHM) in radians of the peak, and  $\theta$  is the Bragg angle.

### 5.3. Results and Discussion

Using the synthesis method outlined above, two shapes of HAp nanoparticles were produced, near-spherical and nanofiber. The following section will describe the nanoparticle characterization as well as results of nanocomposite characterization.

#### 5.3.1. Morphology of nanoparticles

Figures 5.1 and 5.2 give the morphologies of the calcium phosphate nanoparticles as seen in TEM. As observed from TEM, the shape of the NS-CaP nanoparticles was nearly spherical consisting of short rods with an aspect ratio of approximately 2. The NF-CaP nanoparticles had a whisker like morphology with mean aspect ratio of 28. The aspect ratio was calculated from the particle size measurement done on the TEM images.

Dimensions of 160 nanofibers and 106 near-spherical nanoparticles were calculated from the TEM images. The NF-CaP also contained some platelets of similar length as fibers. A total of 2894 particles were counted, out of which 195 were platelets and the rest were nanofibers. The SEM images of particles are given in Appendix D.

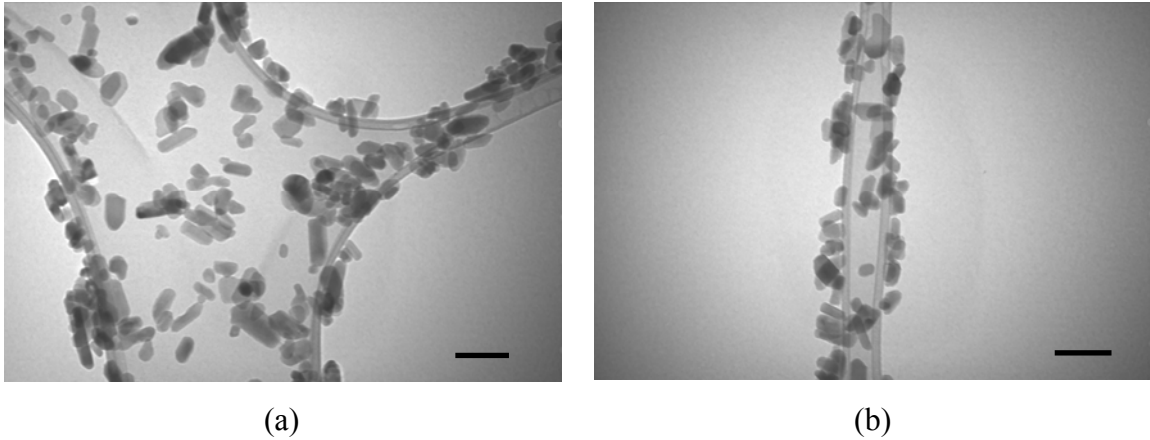


Figure 5. 1. Morphology of the near-spherical calcium phosphate nanoparticles as seen in TEM. The scale bar in both the images represents 100nm.

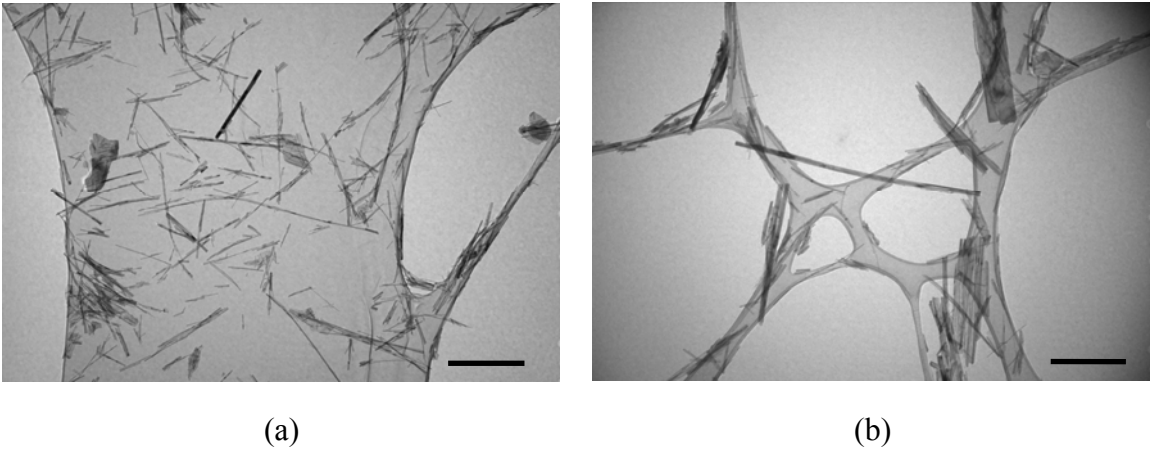


Figure 5. 2. Morphology of the nanofiber calcium phosphate nanoparticles as seen in TEM. Some platelets were also seen but they constituted small percentage (7%). The scale bar in both the images represents 1 $\mu$ m.

### 5.3.2. Chemical structure

The FTIR spectra of the NS and NF-CaP nanoparticles normalized to the phosphate peak ( $\text{PO}_4^{3-}$   $1030\text{cm}^{-1}$ ) is given in Figure 5.3. The absorption bands at 465, 563, 602, 961, 1034 and  $1090\text{cm}^{-1}$  in the NS-CaP spectra are associated with the vibrations of the  $\text{PO}_4$  group. The peaks at 1034 and  $1090\text{cm}^{-1}$  are attributed to the triply degenerated asymmetric stretching mode vibration,  $\nu_3$ , whereas the band at  $961\text{cm}^{-1}$  is assigned to the nondegenerated symmetric stretching mode  $\nu_1$  of the P-O bond of the  $\text{PO}_4$  group. The bands at 563, 602 and  $465\text{cm}^{-1}$  are associated with the triply and doubly degenerated bending modes  $\nu_4$  and  $\nu_2$  of the phosphate group, respectively. The peaks at  $3570$  and  $631\text{cm}^{-1}$  in the near-spherical HAp spectra correspond to the vibrations of the OH group. The spectra of NS-CaP nanoparticles is characteristic spectra of both stoichiometric and calcium-deficient HAp (CDHAp) found in the literature.<sup>[127, 190-194]</sup>

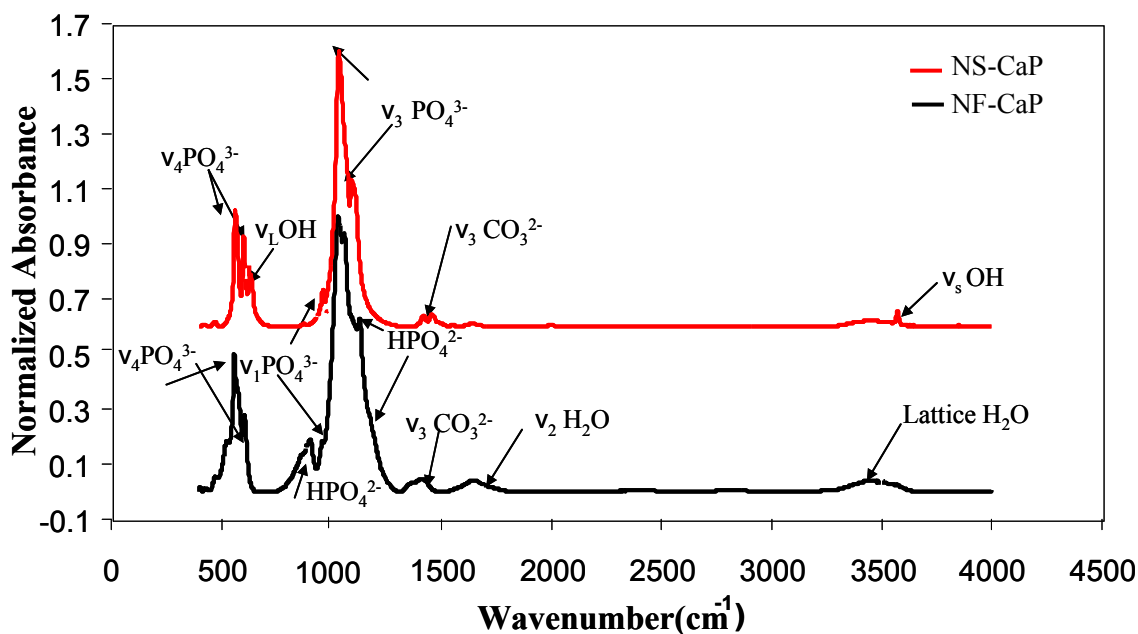


Figure 5. 3. Infrared spectra of as synthesized near-spherical (NS) and nanofiber calcium phosphate (NF-CaP) nanoparticles normalized to the highest intensity peak corresponding to phosphate functional group ( $\text{PO}_4^{3-}$   $1030\text{cm}^{-1}$ ).

In case of the NF-CaP spectra, the absorption bands at 467, 521, 559, 604, 957, 1028 and 1042  $\text{cm}^{-1}$  are attributed to stretching and triply degenerate vibration modes of the  $\text{PO}_4^{3-}$  ions. The absorption band at 1126 and the shoulder at 1175  $\text{cm}^{-1}$  in the fiber spectra are not seen in the near-spherical nanoparticle spectra and arise due to the presence of  $\text{HPO}_4^{2-}$  ions and have been observed in the IR spectra of monetite. [195, 196] The difference in shape of the peaks around the O-P-O bending (900-1250 $\text{cm}^{-1}$ ) also indicates that the fiber particles have  $\text{HPO}_4^{2-}$  ions. [127] The shoulder at 864 and the peak at 899  $\text{cm}^{-1}$  in the fiber spectra indicates the presence of octacalcium phosphate (OCP) in the powder. [197] The broad peak at 3443  $\text{cm}^{-1}$  in the fiber spectra corresponds to the  $\text{H}_2\text{O}$  in the lattice as this band exists in the range of 3200-3550  $\text{cm}^{-1}$ . [198] A shoulder was observed at 3561  $\text{cm}^{-1}$  in the fiber spectra compared to a sharp peak in the near-spherical particle spectra and no peak corresponding to OH librational mode was observed in fiber spectra. The broad absorption band at 1629  $\text{cm}^{-1}$  is associated with the bending mode vibration from the absorbed water. [127, 193, 195, 198] The presence of  $\text{CO}_3^{2-}$  ions was indicated by the absorption bands between 1320 and 1500 $\text{cm}^{-1}$  in both types of nanoparticle spectrums. [93, 127, 191-193, 195] These are due to the absorption of carbon dioxide in the air during the synthesis process. The NF-CaP spectra has some differences from the NS-CaP spectra indicating the existence of other phases in NF-CaP nanoparticles.

### 5.3.3. Crystal structure

The NS-CaP and NF-CaP nanoparticles were characterized for their crystal structure using X-ray diffraction. Figure 5.4. gives the XRD patterns of NS and NF-CaP nanoparticles. The diffraction pattern of NS-CaP matched completely with calcium-

deficient HAp (CDHAp) (PDF card file No. 00-046-0905) where the star symbol corresponds to the standard characteristic peaks of CDHAp. One peak corresponding to octacalcium phosphate was observed in the XRD pattern of NS-CaP nanoparticles. The dimensions of NS-CaP corresponding to a hexagonal unit cell were calculated as  $a = b = 9.451 \text{ \AA}$  and  $c = 6.882 \text{ \AA}$ , similar to the dimensions from the PDF card file of CDHAp ( $a = b = 9.441 \text{ \AA}$  and  $c = 6.881 \text{ \AA}$ ). The shape and intensity of the diffraction peaks indicated that the particles are highly crystallized. The peak profile fitting using the MDI Jade software indicated crystallinity more than 99%.

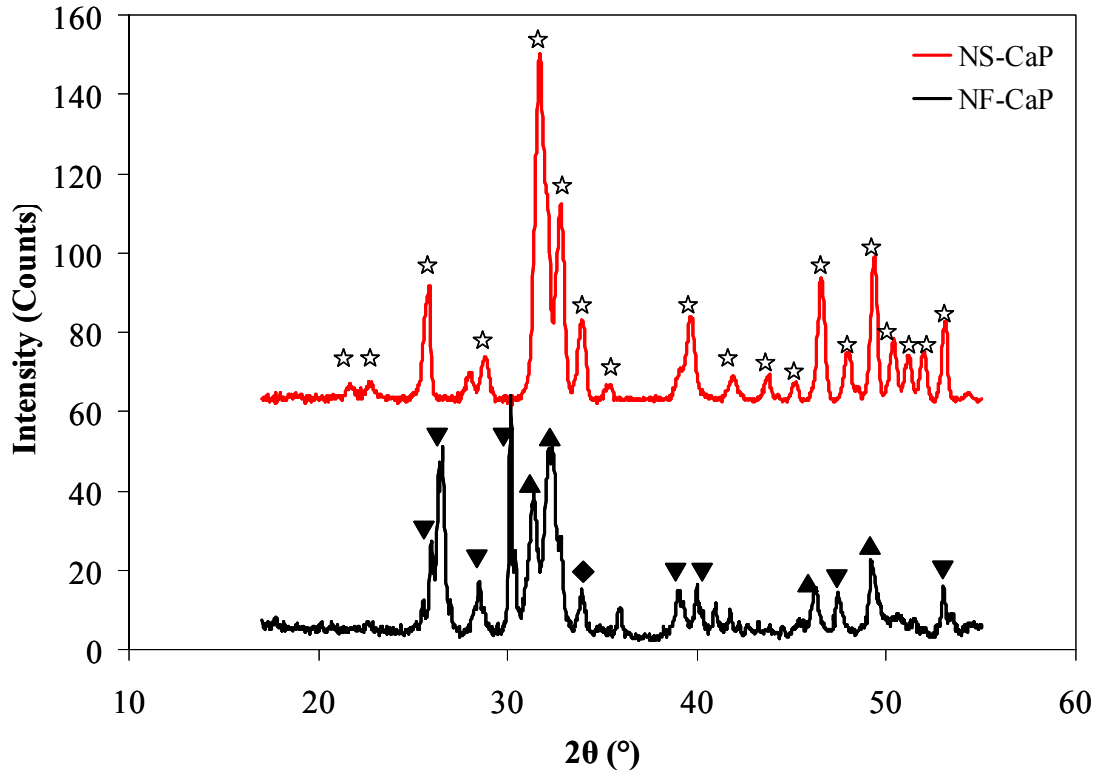


Figure 5. 4.XRD patterns of synthesized near-spherical (NS) and nanofiber calcium phosphate (NF-CaP) nanoparticles. All peaks in NS-CaP correspond to calcium deficientHAp (CDHAp) (☆). In NF-CaP pattern most peaks are from monetite (▼) but there are peaks from other calcium phosphates such as chlorapatite (▲), and octa-calcium phosphate (OCP) (◆).

The diffraction pattern of NF-CaP nanoparticles given in Figure 5.4, showed the presence of chlorapatite and dicalcium phosphate anhydrous (DCPA/Monetite) as the major phases with traces of OCP. The weight percentage of the phases was estimated using Rietveld quantitative phase analysis method. The chlorapatite was approximately 56 wt. % and that of DCPA/monetite was 44 wt. %. Table 5.1 shows the  $2\theta$  and d-spacing of NF-CaP nanoparticles along with the peak intensities in comparison the International Center for Diffraction Data (ICDD) PDF card files of DCPA/Monetite and chlorapatite. It can be observed that d-spacings for the NF-CaP nanoparticles matched with those listed for the two phases from the ICDD PDF card files.  $2\theta$  and d-spacing of NS-CaP and NF-CaP nanoparticles from XRD scan in descending order of intensity compared to d-spacing from other calcium phosphate phases is given in Appendix D.

Table 5.  $2\theta$  and d-spacing of NF-CaP nanoparticles from XRD scan in descending order of intensity compared to d-spacing from PDF card files of DCPA/Monetite and Chlorapatite phases.

<b><math>2\theta</math> (°) NF-CaP</b>	<b>d(Å) NF-CaP</b>	<b>d(Å) Monetite 00-009-0080</b>	<b>d(Å) Chlorapatite 00-002-0851</b>
32.25	2.77 (100)	-	2.78 (100)
26.48	3.36 (94.3)	3.37 (70)	-
30.15	2.96 (78.5)	2.96 (100)	-
31.38	2.85 (67.4)	2.84 (2)	-
25.97	3.43 (38.5)	-	-
32.84	2.73 (30.7)	2.72 (35)	-
30.36	2.94 (23.9)	2.94 (35)	-
46.25	1.96 (23.8)	1.96 (2)	1.96 (16)
49.24	1.85 (23.3)	1.85(20)	-
53.02	1.73 (21.6)	1.73 (20)	-
39.01	2.31 (20.3)	2.31 (10)	-
28.49	3.13 (20)	3.13 (20)	-
47.50	1.91 (20)	1.92 (16)	1.91 (8)
33.92	2.64 (19.5)	-	-
49.48	1.84 (19.3)	-	1.84 (16)
40.00	2.25 (18.7)	2.25 (16)	-

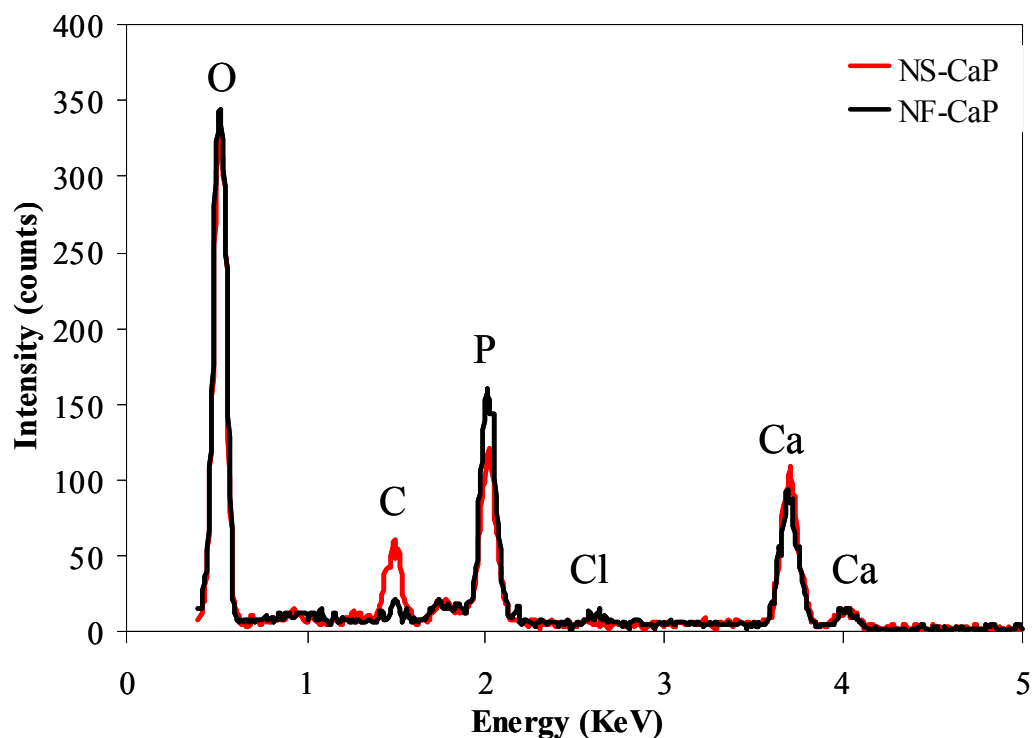


Figure 5. 5. Energy dispersive x-ray analysis (EDX) of the synthesized NS and NF-CaP nanoparticles. The peak of carbon at 1.5 KeV was excluded from the composition.

#### 5.3.4. Elemental analysis, Ca/P ratio and density of nanoparticles

The elemental analysis and chemical stoichiometry (Ca/P ratio) of the NS-CaP and NF-CaP nanoparticles was investigated with EDX. Figure 5.5 gives the EDX spectra of both NS and NF-CaP nanoparticles. Both of the nanoparticles contained peaks corresponding to the calcium, phosphorous and oxygen. Some traces of carbon were also found in both nanoparticles which are attributed to the carbon tape on the SEM stubs. In addition, the NF-CaP spectra also showed some traces of chlorine element. The presence of chlorine as one of the elements in the NF-CaP coincides with chlorapatite as one of the phases in the XRD. The atomic ratio of Ca/P in the powders of both type of nanoparticles



were obtained from the average of four scans. The mean Ca/P ratio for NS-CaP nanoparticles was 1.5 and that of NF-CaP was 1.0. These ratios indicate that the NS-CaP has stoichiometric ratio corresponding to Ca-deficient HAp (CDHAp) and NF-CaP had Ca/P ratio similar to dicalcium phosphate dihydrate (DCPD)(CaHPO<sub>4</sub>·2H<sub>2</sub>O) and dicalcium phosphate anhydrous(DCPA/Monetite)(CaHPO<sub>4</sub>).<sup>[78, 199]</sup>

The densities of the NS-CaP and NF-CaP nanoparticles were measured using a glass pycnometer. The density of NS-CaP nanoparticles was 2.81 g/cm<sup>3</sup> while the density of NF-CaP nanoparticles was 2.22 g/cm<sup>3</sup>. The density of NF-CaP is similar to the density of the density of chlorapatite found in the literature.<sup>[200]</sup>

Table 5. 2. Particle size measurement from DLS and TEM and comparison of surface area of nanoparticles measured from TEM dimensions and from BET.

Nanoparticles	Particle Size (nm)		Surface Area (m <sup>2</sup> /g)	Surface area BET (m <sup>2</sup> /g)
	DLS(D <sub>H</sub> )	TEM	TEM	
NS-CaP	106 ± 8	h = 76 ± 28 d = 34 ± 8	53.5 ± 10	50
NF-CaP	483 ± 64	l = 599 ± 438 b = h = 22 ± 9	96 ± 37	49.5

### 5.3.5. Nanoparticle Size and Specific Surface Area

Table 5.2 compares the particle size and surface area as measured from DLS and TEM as well as BET. The mean effective hydrodynamic diameter of the NS-CaP and NF-CaP nanoparticles measured using DLS and deduced from CONTIN analysis was 106 ± 8 nm and 483 ± 64 nm, respectively. The deviation from the mean given here describes the variation in the mean value calculated from two separate dynamic light

scattering experiments. The size of the particles was also measured from TEM images. The near-spherical nanoparticles were short rods with the mean length of the longer side (h) in the near-spherical nanoparticles was  $76 \pm 28$  nm calculated from approximately 106 nanoparticles. The mean dimension of the other side (diameter of rods d) was  $34 \pm 8$  nm. The mean length (l) and width (b=h) of nanofibers was approximately  $599 \pm 438$  nm and  $22 \pm 9$  nm respectively. The standard deviation ( $\sigma$ ) from the mean was calculated from size measurements of 160 fibers. The large deviations from the mean size indicated the polydispersity in size distribution of both types of nanoparticles. The specific surface area of near-spherical and fiber like nanoparticles measured from BET was 50 and 49.5 m<sup>2</sup>/g, respectively. The surface area of the NS-CaP and NF-CaP nanoparticles was also calculated using particle size from TEM taking the particles as cylinders and as rectangular cuboids respectively. It can be observed that the surface area calculated using nanoparticle dimensions from TEM is similar to that from BET for NS-CaP nanoparticles but higher for NF-CaP nanoparticles.

#### **5.3.6. Dispersion and Distribution of Nanoparticles in Nanocomposites**

The results of the characterization of the nanocomposite properties indicated that the shape of nanoparticles affected the nanocomposite properties through changes in dispersion characteristics, crystallization kinetics and thermomechanical properties. In order to understand the differences between dispersion and distribution in context of this research, dispersion was defined as single nanoparticles with increased surface area available to the polymer and distribution was defined as a homogeneous distribution of nanoparticles in the matrix in the form of cluster (combination of 2-4 nanoparticles) or

aggregates(combination of several clusters). Figure 5.6 shows the SEM images of the cryo-fractured surfaces of 0.5, 1, 5, 10, 15 and 20 wt. % NS-CaP/PHB composite samples. It can be observed that the near-spherical calcium phosphate (NS-CaP) nanoparticles were distributed homogeneously for all concentrations. However, the dispersion to single particle level was seen in only 0.5 wt. % composites samples. 1 wt. % composite consisted of particles distributed in the form of both single and as clusters of 2-3 nanoparticles. At 5 wt. % and higher concentrations composite samples, smaller clusters which were formed by combination of 2 or more primary particles as well as bigger aggregates were observed. The size of clusters was 300-500 nm and aggregates was 1- 8  $\mu\text{m}$  for 5 and 15 wt. % NS-CaP/PHB nanocomposites. The 10 wt. % composite sample had clusters in the size range 200-300 nm whereas aggregates were in the range of 3 - 5  $\mu\text{m}$ . The cluster and aggregates size for 20 wt. % NS-CaP/PHB composites was 300-600 nm and 1-12  $\mu\text{m}$ , respectively. The clusters and aggregates were homogeneously distributed throughout the polymer matrix at all filler loadings. No region in the composite samples was observed to be completely devoid of particles.

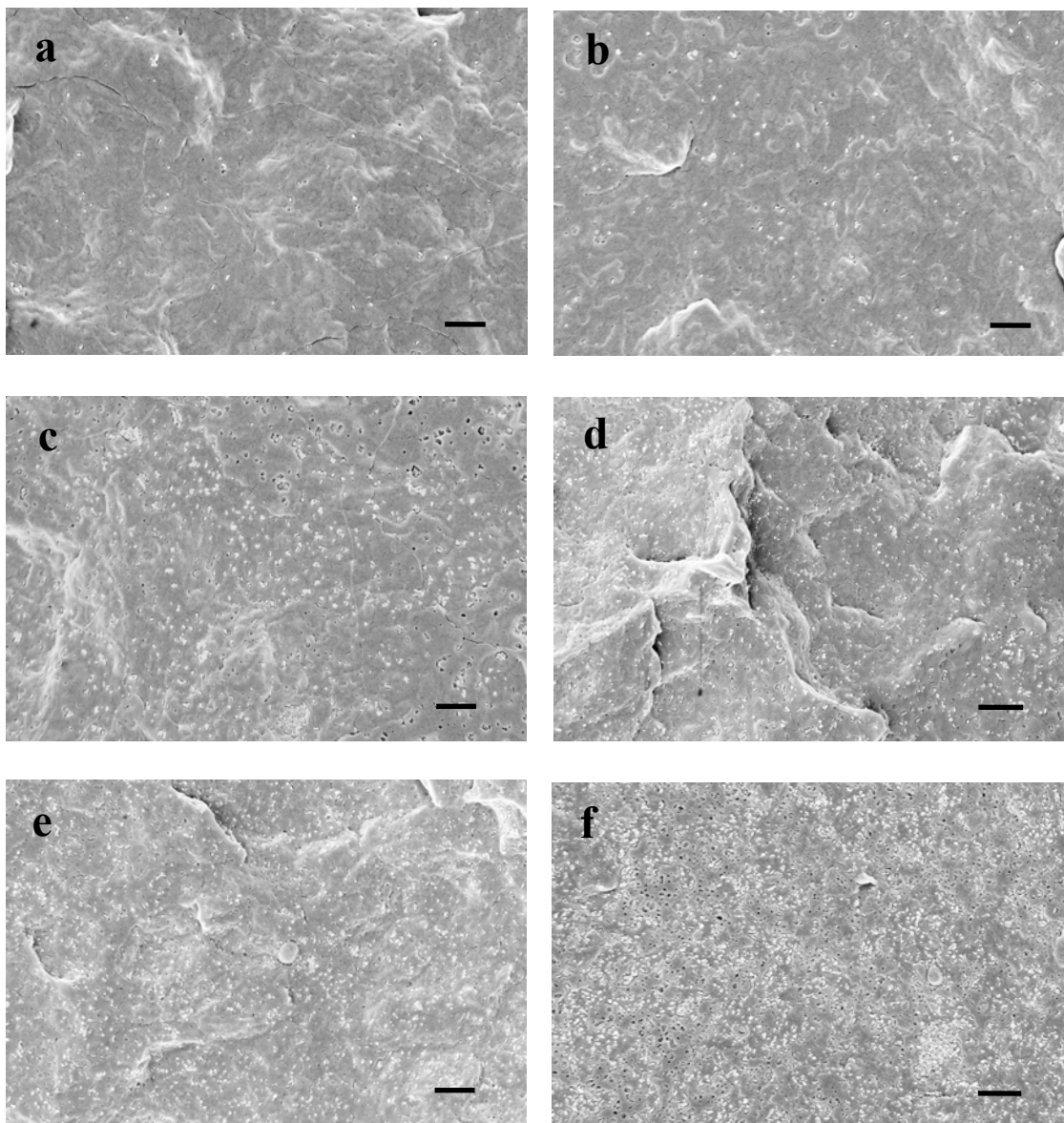


Figure 5. 6. SEM images of a) 0.5wt. % HAp-NS, b) 1wt. % HAp-NS, c) 5wt. % HAp-NS, d) 10wt. % HAp-NS, e) 15wt. % HAp-NS, and f) 20wt. % HAp-NS and PHB composites. The scale bar in all images represents 1  $\mu\text{m}$ .

The SEM images of cryo-fractures surfaces of 0.5, 1, 5 and 10 wt. % NF-CaP composites samples are shown in Figure 5.7. The nanofibers were well distributed at all concentrations. The fibers were dispersed as isolated particles for 0.5 and 1 wt. %

composite samples. At higher loadings, the nanofibers were dispersed both in the form of isolated particles as well as in the form of fiber bundles. Some platelets were also observed along with nanofibers at higher concentrations. The percentage of platelets and nanofibers was calculated by counting the number of nanofibers and platelets from 18 SEM images. It was found that nanofibers constituted 93% and the platelets 7% of the total nanoparticles. These numbers were consistent with the numbers obtained from TEM images of the nanoparticles.

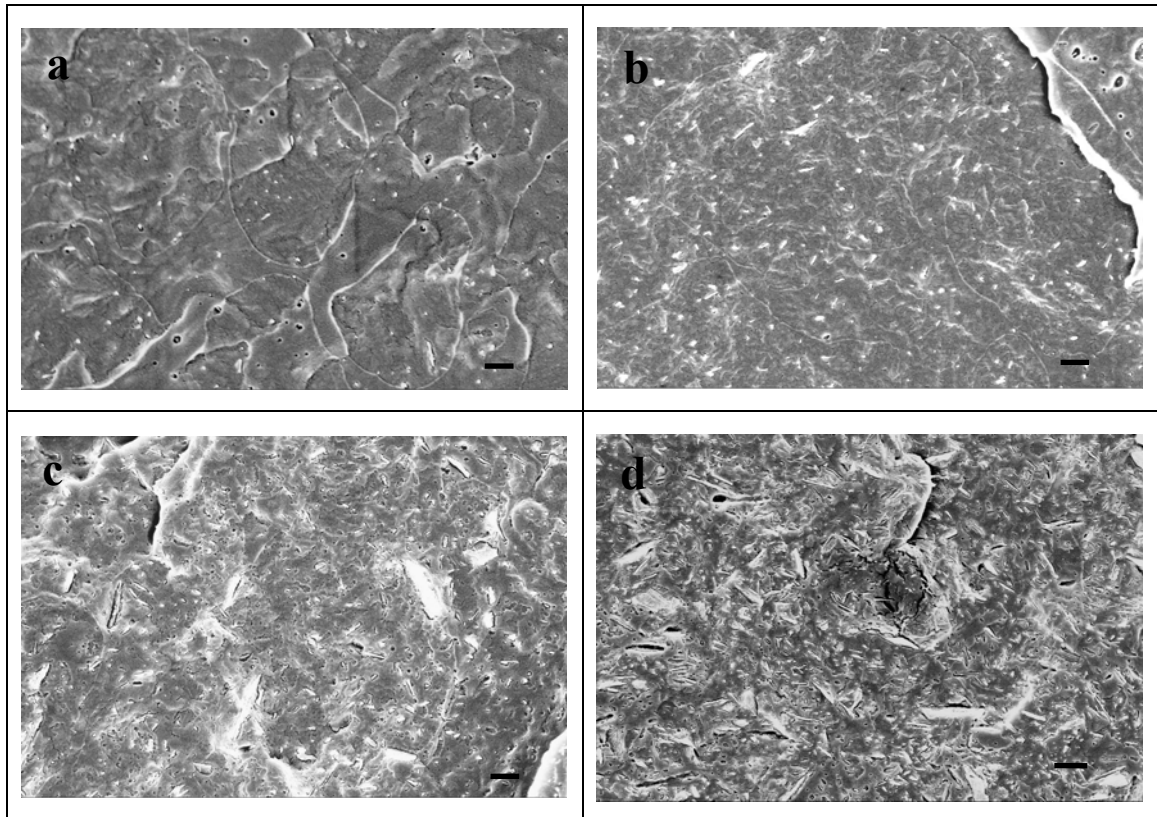


Figure 5. 7. SEM images of a) 0.5wt% HAp-NF, b) 1wt% HAp-NF, c) 5wt% HAp-NF, and d) 10wt% HAp-NF and PHB composites. The scale bar in all images represents 1  $\mu\text{m}$ .

The dispersion characteristics of both NS and NF-CaP nanoparticles in the PHB matrix indicate that dispersion was homogeneous at low loadings. It has been seen that in case of pristine nanoparticles of any type that the dispersion deteriorates with the increase in nanoparticle concentration.<sup>[201-203]</sup>

### **5.3.7. Thermal Properties and Crystallization Kinetics of Nanocomposites**

The effect of nanoparticle shape on thermal properties of nanocomposites was studied with DSC through nonisothermal, isothermal and modulated experiments. Table 5.3. shows the peak melting ( $T_m$ ) and crystallization ( $T_c$ ) temperatures of neat PHB, NS-CaP/PHB nanocomposites and NF-CaP/PHB nanocomposites from the first heating and cooling cycle. The purification of the PHB polymer by refluxing and filtering led to the disappearance of the dual melting peak in the DSC experiments. The thermal transitions from the first heating and cooling cycle will determine if the nanoparticles have any effect on the crystallization of the polymer matrix. The first heat crystallinity values are required to confirm that the thermomechanical properties of the composites are not influenced by the differences in the crystallinity between the samples. The peak melting temperature was not affected by the difference in the shapes of the nanoparticles. The melting temperature for the NS-CaP/PHB composites samples was within  $-2^\circ\text{C}$  of the neat PHB ( $173^\circ\text{C}$ ) whereas the melting temperature for the NF-CaP/PHB composites samples was  $\pm 1^\circ\text{C}$  of the neat PHB. The peak crystallization temperatures of both NS-CaP and NF-CaP/PHB composites samples did not show significant shifts from the peak crystallization temperature of neat PHB with a few exceptions. 5 and 20 wt. % NS-CaP/PHB composites showed 2-3% decrease in crystallization temperature whereas 1 wt.

% NF-CaP/PHB composite showed a 2% increase in the peak crystallization temperature. The peak crystallization temperatures of both NS and NF-CaP nanocomposites were within +1°C of the neat PHB (109°C) but within -2-3°C of the neat PHB for 5 and 20 wt. % NS-CaP/PHB composite. Peak Melting ( $T_m$ ) and crystallization ( $T_c$ ) temperatures of neat PHB, NS-CaP/PHB and NF-CaP/PHB nanocomposites from second heating and cooling cycle are given in Appendix D.

Table 5. 3. Peak melting ( $T_m$ ) and crystallization ( $T_c$ ) temperatures of neat PHB, NS-CaP/PHB nanocomposites and NF-CaP/PHB nanocomposites from first heating and cooling cycle.

<b>Conc. wt.%</b>	<b><math>T_m</math> of NS-CaP/PHB composites</b>	<b><math>T_m</math> of NF-CaP/PHB composites</b>	<b><math>T_c</math> of NS-CaP/PHB composites</b>	<b><math>T_c</math> of NF-CaP/PHB composites</b>
0	173 ± 0.6	173 ± 0.6	109 ± 0.6	109 ± 0.6
0.5	173 ± 0.4	174 ± 0.4	109 ± 0.3	110 ± 0.1
1	173 ± 0.1	173 ± 0.2	110 ± 0.3	111 ± 0.1
5	171 ± 1.2	172 ± 0.5	107 ± 0.3	109 ± 0.1
10	172 ± 0.1	172 ± 0.0	110 ± 0.1	109 ± 0.0
15	171 ± 0.3		110 ± 0.2	
20	171 ± 0.1		106 ± 0.1	

Figure 5.8. shows the change in crystallinity of NS-CaP and NF-CaP/PHB composites from first heat with respect to filler concentration and its deviation from the neat PHB. The crystallinity of neat PHB was approximately 68% and the crystallinity of both NS-CaP and NF-CaP/PHB composites was within 2% of the neat PHB. The crystallinity was not significantly affected by the increase in nanoparticle concentration for both types of systems. The amount of crystallinity achieved in both the composite

systems from the second heating data was within 1% of the neat PHB. The table of percent crystallinity of neat PHB, NS-CaP/PHB and NF-CaP/PHB composite samples from first and second heating cycles of DSC is given in Appendix D.

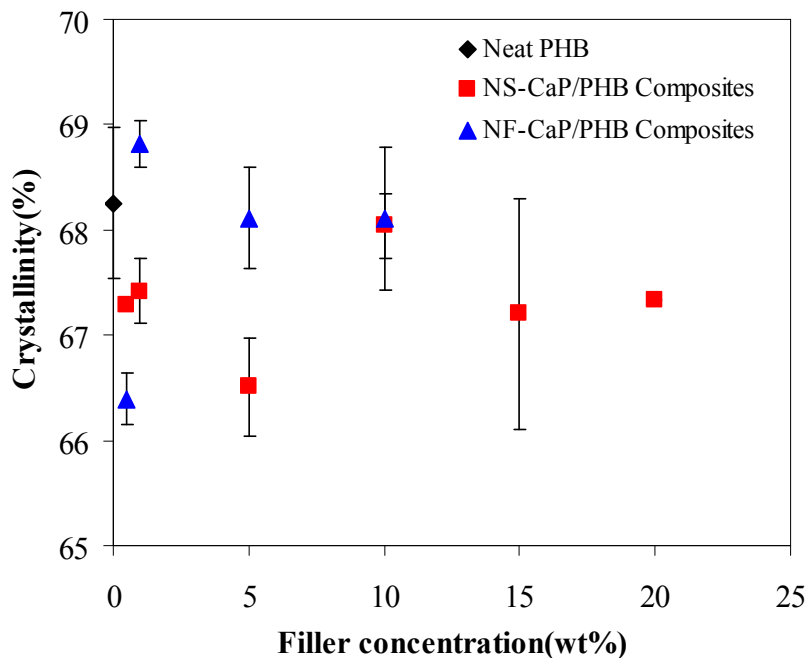


Figure 5. 8. Crystallinity from first heat as a function of filler content for neat PHB and NS-CaP/PHB as well as NF-CaP/PHB composite samples.

Isothermal crystallization studies were conducted on neat PHB and both nanocomposite systems at 120, 125 and 130°C to understand the differences in crystallization kinetics because of nanoparticle shape.<sup>[163]</sup> The temperature at which maximum rate of nucleation takes place is 80°C.<sup>[163, 164]</sup> This indicates that the isothermal temperatures used for the study are nucleation controlled rather than diffusion controlled. Isothermal crystallization data were analyzed using the modified Avrami equation<sup>[165]</sup>

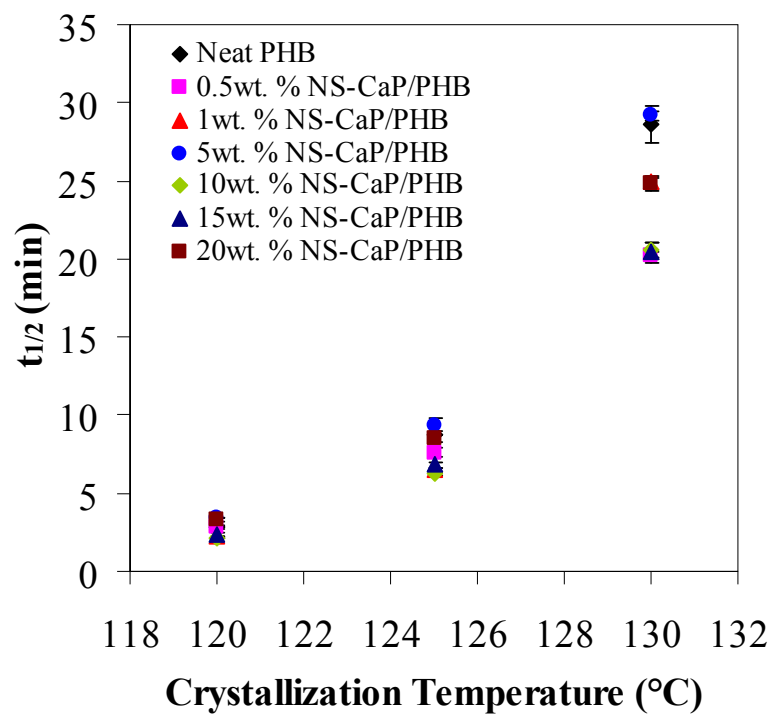
$$\ln(1-X_t) = - (Zt)^n \quad (4)$$

where  $Z$  is the crystallization rate constant,  $n$  is the Avrami exponent which relates to the mechanism of crystallization, and  $X_t$  is the relative crystallinity at time  $t$ . The values of  $Z$

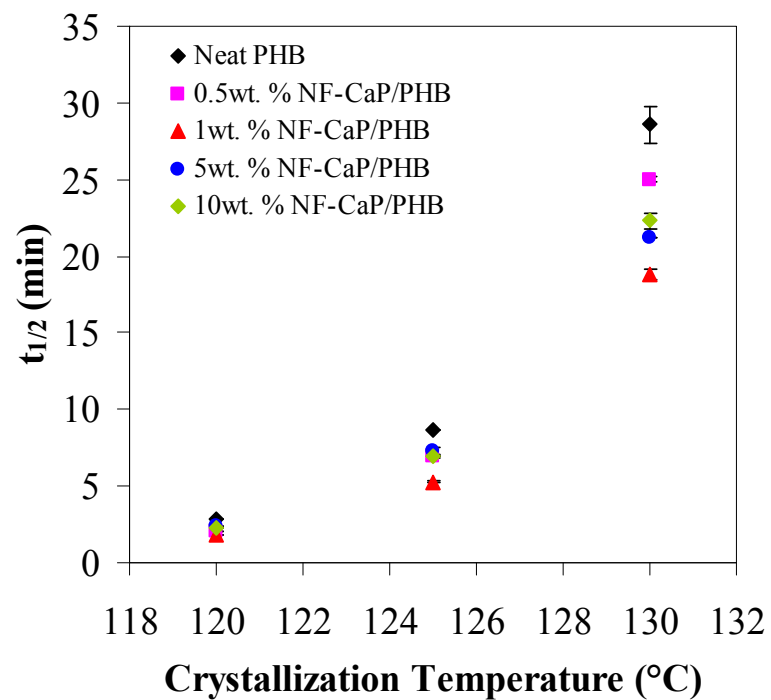


and  $n$  were obtained by plotting a graph of  $\ln(-\ln(1-X_t))$  against  $\ln(t)$ . The half time for crystallization,  $t_{1/2}$  was taken as the time required for 50% transformation to crystal.

Figure 5.9 shows the half-time crystallization as a function of crystallization temperature for neat PHB and NS-CaP/PHB and NF-CaP/PHB nanocomposites. As seen from the Figure 5.9a, all NS-CaP/PHB composites except 5 wt. % at all temperatures and 20 wt. % at one temperature had lower  $t_{1/2}$  than the neat PHB. 5 wt. % NS-CaP/PHB composite sample showed the highest  $t_{1/2}$  and hence the lowest rate of crystallization compared to other composites as well as neat PHB. This was consistent with the decrease in the peak  $T_c$  of 5 wt. % NS-CaP/PHB sample compare to neat PHB in the non-isothermal DSC experiments. The SEM images also showed the appearance of aggregates in the 5 wt. % NS-CaP/PHB composite sample. The size of the clusters was 300-500 nm and that of aggregates was 1-8  $\mu\text{m}$  for 5 wt. % NS-CaP composite and therefore the reduction in crystallization rate was attributed to the decrease in the surface area of the nanoparticles due to aggregation. The 20 wt. % NS-CaP/PHB composite sample showed the next highest  $t_{1/2}$  than the 5wt. % NS-CaP/PHB the trend again being consistent with the results of non-isothermal DSC and increase in aggregate size from SEM images. However, this decrease in crystallization kinetics was not observed for 10 and 15 wt. % NS-CaP/PHB nanocomposite samples. This behavior was found to be related to the variation in size distribution of the clusters and aggregates at all these concentrations as observed through SEM imaging. Both 1 and 10 wt. % NS-CaP/PHB composites showed



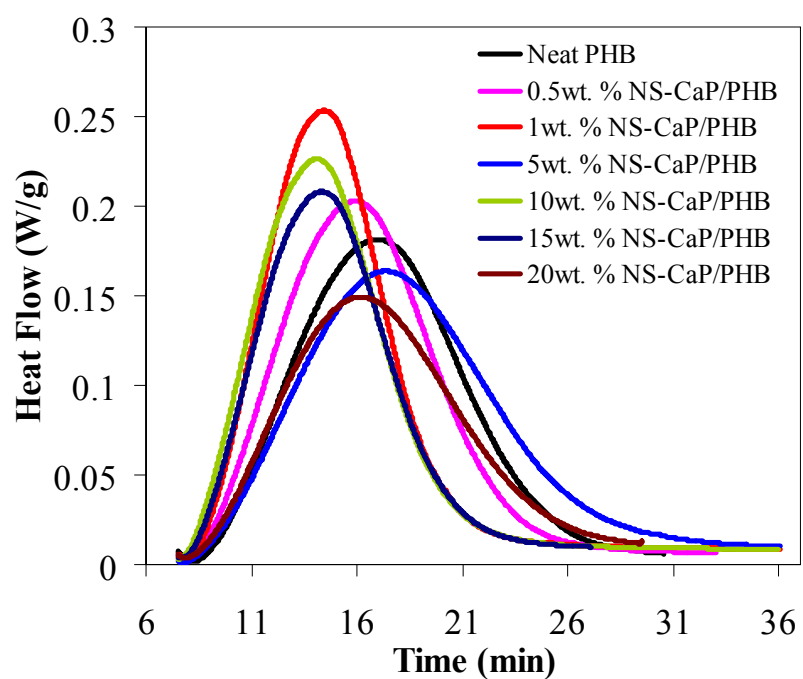
(a)



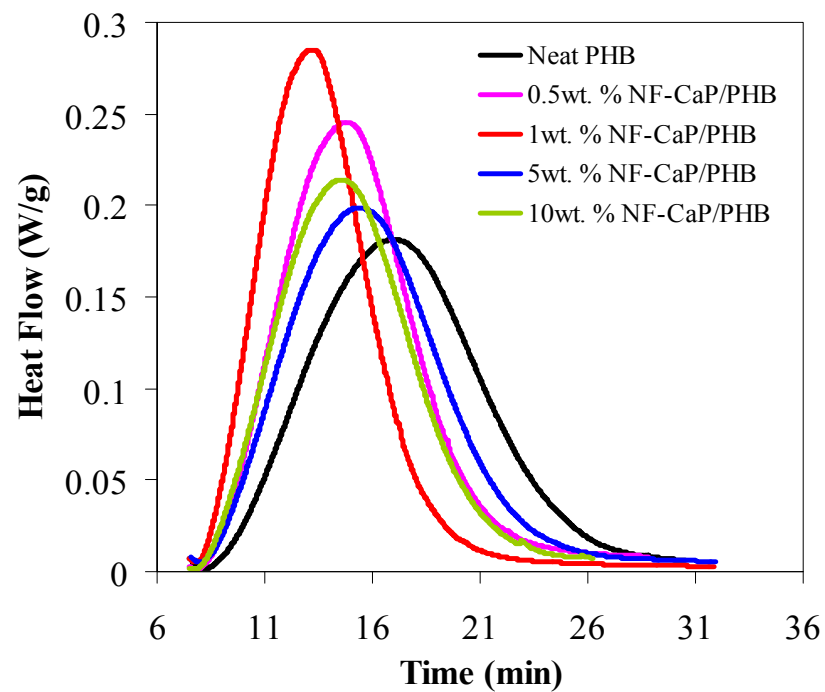
(b)

Figure 5. 9. Half-time crystallization of (a) NS-CaP/PHB and (b) NF-CaP/PHB nanocomposites samples as a function of crystallization temperature.

the lowest  $t_{1/2}$  at the crystallization temperatures of 120 and 125°C followed by 15 and then 0.5 wt. % NS-CaP/PHB composite samples. At 130°C, the lowest  $t_{1/2}$  was observed in 0.5, 10 and 15 wt. % NS-CaP/PHB samples followed by 1wt. % NS-CaP/PHB composite sample. Figure 5.10a shows the trends of NS-CaP/PHB composite compared to the neat PHB at the isothermal crystallization temperature of 125°C. Table 5.4 gives the actual values of the crystallization parameters  $n$ ,  $Z$  and  $t_{1/2}$ . In case of the NF-CaP/PHB nanocomposite system, all concentrations at all temperatures had a lower  $t_{1/2}$  and higher rate of crystallization than neat PHB. 1 wt. % NF-CaP/PHB composite had the fastest rate of crystallization and the lowest  $t_{1/2}$  at all temperatures followed by 0.5, 10 and 5 wt. % NF-CaP/PHB composite samples. 5 wt. % NF-CaP/PHB gave the highest  $t_{1/2}$  at 120 and 125°C and 10wt. % NF-CaP/PHB gave the highest  $t_{1/2}$  at 130°C. The trends in NF-CaP/PHB composite samples at the isothermal crystallization temperature of 125°C can be seen in Figure 5.10b. In comparing the two nanoparticle systems, except 10 wt. % NF-CaP/PHB at one temperature and 5 wt. % NF-CaP/PHB composite at two temperatures, all other NF-CaP composite samples had lower  $t_{1/2}$  and faster crystallization kinetics than NS-CaP/PHB composites. This is related to the nanoparticle shape. The spherical aggregates of needle like particles could also nucleate and enhance the crystallization kinetics as seen in Chapter 2. As the surface area of both nanoparticles is similar so these differences in crystallization kinetics are linked to the morphology or shape of the nanoparticles. Isothermal crystallization plots of NS-CaP/PHB and NF-CaP/PHB composites at 120 and 130 °C are given in Appendix D.



(a)



(b)

Figure 5. 10. Isothermal crystallization of (a) NS-CaP/PHB composites and (b) NF-CaP/PHB composites at 125°C.

Table 5. 4.Isothermal crystallization parameters for NS-CaP/PHB and NF-CaP/PHB nanocomposite samples at  $T_c = 120, 125$  and  $130^\circ\text{C}$ .

Conc. (wt. %)		Crystallization Temperature ( $^\circ\text{C}$ )		
		120	125	130
<b>0</b> <b>(Neat PHB)</b>	$n$	$2.7 \pm 0.0$	$2.6 \pm 0.0$	$2.6 \pm 0.0$
	$t_{1/2}$ (min)	$2.8 \pm 0.0$	$8.7 \pm 0.0$	$28.6 \pm 1.2$
	$Z(\text{min}^{-1})$	$3.2 \cdot 10^{-1} \pm 1.5 \cdot 10^{-3}$	$1.0 \cdot 10^{-1} \pm 2.3 \cdot 10^{-4}$	$3.0 \cdot 10^{-2} \pm 1.2 \cdot 10^{-3}$
<b>0.5 NS-CaP</b>	$n$	$2.6 \pm 0.0$	$2.6 \pm 0.0$	$2.6 \pm 0.0$
	$t_{1/2}$ (min)	$2.9 \pm 0.1$	$7.6 \pm 0.3$	$20.3 \pm 0.2$
	$Z(\text{min}^{-1})$	$3.1 \cdot 10^{-1} \pm 7.5 \cdot 10^{-3}$	$1.1 \cdot 10^{-1} \pm 3.7 \cdot 10^{-3}$	$4.3 \cdot 10^{-2} \pm 2.8 \cdot 10^{-4}$
<b>1 NS-CaP</b>	$n$	$2.7 \pm 0.0$	$2.7 \pm 0.0$	$2.8 \pm 0.0$
	$t_{1/2}$ (min)	$2.2 \pm 0.1$	$6.5 \pm 0.1$	$24.9 \pm 0.4$
	$Z(\text{min}^{-1})$	$4.0 \cdot 10^{-1} \pm 8.7 \cdot 10^{-3}$	$1.4 \cdot 10^{-1} \pm 1.5 \cdot 10^{-3}$	$3.5 \cdot 10^{-2} \pm 6.0 \cdot 10^{-4}$
<b>5 NS-CaP</b>	$n$	$2.6 \pm 0.0$	$2.6 \pm 0.0$	$2.5 \pm 0.0$
	$t_{1/2}$ (min)	$3.4 \pm 0.0$	$9.4 \pm 0.3$	$29.2 \pm 0.3$
	$Z(\text{min}^{-1})$	$2.6 \cdot 10^{-1} \pm 2.0 \cdot 10^{-3}$	$9.3 \cdot 10^{-2} \pm 3.6 \cdot 10^{-3}$	$3.0 \cdot 10^{-2} \pm 3.2 \cdot 10^{-4}$
<b>10 NS-CaP</b>	$n$	$2.7 \pm 0.0$	$2.4 \pm 0.0$	$2.6 \pm 0.0$
	$t_{1/2}$ (min)	$2.1 \pm 0.0$	$6.3 \pm 0.1$	$20.6 \pm 0.5$
	$Z(\text{min}^{-1})$	$4.1 \cdot 10^{-1} \pm 1.8 \cdot 10^{-3}$	$1.4 \cdot 10^{-1} \pm 3.1 \cdot 10^{-3}$	$4.2 \cdot 10^{-2} \pm 8.2 \cdot 10^{-4}$
<b>15 NS-CaP</b>	$n$	$2.6 \pm 0.0$	$2.6 \pm 0.0$	$2.5 \pm 0.0$
	$t_{1/2}$ (min)	$2.4 \pm 0.1$	$6.8 \pm 0.2$	$20.4 \pm 0.6$
	$Z(\text{min}^{-1})$	$3.6 \cdot 10^{-1} \pm 1.9 \cdot 10^{-2}$	$1.3 \cdot 10^{-1} \pm 3.3 \cdot 10^{-3}$	$4.2 \cdot 10^{-2} \pm 1.3 \cdot 10^{-3}$
<b>20 NS-CaP</b>	$n$	$2.6 \pm 0.0$	$2.6 \pm 0.0$	$2.5 \pm 0.0$
	$t_{1/2}$ (min)	$3.3 \pm 0.1$	$8.5 \pm 0.2$	$24.8 \pm 0.5$
	$Z(\text{min}^{-1})$	$2.7 \cdot 10^{-1} \pm 1.0 \cdot 10^{-2}$	$1.0 \cdot 10^{-1} \pm 2.7 \cdot 10^{-3}$	$3.5 \cdot 10^{-2} \pm 4.9 \cdot 10^{-4}$
<b>0.5 NF-CaP</b>	$n$	$2.7 \pm 0.1$	$2.8 \pm 0.0$	$2.8 \pm 0.0$
	$t_{1/2}$ (min)	$2.0 \pm 0.0$	$7.0 \pm 0.0$	$25.0 \pm 0.2$
	$Z(\text{min}^{-1})$	$4.4 \cdot 10^{-1} \pm 5.3 \cdot 10^{-3}$	$1.3 \cdot 10^{-1} \pm 8.8 \cdot 10^{-4}$	$3.5 \cdot 10^{-2} \pm 1.5 \cdot 10^{-4}$
<b>1 NF-CaP</b>	$n$	$2.8 \pm 0.1$	$2.7 \pm 0.0$	$2.7 \pm 0.0$
	$t_{1/2}$ (min)	$1.8 \pm 0.0$	$5.3 \pm 0.1$	$18.8 \pm 0.3$
	$Z(\text{min}^{-1})$	$4.9 \cdot 10^{-1} \pm 1.3 \cdot 10^{-2}$	$1.6 \cdot 10^{-1} \pm 4.3 \cdot 10^{-3}$	$4.6 \cdot 10^{-2} \pm 8.7 \cdot 10^{-4}$
<b>5 NF-CaP</b>	$n$	$2.6 \pm 0.0$	$2.6 \pm 0.0$	$2.5 \pm 0.0$
	$t_{1/2}$ (min)	$2.4 \pm 0.0$	$7.3 \pm 0.2$	$21.2 \pm 0.0$
	$Z(\text{min}^{-1})$	$3.7 \cdot 10^{-1} \pm 1.4 \cdot 10^{-3}$	$1.2 \cdot 10^{-1} \pm 3.4 \cdot 10^{-3}$	$4.1 \cdot 10^{-2} \pm 1.2 \cdot 10^{-4}$
<b>10 NF-CaP</b>	$n$	$2.8 \pm 0.0$	$2.7 \pm 0.0$	$2.5 \pm 0.1$
	$t_{1/2}$ (min)	$2.3 \pm 0.0$	$6.9 \pm 0.1$	$22.3 \pm 0.5$
	$Z(\text{min}^{-1})$	$3.9 \cdot 10^{-1} \pm 2.3 \cdot 10^{-3}$	$1.3 \cdot 10^{-1} \pm 1.8 \cdot 10^{-3}$	$3.9 \cdot 10^{-2} \pm 5.9 \cdot 10^{-4}$

The parameter  $n$  which gives the mechanism of crystallization had value in the range of 2.4 – 2.8 for both NS-CaP as NF-CaP/PHB nanocomposites. Similar  $n$  values have been observed in nanocomposites of PHB with platelet shaped fillers.<sup>[168, 169]</sup> PHB is a high purity polymer as it is produced by bacteria and undergoes mostly homogenous nucleation through self-seeding, when not heated far above the melting point. Any impurities added to this polymer play the role of stabilizing the self-seeding process. The nucleating effect of these impurities vanishes when the polymer is heated to about 25-30 °C above the melting temperature.<sup>[163]</sup> It can be observed in both NS and NF-CaP/PHB composites that the  $n$  value does not change significantly. This is indicative of the fact that the nanoparticles are playing the same role as the impurities, and some of the polymer chains get adsorbed on the nanoparticle surface when in the melt. When the melt is cooled, these nanoparticles adsorbed with polymer act as stabilized nucleating agents and affect the crystallization kinetics instead of acting as heterogeneous nucleating agents.<sup>[163]</sup>

Table 5. 5.Rigid amorphous fraction (RAF) of NS-CaP/PHB and NF-CaP/PHB nanocomposites as a function of nanoparticle concentration.

<b>Nanoparticle Concentration (wt. %)</b>	<b>RAF% in NS-CaP/PHB Composites</b>	<b>RAF% in NF-CaP/PHB Composites</b>
0	7.6 ± 0.6	7.6 ± 0.6
0.5	8.4 ± 0.2	9.1 ± 0.2
1	5.4 ± 1.0	6.2 ± 0.7
5	9.0 ± 0.6	6.7 ± 0.6
10	8.2 ± 0.2	9.3 ± 0.2
15	9.5 ± 0.7	
20	9.2 ± 0.3	

Modulated DSC was used to determine the MAF for the neat PHB and NS and NF-CaP/PHB composites. Equation 2 was used then to determine the rigid amorphous fraction (RAF) of neat PHB and the composites. Table 5.5 gives the RAF of NS-CaP/PHB and NF-CaP/PHB composites along with neat PHB. The RAF of neat PHB was approximately 8%. The RAF for 0.5 and 10 wt. % NS-CaP/PHB composite was nearly same as the neat polymer whereas it decreased by 29% for 1 wt. % NS-CaP/PHB nanocomposite. The RAF increased for 15 and 20 wt. % NS-CaP/PHB nanocomposite by 25 and 21%, respectively. In case of the NF-CaP/PHB nanocomposites, both 0.5 and 10 wt. % composites showed an increase in the RAF by 20 and 22%, respectively whereas 1 and 5 wt. % showed a slight decrease compared to the neat PHB. 0.5 wt. % NF-CaP/PHB composite showed a higher RAF compared to 0.5 wt. % NS-CaP/PHB. Assuming the weight of composite as 1 gram, the weight of nanoparticles is 0.005 g and that of polymer is 0.995 g. The total surface area of 0.5 wt. % nanoparticles in the composite is  $0.25 \text{ m}^2$  (Surface area of both nanoparticle shapes is approximately  $50 \text{ m}^2/\text{g}$ ). The 1.5% increase in RAF of 0.5 wt. % NF-CaP/PHB composite compared to neat PHB constitutes about  $0.0126 \text{ cm}^3$  of the total volume of PHB assuming the RAF density is same as density of purely amorphous PHB<sup>[158]</sup> ( $1.18 \text{ g/cm}^3$ ). If the filler particles entirely contribute to this increase in RAF, then the thickness of the adsorbed polymer chains can be calculated by dividing the volume of RAF by the available surface area of nanoparticles in the composite. The thickness of the adsorbed polymer is approximately 51 nm which constitutes approximately 2 radius of gyrations ( $R_g$ ) of PHB.<sup>[204]</sup> This indicates that the some polymer is adsorbed or immobilized when the particles are well dispersed and amount of surface area available to polymer is same as the actual surface area of

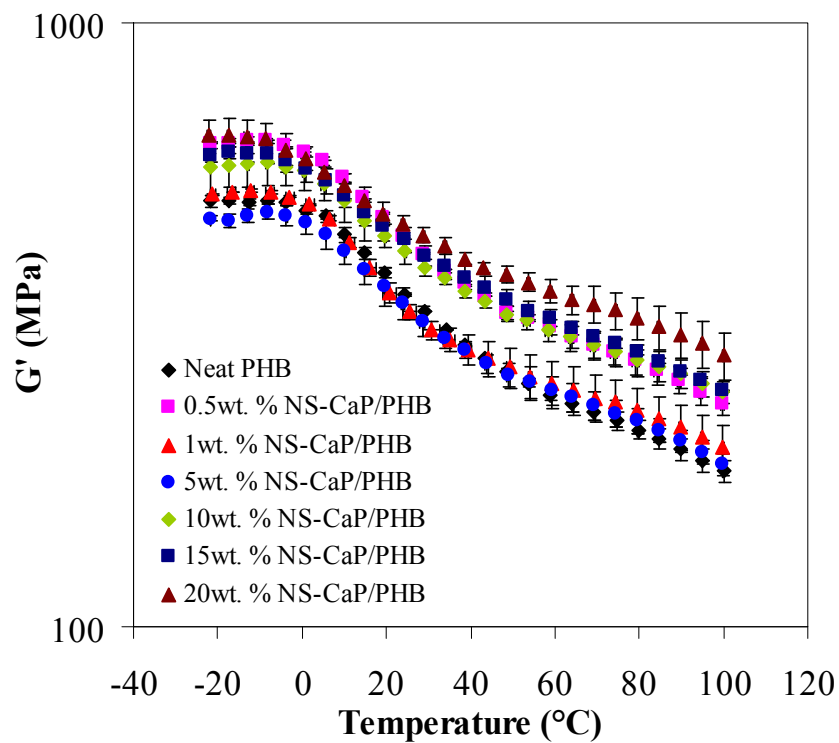
nanoparticles. The surface area decreases for 1 and 5 wt. % NF-CaP/PHB due to aggregation and RAF also shows a decrease. The differences in the RAF value between the 0.5 wt. % NF-CaP and 0.5 wt. % NS-CaP/PHB composite samples are attributed to the morphology of the nanoparticles as the dispersion characteristics are same for both composite samples. The crystallization kinetics results also showed that NF-CaP nanoparticles increased the crystallization rate of PHB as compared to NS-CaP nanoparticles. As the concentration of nanoparticles is increased in both NS-CaP and NF-CaP/PHB composites, the nanoparticles aggregate and the surface area decreases. However the RAF decreased more for 1 wt. % NS-CaP composite relative to neat PHB. The DSC experiments indicated that the crystallinity of the composites did not change significantly when compared to neat PHB and was within the experimental error. The melting temperatures of the composites and the neat PHB did not show large variations. This indicates that the changes in RAF observed in this study are related to the nanoparticle shape. The RAF increases for the composites with highest concentrations of nanoparticles in both cases. It is possible that after a certain nanoparticle concentration, the total surface area of clusters and aggregates reaches close to that of the dispersed nanoparticles leading to an increase in RAF. In this study we saw changes in RAF for low concentrations of nanoparticles, however, in other studies significant changes in RAF have been observed at filler concentrations above 20 wt. %. [205, 206]

#### **5.3.8. Viscoelastic Properties of Nanocomposites**

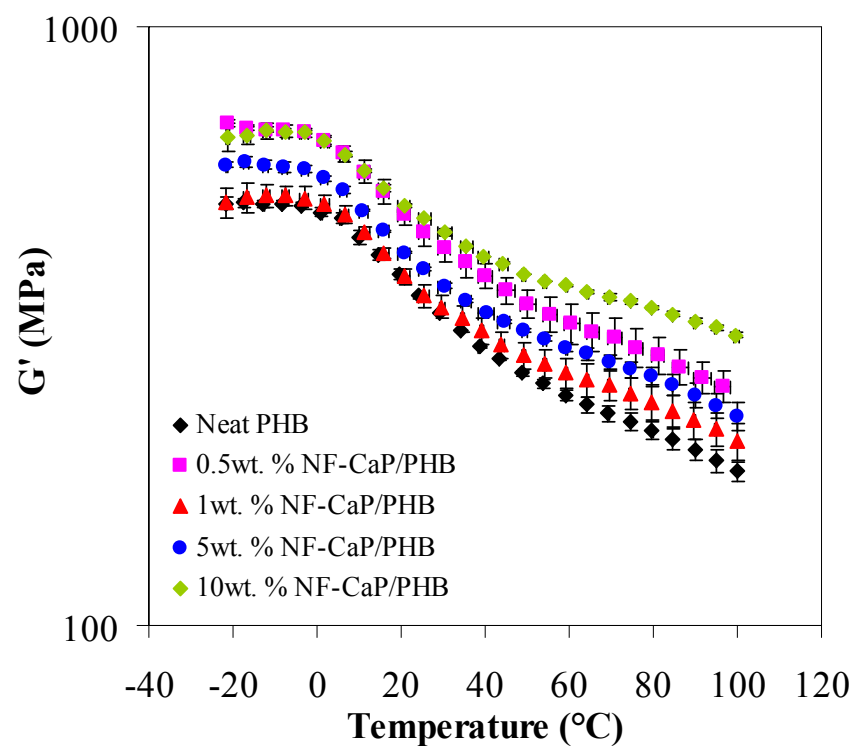
The thermomechanical properties of NS-CaP/PHB and NF-CaP/PHB composites indicated that the reinforcement was a function of both the morphology of the matrix and



that of nanoparticles as well as the inherent properties of the nanoparticles. Figure 5.11 shows the shear storage modulus  $G'$  of the NS-CaP/PHB and NF-CaP/PHB nanocomposites along with the neat PHB. The points in each figure represents average of  $G'$  value from temperature sweep test at 1 Hz and corresponding  $G'$  value at 1 Hz from a frequency sweep done at 5°C temperature intervals from -25 to 100°C. The error bar represents the deviation of data from the mean obtained from the two separate tests. The highest reinforcement 25°C below the  $T_g$  of the polymer matrix was observed for 0.5 and 20 wt. % NS-CaP/PHB and 0.5 and 10 wt. % NF-CaP nanocomposites. The  $G'$  showed an increase of approximately 28% for both 0.5 and 20 wt. % NS-CaP/PHB composites with respect to neat PHB whereas approximately 33% increase in  $G'$  was observed for both 0.5 and 10 wt. % NF-CaP/PHB nanocomposites 25°C below the  $T_g$  of the neat PHB. The increase in glassy modulus of 10 and 15 wt. % NS-CaP/PHB nanocomposites was nearly same to 0.5 and 20 wt. % composite samples when considering the experimental error. The reinforcement in the glassy modulus is related to both the inherent mechanical properties of the nanoparticles as well as the dispersion characteristics. The highest reinforcement for 0.5 wt. % in both near-spherical and nanofiber nanocomposites was found to be governed by the good dispersion of both type of nanoparticles at this concentration. The SEM images confirmed the homogeneous dispersion for both systems at 0.5 wt. %. The reinforcement at this concentration is attributed to the large amounts of surface area of nanoparticles as they are dispersed. The  $G'$  decreased for both 1 and 5wt. % NS-CaP/PHB and NF-CaP/PHB nanocomposites, and was nearly similar to neat PHB for 1 and 5 wt. % NS-CaP/PHB composite samples. However, 5 wt. % NF-CaP/PHB nanocomposite showed higher modulus compared to 5



(a)



(b)

Figure 5. 11. Shear storage modulus ( $G'$ ) values of neat PHB and (a) NS-CaP/PHB and (b) NF-CaP/PHB nanocomposite samples as a function of temperature. The points represent the average value of two separate experiment

wt. % NS-CaP/PHB nanocomposite. The drop in the modulus was associated with the aggregation of nanoparticles at these concentrations. The DSC experiments also showed decreased crystallization kinetics for 5 wt. % NS-CaP/PHB nanocomposite and the SEM also confirmed the presence of aggregates. However, the dispersion for 5 wt. % NF-CaP was better than the 5 wt. % NS-CaP nanocomposite and hence the drop in modulus was lower compared to NS-CaP composite. An increase in reinforcement of glassy modulus with particle concentration was not observed in both systems. SEM confirmed that the dispersion was good for low nanoparticle concentrations. Therefore, the reinforcement behavior below  $T_g$  was governed by the dispersion characteristics of the two nanoparticle systems.

The reinforcement behavior above the  $T_g$  of the polymer matrix for both nanoparticle systems shows some variations with nanoparticle concentration. The  $G'$  50°C above the  $T_g$  of the matrix increased by 29% for 0.5 wt. % NS-CaP/PHB nanocomposite with respect to neat PHB. The  $G'$  for 1 and 5 wt. % NS-CaP/PHB composites was similar to neat PHB when considering the experimental error. The 10 wt. % NS-CaP composite sample gave similar reinforcement of rubbery modulus as 0.5 wt. % NS-CaP/PHB composite. A 34 and 49% increase in  $G'$  with respect to neat PHB was observed for 15 and 20 wt. % NS-CaP/PHB composite samples, respectively. The drop in rubbery modulus for 1 and 5 wt. % NS-CaP/PHB composite samples was associated with the decrease in surface area of the nanoparticles due to aggregation at these concentrations. The increase in reinforcement for nanoparticle concentrations of 10 wt. % and above is due to the reduction in effective volume fraction of the matrix due to increase in the number of nanoparticle aggregates. Some variations in the distribution of

clusters and aggregates between NS-CaP nanoparticle concentrations as observed in SEM explain the differences in the reinforcement behavior for composites of this system. The reinforcement for 20 wt. % NS-CaP/PHB composite was higher compared to 10 and 15 wt. % composite samples. The calculated theoretical percolation threshold of rods of low aspect ratio is 0.087 vol. % or 24 wt. % <sup>[207-209]</sup> considering  $2.81 \text{ g/cm}^3$  as the density of NS-CaP nanoparticles. Therefore, the increase in modulus for 20 wt. % NS-CaP/PHB composite is attributed to the concentration of near-spherical nanoparticles approaching geometrical percolation or particle network.

In case of the NF-CaP/PHB nanocomposites the  $G'$  above  $T_g$ , increased by 32% for 0.5 wt. % NF-CaP composite sample with respect to neat PHB. 1 wt. % NF-CaP/PHB composite had slightly higher rubbery modulus than the neat PHB. An increase in  $G'$  of 22 and 55% with respect to neat polymer was observed for 5 and 10 wt. % NF-CaP/PHB nanocomposites, respectively. The increase in rubbery modulus of 0.5 wt. % NS-CaP and NF-CaP/PHB composites was approximately equal. However, the reinforcement at other concentrations for NF-CaP/PHB composites was higher compared to NS-CaP/PHB composites. The surface area of near-spherical and nanofiber nanoparticles is same ( $50 \text{ m}^2/\text{g}$ ), however, there are some differences in the aspect ratio between the two types of nanoparticles. The average aspect ratio for near-spherical nanoparticles is 2 whereas that of nanofibers is 28. Taking these differences of aspect ratio in consideration, the reinforcement in nanofiber composites should be higher than near-spherical nanocomposites. However, these differences have been considered as insignificant to cause reinforcement changes by both experimental and computational studies. Moreover, the true realization of aspect ratio in nanofibers was not observed as the size of

nanofibers reduced due to sonication leading to polydispersity in the effective aspect ratio ranging from 8-60. The theoretical percolation threshold for geometrical percolation for an aspect ratio of 28 considering a monodisperse population of nanofibers is approximately 4 vol. % or 8 wt. % considering the density of NF-CaP nanoparticles is  $2.22 \text{ g/cm}^3$ . If the polydispersity in the aspect ratio of nanofibers is considered, the percolation threshold is approximately 8.4 wt. %.<sup>[210]</sup> Therefore, the increase in reinforcement of the 10 wt. % NF-CaP/PHB composite was attributed to the increase in particle-particle interactions associated with the formation of a percolated particle network. The formulas used for calculating percolation thresholds are given in Appendix D.

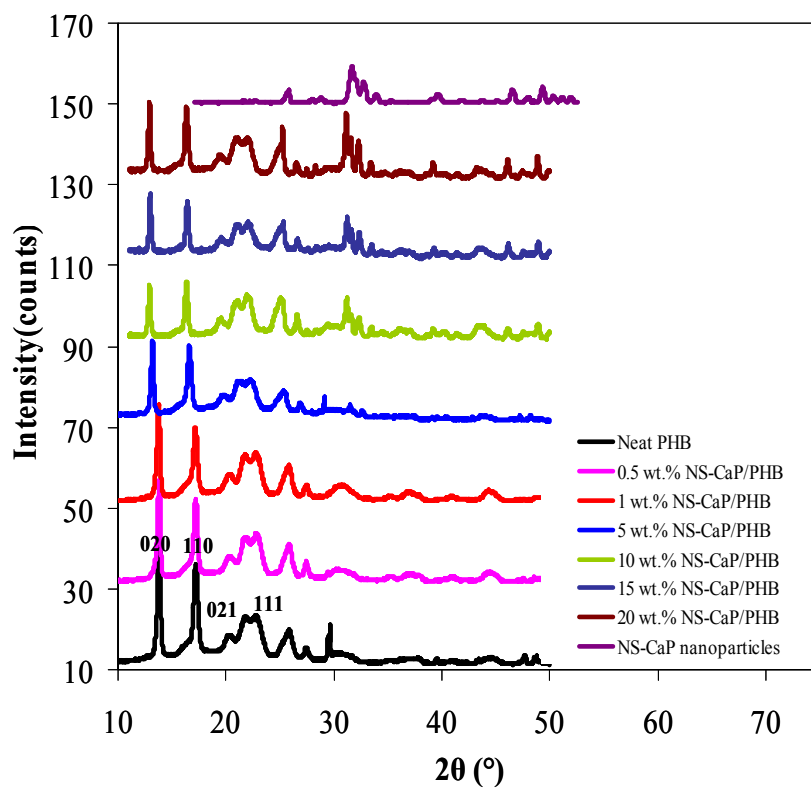
The overall reinforcement behavior of both nanoparticle systems was governed by the dispersion characteristics of the nanoparticles and the concentration in the nanocomposites. The nanoparticle shape played the role in controlling the threshold concentrations for geometrical percolation. The higher aspect ratio nanofibers having a lower threshold concentration for particle network compared to the near-spherical nanoparticles. The particle-polymer interactions were not seen to play a major role in reinforcement above 0.5 wt. % as the dispersion characteristics were not uniform with concentration for both nanoparticle shapes. The ratio of rubbery (65 °C) to glassy modulus (-10 °C) for NS-CaP/PHB nanocomposites was in the range of 0.47 to 0.52 for all concentrations and increased to 0.54 for 20 wt. % composite. Similarly, the ratio was 0.46-0.48 for 0.5, 1 and 5 wt. % NF-CaP/PHB composite and increased to 0.54 for 10 wt. % NF-CaP/PHB composite. The similar ratio of reinforcement for all concentrations in one system and also between systems, indicate that the reinforcement was governed by

the nanoparticle dispersion characteristics, concentration and particle-particle interactions. Another possible common observation for PHB composites in Chapter 4 and 5 is that the morphology of composites changes from bulk to particle network without undergoing formation of interphase network. This behavior is related to the morphology of the polymer matrix itself as well as the dispersion of nanoparticles. The crystallinity of the matrix is inversely related to the percolation threshold <sup>[156]</sup> and the formation of particle network seems to be governed by PHB crystallinity. The storage modulus curves of NS-CaP/PHB and NF-CaP/PHB at other frequencies (50, 10 and 0.1 Hz) are given in Appendix D.

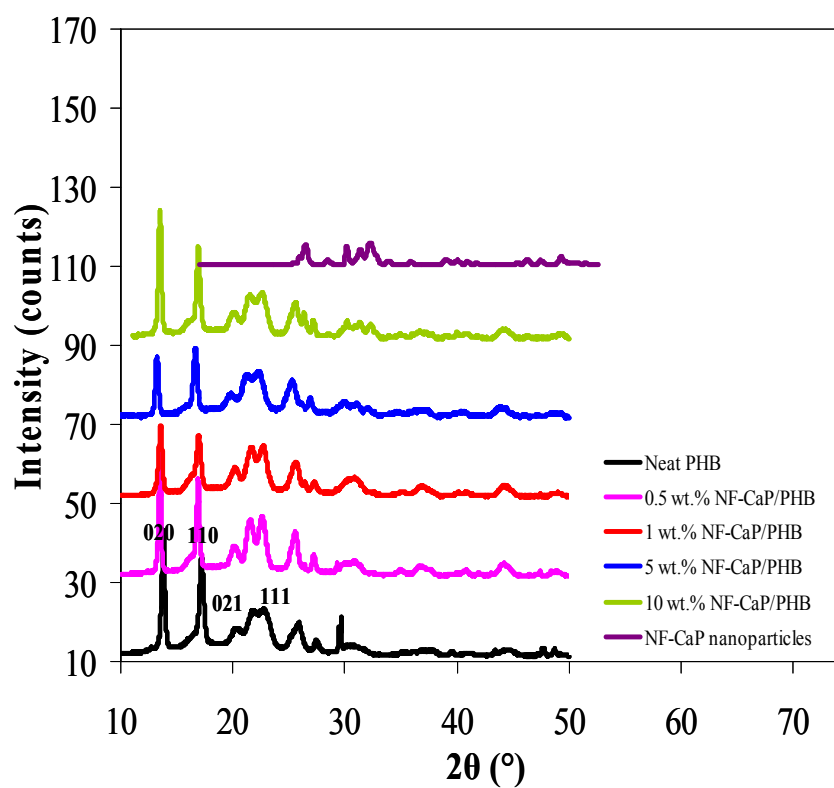
#### **5.3.9. X-ray Diffraction of Nanocomposites**

In order to observe any changes to the crystalline structure of PHB in presence of near-spherical or nanofiber nanoparticles, wide angle x-ray diffraction (WAXD) was performed on neat PHB and both NS-CaP and NF-CaP/PHB nanocomposite films. Figure 5.12 shows the WAXD patterns of neat PHB, NS-CaP/PHB and NF-CaP/PHB nanocomposites along with the diffraction patterns of pristine NS-CaP and NF-CaP calcium phosphate nanoparticles. Table 5.6 gives effect of addition of nanoparticles on the full width half maximum (FWHM) and crystalline lamella size for (020) and (110) reflections of PHB polymer. The characteristic reflections of neat PHB have been reported in the literature.<sup>[167, 211]</sup> The addition of both NS and NF-CaP nanoparticles did not change the unit cell of the PHB polymer and it crystallized in its typical crystalline form. Some changes in FWHM of (020) and (110) peaks for NS-CaP and NF-CaP/PHB nanocomposites compared to neat PHB indicated that the peaks were

mostly sharper compared to neat PHB. The crystallite size for the direction normal to (020) and (110) planes was calculated using Scherrer's equation. The crystallite size for the (020) reflection increased slightly for 5, 10, 15 and 20 wt. % NS-CaP/PHB and for 0.5 wt. % NF-CaP/PHB nanocomposites. Some variations in the crystallite size with nanoparticle concentration were also seen for the (110) reflection. A decrease in the crystallite size normal to planes has been associated with less ordered crystal structure and nanofiller confinement effects on crystal growth.<sup>[212]</sup> In this study, the changes observed in the crystallite sizes are not very significant which is in tandem with the DSC results. It was observed from the DSC results that the crystallinity as well as melting temperatures of both near-spherical and nanofiber composites were not changed significantly with the increase in nanoparticle concentration. Thus the DSC and the X-ray experimental results indicated that both type of nanoparticles did not influence the crystal structure of PHB.



(a)



(b)

Figure 5. 12.X-ray diffraction of (a) neat PHB, NS-CaP/PHB nanocomposites and NS-CaP nanoparticles, and (b) NF-CaP/PHB nanocomposites and NF-CaP nanoparticles. The figure also shows some major reflections of neat PHB.



Table 5. 6.Effect of NS-CaP and NF-CaP nanoparticles on the FWHM and crystallite size for (020) and (110) reflections.

<b>Samples</b>	<b>FWHM 020</b>	<b>Crystallite size (nm) 020</b>	<b>FWHM 110</b>	<b>Crystallite size (nm) 110</b>
Neat PHB	0.269 ± 0.003	30 ± 0	0.427 ± 0.002	19 ± 0
0.5 wt. % NS- CaP/PHB	0.250 ± 0.001	32 ± 0	0.373 ± 0.018	22 ± 0
1 wt. % NS- CaP/PHB	0.276 ± 0.008	29 ± 1	0.409 ± 0.002	20 ± 0
5 wt. % NS- CaP/PHB	0.230 ± 0.003	35 ± 0	0.407 ± 0.002	20 ± 0
10 wt. % NS- CaP/PHB	0.222 ± 0.003	36 ± 0	0.336 ± 0.002	24 ± 0
15 wt. % NS- CaP/PHB	0.230 ± 0.008	35 ± 1	0.301 ± 0.003	27 ± 0
20 wt. % NS- CaP/PHB	0.206 ± 0.019	39 ± 4	0.336 ± 0.005	24 ± 0
0.5 wt. % NF- CaP/PHB	0.191 ± 0.005	42 ± 1	0.378 ± 0.075	22 ± 4
1 wt. % NF- CaP/PHB	0.322 ± 0.005	25 ± 0	0.421 ± 0.003	19 ± 0
5 wt. % NF- CaP/PHB	0.255 ± 0.016	31 ± 2	0.398 ± 0.018	20 ± 1
10 wt.% NF- CaP/PHB	0.295 ± 0.012	27 ± 1	0.418± 0.000	19 ± 0

### 5.3.8 Micromechanical Modelling

The viscoelastic properties of NS-CaP/PHB and NF-CaP/PHB nanocomposites were modeled using modified Guth equation,<sup>[213]</sup> Cox model <sup>[214]</sup> and Halpin-Tsai micromechanical model for an isotropic composite containing discontinuous fibers.<sup>[215]</sup> The Halpin Tsai was used as predicted values were closer to experimental than other models. The equations used are given below as Equations 5-9.

$$G_{random} = \frac{1}{8} E_L + \frac{1}{4} E_T \quad (5)$$

$$E_L = \frac{1 + 2(l/d)\eta_L V_f}{1 - \eta_L V_f} E_m \quad (6)$$

$$E_T = \frac{1 + 2\eta_T V_f}{1 - \eta_T V_f} E_m \quad (7)$$

$$\eta_L = \frac{(E_f / E_m) - 1}{(E_f / E_m) + 2(l/d)} \quad (8)$$

$$\eta_T = \frac{(E_f / E_m) - 1}{(E_f / E_m) + 2} \quad (9)$$

The  $G_{\text{random}}$  is the shear modulus of the isotropic composite,  $E_L$  is the longitudinal elastic modulus of the composite,  $E_T$  is the transverse elastic modulus of the composite,  $E_f$  is the elastic modulus of the fiber take as 110 GPa<sup>[216]</sup> for NS-CaP and NF-CaP nanoparticles and is the highest value reported for HAp in literature, the shear modulus of the matrix was converted to the elastic modulus  $E_m$  using 0.4 as the Poisson's ratio,<sup>[217]</sup>  $l/d$  is the aspect ratio of the fiber and  $V_f$  is the fiber volume fraction. The volume fraction of the nanoparticles was calculated using density of polymer as 1.233 g/cm<sup>3</sup> for 0.5 wt. % NS-CaP/PHB and 1.232 g/cm<sup>3</sup> for 0.5 wt. % NF-CaP/PHB calculated from DSC corresponding to the crystallinity of the polymer in both composites, NS-CaP nanoparticles density of 2.81 g/cm<sup>3</sup> and NF-CaP nanoparticle density of 2.22 g/cm<sup>3</sup>. The  $G'$  value of 0.5 wt. % NS-CaP and NF-CaP/PHB nanocomposites at 25°C was compared to  $G_{\text{random}}$  obtained from the model by varying the aspect ratio keeping the concentration fixed at 0.5 wt. %. The mean aspect ratio ( $l/d$ ) of NS-CaP nanoparticles was 2 and that of NF-CaP nanoparticles was 28.

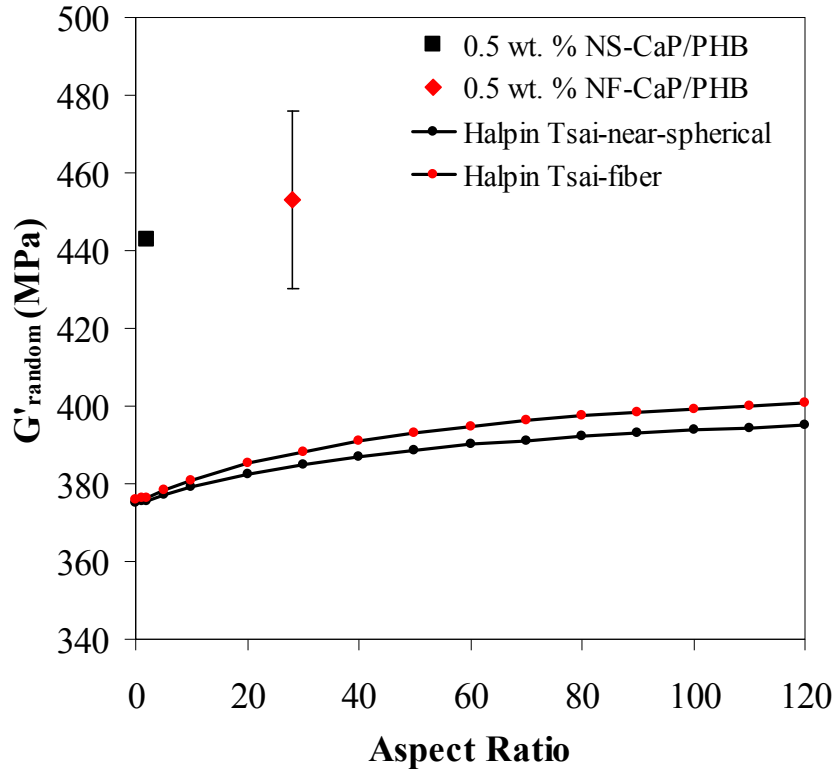


Figure 5. 13.Theoretical  $G'_{\text{random}}$  of 0.17 and 0.22 vol. % of NS-CaP and NF-CaP nanoparticles as a function of aspect ratio in comparison to experimental modulus  $G'$  at 25°C for 0.5 wt. % NS-CaP/PHB and NF-CaP/PHB nanocomposites.

Figure 5.13 shows the theoretical  $G'_{\text{random}}$  modulus of 0.5 wt. % NS-CaP and NF-CaP/PHB composites as a function of aspect ratio. The experimental  $G'$  modulus of 0.5 wt. % NS-CaP/PHB and NF-CaP/PHB composite is also shown in the Figure. It can be observed that the modulus values for both composites at 0.5 wt. % concentration were higher than the model predicted values. However, between the two nanoparticle shapes, the modulus does not change significantly. For the aspect ratios considered, the micromechanics also predict similar values for modulus. Therefore, there is a qualitative agreement between the micromechanics modulus predictions for low aspect ratio

nanoparticles and the experimental modulus differences for near-spherical and nanofiber nanoparticles obtained in this study. The relatively lower predicted model values compared to the experimental modulus are related to the limitations of the micromechanical model. Similar observations of discrepancy in model predictions have been made for fiber and flake-like inclusions when the ratio of filler modulus to matrix modulus is very large, which was 110 in our case.<sup>[218]</sup> In addition, the Halpin Tsai model has been shown to underestimate the reinforcement potential of whisker and platelet reinforced polymers for moderate aspect ratios compared to numerical simulation predictions.<sup>[219]</sup>

#### **5.4. Conclusions**

Polymer nanocomposites containing calcium phosphate nanoparticles with similar surface area but differing in morphology were prepared and characterized for understanding the effect of nanoparticle shape on nanocomposite properties. Both crystallization kinetics and composite microstructure were found to be governed by the shape of the nanoparticles. Both near-spherical and fiber nanoparticles were well dispersed at 0.5 wt. % and homogeneously distributed at higher concentrations in the polymer matrix. The differences in the shape of nanoparticles did not reflect any changes to the crystallinity of the matrix. However, some variations in the crystallization temperatures observed in the near-spherical nanocomposites were attributed to the dispersion characteristics of the nanoparticles. The shape of the nanoparticles significantly influenced the crystallization kinetics of PHB such that nanofiber nanoparticles enhanced the crystallization kinetics more compared to near-spherical

particles. The changes in the RAF between the composites were also attributed to the morphology differences in the particles. Both systems showed significant reinforcement in glassy and rubbery modulus at the lowest nanoparticle concentration of 0.5 wt. % attributed to the higher surface area available due to good dispersion. The reinforcement at higher concentrations was a function of the dispersion characteristics of nanoparticles in both systems. Enhanced rubbery reinforcement at the highest nanoparticle concentrations was attributed to formation of the particle-particle network near 20 wt. % in near-spherical and 8.4 wt. % in nanofiber composite system. Therefore, the shape of nanoparticles not only influenced the crystallization kinetics of PHB but also controlled the threshold percolation concentrations for particle network formation which was low for fiber and higher for near-spherical nanoparticles.

## **CHAPTER 6**

### **CONCLUSIONS AND FUTURE RECOMMENDATIONS**

#### **6.1. Conclusions**

The following section gives the overall conclusions of this work. The conclusions of this work are limited to the processing as well as experimental conditions used in this work and the results obtained thereby.

##### **6.1.1. Chapter 3 – Effect of Nanoparticle Surface Area**

- Effect of nanoparticle surface area on the properties of the nanocomposites was investigated by synthesizing HAp nanoparticles of controlled surface areas 60 and 111 m<sup>2</sup>/g and processing into nanocomposites using PCL as the matrix.
- The thermal transitions and the crystalline content of PCL were not affected by the differences in the surface area of nanoparticles indicating that the polymer-particle interfacial interactions were weakly attractive.
- The nanoparticles acted as nucleating agents and affected the crystallization kinetics of PCL at sufficient nanoparticle concentrations. However, as the crystalline morphology did not change significantly, the nucleating effect of nanoparticles was due to increased polymer viscosity in presence of nanoparticles.
- The thermomechanical properties show a dependence on the surface area of the nanoparticles. The temperature dependent reinforcement indicated that the interaction of nanoparticles was mainly with the amorphous polymer chains and nanoparticles restricted the mobility of these polymer chains.

- The deviations from the micromechanics predictions and the discontinuous increase in modulus above  $T_g$  indicated the formation of interphase network at 5 wt. % HAp60 and at 10 wt. % HAp111/PCL composite. These differences in the concentrations of formation of interphase network were attributed to differences in dispersion characteristics.
- The reinforcement could be scaled with surface area in both amorphous and semi-crystalline composites with low aspect ratio nanoparticles and surface area can be used as a parameter for nanocomposite design and modeling of nanocomposite properties. However, this scaling does not appear to apply to semi-crystalline matrices with high crystallinity due to inadequate particle dispersion.

#### **6.1.2. Chapter 4 – Effect of Matrix Crystallinity**

- The effect of matrix crystallinity on the properties of nanocomposites was studied using similar filler but different matrices PCL and PHB, which differed by approximately 30 % in the amount of crystallinity. Spherical assemblies of HAp nanoparticles with surface area  $111 \text{ m}^2/\text{g}$  were used to design composites with PHB matrix.
- The amount of available mobile amorphous regions guided the particle distribution in both polymer matrices, particles being dispersed at all concentrations in PCL but dispersed at only lower concentrations in PHB.
- The nanoparticles were likely to be located in the amorphous regions of the matrix as the crystalline content of both polymer matrices did not change significantly with the increase in particle concentration.

- Because of the high purity of PHB, the nanoparticles acted as self-seeding nucleation stabilizers under the melting temperatures studied and hence significantly affected the thermal transitions and crystallization kinetics of PHB compared to PCL.
- The differences in the thermomechanical behavior of the two polymer systems were attributed to the different dispersion characteristics. The reduced amorphous content in PHB led to poor dispersion characteristics at higher concentrations and hence reduced interfacial strength due to decrease in surface area of particles.
- The matrix crystallinity guided the composite microstructure as in lower crystallinity matrix, it changed from bulk to interphase network whereas in high crystallinity matrix, it changed from bulk to particle network. Therefore, the matrix crystallinity controlled the particle distribution, reinforcement behavior and composite microstructure.

#### **6.1.3. Chapter 5 – Effect of Nanoparticle Shape**

- In order to understand the influence of nanoparticle shape on the nanocomposite properties, calcium phosphate nanoparticles with similar surface area but different shapes, near-spherical and fiber-like were synthesized and processed into composites using PHB as a matrix.
- Both nanoparticle shapes were dispersed at the lowest concentration and homogeneously distributed at higher concentrations in the polymer matrix. Some differences in dispersion characteristics between two shapes as well as between different concentrations were attributed to the variations in cluster and aggregate sizes.



- The crystallinity of the PHB was not affected significantly by the differences in the nanoparticle shapes which indicated that the interfacial interactions between polymer and both particle systems were weakly attractive.
- The crystallization kinetics were strongly impacted by nanoparticle shape, fiber calcium phosphate nanocomposites showed higher crystallization rate compared to near-spherical calcium phosphate nanocomposites. As the surface area of both type of nanoparticles was same, the elongated and high aspect ratio nanofibers acted as better self-seeding nucleation stabilizers than near-spherical nanoparticles.
- The changes in RAF between the composites were also in tandem with the crystallization kinetics and were influenced by the shape differences between the nanoparticles. The thickness of adsorbed polymer as determined by the increase in RAF in nanofiber composite was 2 times the  $R_g$  of PHB which also confirmed that the some amount of polymer is adsorbed or immobilized on the filler surface.
- The thermomechanical properties were governed by the dispersion characteristics of the nanoparticles. Both near-spherical and nanofiber composites showed highest reinforcement at 0.5 wt. %, attributed to the good dispersion of nanoparticles and hence higher effective surface area. At higher concentrations, the modulus was function of the dispersion characteristics of nanoparticles in the two systems and was related to the effective surface area available at that concentration. However, the thermomechanical properties were not as sensitive to the differences in shape as crystallization kinetics.

- The matrix crystallinity and nanoparticle shape showed a coupled effect in guiding the composite microstructure. The higher crystallinity of the matrix led to the formation of percolated particle network in both particle systems with higher aspect ratio nanofiber particles forming the network at lower concentration compared to the near-spherical nanoparticles.

#### *Impact on Possible Biomedical Applications*

Polymer nanocomposites are used as bone graft substitutes, tissue scaffolds, guided bone regenerative membranes and bone drug delivery as well as dental implants. Nanocomposites designed in this work can be used for implants which need enhancement in mechanical properties without changing any other properties such as crystallinity and degradation rate. Nanoparticles of fiber shape have been shown to be better in some biomedical applications than particles and the higher surface area of these particles can be utilized with even lower volume fractions. Moreover, the nanoparticle network formation in high crystallinity matrices can be made use in tissue engineering scaffolds as bone cell growth and proliferation may be guided through this network.

### **6.2. Recommendations for Future Work**

The nucleating effect of calcium phosphate nanoparticles and its affect on the crystallization kinetics of PHB should be examined and investigated using polarized optical microscopy. Moreover, the change in surface area of nanoparticles due to aggregation should be evaluated using more molecular level techniques such as neutron scattering and ultra small angle x-ray scattering. We have looked at the effect of nanoparticles of near-spherical and fiber shape which are low aspect ratio (2-30) nanoparticles. In future high aspect ratio (100-500) or more fiber nanoparticles should be

synthesized and their nanocomposite properties studied. In addition, effect of platelet shaped nanoparticles on properties of nanocomposites studied in order to have a comparison between, near-spherical, fiber and platelet shapes similar to silica, CNFs and clay morphologies of fillers. In future, properties of the annealed nanocomposite samples should also be characterized for comparison to this work.

It was examined in this work that the method employed for the synthesis of nanoparticles of controlled surface areas and shapes, required removal of organic matter like surfactants using centrifuge or calcination. This step for removing organic matter led to the formation of clusters and agglomerates of nanoparticles due to strong intermolecular forces which made it difficult to disperse these nanoparticles. In future, alternative methods for synthesis should be investigated such as use of block copolymer surfactants. This work looks at the effect of pristine nanoparticle surface area and shape on the properties of the nanocomposites and understanding the effect of the same particles with surface modification would be very informative.

## APPENDIX A

Table A. 1. Different phases of calcium phosphates, their chemical formulas, Ca/P ratios, density and crystal structure. <sup>[75, 220-222]</sup>

Compound	Chemical Formula	Ca/P ratio	Density	Crystal Structure
MCPM	$\text{Ca}(\text{H}_2\text{PO}_4)_2 \cdot \text{H}_2\text{O}$	0.5	2.23	Triclinic
MCPA	$\text{Ca}(\text{H}_2\text{PO}_4)_2$	0.5	2.58	Triclinic
DCPD	$\text{CaHPO}_4 \cdot 2\text{H}_2\text{O}$	1.0	2.32	Monoclinic
DCPA	$\text{CaHPO}_4$	1.0	2.89	Triclinic
OCP	$\text{Ca}_8(\text{HPO}_4)_2(\text{PO}_4)_4 \cdot 5\text{H}_2\text{O}$	1.33	2.61	Triclinic
ACP	$\text{Ca}_x\text{H}_y(\text{PO}_4)_z \cdot n\text{H}_2\text{O}$ , $n = 3-4.5$ ; 15–20% $\text{H}_2\text{O}$	1.2-2.2		N/A
CDHA	$\text{Ca}_{10-x}(\text{HPO}_4)_x(\text{PO}_4)_{6-x}$ $(\text{OH})_{2-x}$ ( $0 < x < 1$ )	1.5-1.67		
$\beta$ -TCP	$\beta$ - $\text{Ca}_3(\text{PO}_4)_2$	1.5	3.08	Rhombohedral
$\alpha$ -TCP	$\alpha$ - $\text{Ca}_3(\text{PO}_4)_2$	1.5	2.86	Monoclinic
HAp	$\text{Ca}_{10}(\text{PO}_4)_6(\text{OH})_2$	1.67	3.16	Monoclinic or Hexagonal
TTCP	$\text{Ca}_4(\text{PO}_4)_2\text{O}$	2.0	3.05	Monoclinic

## APPENDIX B

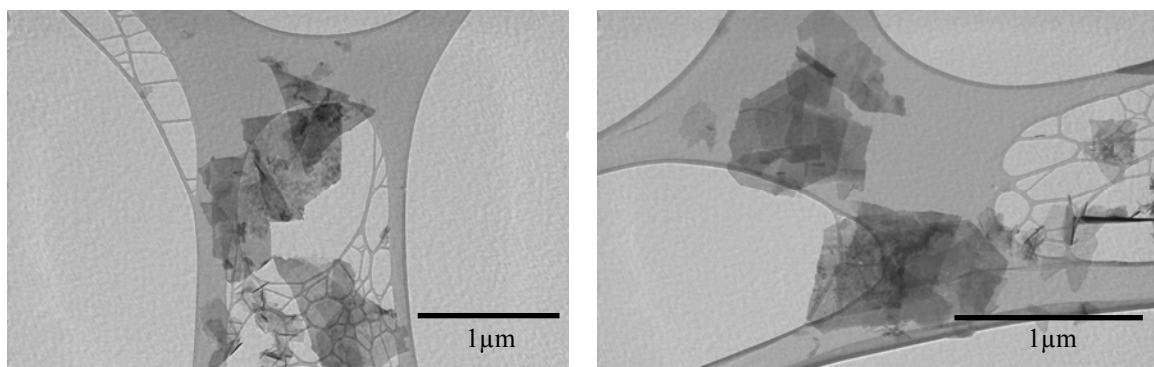


Figure B. 1. TEM images of HAp60 nanoparticles with platelet morphology.

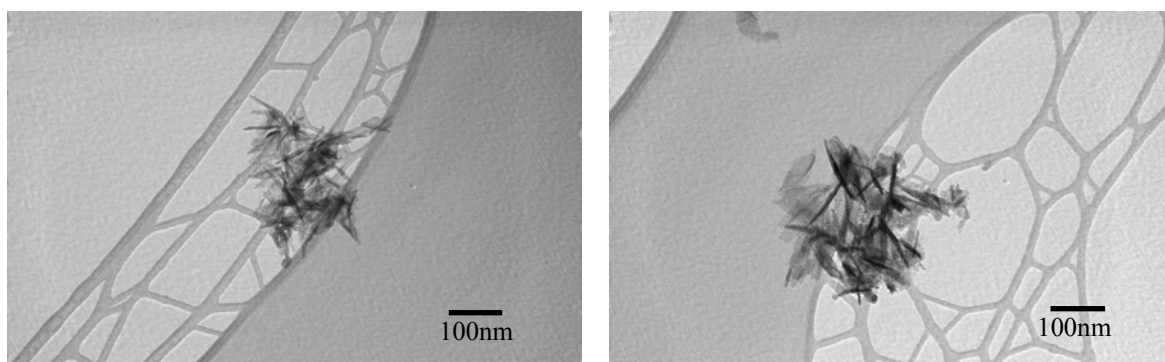


Figure B. 2. TEM images of HAp111 nanoparticles with spherical assemblies of needle-like nanoparticles.

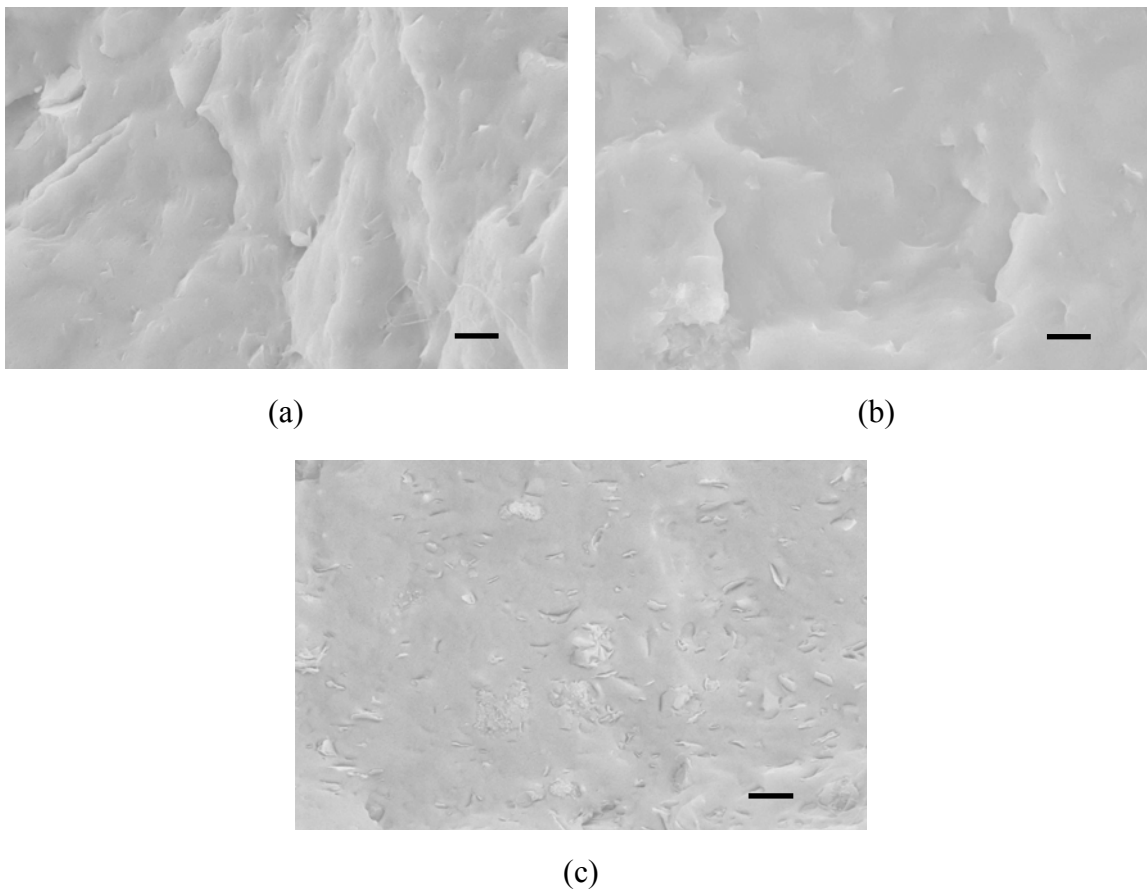


Figure B. 3. SEM images of (a) 0.5 wt. %, (b) 1 wt. % and, (c) 5 wt. % HAp60/PCL composites. The scale bar in all the images represents 2 $\mu$ m.

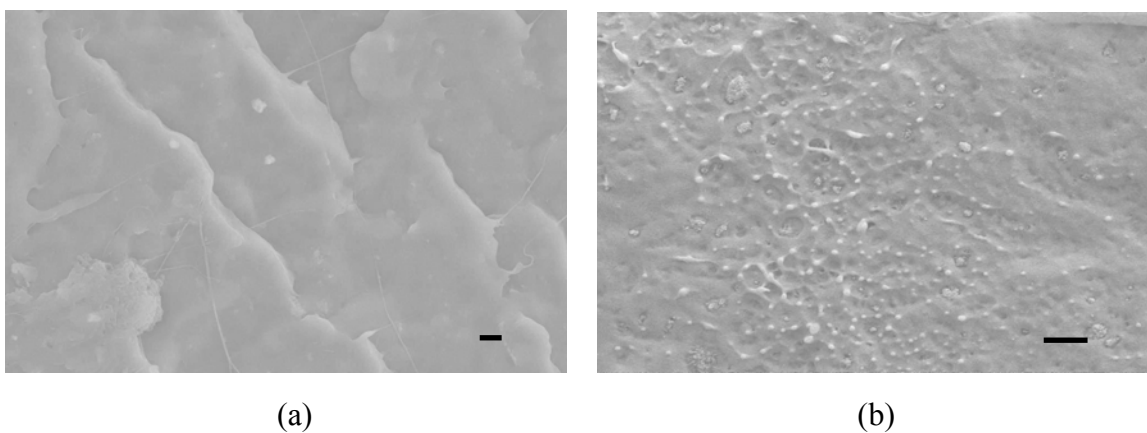


Figure B. 4. SEM images of (a) 0.5 wt. % and, (b) 5 wt. % HAp111/PCL composites. The scale bar in all the images represents 2 $\mu$ m.

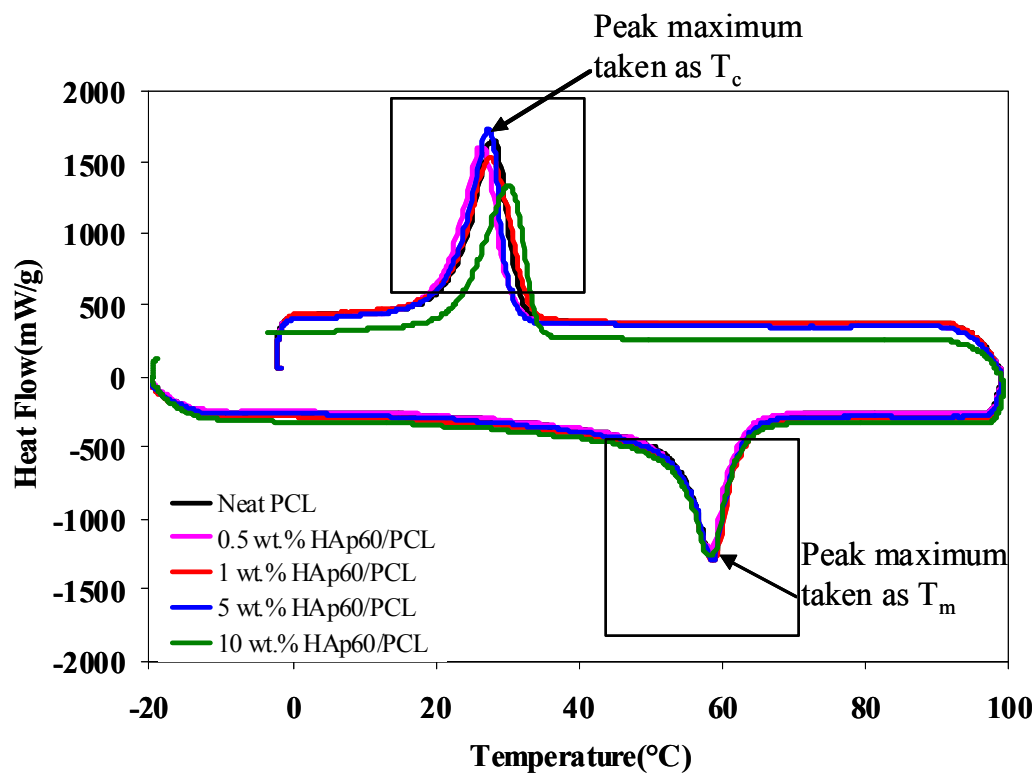


Figure B. 5.DSC first heating and cooling cycle of neat PCL and HAp60/PCL composites. The figure shows that the peak maximum was chosen for both crystallization and melting transitions.

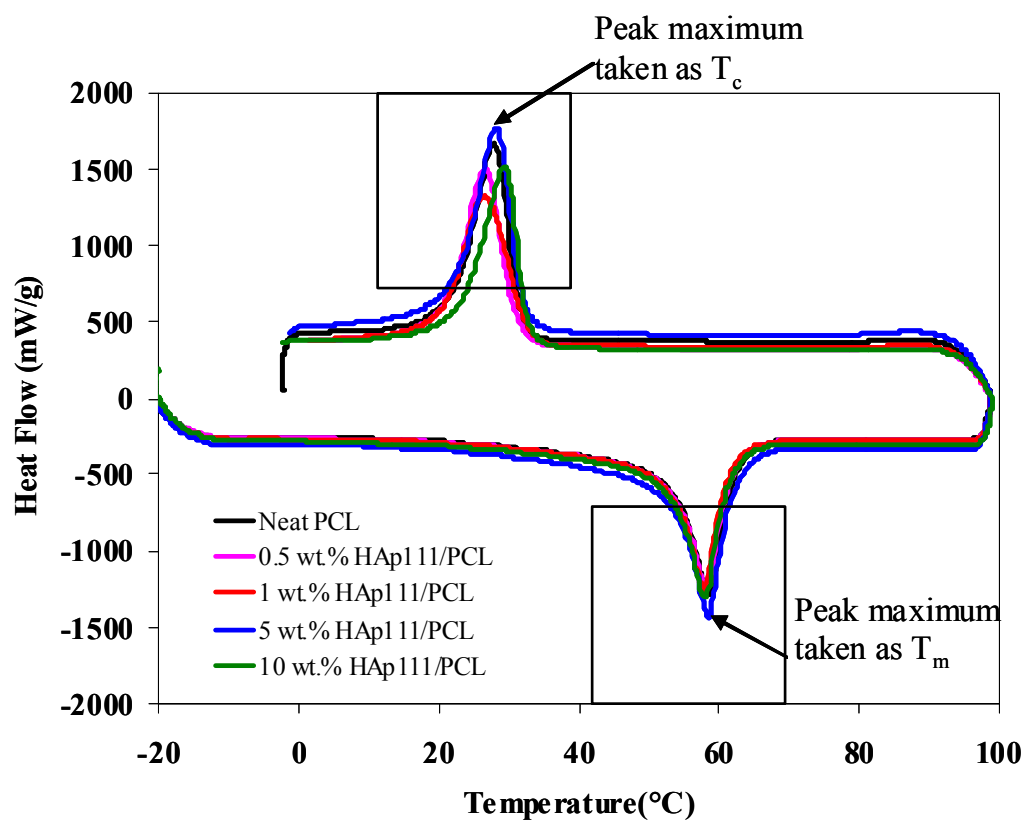


Figure B. 6.DSC first heating and cooling cycle of neat PCL and HAp111/PCL composites. The figure shows that the peak maximum was chosen for both crystallization and melting transitions.



Table B. 1. Isothermal crystallization parameters of neat PCL, HAp60 and HAp111/PCL composites at 40, 42, 44 and 46°C.

		T <sub>c</sub> (°C)		
		42	44	46
PCL-neat	t <sub>1/2</sub> (min)	5.4 ± 0.3	11.9 ± 0.2	30.0 ± 0.7
	<i>n</i>	2.7 ± 0.0	2.7 ± 0.0	2.9 ± 0.1
	<i>k</i> (min <sup>-1</sup> )	7.9·10 <sup>-03</sup> ± 9.1·10 <sup>-04</sup>	9.8·10 <sup>-04</sup> ± 4.9·10 <sup>-05</sup>	4.3·10 <sup>-05</sup> ± 7.8·10 <sup>-06</sup>
1 wt. % HAp60	t <sub>1/2</sub> (min)	4.3 ± 0.2	10.2 ± 0.4	23.9 ± 0.3
	<i>n</i>	2.5 ± 0.1	2.5 ± 0.0	2.8 ± 0.2
	<i>k</i> (min <sup>-1</sup> )	1.8·10 <sup>-02</sup> ± 2.6·10 <sup>-04</sup>	2.2·10 <sup>-03</sup> ± 3.1·10 <sup>-04</sup>	1.2·10 <sup>-04</sup> ± 5.8·10 <sup>-05</sup>
5 wt. % HAp60	t <sub>1/2</sub> (min)	5.7 ± 0.1	12.9 ± 0.3	30.0 ± 0.4
	<i>n</i>	2.4 ± 0.0	2.4 ± 0.0	2.7 ± 0.1
	<i>k</i> (min <sup>-1</sup> )	1.1·10 <sup>-02</sup> ± 2.6·10 <sup>-04</sup>	1.6·10 <sup>-03</sup> ± 1.1·10 <sup>-04</sup>	8.6·10 <sup>-05</sup> ± 2.8·10 <sup>-05</sup>
10 wt.% HAp60	t <sub>1/2</sub> (min)	5.2 ± 1.2	7.9 ± 0.4	22.1 ± 0.6
	<i>n</i>	2.1 ± 0.2	2.5 ± 0.0	2.6 ± 0.1
	<i>k</i> (min <sup>-1</sup> )	2.4·10 <sup>-02</sup> ± 5.8·10 <sup>-03</sup>	4.5·10 <sup>-03</sup> ± 4.2·10 <sup>-04</sup>	2.5·10 <sup>-04</sup> ± 6.1·10 <sup>-05</sup>
1 wt. % HAp111	t <sub>1/2</sub> (min)	5.1 ± 0.2	12.4 ± 1.6	29.7 ± 1.6
	<i>n</i>	2.6 ± 0.2	2.4 ± 0.1	2.7 ± 0.1
	<i>k</i> (min <sup>-1</sup> )	1.1·10 <sup>-02</sup> ± 5.4·10 <sup>-05</sup>	1.6·10 <sup>-03</sup> ± 0.0·10 <sup>+00</sup>	7.3·10 <sup>-05</sup> ± 8.0·10 <sup>-06</sup>
5. wt. % HAp111	t <sub>1/2</sub> (min)	5.1 ± 0.3	10.4 ± 0.1	24.7 ± 0.2
	<i>n</i>	2.6 ± 0.2	2.7 ± 0.0	2.7 ± 0.1
	<i>k</i> (min <sup>-1</sup> )	1.0·10 <sup>-02</sup> ± 8.2·10 <sup>-04</sup>	1.4·10 <sup>-03</sup> ± 2.8·10 <sup>-05</sup>	1.1·10 <sup>-04</sup> ± 2.3·10 <sup>-05</sup>
10 wt. % HAp111	t <sub>1/2</sub> (min)	4.1 ± 0.0	8.7 ± 1.0	20.5 ± 1.3
	<i>n</i>	2.3 ± 0.2	2.3 ± 0.1	2.4 ± 0.0
	<i>k</i> (min <sup>-1</sup> )	2.7·10 <sup>-02</sup> ± 1.3·10 <sup>-04</sup>	4.5·10 <sup>-03</sup> ± 6.1·10 <sup>-04</sup>	5.5·10 <sup>-04</sup> ± 5.2·10 <sup>-04</sup>

## APPENDIX C

Table C. 1. First and second heat crystallinity values of neat PHB and HAp111/PHB composites.

Samples	% Crystallinity First Heat	% Crystallinity Second Heat
Neat PHB	$71.1 \pm 0.6$	$68.9 \pm 1.3$
0.5 wt. % HAp111/PHB	$71.8 \pm 0.0$	$67.5 \pm 0.5$
1 wt.% HAp111/PHB	$68.3 \pm 0.2$	$68.4 \pm 0.3$
5 wt. % HAp111/PHB	$66.3 \pm 0.4$	$68.1 \pm 0.2$
10 wt. % HAp111/PHB	$68.3 \pm 0.2$	$66.9 \pm 0.6$

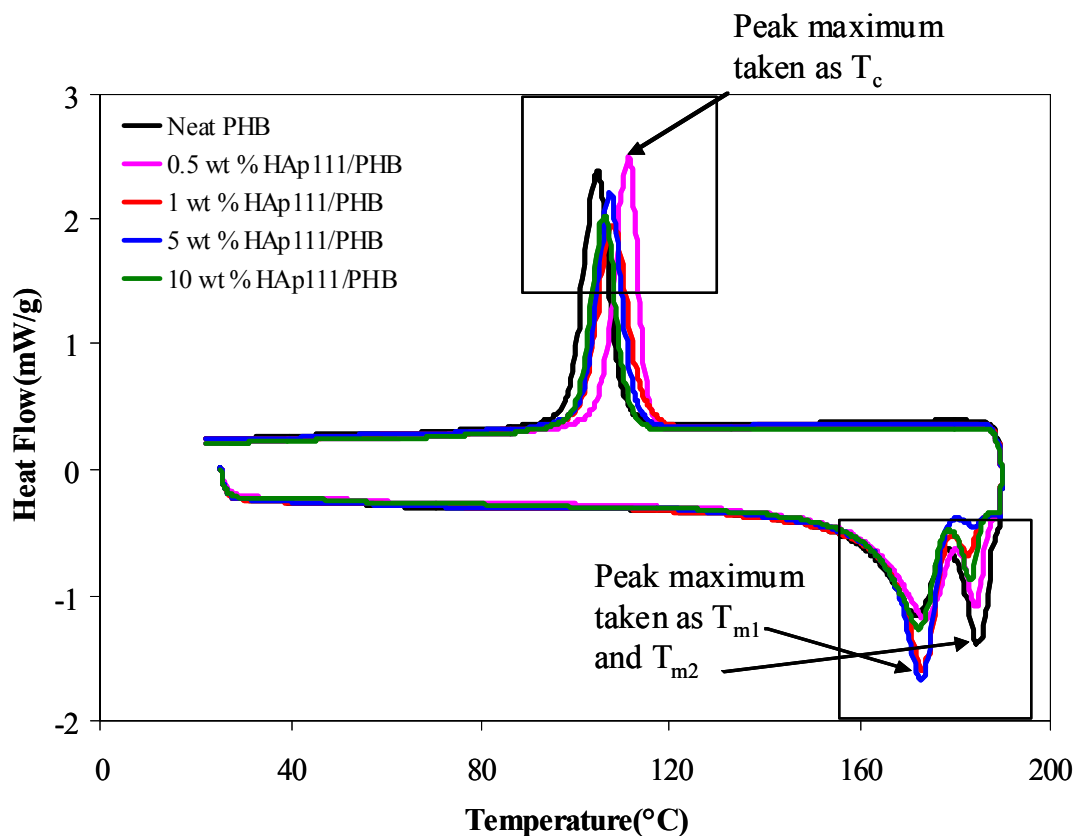


Table C. 2. Melting ( $T_m$ ) and crystallization ( $T_c$ ) temperatures of neat PHB and PCL and their composites with HAp111 nanoparticles from second heat.

Conc.	$T_m$ of PCL matrix composites	$T_m$ of PHB matrix composites	$T_c$ of PCL matrix composites	$T_c$ of PHB matrix composites
0 wt. %	$58.7 \pm 0.1$	$172 \pm 0.6$	$27.8 \pm 0.4$	$104 \pm 0.3$
0.5 wt. %	$58.0 \pm 0.3$	$174 \pm 0.3$	$26.3 \pm 0.4$	$111 \pm 0.0$
1 wt. %	$57.9 \pm 0.1$	$173 \pm 0.1$	$26.1 \pm 0.5$	$108 \pm 0.0$
5 wt. %	$58.2 \pm 0.4$	$172 \pm 0.1$	$28.2 \pm 0.7$	$107 \pm 0.0$
10 wt. %	$57.9 \pm 0.1$	$171 \pm 0.8$	$29.2 \pm 0.0$	$106 \pm 0.1$

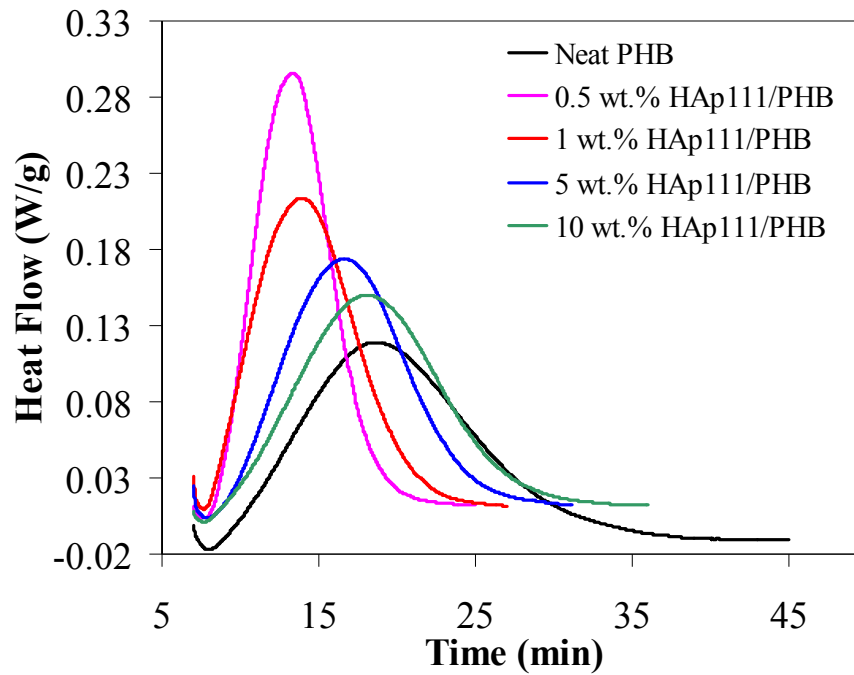


Figure C. 2. Isothermal crystallization of HAp111/PHB composites at 125 °C.

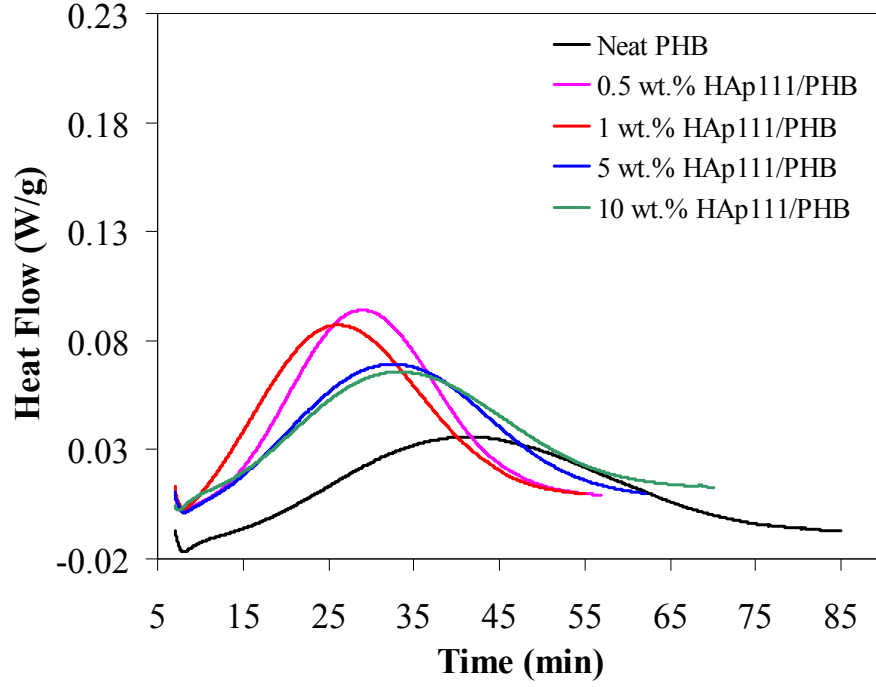


Figure C. 3. Isothermal crystallization of HAp111/PHB composites at 130 °C.

### Work of Adhesion

Strength of interaction between the filler and the polymer matrix can also be obtained from the reversible work of adhesion ( $W_{AB}$ ). The Dupre Equation relates  $W_{AB}$  to the surface tensions of the filler ( $\gamma_A$ ) and the polymer ( $\gamma_B$ ) as well as the interfacial tension ( $\gamma_{AB}$ ) between the two components.

$$W_{AB} = \gamma_A + \gamma_B - \gamma_{AB} \quad (2)$$

The interfacial tension ( $\gamma_{AB}$ ) can be calculated as,

$$\gamma_{AB} = \gamma_A + \gamma_B - 2(\gamma_A \gamma_B)^{1/2} \quad (3)$$

The dispersive components of surface tensions of PCL and PHB are 41<sup>[223]</sup> and 40.6<sup>[224]</sup> mJ/m<sup>2</sup> and that of HAp is 44 ± 2<sup>[225]</sup> mJ/m<sup>2</sup>. Using these numbers the  $W_{AB}$  for PCL and HAp is 84.9 ± 2 mJ/m<sup>2</sup> and for PHB and HAp is 84.5 ± 2 mJ/m<sup>2</sup>.

## APPENDIX D

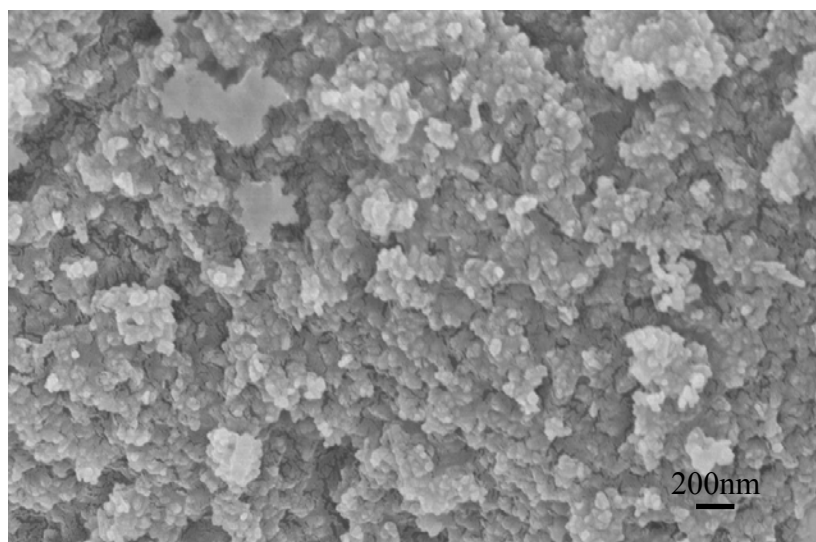


Figure D. 1. SEM image of near-spherical calcium phosphate (NS-CaP) nanoparticles.

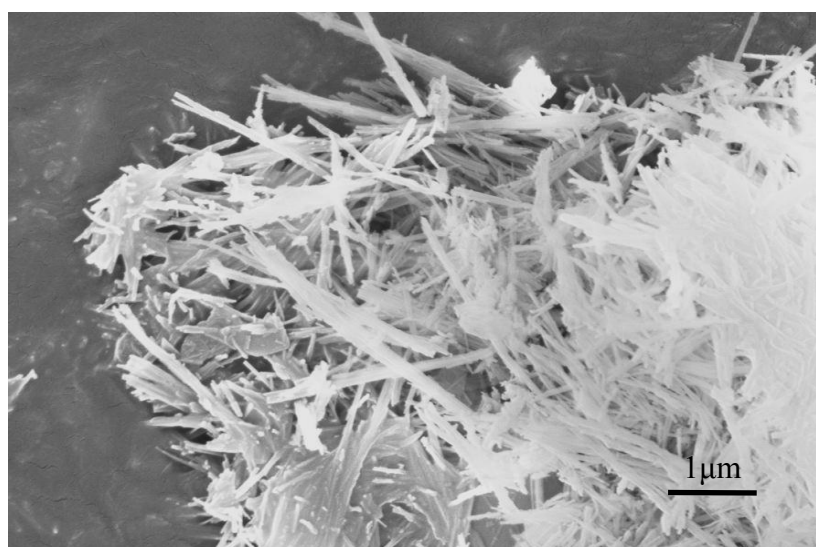


Figure D. 2. SEM image of nanofiber calcium phosphate (NF-CaP) nanoparticles.

Table D. 1.2 $\theta$  and d-spacing of NF-CaP nanoparticles from XRD scan in descending order of intensity compared to d-spacing from PDF card files of other phases of calcium phosphates.

<b>2 <math>\theta</math> (°)</b> <b>NF-CaP</b>	<b>d(Å)</b> <b>NF-CaP</b>	<b>d(Å)</b> <b>Monetite<sup>a</sup></b>	<b>d(Å)</b> <b>Calcium</b> <b>Phosphate<sup>b</sup></b>	<b>d(Å)</b> <b>Octacalcium</b> <b>phosphate<sup>c</sup></b>	<b>d(Å)</b> <b>CDHAp<sup>d</sup></b>	<b>d(Å)</b> <b>HAp<sup>e</sup></b>	<b>d(Å)</b> <b>Carbonate</b> <b>Apatite<sup>f</sup></b>	<b>d(Å)</b> <b>Chlorapatite<sup>g</sup></b>
32.252	2.773 (100)	-	2.770 (89)	2.779 (15)	2.781 (48)	2.778 (60)	2.780 (100)	2.779 (100)
26.484	3.363 (94.3)	3.370 (70)	3.368 (7)	-	-	-	-	-
30.147	2.962 (78.5)	2.958 (100)	-	-	-	-	-	-
31.376	2.849 (67.4)	2.843 (2)	2.854 (4)	-	-	-	-	-
25.973	3.428 (38.5)	-	-	3.424 (20)	-	-	-	-
32.839	2.725 (30.7)	2.721 (35)	-	-	2.726 (72)	2.720 (60)	-	-
30.364	2.940 (23.9)	2.937 (35)	-	2.946 (5)	-	-	-	-
46.245	1.962 (23.8)	1.959 (2)	1.957 (4)	1.957 (2)	-	-	-	1.964 (16)
49.243	1.849 (23.3)	1.850 (20)	-	1.848 (7)	-	-	-	-
53.024	1.726 (21.6)	1.725 (20)	1.728 (3)	-	-	1.722 (20)	-	-
39.007	2.307 (20.3)	2.305 (10)	-	2.304 (2)	-	-	-	-
28.489	3.131 (20)	3.130 (20)	3.125 (5)	3.132 (3)	-	-	-	-
47.496	1.913 (20)	1.915 (16)	1.911 (3)	1.914 (4)	-	-	-	1.912 (8)
33.921	2.641 (19.5)	-	-	2.637 (12)	-	-	-	-
49.475	1.841 (19.3)	-	-	-	1.842 (28)	1.841 (40)	1.838(16)	1.843 (16)
40.002	2.252 (18.7)	2.251 (16)	-	2.258 (2)	-	-	-	-

<sup>a</sup> PDF card file No. 00-009-0080

<sup>b</sup> PDF card file No. 00-050-0584

<sup>c</sup> PDF card file No. 00-026-1056

<sup>d</sup> PDF card file No. 00-046-0905

<sup>e</sup> PDF card file No. 00-009-0432

<sup>f</sup> PDF card file No. 00-019-0272

<sup>g</sup> PDF card file No. 00-027-0074

Table D. 2. 2 $\theta$  and d-spacing of NS-CaP nanoparticles from XRD scan in descending order of intensity compared to d-spacing from PDF card file of CDHAp (00-046-0905).

<b>2 <math>\theta</math> (°) NS-CaP</b>	<b>d(Å) NS-CaP</b>	<b>d(Å) Ca-deficient HAp<sup>d</sup></b>
31.71	2.82(100)	2.82(100)
32.79	2.73(54.9)	2.73(72)
31.38	1.85(41.5)	1.85(28)
49.37	1.95(36.7)	1.95(30)
25.84	3.45(33.3)	3.44(31)
39.67	2.27(24)	2.27(23)
33.92	2.64(22.6)	2.63(22)
50.39	1.81(16)	1.81(15)
47.92	1.90(14)	1.89(13)

Table D. 3. Percent crystallinity of neat PHB and NS-CaP/PHB composite samples from first and second heating cycles of DSC.

<b>Samples</b>	<b>% Crystallinity First Heat</b>	<b>% Crystallinity Second Heat</b>
Neat PHB	68.3 $\pm$ 0.7	67.7 $\pm$ 0.6
0.5 wt. % NS-CaP/PHB	67.3 $\pm$ 0.0	67.8 $\pm$ 0.1
1 wt.% NS-CaP /PHB	67.4 $\pm$ 0.3	67.2 $\pm$ 0.3
5 wt. % NS-CaP /PHB	66.5 $\pm$ 0.5	67.1 $\pm$ 0.0
10 wt. % NS-CaP /PHB	68.0 $\pm$ 0.3	67.9 $\pm$ 0.2
15 wt. % NS-CaP /PHB	67.2 $\pm$ 1.1	67.4 $\pm$ 0.3
20 wt. % NS-CaP /PHB	67.3 $\pm$ 0.0	66.9 $\pm$ 0.2

Table D. 4. Percent crystallinity of neat PHB, and NF-CaP/PHB composite samples from first and second heating cycles of DSC.

<b>Samples</b>	<b>% Crystallinity First Heat</b>	<b>% Crystallinity Second Heat</b>
Neat PHB	$68.3 \pm 0.7$	$67.7 \pm 0.6$
0.5 wt. % NF-CaP/PHB	$66.4 \pm 0.2$	$67.5 \pm 0.0$
1 wt.% NF-CaP /PHB	$68.8 \pm 0.2$	$68.3 \pm 0.4$
5 wt. % NF-CaP /PHB	$68.1 \pm 0.5$	$68.1 \pm 0.4$
10 wt. % NF-CaP /PHB	$68.1 \pm 0.7$	$67.4 \pm 0.9$

Table D. 5. Peak Melting ( $T_m$ ) and crystallization ( $T_c$ ) temperatures of neat PHB, NS-CaP/PHB and NF-CaP/PHB nanocomposites from second heating and cooling cycle.

<b>Conc. wt.%</b>	<b><math>T_m</math> of NS-CaP/PHB composites</b>	<b><math>T_m</math> of NF-CaP/PHB composites</b>	<b><math>T_c</math> of NS-CaP/PHB composites</b>	<b><math>T_c</math> of NF-CaP/PHB composites</b>
0	$173 \pm 0.6$	$173 \pm 0.6$	$109 \pm 0.6$	$109 \pm 0.6$
0.5	$172 \pm 0.3$	$172 \pm 0.2$	$108 \pm 0.2$	$110 \pm 0.4$
1	$173 \pm 0.4$	$173 \pm 0.5$	$110 \pm 0.3$	$111 \pm 0.0$
5	$170 \pm 1.3$	$172 \pm 0.4$	$107 \pm 0.3$	$109 \pm 0.0$
10	$171 \pm 0.0$	$171 \pm 0.7$	$109 \pm 0.1$	$109 \pm 0.0$
15	$170 \pm 0.6$		$109 \pm 0.2$	
20	$170 \pm 0.1$		$105 \pm 0.1$	



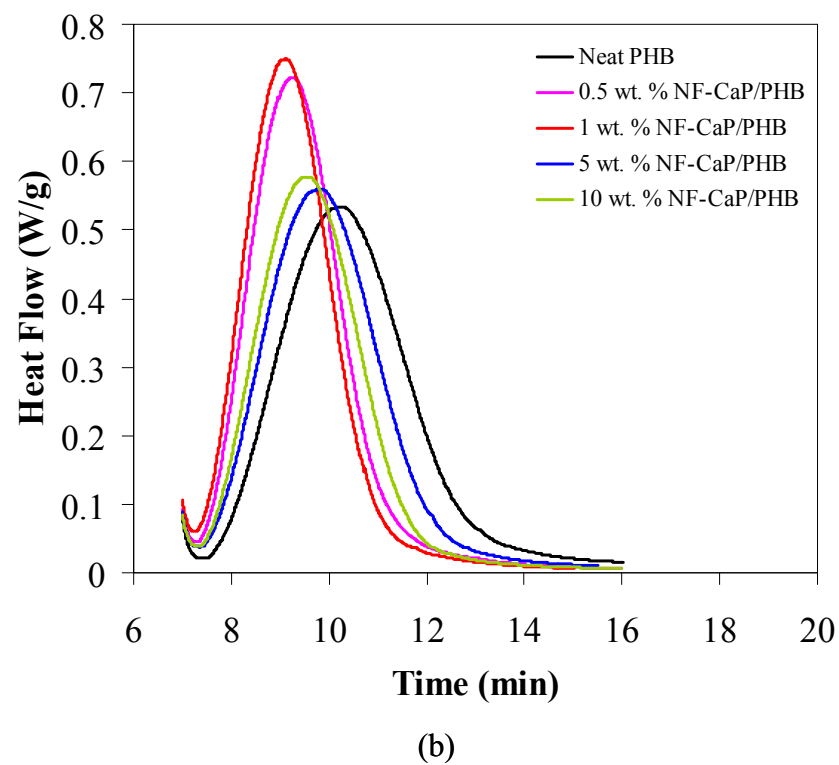
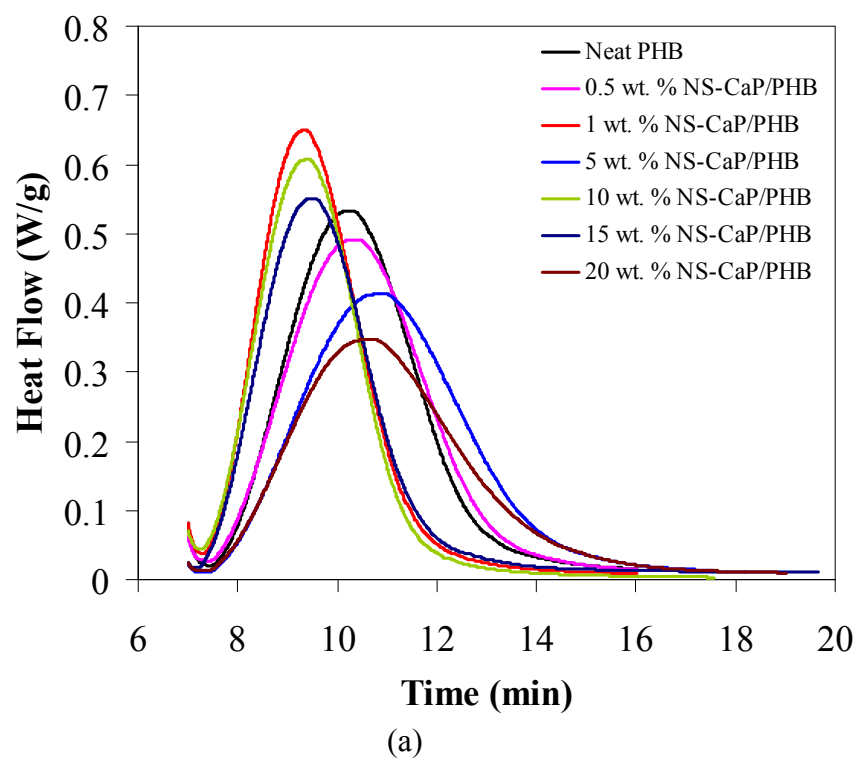


Figure D. 3. Isothermal crystallization of (a) NS-CaP/PHB composites and (b) NF-CaP/PHB composites at 120 °C.

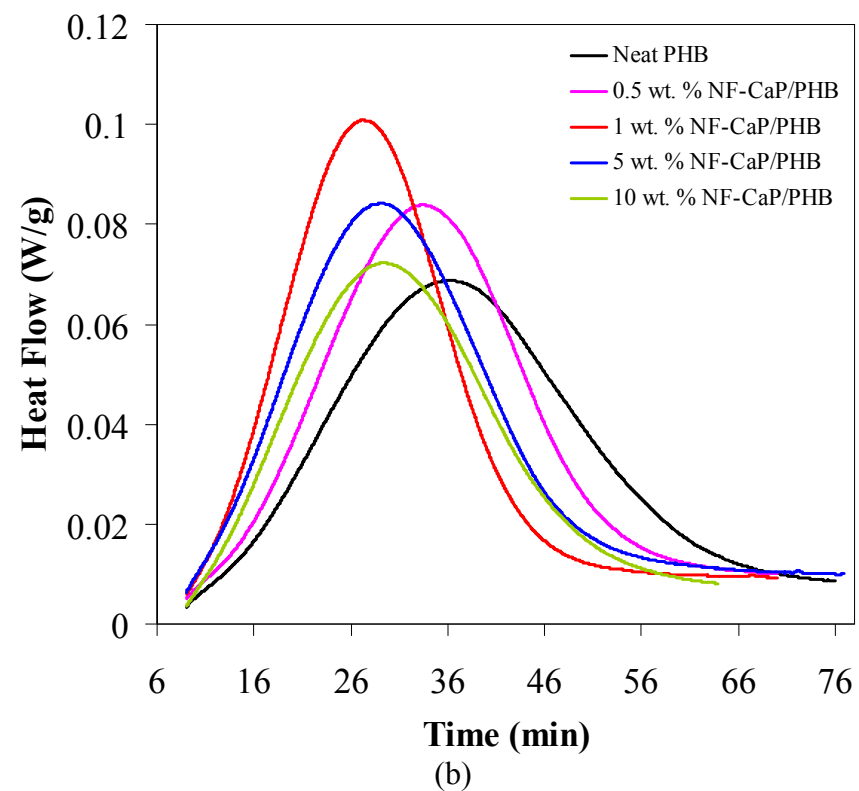
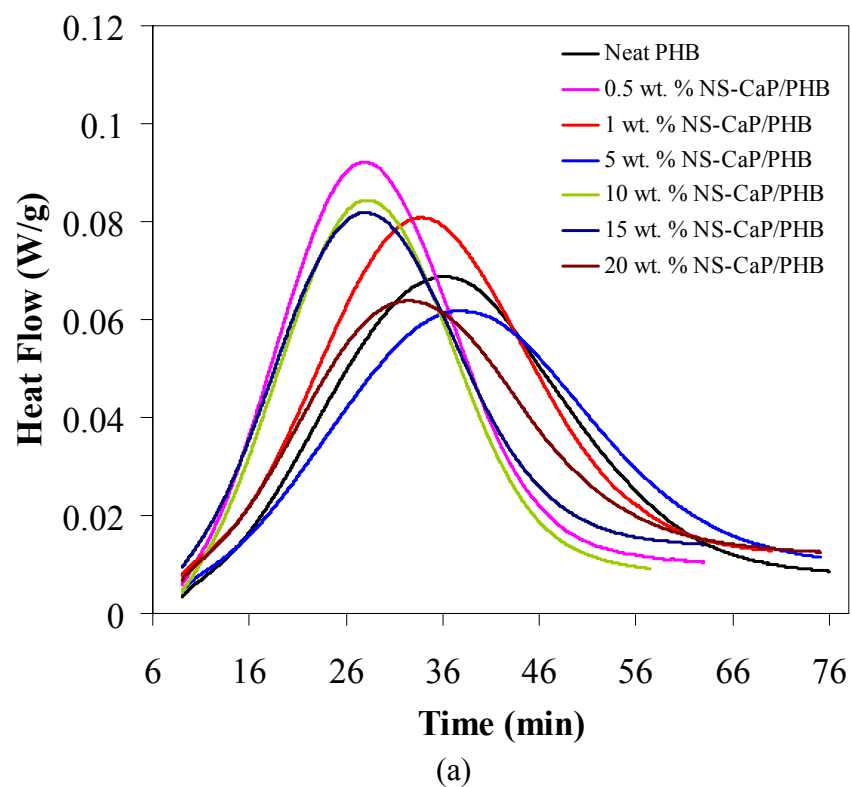


Figure D. 4. Isothermal crystallization of (a) NS-CaP/PHB composites and (b) NF-CaP/PHB composites at 130°C.

### Calculations for percolation threshold concentrations:

For NS-CaP/PHB composites, the following equations were used assuming particles to be short cylinders:

$$\phi_c = \frac{V}{V_{ex}} \quad (1)$$

$$\text{Where, } V = \frac{4\pi}{3} R^3 + \pi R^2 L \quad \text{and} \quad V_{ex} = \frac{32\pi}{3} R^3 \left[ 1 + \frac{3}{4} \left( \frac{L}{R} \right) + \frac{3}{32} \left( \frac{L}{R} \right)^2 \right]$$

$R = 17 \text{ nm}$  and  $L = 76 \text{ nm}$ .

For NF-CaP/PHB composites, the following equations were used:

$$\phi_{monodisperse} = \frac{2n_c (L_0 / R_0)}{\left[ \left( \frac{L_0}{R_0} \right)^2 + (\pi + 3) \left( \frac{L_0}{R_0} \right) + \pi \right]} \quad (2)$$

For polydisperse system,

$$\phi(R_0, L_1) = \frac{2n_c (L_n / R_0)}{\left\{ \left( \frac{L_1}{R_0} \right) \left[ \left( \frac{L_n}{R_0} \right) + \frac{(3 + \pi)}{2} \right] + \pi + \left( \frac{3 + \pi}{2} \right) \left( \frac{L_n}{R_0} \right) \right\}} \quad (3)$$

Where  $n_c = 0.6$  is the number of contacts per rod,  $L_n/R_0$  is the mean aspect ratio taken as 28 and  $L_l$  is the length of the rods (would change based on polydispersity) and  $R_0 = 22 \text{ nm}$ .

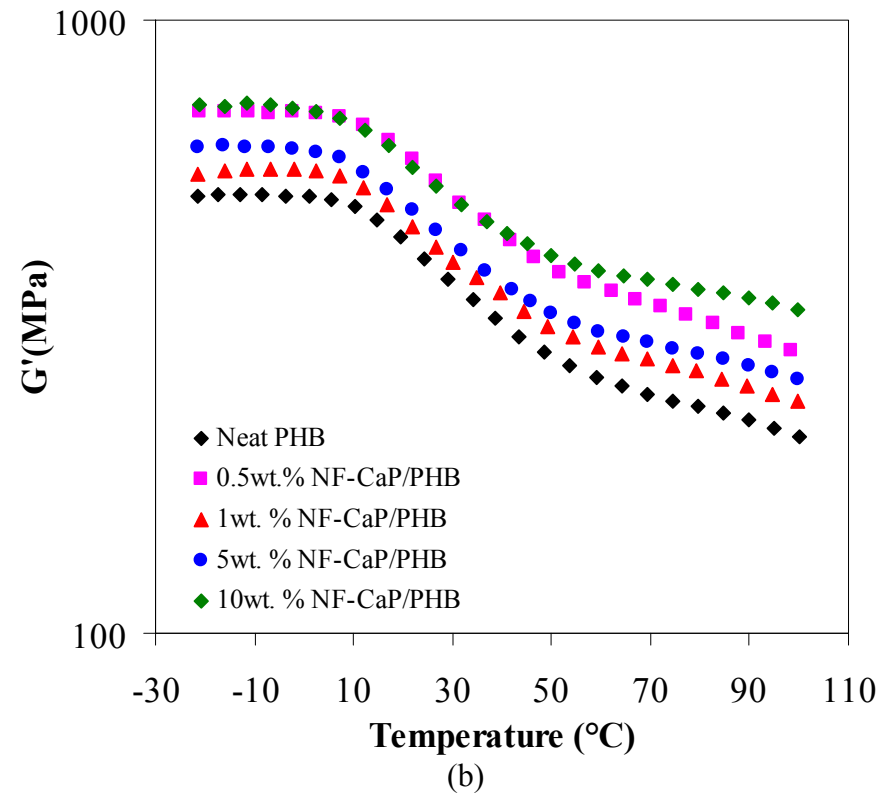
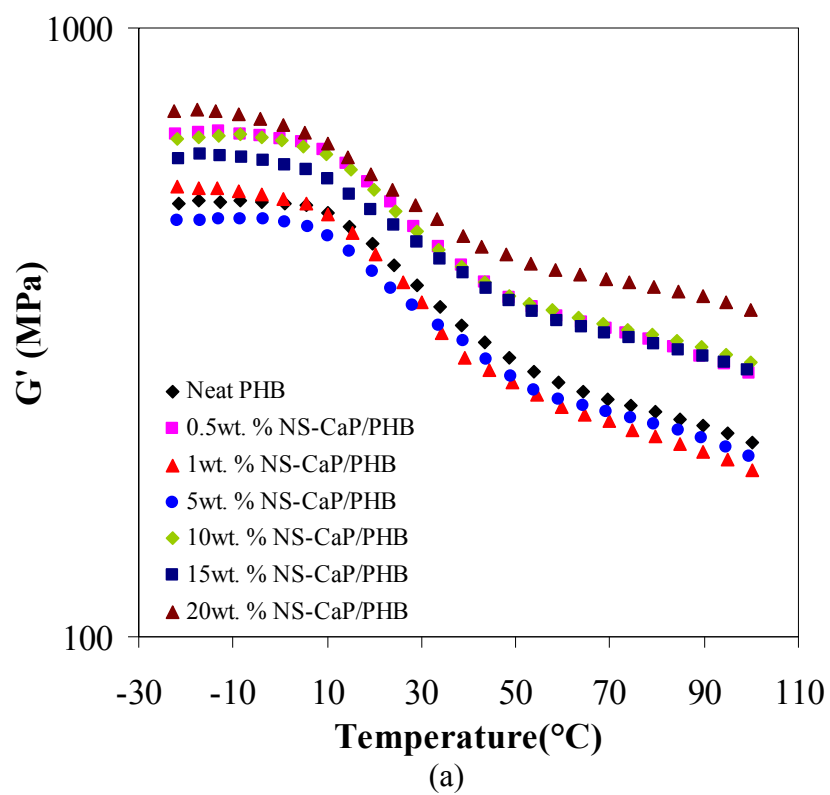
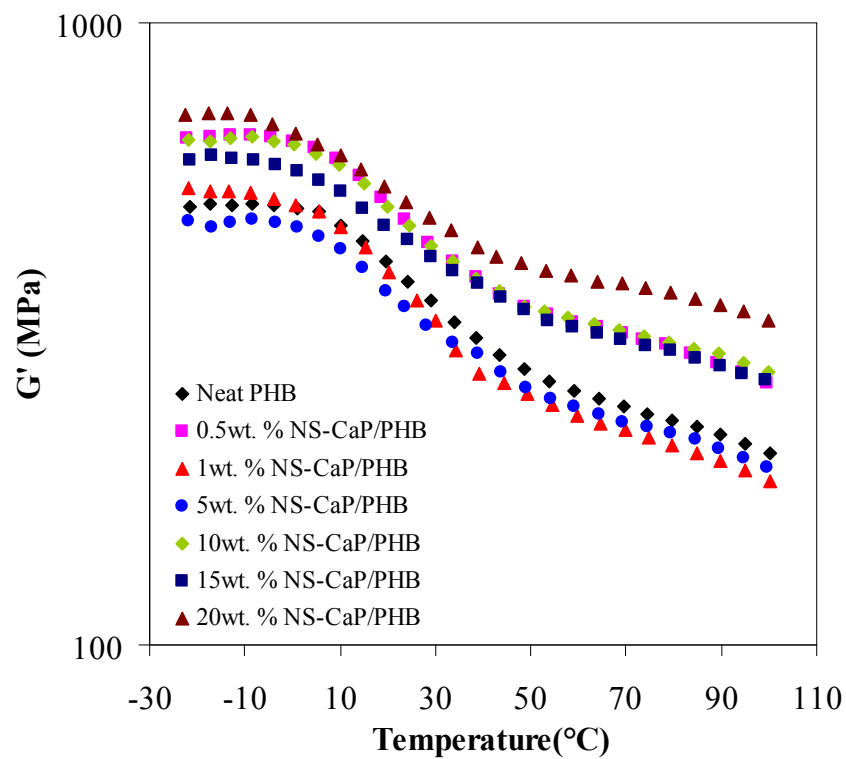
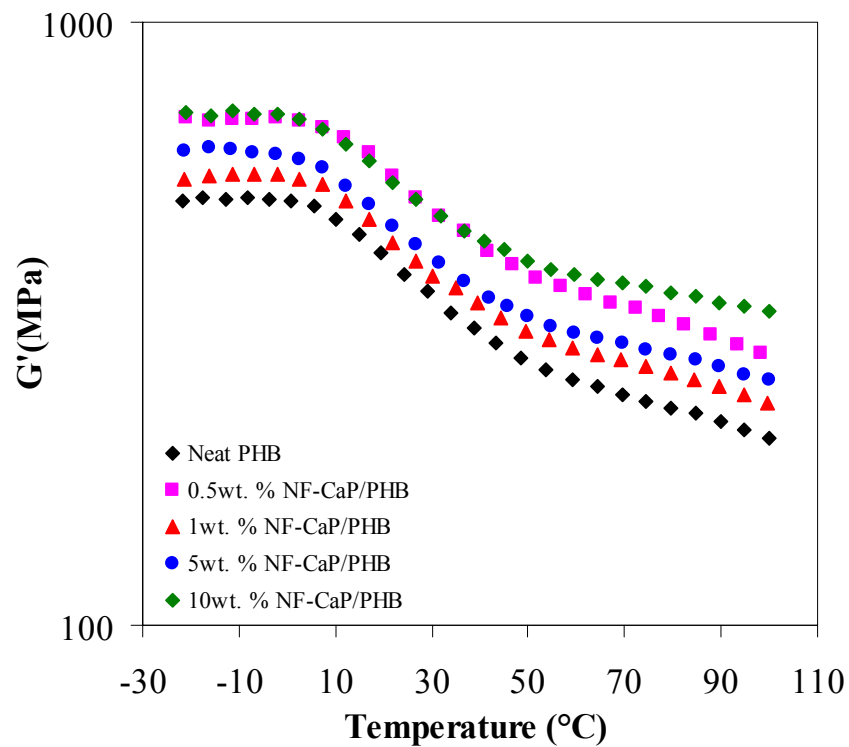


Figure D. 5. Shear storage modulus ( $G'$ ) values of neat PHB and (a) NS-CaP/PHB and (b) NF-CaP/PHB nanocomposite samples as a function of temperature at a frequency of 50 Hz.



(a)



(b)

Figure D. 6. Shear storage modulus ( $G'$ ) values of neat PHB and (a) NS-CaP/PHB and (b) NF-CaP/PHB nanocomposite samples as a function of temperature at a frequency of 10 Hz.

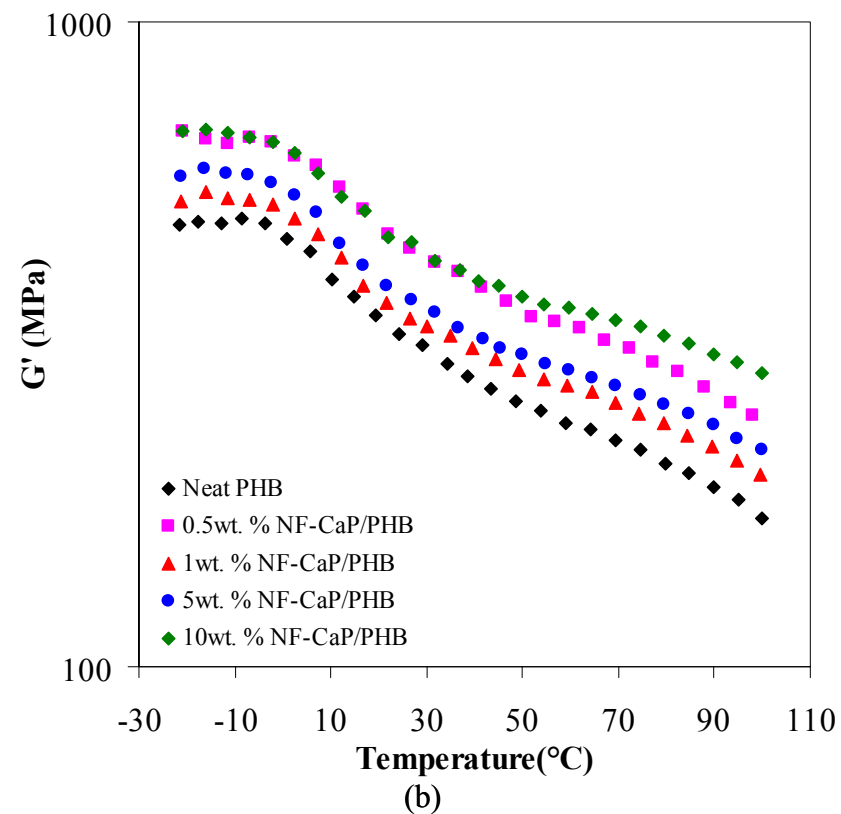
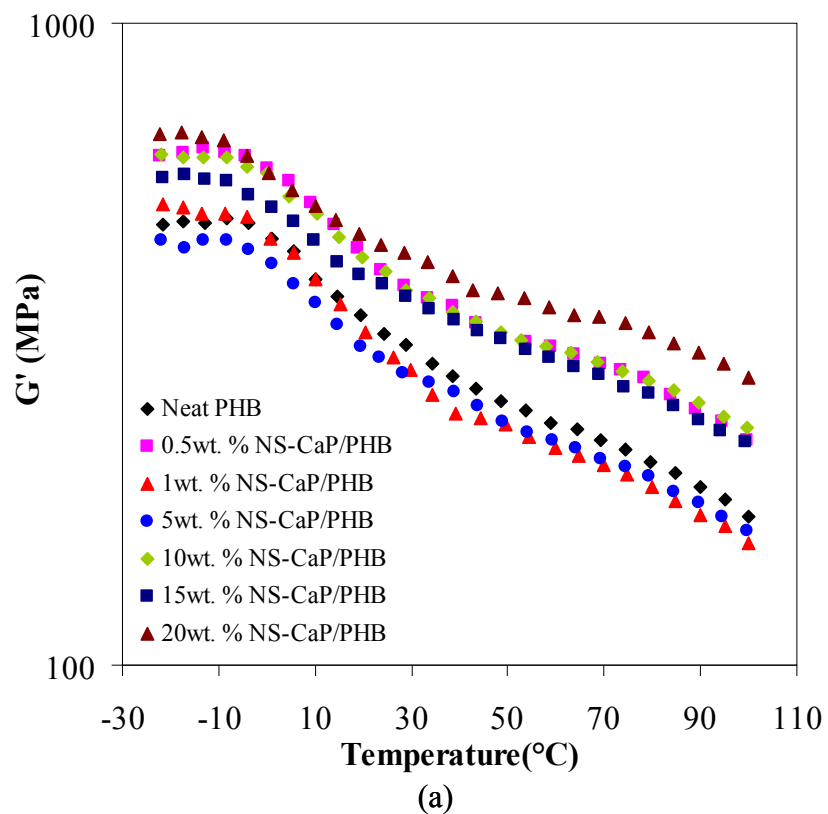


Figure D. 7. Shear storage modulus ( $G'$ ) values of neat PHB and (a) NS-CaP/PHB and (b) NF-CaP/PHB nanocomposite samples as a function of temperature at a frequency of 0.1 Hz.

Table D. 6. Thermogravimetric analysis of neat PHB, NS-CaP/PHB and NF-CaP/PHB nanocomposites. The temperature of 50% weight loss and peak temperature of degradation from derivative of weight% with respect to temperature.

Nanoparticle Concentration	HAp-NS-PHB Composites		NF-CaP/PHB Composites	
	Temp at 50% polymer wt. loss(°C)	Peak Temp of Deriv. Weight(%/ °C)	Temp at 50% polymer wt. loss(°C)	Peak Temp of Deriv. Weight(%/ °C)
0wt%	283.3 ± 1.3	287.3 ± 1.1	283.3 ± 1.3	287.3 ± 1.1
0.5wt%	280.6 ± 1.9	284.1 ± 1.9	282.4 ± 1.9	285.9 ± 2.1
1 wt%	277.9 ± 2.2	282.1 ± 1.7	291.8 ± 0.2	295.6 ± 0.4
5 wt%	289.3 ± 1.9	294.2 ± 1.7	294.2 ± 0.1	297.7 ± 0.0
10 wt%	287.6 ± 0.1	292.8 ± 0.3	293.2 ± 0.2	298.0 ± 0.3
15 wt%	281.9 ± 0.5	288.1 ± 0.8		
20 wt%	273.9 ± 0.1	281.0 ± 0.0		

## REFERENCES

1. Vaia RA, Maguire JF. Polymer nanocomposites with prescribed morphology: Going beyond nanoparticle-filled polymers. *Chemistry of Materials* 2007 May; 19(11):2736-2751.
2. Ciprari D, Jacob K, Tannenbaum R. Characterization of polymer nanocomposite interphase and its impact on mechanical properties. *Macromolecules* 2006 Sep; 39(19):6565-6573.
3. Dufresne A. Dynamic mechanical analysis of the interphase in bacterial polyester/cellulose whiskers natural composites. *Composite Interfaces* 2000; 7(1):53-67.
4. Pukanszky B. Interfaces and Interphases in multicomponent materials: past, present, future. *European Polymer Journal* 2005; 41:645-662.
5. Vollenberg PHT, Heikens D. Particle size dependence of the Young's Modulus of Filled Polymers: 1. Preliminary Experiments. *Polymer* 1989; 30(September):1656-1662.
6. Wu CL, Zhang MQ, Rong MZ, Friedrich K. Tensile performance improvement of low nanoparticles filled-polypropylene composites. *Composites Science and Technology* 2002; 62(10-11):1327-1340.
7. Kojima Y, Fukumori K, Usuki A, Okada A, Kurauchi T. Gas Permeabilities in Rubber Clay Hybrid. *Journal of Materials Science Letters* 1993 Jun; 12(12):889-890.
8. Yano K, Usuki A, Okada A, Kurauchi T, Kamigaito O. Synthesis and Properties of Polyimide Clay Hybrid. *Journal of Polymer Science Part A-Polymer Chemistry* 1993 Sep; 31(10):2493-2498.
9. Gilman JW, Kashiwagi T, Lichtenhan JD. Nanocomposites: A revolutionary new flame retardant approach. *SAMPE J* 1997 Jul-Aug; 33(4):40-46.
10. Winey KI, Vaia RA. Polymer nanocomposites. *MRS Bulletin* 2007 Apr; 32(4):314-319.
11. Gao HJ, Ji BH, Jager IL, Arzt E, Fratzl P. Materials become insensitive to flaws at nanoscale: Lessons from nature. *Proceedings of the National Academy of Sciences of the United States of America* 2003 May; 100(10):5597-5600.
12. Thostenson ET, Li CY, Chou TW. Nanocomposites in context. *Composites Science and Technology* 2005 Mar; 65(3-4):491-516.



13. Hussain F, Hojjati M, Okamoto M, Gorga RE. Review article: Polymer-matrix nanocomposites, processing, manufacturing, and application: An overview. *Journal of Composite Materials* 2006 Sep; 40(17):1511-1575.
14. Kojima Y, Usuki A, Kawasumi M, Okada A, Fukushima Y, Kurauchi T, Kamigaito O. Mechanical-Properties of Nylon 6-Clay Hybrid. *Journal of Materials Research* 1993 May; 8(5):1185-1189.
15. Kawasumi M, Hasegawa N, Kato M, Usuki A, Okada A. Preparation and mechanical properties of polypropylene-clay hybrids. *Macromolecules* 1997 Oct; 30(20):6333-6338.
16. Lan T, Kaviratna PD, Pinnavaia TJ. Mechanism of Clay Tactoid Exfoliation in Epoxy-Clay Nanocomposites. *Chemistry of Materials* 1995 Nov; 7(11):2144-2150.
17. Ray SS, Okamoto M. Polymer/layered silicate nanocomposites: a review from preparation to processing. *Progress in Polymer Science* 2003 Nov; 28(11):1539-1641.
18. Vaia RA, Ishii H, Giannelis EP. Synthesis and Properties of 2-Dimensional Nanostructures by Direct Intercalation of Polymer Melts in Layered Silicates. *Chemistry of Materials* 1993 Dec; 5(12):1694-1696.
19. Luo JJ, Daniel IM. Characterization and modeling of mechanical behavior of polymer/clay nanocomposites. *Composites Science and Technology* 2003 Aug; 63(11):1607-1616.
20. Alexandre M, Dubois P. Polymer-layered silicate nanocomposites: preparation, properties and uses of a new class of materials. *Materials Science & Engineering R-Reports* 2000 Jun; 28(1-2):1-63.
21. Tjong SC. Structural and mechanical properties of polymer nanocomposites. *Materials Science & Engineering R-Reports* 2006 Aug; 53(3-4):73-197.
22. Ke YC, Stroeve, P. *Polymer-Layered Silicate and Silica Nanocomposites*. First ed. Amsterdam: Elsevier, 2005.
23. Kim H, Macosko CW. Morphology and properties of polyester/exfoliated graphite nanocomposites. *Macromolecules* 2008 May; 41(9):3317-3327.
24. Pan YX, Yu ZZ, Ou YC, Hu GH. A new process of fabricating electrically conducting nylon 6/graphite nanocomposites via intercalation polymerization. *Journal of Polymer Science Part B-Polymer Physics* 2000 Jun; 38(12):1626-1633.
25. Zou JF, Yu ZZ, Pan YX, Fang XP, Ou YC. Conductive mechanism of polymer/graphite conducting composites with low percolation threshold. *Journal of Polymer Science Part B-Polymer Physics* 2002 May; 40(10):954-963.

26. Higgins BA, Brittain WJ. Polycarbonate carbon nanofiber composites. *European Polymer Journal* 2005 May; 41(5):889-893.
27. Kumar S, Doshi H, Srinivasarao M, Park JO, Schiraldi DA. Fibers from polypropylene/nano carbon fiber composites. *Polymer* 2002 Mar; 43(5):1701-1703.
28. Hu XL, Johnson RB, Schlea MR, Kaur J, Shofner ML. The effect of matrix morphology on nanocomposite properties. *Polymer* Feb; 51(3):748-754.
29. Ma HM, Zeng JJ, Realff ML, Kumar S, Schiraldi DA. Processing, structure, and properties of fibers from polyester/carbon nanofiber composites. *Composites Science and Technology* 2003 Aug; 63(11):1617-1628.
30. Patton RD, Pittman CU, Wang L, Hill JR. Vapor grown carbon fiber composites with epoxy and poly(phenylene sulfide) matrices. *Compos Pt A-Appl Sci Manuf* 1999; 30(9):1081-1091.
31. Endo M, Kim YA, Ezaka M, Osada K, Yanagisawa T, Hayashi T, Terrones M, Dresselhaus MS. Selective and efficient impregnation of metal nanoparticles on cup-stacked-type carbon nanofibers. *Nano Letters* 2003 Jun; 3(6):723-726.
32. Endo M, Kim YA, Hayashi T, Fukai Y, Oshida K, Terrones M, Yanagisawa T, Higaki S, Dresselhaus MS. Structural characterization of cup-stacked-type nanofibers with an entirely hollow core. *Applied Physics Letters* 2002 Feb; 80(7):1267-1269.
33. Jayaraman K, Kotaki M, Zhang YZ, Mo XM, Ramakrishna S. Recent advances in polymer nanofibers. *Journal of Nanoscience and Nanotechnology* 2004 Jan-Feb; 4(1-2):52-65.
34. Larrondo L, Manley RSJ. Electrostatic Fiber Spinning from Polymer Melts .1. Experimental-Observations on Fiber Formation and Properties. *Journal of Polymer Science Part B-Polymer Physics* 1981; 19(6):909-920.
35. Wong EW, Sheehan PE, Lieber CM. Nanobeam mechanics: Elasticity, strength, and toughness of nanorods and nanotubes. *Science* 1997 Sep; 277(5334):1971-1975.
36. Dresselhaus MS, Dresselhaus G, Charlier JC, Hernandez E. Electronic, thermal and mechanical properties of carbon nanotubes. *Philos Trans R Soc Lond Ser A-Math Phys Eng Sci* 2004 Oct; 362(1823):2065-2098.
37. Iijima S. Helical Microtubules of Graphitic Carbon. *Nature* 1991 Nov; 354(6348):56-58.
38. Eklund PC, Pradhan BK, Kim UJ, Xiong Q, Fischer JE, Friedman AD, Holloway BC, Jordan K, Smith MW. Large-scale production of single-walled carbon

- nanotubes using ultrafast pulses from a free electron laser. *Nano Letters* 2002 Jun; 2(6):561-566.
39. Thess A, Lee R, Nikolaev P, Dai HJ, Petit P, Robert J, Xu CH, Lee YH, Kim SG, Rinzler AG, Colbert DT, Scuseria GE, Tomanek D, Fischer JE, Smalley RE. Crystalline ropes of metallic carbon nanotubes. *Science* 1996 Jul; 273(5274):483-487.
  40. Kong J, Cassell AM, Dai HJ. Chemical vapor deposition of methane for single-walled carbon nanotubes. *Chemical Physics Letters* 1998 Aug; 292(4-6):567-574.
  41. Tibbetts GG. Why Are Carbon Filaments Tubular. *Journal of Crystal Growth* 1984; 66(3):632-638.
  42. Sjöström E. Wood chemistry : fundamentals and applications. New York :: Academic Press, 1981.
  43. Ranby BG. Cellulose and Muscle - The Colloidal Properties of Cellulose Micelles. *Discussions of the Faraday Society* 1951(11):158.
  44. Dubief D, Samain E, Dufresne A. Polysaccharide microcrystals reinforced amorphous poly(beta-hydroxyoctanoate) nanocomposite materials. *Macromolecules* 1999 Sep; 32(18):5765-5771.
  45. Carrara S. Nano-Bio-Technology and Sensing Chips: New Systems for Detection in Personalized Therapies and Cell Biology. *Sensors* Jan; 10(1):526-543.
  46. Biju V, Itoh T, Anas A, Sujith A, Ishikawa M. Semiconductor quantum dots and metal nanoparticles: syntheses, optical properties, and biological applications. *Anal Bioanal Chem* 2008 Aug; 391(7):2469-2495.
  47. Pileni MP. Nanosized particles made in colloidal assemblies. *Langmuir* 1997 Jun; 13(13):3266-3276.
  48. Pileni MP, Taleb A, Petit C. Silver metal nanosized particles: Control of particle size, self assemblies in 2D and 3D superlattices and optical properties. *Journal of Dispersion Science and Technology* 1998; 19(2-3):185-206.
  49. Qi LM, Ma JM, Cheng HM, Zhao ZG. Microemulsion-mediated synthesis of calcium hydroxyapatite fine powders. *Journal of Materials Science Letters* 1997; 16:1779-1781.
  50. Byrappa K, Adschiri T. Hydrothermal technology for nanotechnology. *Prog Cryst Growth Charact Mater* 2007; 53(2):117-166.
  51. Wei K, Wang YJ, Lai C, Ning CY, Wu DX, Wu G, Zhao NR, Chen XF, Ye RS. Synthesis and characterization of hydroxyapatite nanobelts and nanoparticles. *Materials Letters* 2005; 59:220-225.

52. Vijayakumar R, Koltypin Y, Felner I, Gedanken A. Sonochemical synthesis and characterization of pure nanometer-sized Fe<sub>3</sub>O<sub>4</sub> particles. *Materials Science and Engineering a-Structural Materials Properties Microstructure and Processing* 2000 Jun; 286(1):101-105.
53. Kundu S, Wang K, Liang H. Photochemical Generation of Catalytically Active Shape Selective Rhodium Nanocubes. *J Phys Chem C* 2009 Oct; 113(43):18570-18577.
54. Scaiano JC, Billone P, Gonzalez CM, Maretti L, Marin ML, McGilvray KL, Yuan N. Photochemical routes to silver and gold nanoparticles. *Pure Appl Chem* 2009 Apr; 81(4):635-647.
55. Zhu SP, Tang SC, Meng XK. Monodisperse Silver Nanoparticles Synthesized by a Microwave-Assisted Method. *Chin Phys Lett* 2009 Jul; 26(7):4.
56. Nie M, Sun K, Meng DD. Formation of metal nanoparticles by short-distance sputter deposition in a reactive ion etching chamber. *Journal of Applied Physics* 2009 Sep; 106(5):5.
57. Huang SX, Ma HY, Zhang XK, Yong FF, Feng XL, Pan W, Wang XN, Wang Y, Chen SH. Electrochemical synthesis of gold nanocrystals and their 1D and 2D organization. *J Phys Chem B* 2005 Oct; 109(42):19823-19830.
58. Deng XM, Hao JY, Wang CS. Preparation and mechanical properties of nanocomposites of poly(D,L-lactide) with Ca-deficient hydroxyapatite nanocrystals. *Biomaterials* 2001; 22:2867-2873.
59. Wang XJ, Li YB, Wei J, de Groot K. Development of biomimetic nano-hydroxyapatite/poly(hexamethylene adipamide) composites. *Biomaterials* 2002 Dec; 23(24):4787-4791.
60. Li HY, Chen YF, Xie YS. Photo-crosslinking polymerization to prepare polyanhydride/needle-like hydroxyapatite biodegradable nanocomposite for orthopedic application. *Materials Letters* 2003 Jun; 57(19):2848-2854.
61. Hong ZK, Qiu X, Sun JR, Deng MX, Chen XS, Jing XB. Grafting polymerization of L-lactide on the surface of hydroxyapatite nano-crystals. *Polymer* 2004; 45:6699-6706.
62. Hong Z, Zhang PB, He CL, Qiu XY, Liu AX, Chen L, Chen XS, Jing XB. Nano-composite of poly(L-lactide) and surface grafted hydroxyapatite: Mechanical properties and biocompatibility. *Biomaterials* 2005; 26:6296-6304.
63. Azevedo MC, Reis RL, Claase BM, Grijpma DW, Feijen J. Development and properties of polycaprolactone/hydroxyapatite composite biomaterials. *Journal of Materials Science-Materials in Medicine* 2003 Feb; 14(2):103-107.

64. Kalfus J, Jancar J. Elastic response of nanocomposite poly(vinylacetate)-hydroxyapatite with varying particle shape. *Polymer Composites* 2007 Jun; 28(3):365-371.
65. Du FM, Scogna RC, Zhou W, Brand S, Fischer JE, Winey KI. Nanotube networks in polymer nanocomposites: Rheology and electrical conductivity. *Macromolecules* 2004 Nov; 37(24):9048-9055.
66. Ramanathan T, Liu H, Brinson LC. Functionalized SWNT/polymer nanocomposites for dramatic property improvement. *J Polym Sci Pt B-Polym Phys* 2005; 43(17):2269-2279.
67. Kota AK, Cipriano BH, Duesterberg MK, Gershon AL, Powell D, Raghavan SR, Bruck HA. Electrical and rheological percolation in polystyrene/MWCNT nanocomposites. *Macromolecules* 2007 Oct; 40(20):7400-7406.
68. Yurekli K, Krishnamoorti R, Tse MF, McElrath KO, Tsou AH, Wang HC. Structure and dynamics of carbon black-filled elastomers. *Journal of Polymer Science Part B-Polymer Physics* 2001 Jan; 39(2):256-275.
69. Ceccia S, Ferri D, Tabuani D, Maffettone PL. Rheology of carbon nanofiber-reinforced polypropylene. *Rheol Acta* 2008 May; 47(4):425-433.
70. Kaur J, Shofner ML. Surface Area Effects in Hydroxyapatite/Poly(epsilon-caprolactone) Nanocomposites. *Macromol Chem Phys* 2009 Apr; 210(8):677-688.
71. Dorozhkin SV. Calcium orthophosphates. *Journal of Materials Science* 2007 Feb; 42(4):1061-1095.
72. Quinten RJP, Wolke Paul GC, Spauwen HM, John A. Jansen. *Tissue Engineering and Artificial Organs*. Third ed: Taylor & Francis Group, LLC, 2006.
73. Dorozhkin SV. Calcium orthophosphate-based biocomposites and hybrid biomaterials. *Journal of Materials Science* 2009 May; 44(9):2343-2387.
74. Murugan R, Ramakrishna S. Development of nanocomposites for bone grafting. *Composites Science and Technology* 2005 Dec; 65(15-16):2385-2406.
75. Elliott JC. *Studies in Inorganic Chemistry* 18. 1994 ed. Amsterdam: Elsevier Science B.V., 1994.
76. Aoki H. *Science and Medical Applications of Hydroxyapatite*. Tokyo: JAAS, 1991.
77. Winand L. Etude Physico-Chimique Du Phosphate Tricalcique Hydrate Et De Lhydroxylapatite. *Annales De Chimie France* 1961; 6(9-1):941.

78. Elliott JC. Structure and chemistry of the apatites and other calcium orthophosphates. Amsterdam [The Netherlands]: Elsevier, 1994.
79. Liou SC, Chen SY, Liu DM. Synthesis and characterization of needlelike apatitic nanocomposite with controlled aspect ratios. *Biomaterials* 2003 Oct; 24(22):3981-3988.
80. Eshtiagh-Hosseini H, Houssaindokht MR, Chahkandhi M, Youssefi A. Preparation of anhydrous dicalcium phosphate, DCPA, through sol-gel process, identification and phase transformation evaluation. *J Non-Cryst Solids* 2008 Aug; 354(32):3854-3857.
81. Mackie PE, Young RA, Elliott JC. Monoclinic Structure of Synthetic  $\text{Ca}_5(\text{PO}_4)_3\text{Cl}$ , Chlorapatite. *Acta Crystallographica Section B-Structural Crystallography and Crystal Chemistry* 1972; B 28(6):1840.
82. Young RA, Elliott JC. Atomic-Scale Bases for Several Properties of Apatites. *Arch Oral Biol* 1966; 11(7):699.
83. Prener JS. Growth and Crystallographic Properties of Calcium Fluor- and Chlorapatite Crystals. *J Electrochem Soc* 1967; 114(1):77.
84. Schlesinger PH, Blair HC, Teitelbaum SL, Edwards JC. Characterization of the osteoclast ruffled border chloride channel and its role in bone resorption. *J Biol Chem* 1997 Jul; 272(30):18636-18643.
85. Koumoulidis GCK, Katsoulidis AP, Ladavos AK, Pomonis PJ, Trapalis CC, Sdoukos, AT, Vaimakis TC. Preparation of hydroxyapatite via microemulsion route. *Journal of Colloid and Interface Science* 2003; 259:254-260.
86. Shirkhanzadeh M, Azadegan M. Hydroxyapatite Particles Prepared by Electrocrystallization from Aqueous-Electrolytes. *Materials Letters* 1993 Jan; 15(5-6):392-395.
87. Lerner E, Sarig S, Azoury R. Enhanced Maturation of Hydroxyapatite from Aqueous-Solutions Using Microwave Irradiation. *Journal of Materials Science-Materials in Medicine* 1991 Jul; 2(3):138-141.
88. Pileni MP. The role of soft colloidal templates in controlling the size and shape of inorganic nanocrystals. *Nature Materials* 2003 Mar; 2(3):145-150.
89. Fendler JH. Atomic and Molecular Clusters in Membrane Mimetic Chemistry. *Chemical Reviews* 1987 Oct; 87(5):877-899.
90. Xu W, Akins DL. Reverse micellar synthesis of CdS nanoparticles and self-assembly into a superlattice. *Materials Letters* 2004 Aug; 58(21):2623-2626.

91. Chiang CL. Controlled growth of gold nanoparticles in aerosol-OT/sorbitan monooleate/isooctane mixed reverse micelles. *Journal of Colloid and Interface Science* 2000 Oct;230(1):60-66.
92. Lai C, Tang SQ, Wang YJ, Wei K, Zhang SY. Insight into shape control mechanism of calcium phosphate nanoparticles in reverse micelles solution. *Synthesis and Reactivity in Inorganic Metal-Organic and Nano-Metal Chemistry* 2005; 35(9):717-725.
93. Wei K, Lai C, Wang YJ. Solvothermal synthesis of calcium phosphate nanowires under different pH conditions. *J Macromol Sci Part A-Pure Appl Chem* 2006 Oct; 43(10):1531-1540.
94. Uskokovic V, Drofenik M. Synthesis of materials within reverse micelles. *Surface Review and Letters* 2005 Apr; 12(2):239-277.
95. Ren W, Li SP, Wang YF, Cao XY, Chen XM. Preparation and characterization of nanosized hydroxyapatite particles in AOT inverse microemulsion. *Journal of Wuhan University of Technology-Materials Science Edition* 2004 Jun; 19(2):24-29.
96. Levinger NE. Water in confinement. *Science* 2002 Nov; 298(5599):1722-1723.
97. Wang YJ, Lai C, Wei K, Tang SQ. Influence of temperature, ripening time, and cosurfactant on solvothermal synthesis of calcium phosphate nanobelts. *Materials Letters* 2005; 59:1098-1104.
98. Palazzo G, Lopez F, Giustini M, Colafemmina G, Ceglie A. Role of the cosurfactant in the CTAB/water/n-pentanol/n-hexane water-in-oil microemulsion. 1. Pentanol effect on the microstructure. *J Phys Chem B* 2003 Feb; 107(8):1924-1931.
99. Kosak A, Makovec D, Drofenik M. Microemulsion synthesis of MnZn-ferrite nanoparticles. In: Uskokovic DP, Milonjic SK, Rakovic DI, editors. *Progress in Advanced Materials and Processes*. Zurich-Uetikon: Trans Tech Publications Ltd, 2004. p. 219-224.
100. Uota M, Arakawa H, Kitamura N, Yoshimura T, Tanaka J, Kijima T. Synthesis of High Surface Area hydroxyapatite nanoparticles by mixed surfactant-mediated Approach. *Langmuir* 2005; 21:4724-4728.
101. Bose S, Saha SK. Synthesis and Characterization of hydroxyapatite nanopowders by emulsion technique. *Chem Mater* 2003; 15:4464-4469.
102. Sonoda K, Furuzono T, Walsh D, Sato K, Tanaka J. Influence of emulsion on crystal growth of hydroxyapatite. *Solid State Ionics* 2002; 151:321-327.

103. Mohanty AK, Misra M, Drzal LT. Sustainable bio-composites from renewable resources: Opportunities and challenges in the green materials world. *J Polym Environ* 2002 Apr; 10(1-2):19-26.
104. Mohanty AK, Misra M, Hinrichsen G. Biofibres, biodegradable polymers and biocomposites: An overview. *Macromolecular Materials and Engineering* 2000 Mar; 276(3-4):1-24.
105. Nair LS, Laurencin CT. Biodegradable polymers as biomaterials. *Progress in Polymer Science* 2007 Aug-Sep; 32(8-9):762-798.
106. Rezwan K, Chen QZ, Blaker JJ, Boccaccini AR. Biodegradable and bioactive porous polymer/inorganic composite scaffolds for bone tissue engineering. *Biomaterials* 2006; 27(18):3413-3431.
107. Zinn M, Witholt B, Egli T. Occurrence, synthesis and medical application of bacterial polyhydroxyalkanoate. *Advanced Drug Delivery Reviews* 2001 Dec; 53(1):5-21.
108. Williams SF, Martin DP, Horowitz DM, Peoples OP. PHA applications: Addressing the price performance issue I. Tissue engineering. *International Journal of Biological Macromolecules* 1999 Jun-Jul; 25(1-3):111-121.
109. Mochizuki M, Hiram M. Structural effects on the biodegradation of aliphatic polyesters. *Polymers for Advanced Technologies* 1997 Apr; 8(4):203-209.
110. Pitt CG, Gratzl MM, Kimmel GL, Surles J, Schindler A. Aliphatic Polyesters 2. The Degradation of Poly(DL-Lactide), Poly( $\epsilon$ -caprolactone), and their Copolymers *In vivo*. *Biomaterials* 1981; 2(4):215-220.
111. Bittiger H, Marchess Rh, Niegisch WD. Crystal Structure of Poly( $\epsilon$ -caprolactone). *Acta Crystallographica Section B-Structural Crystallography and Crystal Chemistry* 1970; B 26(DEC15):1923.
112. Middleton JC, Tipton AJ. Synthetic biodegradable polymers as orthopedic devices. *Biomaterials* 2000 Dec; 21(23):2335-2346.
113. Steinbuchel A, Schlegel HG. Physiology and Molecular-Genetics of Physiology and Molecular-Genetics of Poly(Beta-Hydroxy-alkanoic acid) Synthesis in *Alcaligenes-Eutrophus*. *Mol Microbiol* 1991 Mar; 5(3):535-542.
114. Corniber J, Marchess R. Physical Properties of Poly-beta-hydroxybutyrate .4. Conformational-Aanalysis and Crystalline-Structure. *J Mol Biol* 1972; 71(3):735.
115. Chen GQ, Wu Q. The application of polyhydroxyalkanoates as tissue engineering materials. *Biomaterials* 2005 Nov; 26(33):6565-6578.



116. Mishra S, Sonawane SH, Singh RP. Studies on characterization of nano CaCO<sub>3</sub> prepared by the in situ deposition technique and its application in PP-nano CaCO<sub>3</sub> composites. *Journal of Polymer Science Part B-Polymer Physics* 2005 Jan; 43(1):107-113.
117. Douce J, Boilot JP, Biteau J, Scodellaro L, Jimenez A. Effect of filler size and surface condition of nano-sized silica particles in polysiloxane coatings. *Thin Solid Films* 2004 Nov; 466(1-2):114-122.
118. Liu H, Brinson LC. Reinforcing efficiency of nanoparticles: A simple comparison for polymer nanocomposites. *Compos Sci Technol* 2008 May; 68(6):1502-1512.
119. Cadek M, Coleman JN, Ryan KP, Nicolosi V, Bister G, Fonseca A, Nagy JB, Szostak K, Beguin F, Blau WJ. Reinforcement of polymers with carbon nanotubes: The role of nanotube surface area. *Nano Lett* 2004 Feb; 4(2):353-356.
120. Tsagaropoulos G, Eisenberg A. Dynamic-Mechanical Study of the Factors Affecting the 2 Glass-Transition Behavior of Filled Polymers - Similarities and Differences with Random Ionomers. *Macromolecules* 1995 Aug; 28(18):6067-6077.
121. Gagliardi S, Arrighi V, Ferguson R, Telling MTF. Restricted dynamics in polymer-filler systems. *Physica B* 2001 Jul; 301(1-2):110-114.
122. Kong LB, Ma J, Boey F. Nanosized hydroxyapatite powders derived from coprecipitation process. *J Mater Sci* 2002 Mar; 37(6):1131-1134.
123. Provencher SW. A constrained regularization method for inverting data represented by linear algebraic or integral equations. *Computer Physics Communications* 1982; 27(3):213-227.
124. Webb PA, Clyde O. Analytical methods in fine particle technology. Norcross, Georgia: Micromeritics Instruments Corp. , 1997.
125. Crescenzi V, Manzini G, Calzolari G, Borri C. Thermodynamics of Fusion of Poly-Beta-Propiolactone and Poly-Epsilon-Caprolactone - Comparative Analysis of Melting of Aliphatic Polylactone and Polyester Chains. *European Polymer Journal* 1972; 8(3):449-463.
126. Avrami M. Kinetics of phase change I - General theory. *Journal of Chemical Physics* 1939 Dec; 7(12):1103-1112.
127. Koutsopoulos S. Synthesis and characterization of hydroxyapatite crystals: A review study on the analytical methods. *Journal of Biomedical Materials Research* 2002 Dec; 62(4):600-612.
128. Arends J, Christoffersen J, Christoffersen MR, Eckert H, Fowler BO, Heughebaert JC, Nancollas GH, Yesinowski JP. A Calcium Hydroxyapatite

Precipitated from an Aqueous-Solution - an International Multimethod Analysis. *Journal of Crystal Growth* 1987 Sep; 84(3):515-532.

129. Roy M, Nelson JK, Reed CW, MacCrone RK, Keefe RJ, Zenger W, Schadler LS. Polymer nanocomposite dielectrics - The role of the interface. *IEEE Trns Dielectr Electr Insul* 2005 Aug; 12(4):629-643.
130. Lu YL, Zhang GB, Feng M, Zhang Y, Yang MS, Shen DY. Hydrogen bonding in polyamide 66/clay nanocomposite. *J Polym Sci Pt B-Polym Phys* 2003 Oct; 41(19):2313-2321.
131. Chen BQ, Evans JRG. Poly(epsilon-caprolactone)-clay nanocomposites: Structure and mechanical properties. *Macromolecules* 2006 Jan; 39(2):747-754.
132. Hao JY, Yuan ML, Deng XM. Biodegradable and biocompatible nanocomposites of poly(epsilon-caprolactone) with hydroxyapatite nanocrystals: Thermal and mechanical properties. *Journal of Applied Polymer Science* 2002 Oct; 86(3):676-683.
133. Alamo RG, Mandelkern L. Crystallization Kinetics of Random Ethylene Copolymers. *Macromolecules* 1991 Nov; 24(24):6480-6493.
134. Acierno S, Di Maio E, Iannace S, Grizzuti N. Structure development during crystallization of polycaprolactone. *Rheol Acta* 2006 Apr; 45(4):387-392.
135. Avella M, Bondioli F, Cannillo V, Di Pace E, Errico ME, Ferrari AM, Focher B, Malinconico M. Poly(epsilon-caprolactone)-based nanocomposites: Influence of compatibilization on properties of poly(epsilon-caprolactone)-silica nanocomposites. *Composites Science and Technology* 2006 Jun; 66(7-8):886-894.
136. Havet G, Isayev AI. A thermodynamic approach to the rheology of highly interactive filler-polymer mixtures. Part II. Comparison with polystyrene/nanosilica mixtures. *Rheol Acta* 2003 Jan; 42(1-2):47-55.
137. Hu YH, Chen CY, Wang CC. Viscoelastic properties and thermal degradation kinetics of silica/PMMA nanocomposites. *Polymer Degradation and Stability* 2004 Jun; 84(3):545-553.
138. Sternstein SS, Zhu AJ. Reinforcement mechanism of nanofilled polymer melts as elucidated by nonlinear viscoelastic behavior. *Macromolecules* 2002 Sep; 35(19):7262-7273.
139. Kalfus J, Jancar J. Immobilization of polyvinylacetate macromolecules on hydroxyapatite nanoparticles. *Polymer* 2007 Jun; 48(14):3935-3937.
140. Xi QA, Zhao CF, Yuan JZ, Cheng SY. The effects of polymer-nanofiller interactions on the dynamical mechanical properties of PMMA/CaCO<sub>3</sub>

- composites prepared by microemulsion template. *Journal of Applied Polymer Science* 2004 Mar; 91(5):2739-2749.
141. Nielsen LE, Landel RF. *Mechanical Properties of Polymers and Composites*. New York: Marcel Dekker, Inc., 1994.
  142. Lewis TB, Nielsen LE. Dynamic Mechanical Properties of Particulate-Filled Composites. *J Appl Polym Sci* 1970; 14(6):1449-1471.
  143. Bartczak Z, Argon AS, Cohen RE, Weinberg M. Toughness mechanism in semi-crystalline polymer blends: II. High-density polyethylene toughened with calcium carbonate filler particles. *Polymer* 1999 Apr; 40(9):2347-2365.
  144. Avella M, Errico ME, Gentile G. Nylon 6/calcium carbonate nanocomposites: Characterization and properties. *Macromol Symp* 2006; 234:170-175.
  145. Rao YQ, Pochan JM. Mechanics of polymer-clay nanocomposites. *Macromolecules* 2007 Jan; 40(2):290-296.
  146. Varlot K, Reynaud E, Kloppfer MH, Vigier G, Varlet J. Clay-reinforced polyamide: Preferential orientation of the montmorillonite sheets and the polyamide crystalline lamellae. *J Polym Sci Pt B-Polym Phys* 2001 Jun; 39(12):1360-1370.
  147. Shah D, Maiti P, Jiang DD, Batt CA, Giannelis EP. Effect of nanoparticle mobility on toughness of polymer nanocomposites. *Adv Mater* 2005 Mar; 17(5):525.
  148. Weon JI, Gam KT, Boo WJ, Sue HJ, Chan CM. Impact-toughening mechanisms of calcium carbonate-reinforced polypropylene nanocomposite. *J Appl Polym Sci* 2006 Mar; 99(6):3070-3076.
  149. Weon JI, Sue HJ. Mechanical properties of talc- and CaCO<sub>3</sub>-reinforced high-crystallinity polypropylene composites. *J Mater Sci* 2006 Apr; 41(8):2291-2300.
  150. Ning NY, Luo F, Wang K, Du RN, Zhang Q, Chen F, Fu Q. Interfacial enhancement by shish-calabash crystal structure in polypropylene/inorganic whisker composites. *Polymer* 2009 Jul; 50(15):3851-3856.
  151. Kodjie SL, Li LY, Li B, Cai WW, Li CY, Keating M. Morphology and crystallization behavior of HDPE/CNT nanocomposite. *J Macromol Sci Part B-Phys* 2006 Mar; 45(2):231-245.
  152. Khan J, Harton SE, Akcora P, Benicewicz BC, Kumar SK. Polymer Crystallization in Nanocomposites: Spatial Reorganization of Nanoparticles. *Macromolecules* 2009 Aug; 42(15):5741-5744.

153. Chavarria F, Paul DR. Comparison of nanocomposites based on nylon 6 and nylon 66. *Polymer* 2004 Nov; 45(25):8501-8515.
154. Zeng JJ, Saltysiak B, Johnson WS, Schiraldi DA, Kumar S. Processing and properties of poly(methyl methacrylate)/carbon nanofiber composites. *Compos Pt B-Eng* 2004; 35(3):245-249.
155. Kalfus J, Jancar J, Kucera J. Effect of weakly interacting morphology and viscoelastic. *Polym Eng Sci* 2008 May; 48(5):889-894.
156. Li YJ, Xu M, Feng JQ, Cao XL, Yu YF, Dang ZM. Effect of the matrix crystallinity on the percolation threshold and dielectric behavior in percolative composites. *J Appl Polym Sci* 2007 Dec; 106(5):3359-3365.
157. Shofner ML, Kaur J, Lee JH. Effect of Nanoparticles on Matrix Structure in Hydroxyapatite/ Polyhydroxybutyrate Nanocomposites. *Proceedings of the 2009 NSF Engineering Research and Innovation Conference, Honolulu, HI 2009.*
158. Barham PJ, Keller A, Otun EL, Holmes PA. Crystallization and Morphology of a Bacterial Thermoplastic - Poly-3-Hydroxybutyrate. *J Mater Sci* 1984; 19(9):2781-2794.
159. Organ SJ, Barham PJ. On the Equilibrium Melting Temperature of Polyhydroxybutyrate. *Polymer* 1993; 34(10):2169-2174.
160. Bassett DC, Olley RH, Alraheil IAM. On Crystallization Phenomena in PEEK. *Polymer* 1988 Oct; 29(10):1745-1754.
161. Pearce R, Marchessault RH. Multiple Melting in Blends of Isotactic and Atactic Poly(Beta-Hydroxybutyrate). *Polymer* 1994; 35(18):3990-3997.
162. Holdsworth PJ, Turner-Jones A. Melting Behavior of Heat Crystallized Poly(ethylene terephthalate). *Polymer* 1971; 12(3):195.
163. Barham PJ. Nucleation Behavior of Poly-3-Hydroxybutyrate. *J Mater Sci* 1984; 19(12):3826-3834.
164. Bauer H, Owen AJ. Some Structural and Mechanical Properties of Bacterially Produced Poly-Beta-Hydroxybutyrate-Co-Beta-Hydroxyvalerate. *Colloid Polym Sci* 1988 Mar; 266(3):241-247.
165. Khanna YP, Taylor TJ. Comments and Recommendations on the use of the Avrami-Equation for Physicochemical Kinetics. *Polym Eng Sci* 1988 Aug; 28(16):1042-1045.
166. Ong CJ, Price FP. Blends of Poly( $\epsilon$ -caprolactone) with Poly(vinyl chloride) .2. Crystallization Kinetics. *Journal of Polymer Science Part C-Polymer Symposium* 1977(63):59-75.

167. Owen AJ, Heinzl J, Skrbic Z, Divjakovic V. Crystallization and Melting Behavior of PHB and PHB/HV Copolymer. *Polymer* 1992; 33(7):1563-1567.
168. Miloaga DG, Hosein HAA, Misra M, Drzal LT. Crystallization of poly(3-hydroxybutyrate) by exfoliated graphite nanoplatelets. *J Appl Polym Sci* 2007 Nov; 106(4):2548-2558.
169. Hsu SF, Wu TM, Liao CS. Isothermal crystallization kinetics of poly(3-hydroxybutyrate)/layered double hydroxide nanocomposites. *J Polym Sci Pt B-Polym Phys* 2006 Dec ;44(23):3337-3347.
170. Sajkiewicz P, Di Lorenzo ML, Gradys A. Transient nucleation in isothermal crystallization of poly(3-hydroxybutyrate). *e-Polymers* 2009 Jul:16.
171. Zhang Q, Archer LA. Poly(ethylene oxide)/silica nanocomposites: Structure and rheology. *Langmuir* 2002 Dec; 18(26):10435-10442.
172. Pukanszky B, Fekete E. Adhesion and surface modification. *Mineral Fillers in Thermoplastics I*. Berlin: Springer-Verlag Berlin, 1999. p. 109-153.
173. Garces JM, Moll DJ, Bicerano J, Fibiger R, McLeod DG. Polymeric nanocomposites for automotive applications. *Adv Mater* 2000 Dec; 12(23):1835-1839.
174. Prasad PN. Polymer science and technology for new generation photonics and biophotonics. *Curr Opin Solid State Mat Sci* 2004 Jan; 8(1):11-19.
175. Kim HW, Song JH, Kim HE. Nanofiber generation of gelatin-hydroxyapatite biomimetics for guided tissue regeneration. *Adv Funct Mater* 2005 Dec; 15(12):1988-1994.
176. Ashrafi B, Hubert P, Vengallatore S. Carbon nanotube-reinforced composites as structural materials for microactuators in microelectromechanical systems. *Nanotechnology* 2006 Oct; 17(19):4895-4903.
177. Favier V, Canova GR, Cavaille JY, Chanzy H, Dufresne A, Gauthier C. Nanocomposite Materials from Latex and Cellulose Whiskers. *Polymers for Advanced Technologies* 1995 May; 6(5):351-355.
178. Avella M, Cosco S, Di Lorenzo ML, Di Pace E, Errico ME. Influence of CaCO<sub>3</sub> nanoparticles shape on thermal and crystallization behavior of isotactic polypropylene based nanocomposites. *J Therm Anal Calorim* 2005; 80(1):131-136.
179. Bilotti E, Zhang R, Deng H, Quero F, Fischer HR, Peijs T. Sepiolite needle-like clay for PA6 nanocomposites: An alternative to layered silicates? *Compos Sci Technol* 2009 Dec; 69(15-16):2587-2595.

180. Knauert ST, Douglas JF, Starr FW. The effect of nanoparticle shape on polymer-nanocomposite rheology and tensile strength. *J Polym Sci Pt B-Polym Phys* 2007 Jul; 45(14):1882-1897.
181. Me YP, Kohls D, Noda I, Schaefer DW, Akpalu YA. Poly(3-hydroxybutyrate-co-3-hydroxyhexanoate) nanocomposites with optimal mechanical properties. *Polymer* 2009 Sep; 50(19):4656-4670.
182. Sun YX, Guo GS, Tao DL, Wang ZH. Reverse microemulsion-directed synthesis of hydroxyapatite nanoparticles under hydrothermal conditions. *J Phys Chem Solids* 2007 Mar; 68(3):373-377.
183. Curri ML, Agostiano A, Manna L, Della Monica M, Catalano M, Chiavarone L, et al. Synthesis and characterization of CdS nanoclusters in a quarternary microemulsion: The role of the cosurfactant. *J Phys Chem B* 2000 Sep; 104(35):8391-8397.
184. Chen FX, Xu GQ, Hor TSA. Preparation and assembly of colloidal gold nanoparticles in CTAB-stabilized reverse microemulsion. *Mater Lett* 2003 Jul; 57(21):3282-3286.
185. Scandola M, Pizzoli M, Ceccorulli G, Cesaro A, Paoletti S, Navarini L. Viscoelastic and Thermal-Properties of Bacterial Poly(D-(-)-Beta-hydroxybutyrate). *Int J Biol Macromol* 1988 Dec; 10(6):373-377.
186. Schick C, Wurm A, Mohamed A. Vitrification and devitrification of the rigid amorphous fraction of semicrystalline polymers revealed from frequency-dependent heat capacity. *Colloid Polym Sci* 2001 Aug; 279(8):800-806.
187. Schick C, Wurm A, Mohammed A. Formation and disappearance of the rigid amorphous fraction in semicrystalline polymers revealed from frequency dependent heat capacity. *Thermochim Acta* 2003 Feb; 396(1-2):119-132.
188. Suzuki H, Grebowicz J, Wunderlich B. Glass-transition of Poly(oxyethylene). *British Polymer Journal* 1985; 17(1):1-3.
189. Sauer BB, Hsiao BS. Effect of the Heterogeneous Distribution of Lamellar Stacks on Amorphous Relaxations in Semicrystalline Polymers. *Polymer* 1995 Jun; 36(13):2553-2558.
190. Lin KL, Chang J, Cheng RM, Ruan ML. Hydrothermal microemulsion synthesis of stoichiometric single crystal hydroxyapatite nanorods with mono-dispersion and narrow-size distribution. *Mater Lett* 2007 Apr; 61(8-9):1683-1687.
191. Liu JB, Ye XY, Wang H, Zhu MK, Wang B, Yan H. The influence of pH and temperature on the morphology of hydroxyapatite synthesized by hydrothermal method. *Ceram Int* 2003; 29(6):629-633.

192. Viswanath B, Ravishankar N. Controlled synthesis of plate-shaped hydroxyapatite and implications for the morphology of the apatite phase in bone. *Biomaterials* 2008 Dec; 29(36):4855-4863.
193. Wang YJ, Chen JD, Wei K, Zhang SH, Wang XD. Surfactant-assisted synthesis of hydroxyapatite particles. *Mater Lett* 2006 Nov; 60(27):3227-3231.
194. Siddharthan A, Seshadri SK, Kumar TSS. Microwave accelerated synthesis of nanosized calcium deficient hydroxyapatite. *J Mater Sci-Mater Med* 2004 Dec; 15(12):1279-1284.
195. Gadsden JA. *Infrared spectra of minerals and related inorganic compounds*. London: Butterworths, 1975.
196. Tanaka Y, Nakamura M, Nagai A, Toyama T, Yamashita K. Ionic conduction mechanism in Ca-deficient hydroxyapatite whiskers. *Mater Sci Eng B-Adv Funct Solid-State Mater* 2009 Apr; 161(1-3):115-119.
197. Wu W, Nancollas GH. Nucleation and crystal growth of octacalcium phosphate on titanium oxide surfaces. *Langmuir* 1997 Feb; 13(4):861-865.
198. Zhang HB, Zhou KC, Li ZY, Huang SP. Plate-like hydroxyapatite nanoparticles synthesized by the hydrothermal method. *J Phys Chem Solids* 2009 Jan; 70(1):243-248.
199. Buzarovska A, Bogoeva-Gaceva G, Grozdanov A, Avella M. Crystallization behavior of polyhydroxybutyrate in model composites with kenaf fibers. *J Appl Polym Sci* 2006 Oct; 102(1):804-809.
200. Kannan S, Rebelo A, Lemos AF, Barba A, Ferreira JMF. Synthesis and mechanical behaviour of chlorapatite and chlorapatite/beta-TCP composites. *J Eur Ceram Soc* 2007; 27(5):2287-2294.
201. Potschke P, Fornes TD, Paul DR. Rheological behavior of multiwalled carbon nanotube/polycarbonate composites. *Polymer* 2002 May; 43(11):3247-3255.
202. Strawhecker KE, Manias E. Structure and properties of poly(vinyl alcohol)/Na<sup>+</sup> montmorillonite nanocomposites. *Chem Mat* 2000 Oct; 12(10):2943-2949.
203. Yang HC, Bhimaraj P, Yang L, Siegel RW, Schadler LS. Crystal growth in alumina/poly(ethylene terephthalate) nanocomposite films. *J Polym Sci Pt B-Polym Phys* 2007 Apr; 45(7):747-757.
204. Huglin MB, Radwan MA. Behavior of Poly(Beta-Hydroxybutyric Acid) in Dilute-Solution. *Polym Int* 1991; 24(2):119-123.

205. Grady BP, Paul A, Peters JE, Ford WT. Glass Transition Behavior of Single-Walled Carbon Nanotube-Polystyrene Composites. *Macromolecules* 2009 Aug; 42(16):6152-6158.
206. Wurm A, Ismail M, Kretzschmar B, Pospiech D, Schick C. Retarded Crystallization in Polyamide/Layered Silicates Nanocomposites caused by an Immobilized Interphase. *Macromolecules*; 43(3):1480-1487.
207. Balberg I, Anderson CH, Alexander S, Wagner N. Excluded Volume and its Relation to the Onset of Percolation. *Phys Rev B* 1984; 30(7):3933-3943.
208. Bug ALR, Safran SA, Webman I. Continuum Percolation of Rods. *Phys Rev Lett* 1985; 54(13):1412-1415.
209. Philipse AP. The random contact equation and its implications for (colloidal) rods in packings, suspensions, and anisotropic powders. *Langmuir* 1996 Mar; 12(5):1127-1133.
210. Chatterjee AP. Percolation thresholds for rod-like particles: polydispersity effects. *J Phys-Condens Matter* 2008 Jun; 20(25):5.
211. Skrbic Z, Divjakovic V. Temperature influence on changes of parameters of the unit cell of biopolymer PHB. *Polymer* 1996 Feb; 37(3):505-507.
212. Bhimaraj P, Yang H, Siegel RW, Schadler LS. Crystal nucleation and growth in poly(ethylene terephthalate)/alumina-nanoparticle composites. *J Appl Polym Sci* 2007 Dec; 106(6):4233-4240.
213. Guth E. Theory of Filler Reinforcement. *J Appl Phys* 1945; 16(1):20-25.
214. Cox HL. The Elasticity and Strength of Paper and other Fibrous Materials. *British Journal of Applied Physics* 1952; 3(MAR):72-79.
215. Agarwal BD. Analysis and performance of fiber composites. 2nd ed. ed. New York :: Wiley, 1990.
216. Currey JD. The mechanical adaptations of bones. Princeton, N.J.: Princeton University Press, 1984.
217. Owen AJ, Koller I. A note on the Young's modulus of isotropic two-component materials. *Polymer* 1996 Feb; 37(3):527-530.
218. Hui CY, Shia D. Simple formulae for the effective moduli of unidirectional aligned composites. *Polym Eng Sci* 1998 May; 38(5):774-782.
219. Gusev AA. Numerical identification of the potential of whisker- and platelet-filled polymers. *Macromolecules* 2001 Apr; 34(9):3081-3093.



- 220. Amjad Z. Calcium phosphates in biological and industrial systems: Boston: Kluwer Academic Publishers, 1998.
- 221. Notholt AJG, Sheldon RP, Davidson DF. Phosphate deposits of the world. Cambridge: Cambridge University Press, 1989.
- 222. Lide DR. The CRC handbook of chemistry and physics. 86th ed. Boca Raton, Florida: CRC Press, 2005.
- 223. Leiva A, Gargallo L, Radic D. Interfacial properties of poly(caprolactone) and derivatives. J Macromol Sci-Pure Appl Chem 2004 May; A41(5):577-583.
- 224. Smith R, Pitrola R. Influence of casting substrate on the surface free energy of various polyesters. J Appl Polym Sci 2002 Jan; 83(5):997-1008.
- 225. Lopes MA, Monteiro FJ, Santos JD, Serro AP, Saramago B. Hydrophobicity, surface tension, and zeta potential measurements of glass-reinforced hydroxyapatite composites. Journal of Biomedical Materials Research 1999 Jun; 45(4):370-375.